# Monolithic Integration of RF-MEMS Switches with Reconfigurable Phased Array Antennas

Christian James Aguilar Armenta
Thesis submitted for the degree of PhD
University of York
Department of Electronics

December 2013

# Abstract

This project presents a novel copper DC-contact RF-MEMS cantilever switch to operate with microstrip phased array antennas for the main frequency of operation of 12.5 GHz.

Effective performance, low cost, compact size, and full integration are the main requirements that phased array antennas and RF-MEMS technologies should meet to make an impact on the market. Then, a cost-effective all-monolithically integrated architecture of phased array antenna with RF-MEMS switches on a commercial printed circuit board (PCB) laminate has been developed as a solution.

A new manufacturing technique using photolithography processes has been developed for RF-MEMS cantilever switches based on thin copper films ($1\mu m$–$2\mu m$) on a PCB to address the cost and full integration requirements. This technique has allowed fabrication of various switches, of which the mechanical and electromagnetic performance have been measured and found to be suitable for operation with phased arrays.

The accomplishment of an all-monolithically integrated architecture has been demonstrated by means of simulations, having been able to electronically steer the main beam to different positions with acceptable radiation characteristics at 12.5 GHz. Therefore, in this work it has been possible to demonstrate that good performance and cost-effective phased array antennas are potentially viable by monolithically integrating reliable RF-MEMS on commercial PCBs.

Having reliable RF-MEMS built on PCB, there is potential to extend the areas of applications of this type of RF-MEMS, not only for phased array antennas but also for other attractive commercial applications. The research carried out in this project, moreover, represents an important contribution for further development of satisfactory RF-MEMS at very low cost for high frequency systems.

# Contents

# List of Figures

# List of Tables

# Acknowledgements

This thesis was made possible by a scholarship from the Consejo Nacional de Ciencia y Tecnologia (CONACyT).

My greatest thanks go to my supervisors Dr. Stuart Porter and Dr. Yuriy Zakharov for their patience, guidance, knowledge, insights, encouragement, and interest in this project. I would also like to thank Prof. Andy Marvin and Prof. Jeremy Everard for their constructive criticism and support. I am also very grateful to the technical staff, particularly to Dr. Iain Will, Mr. Jonathan Cremer, and Mr. Charanjit Panesar, who always gave me their support during my experiments in the clean room. Very special thanks to Mr. Mark Hough for his excellent technical support and for the several informal chats that we had about my project.

I would like to acknowledge my teachers from the National Autonomous University of Mexico (UNAM), particularly to Dr. Oleksadr Martynyuk who introduced me to the world of microwave devices and encouraged me to achieve my research interests. I would also like to acknowledge Dr. Jorge Cuevas for his support in my interest of pursuing research abroad.

I would like to thank my friends, especially those from the Electronics Department, for sharing many hours of happiness and enjoyable moments. My most truly thanks to my friends in Mexico who encouraged me to carry out with this life project, especially to my best friend Jorge Avila for his unconditional friendship.

On a more personal note, I would like to express my love and gratitude to those who have been suffering from my absence at home, my parents J. Guadalupe Aguilar Serrato and Martha L. Armenta Torres, who have always gave me their unconditional love, support, and encouragement for every decision I have made in my life. I take this space to express my endless admiration for my father and his unbounded wisdom of life. Heartfelt thanks are also due to both sides of my family: Aguilar and Armenta for their support.

Finally, I thank to my partner Anaclara for her unimaginable love, support, help, and trust for making this life project become a reality, fulling my life with happiness.

# Declaration

I declare that this thesis is the result of my own work except where due acknowledgement is given. Two papers have been published, and another one is under submission as part of the research developed in this work:

- Armenta, C. J. A., Porter, S., and Marvin, A.,“Reconfigurable Phased Array Antennas with RF-MEMS on a PCB substrate,” *In Proc. Loughborough Antennas and Propagation Conf. (LAPC), IEEE*, pages 1-5, 2012.
- Armenta, C. J. A., Porter, S., Will, I., and Marvin, A., “DC-Contact RF-MEMS Cantilever Switch on a PCB Substrate for Monolithic Integration with Microstrip Phased Array Antennas,” *In Proc. Loughborough Antennas and Propagation Conf. (LAPC), IEEE*, pages 467-472, 2013.
- Aguilar, C. J. and Porter, S. J., “Cantilever RF-MEMS for Monolithic Integration with Phased Array Antennas on a PCB” (Currently unpublished, under submission to *Journal of Microelectromechanical Systems, IEEE*).

# Chapter 1

# Introduction

## Contents

This work investigates and develops a novel Radio Frequency-Microelectromechanical Systems (RF-MEMS) switch for microstrip phased array antennas operating in the Ku-band (10.9-12.75 GHz) frequencies.

## 1.1 Phased Array Antennas

Antennas are at the front end of every telecommunication system. An antenna enables wireless communication between a transmitter and a receiver in free space by converting electric power to electromagnetic waves, and vice versa [1]. Each antenna has its own radiation pattern, which is the space distribution of the radiated energy when the antenna is transmitting, or the space distribution where the energy from a radiating source can be intercepted when the antenna is receiving [2]. Sometimes the radiation characteristics of a single antenna cannot cope with the demand of different communication systems as, for instance, when the antenna gain or the dynamic steering of the main radiation beam are crucial parameters. In such cases, phased array antennas can be helpful solutions.

A phased array antenna is a system of multiple antennas (radiating elements) in which the overall radiation pattern is reinforced in a desired direction towards a target in space. The main beam of the radiation is electronically steered using phase shift control when feeding each element [3]. This means that the system is able to steer the main beam without any mechanical motion of the array. The system is also able to dynamically scan the main beam in space using phase shifters to alter the phase of the individual elements. Phased array antennas can create a tracking system as well as multiple beams without moving the array.

These capabilities offer many benefits for different applications. Phased array antennas have been used for military radars [4], in various communications systems such as cellular base stations [5], automotive anti-collision radars [6], smart navigation systems [7], satellite communications [8], as well as other applications [9]. Research on phased array antennas for emerging wireless communication systems has increased in recent years [10]. Among fields that could particularly benefit from further research on this area stands out mobile land terminals for satellite communication systems (SATCOM), where there is a growing demand for effective antennas able to track the satellite while the user is in motion [11], [12], [13]. Phased array antennas are thus good candidates for solving these tracking demands. This is one of the possible applications discussed in this work, although the investigation developed here can be extended to others.

Phase shifters are essential components of phased array antennas. They are responsible for giving each array element a relative phase to electronically steer the main beam. There is potential to improve their effectiveness, and thus that of the entire system, reducing the complexity, power losses, and power consumption, by exploiting the advantages of RF-MEMS switches [14].

## 1.2 RF-MEMS Switches

RF-MEMS switches are integrated devices that use micromechanical movement to achieve an open or short circuit in an RF transmission line, covering frequencies up to 50 GHz [14]. Their main advantages include high isolation, low insertion loss, and low power consumption, compared to their counterparts like p-i-n diodes, Gallium Arsenide field-effect transistors (GaAs FETs), and silicon on insulator (SOI) transistors [15].

A recent analysis of the state-of-the-art of RF-MEMS [16], has shown developments in industrial and research sectors towards building reliable RF switches. For instance, switches based on silicon technology like the ones created by Omron [17] and Radant [18], have demonstrated very good performance up to 10 GHz. In the University of California-San Diego (UCSD) a reliable metal-contact Au cantilever switch has been developed, based on a high resistivity silicon substrate, operating up to 10 GHz [19]. However, cost and complexity of full integration with reconfigurable systems are major problems that current RF-MEMS technology faces to succeed in the market. This work focuses on the solution of these two main problems. There are also other aspects to improve, such as the reliability of switches for billions of cycles of actuation, high power handling, packing techniques, and low electrostatic actuation [16]. However these aspects are out of the scope of this project.

According to [16], recent advances in SiGe and CMOS technologies have virtually eliminated RF-MEMS from some areas of application. For instance, cost in cell phone front ends has been the crucial problem for RF-MEMS to compete in this market since semiconductor switches are typically US$0.12-0.16 for a single-pole four-throw (SP4T) switch, whereas the current value of RF-MEMS is of around US$100. High-dense integration and high-performance are other issues in which silicon on insulator (SOI) transistors have won the battle over RF-MEMS in technologies such as cellular and wireless networks for frequencies of 0.7 to 2.8 GHz.

Nevertheless, as it is also stated in [16], there are other applications well suited for RF-MEMS, where neither silicon nor GaAs technologies can meet their requirements. For instance, applications such as automated test equipment and spectrum analysers that use mechanical relays and p-i-n diodes can be replaced with RF-MEMS for better performance. Also, high frequency systems (2-50 GHz), such as satellite switching networks, wideband receivers/transmitters, and true-time-delay phase shifters are the most favourable applications of RF-MEMS because of their good performance at these frequencies.

Intelligent base-station antennas is the area of application that would directly benefit from this work, because as [16] suggests, RF-MEMS can be used for a new generation of intelligent base stations with beam scanning capabilities and pattern nulling for high interference systems. The application area is mostly in passive receive-only systems that require low-power handle circuits, in which RF-MEMS can operate properly. This further suggests the potential aptness of this work for using phased array antennas to solve the tracking demands of satellite systems for mobile land terminals, particularly in the Ku-band frequencies (10.9-12.75 GHz).

## 1.3 Hypothesis

The ambition of this work is to combine phased array antennas and RF-MEMS technologies in a cost-effective system, in order to obtain the benefits of both for applications such as receive-only intelligent antennas.

Microstrip antennas have been chosen as the main elements of the phased array because of their low cost and versatile fabrication on commercial laminate substrates by printed circuit board (PCB) techniques [20]. Because of incompatibilities between semiconductor and PCB technologies, degradation of the system performance, and cost issues arising from the integration of current RF-MEMS with antennas on PCB [14], it is attractive to develop a cost-effective integration process of RF-MEMS switches with phased array antennas on the same PCB. The hypothesis of this work states that:

> *"good performance and low cost phased array antennas can be achieved by monolithically integrating reliable RF-MEMS on commercial PCBs".*

Therefore, the challenge of this work is to create a low cost and simple technique of manufacturing RF-MEMS on commercial PCBs. Thus, the aim is to design a new all-monolithically integrated architecture of phased array antenna with RF-MEMS phase shifters on a PCB, with acceptable radiation characteristics.

## 1.4 Motivation and Scope of the Thesis

Some RF-MEMS switches [21], [22], [23], [24], [25], [26] compatible with PCB techniques have been reported in the literature. However the RF-MEMS are bridge-type switches on coplanar waveguide transmission lines (CPW), most of which use polyimide films that require complicated and highly precise manufacturing processes. Similarly, phase shifters on PCB [27], [28] use the loaded line technique requiring RF-MEMS bridges to obtain a phase shift. Thus, most of the reconfigurable antennas on PCB [29], [30], [31] rely either on these type of phase shifters or on bridge-type RF-MEMS. Other works like [32], [33] have reported reconfigurable arrays with RF-MEMS on different substrates using hybrid integrated circuit technology to incorporate the switches on the same board. However the hybrid integration results in a degradation of the system performance because of the potential increase of power losses in the system.

Consequently, this project focuses on a novel cantilever-type RF-MEMS switch built on commercial PCBs, using a low cost and simple fabrication process able to monolithically integrate the switch with phased array antennas on the same PCB. Such RF-MEMS should present an adequate electromagnetic performance to operate with the phased array at 12.5 GHz. Related works have been reported in [34], [35] on liquid crystal polymer (LCP) substrates, that use a multilayer design which increases the complexity of the fabrication process. Unlike these designs, the purpose of this project is a simple architecture of phased array antenna with RF-MEMS, using a single layer design on Rogers 4003c substrate.

Therefore in this project:

- A novel copper DC-contact RF-MEMS cantilever switch has been designed, fabricated, and measured at the frequency of operation of 12.5 GHz. The fabrication of this switch has been developed using a simple manufacturing technique, based on photolithography processes, able to monolithically integrate the switch with microstrip phased array antennas on a Rogers 4003c substrate.

- A microstrip digital phase shifter has been designed and implemented on Rogers 4003c substrate, using the switched delay-line technique, in order to use the RF-MEMS to dynamically change the connections of the delay-lines of the phase shifter, and to give each array element the required phase shift to electronically steer the main beam.
- Reconfigurable microstrip phased array antennas have been designed, fabricated, and measured on Rogers 4003c substrate, in order to demonstrate that low cost of production and good performance are potentially viable, incorporating cost-effective RF-MEMS cantilevers for an all-monolithically integrated architecture.

## 1.5 Original Contributions

This project presents three original contributions to phased array antennas and RF-MEMS technologies:

1. A reconfigurable $2 \times 2$ microstrip phased array antenna on Rogers 4003c, with two digital phase shifters based on the switched delay-line technique, suitable for the monolithic integration of eight DC-contact RF-MEMS cantilever switches at the frequency of operation of 12.5 GHz
2. A new manufacturing technique using photolithography processes for RF-MEMS cantilever switches based on thin copper films ($1\mu m - 2\mu m$) on Rogers 4003c substrate
3. A novel DC-contact RF-MEMS cantilever switch on Rogers 4003c for frequency of operation of 12.5 GHz

## 1.6 Outline of the Thesis

**Chapter 2** gives a general background of phased array antennas. An electromagnetic analysis is presented to describe the operability of phased arrays to steer the main beam to a desired direction. Models for electromagnetic analysis of microstrip antennas are given as well to present their main electromagnetic parameters, and a method to design rectangular microstrip antennas for a desired frequency of operation. Transmission line configurations for power distribution and impedance matching are provided for designing feeding networks for an array. Finally, possible applications of phased array antennas, particularly on satellite communications for land mobile terminals in the Ku-band frequencies, have been analysed.

**Chapter 3** gives a general background of RF-MEMS switches. Types, characteristics, models of analysis, and guidelines for designing RF-MEMS are exposed. The state-of-the-art of RF-MEMS is presented in order to point out different applications where this switch technology has a promising future, as well as those in which current technologies such as p-i-n diodes, FETs transistors, SiGe, and CMOS are not able to meet the requirements of these applications. Current issues and challenges of RF-MEMS are described, where cost, full integration, and reliable performance are the critical factors that have hindered the success of this technology in the market. Finally, a general background of digital phase shifter is given as well.

**Chapter 4** presents the design of a representative architecture of reconfigurable microstrip phased array antenna, suitable for the monolithic integration of RF-MEMS. The evaluation of the performance of this architecture is given as well. Therefore, simulations, measurements, and analysis of results of different physical designs of microstrip phased array antennas are provided, in order to describe the sequence of the procedure followed and the analysis developed in each design, to achieve the final architecture of reconfigurable phased array antenna.

**Chapter 5** presents a novel DC-contact RF-MEMS cantilever switch on Rogers 4003c substrate, able to operate with the reconfigurable phased array designed in Chapter 4. Simulation, fabrication, measurements, and analysis of results are provided, evaluating the mechanical and electromagnetic behaviour of various switches. The manufacturing technique of RF-MEMS cantilever switches on PCB is described as well. The evaluation and validation of the electromagnetic performance of the switches are given, presenting the analysis of the measurements of S-parameters of different switches built. Finally, the equivalent circuits of the RF-MEMS are obtained to demonstrate the adequate electromagnetic behaviour of an open and short circuit at 12.5 GHz.

**Chapter 6** presents a new all-monolithically integrated architecture of microstrip phased array antenna using the novel design of RF-MEMS developed in Chapter 5. The demonstration of the acceptable performance of the phased array with RF-MEMS switches on the same PCB is presented. Then, the evaluation of the electronically steering of the main beam with acceptable radiation characteristics is given as well, demonstrating that the dynamic reposition of the main beam is achievable using various RF-MEMS cantilever switches by manipulating their connections on the system.

**Chapter 7** presents the conclusions and future work that can be developed from this project. Then, the sequential procedure used to accomplish the aim of this work is reviewed, highlighting the main goals reached in this project. It also establishes the validity of the hypothesis.

# Chapter 2

# Background Analysis of Microstrip and Phased Array Antennas

## Contents

## 2.1 Introduction

Wireless communication systems have become crucial in the technological development of new systems that are able to provide network communication to mobile users. In these systems, antenna technology plays an important role, taking into account that the main purpose of a modern antenna is to enhance the communication between a transmitter and a receiver.

An array of antennas can be used to increase the overall gain and have more control over the radiation pattern, considering that the multiplicity of elements allows more precise determination [1]. Phased array antennas have the capability to create electronically steerable beam patterns in space without the necessity to physically move the array, using phase shift control at each element [3]. This characteristic offer many benefits for different applications [4], [5], [6], [7], [8], [9], [10]. In satellite communications (SATCOM), for example, a dynamic repositioning of the main beam would be crucial to maintain the communication link with the satellite when either the receiver or the transmitter is in motion [11], [12], [13]. This is an attractive area of application for phased array antennas.

The aim of this chapter is to present an analysis of the general background of phased array antennas, in order to understand and exploit the advantage of electronically steering their main beam to the desired direction, by manipulating the phase excitation at each element. Some of the fundamental parameters to evaluate their performance are presented as well. The methods for the analysis of the main electromagnetic characteristics and for the design of microstrip antennas are also exposed, as these are used as the main elements of the phased arrays. Additionally, the analysis of different transmission line configurations are presented for power distribution and impedance matching for the design of the feeding network. Finally, a possible application of the microstrip phased array antennas is explored, according to the new trends in mobile communications by considering a cost-effective design.

## 2.2 Phased Array Antennas

This part of the chapter focuses on the background of phased array antennas or arrays that are able to electronically steer their main beams towards the desired direction. This section is intended to provide the definition, electromagnetic analysis, and fundamental parameters that characterize linear and planar phased arrays, such as gain, directivity, bandwidth, beamwidth, side lobes, and scan loss, in order to have the essential parameters to design, measure, and evaluate the performance of the phased array antennas presented in Chapter 4. The purpose is to have the elements to design a representative architecture of reconfigurable microstrip phased array antenna, suitable for the monolithic integration of RF-MEMS on the same PCB, in order to demonstrate the electronically steering of the main beam.

### 2.2.1 Definition

Typical phased array antennas consist of multiple stationary elements of the same kind, distributed geometrically over a line, plane, or volume, which are fed coherently and use variable phase or time-delay control at each element to electronically scan the main beam to given angles in space [3].

Some of the main benefits of these antennas are their possibilities to produce multiple and simultaneous beams, modify the shape of the radiation pattern, or produce maximum radiation intensity toward a certain direction (main beam), as a result of the constructive and destructive interference of electromagnetic waves from the radiation of each element. According to [1] there are five controls that can be used to shape the overall pattern of an array. These are:

1. the geometrical distribution of the overall array;
2. the relative separation between the elements
3. the relative pattern of the individual elements
4. the excitation amplitude of the individual elements
5. the excitation phase of the individual elements

These controls allow a precise command over the radiation pattern and can work to avoid interference from some specific directions. Also, they have the potential to reduce the side lobes of the radiation pattern and provide better directivity. These controls can be applied together, or just one at a time, but the complexity of the system increases as the number of controls rises. For instance, the excitation amplitude control can be used in order to only modify the pattern shape.

In accordance with the aim of the project, this chapter focuses on the last control, where the array is fed coherently but with variable phase excitation or time-delay at each element, in order to steer the main beam to any desired angle in space without the necessity to physically move the array. Therefore, it can be said that phased array antennas are a particular case within the array theory. It is also important to specify that linear and planar distributions of phased array antennas of the same kind are the scenarios under analysis in this work, considering that they are the easiest configurations for accomplishing the aim of this work.

In order to generate electronically steerable beams, the phase variation is controlled by devices called phase shifters. Figure 2.1 shows an example of phased array antennas fed in parallel with their respective phase shifters at each element. This array performs a shifted plane wave front in the far-field.

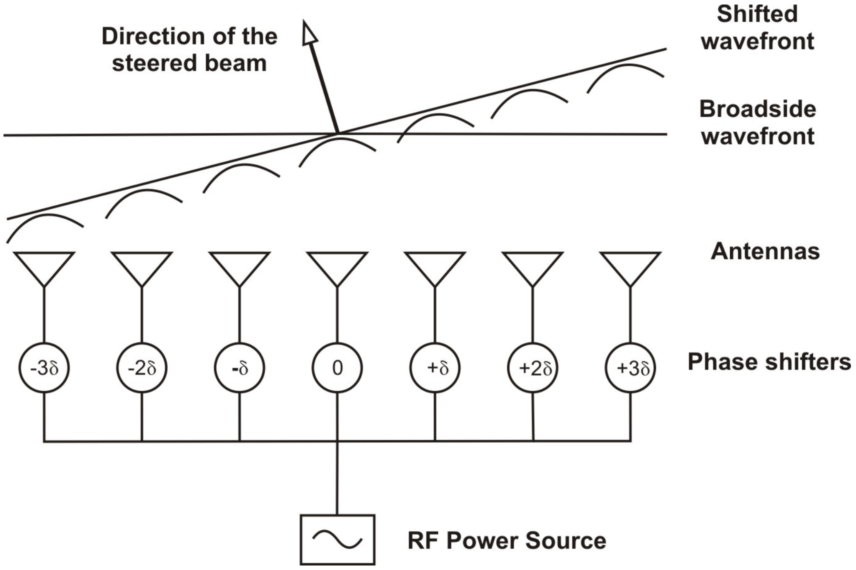

Figure 2.1: Phased array antennas with shifted wave front.

### 2.2.2 Classification

Phased array antennas can be classified as active or passive arrays [3]. Active phased array antennas are the ones that use solid-state amplifiers for either transmitting or receiving configurations. In this type of array, one of the possible configurations when the array is working as the transmitter, the signal goes through power amplifiers located just before each element. The inverse process happens when the array is working as the receiver because the signal goes through Low Noise Amplifiers (LNA) after it has passed through

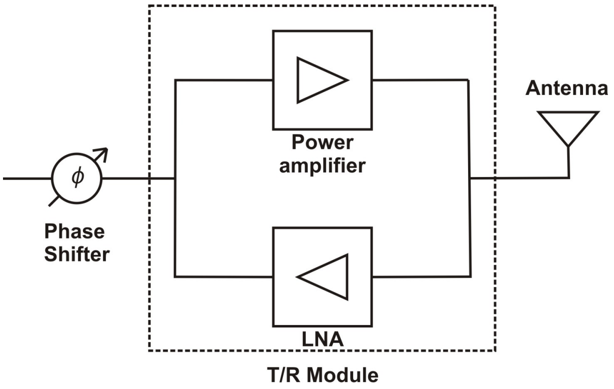

Figure 2.2: Single T/R module with solid-state amplifiers.

the antennas. Figure 2.2 presents an example of one single transmitter-receiver (T/R) module, where solid-state amplifiers are used for both the transmission and reception of a signal. Alternatively, passive phased array antennas are those that have a single RF power source when the array is transmitting, or a single receiver for the opposite case. Hence, the phase shifters and the antenna elements are the only ones in charge of modifying the phase of the signal and giving gain to the signal, respectively. Figure 2.3 shows some examples of these types of passive phased array antennas.

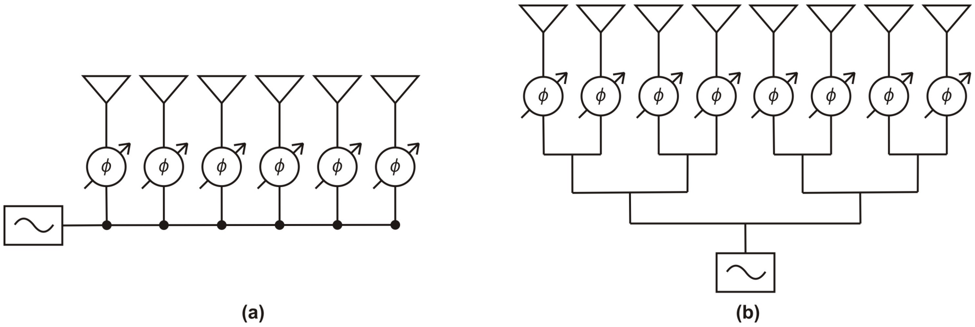

Figure 2.3: Passive phased array antennas. (a) Serial feed. (b) Parallel feed.

## 2.2.3 Analytical Pattern Multiplication

As mentioned above, phased array antennas produce a resultant plane wavefront in the far-field when constructive and destructive interferences happen between the electromagnetic waves radiated from each element of the array. Therefore, in order to know the resultant electric field at any point in space (P), it is necessary to consider many specific aspects from each element such as their exact electromagnetic model, and the interaction between them to have an accurate evaluation of the electric field vector at that point. However, the principle of pattern multiplication [36] grants a general insight into the electromagnetic behaviour in the far-field of arrays made up of nearly identical elements which are not isotropic. The analytical expression of the principle of pattern multiplication helps to obtain a general expression of the electric field generated from $N$ elements, which are arbitrarily positioned in space and fed with different current and phase. The analytical expression factorizes the general pattern of an array into an element pattern and an Array Factor (AF). In order to obtain the analytical expression of an arbitrary array, both the individual radiation pattern and the position of each element are considered. For overview of the explanation, Figure 2.4 shows the configuration of an arbitrary antenna array where each element radiates an electric field vector ($\vec{E_i}$) towards point P.

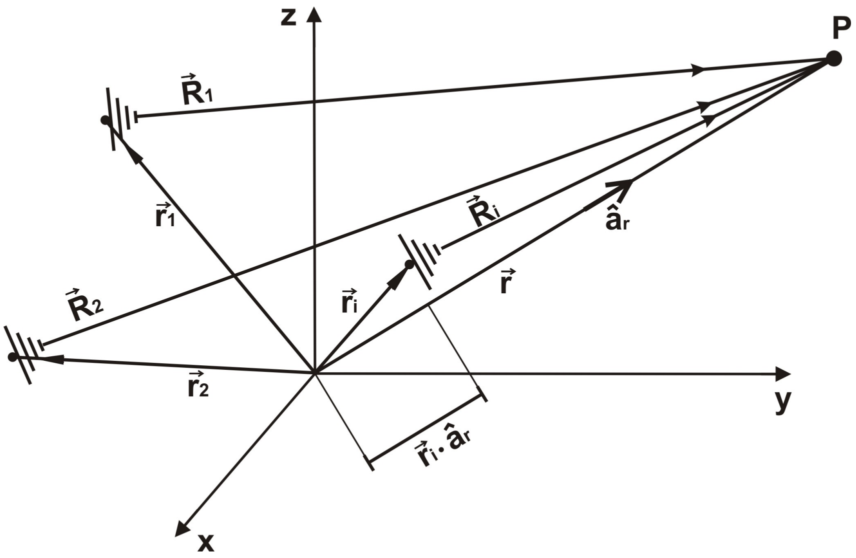

Figure 2.4: An arbitrary antenna array.

According to Figure 2.4 it is necessary to take into account some conditions for the analysis:

- all the elements ($N$) must be oriented towards point $P$, where the position of any element relative to the origin is given by the position vector $\vec{r_i}$
- the distance between the $i$-th element and point $P$ is given by the vector $\vec{R_i}$
- the position of the point $P$ is given by the vector $\vec{r}$
- the magnitude of the current and phase of the $i$-th element are $C_i$ and $\alpha_i$, respectively. Therefore, the current and phase excitation are given by the expression: $I_i = C_i e^{j\alpha_i}$.

Considering only a single element at the origin, a general expression for the electric field would be as follows:

$$\vec{E}_o = \frac{e^{-j\beta r}}{4\pi r}\vec{f}(\theta, \phi) \tag{2.1}$$

where $\beta = 2\pi/\lambda$ is the phase constant, $e^{-j\beta r}/4\pi r$ is the spherical wave dependence, and $\vec{f}(\theta, \phi)$ is the pattern element or the function that represents the radiation of each antenna. Then, to know the total electric field ($E_T$) produced by the array at point $P$, it is necessary to consider the electric field contribution from each element as follows:

$$\vec{E_T} = \vec{E_o} + \vec{E_1} + \vec{E_2} + ... + \vec{E_i} + ... + \vec{E_N} \tag{2.2}$$

Now, because the distance from the origin to the point $P$ is far away compared to the distance of any $i$-th element, the attenuation of the electric field from all the antennas is approximately the same at point P, and then it is possible to say that:

$$|\vec{R_1}| = |\vec{R_2}| = |\vec{R_i}| = |\vec{R_N}| = |\vec{r}| \tag{2.3}$$

However, in order to know the phase differences among the electric fields from the elements when all reach point P, it is necessary to consider the small path length difference between them. For that purpose, given that:

$$\vec{R_i} = \vec{r} - \vec{r_i} \cdot \vec{a_r} \tag{2.4}$$

where $\vec{a_r}$ is the unit vector of $\vec{r}$, the total electric field from the array is given by:

$$\begin{aligned} \vec{E_T} \simeq \frac{e^{-j\beta r}}{4\pi r}\vec{f}(\theta, \phi) + \\ + \frac{e^{-j\beta(r-\vec{r_1}\cdot\vec{a_r})}}{4\pi r}\vec{f}(\theta, \phi) + \\ + \frac{e^{-j\beta(r-\vec{r_2}\cdot\vec{a_r})}}{4\pi r}\vec{f}(\theta, \phi) + ... \\ + \frac{e^{-j\beta(r-\vec{r_i}\cdot\vec{a_r})}}{4\pi r}\vec{f}(\theta, \phi) + ... \\ + \frac{e^{-j\beta(r-r_{\vec{N}}\cdot\vec{a_r})}}{4\pi r}\vec{f}(\theta, \phi) \end{aligned} \tag{2.5}$$

The above equation is valid if the magnitudes and phases of the currents for each element are the same. Thus, taking into account the individual magnitude and phase of each element, the expression for the electric field is:

$$\begin{aligned}\vec{E_T} \simeq \sum_{i=0}^{N} \vec{E_i} \simeq C_0 e^{j\alpha_0} \frac{e^{-j\beta r}}{4\pi r} \vec{f}(\theta,\phi) + \\ C_1 e^{j\alpha_1} \frac{e^{-j\beta (r - \vec{r_1}\cdot\vec{a_r})}}{4\pi r} \vec{f}(\theta,\phi) + \\ C_2 e^{j\alpha_2} \frac{e^{-j\beta (r - \vec{r_2}\cdot\vec{a_r})}}{4\pi r} \vec{f}(\theta,\phi) + ... \\ + C_N e^{j\alpha_N} \frac{e^{-j\beta (r - \vec{r_N}\cdot\vec{a_r})}}{4\pi r} \vec{f}(\theta,\phi)\end{aligned} \tag{2.6}$$

and therefore, a general and compact expression for the array can be written as follows:

$$\vec{E_T} \simeq \frac{e^{-j\beta r}}{4\pi r} \left[\vec{f}(\theta,\phi)\right] \sum_{i=0}^{N} C_i e^{j\alpha_i + j\beta(\vec{r_i}\cdot\vec{a_r})} \tag{2.7}$$

From the above expression, the radiation pattern of an arbitrary array that satisfies the initial conditions, results from multiplying the individual radiation pattern of an element (considering that all of them are of the same kind) by another factor of an array of isotropic point sources, having the same relative position, amplitudes and phases of the individual antennas: the Array Factor (AF).

### 2.2.4 Graphic Pattern Multiplication

The analytical pattern multiplication has a particular scenario when all the elements in the array are aligned. Therefore if the geometry of both the pattern element and Array Factor are known, it is possible to apply a simple graphical analysis in order to have a relatively fast calculation of the array radiation pattern. This analysis consists of the graphic multiplication of the two radiation patterns. One of them is the individual radiation pattern of one of the antennas that belongs to the array, and the other is the Array Factor formed by the position of all the antennas but considering that these are isotropic. For example, if there is an array of two dipoles with one reflector, aligned and separated by $\lambda_0$, the array radiation pattern can be obtained by overlapping the drawings of the two patterns. This means that the resultant pattern is the region where both patterns overlap each other. Figure 2.5c shows in black colour the final radiation pattern of the array obtained through the graphical analysis. This is very useful if a quick calculation of the final radiation pattern from an aligned array is needed, instead of performing the derivations to find the analytical expression.

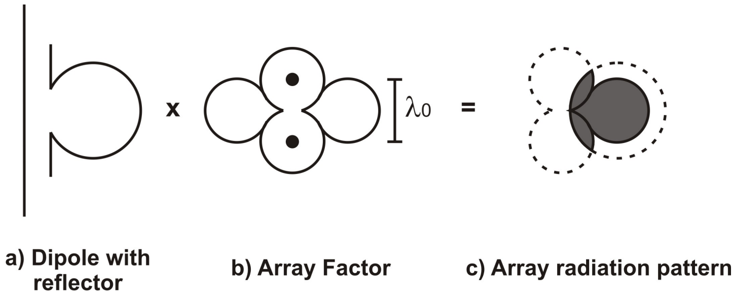

Figure 2.5: Graphic Pattern Multiplication.

### 2.2.5 Linear Array Analysis

The analytical pattern multiplication method has shown a practical synthesis for a generalized distribution of array elements in the space. However, in order to better understand how phased array antennas work, the analysis of an array of just two aligned isotropic antennas will be the first subject of this section, followed by the linear array of $n$ antennas, and finally the planar array of $m$ by $n$ elements.

In order to analyse the addition of the radiated electric fields from the elements in an array, let us first consider the equation of an electric field plane wave in the far-field from Maxwell's Equations. According to [37] the wave equation in its phasor form for a lossy ($\sigma \neq 0$), source-free ($\rho = 0$), linear and isotropic medium with only $\vec{x}$ component is:

$$\frac{\partial^2 E_x}{\partial z^2} - \gamma^2 E_x = 0 \tag{2.8}$$

where the complex propagation constant $\gamma$ is:

$$\gamma = j\omega\sqrt{\mu\varepsilon}\sqrt{1 - j\frac{\sigma}{\omega\varepsilon}} = \alpha + j\beta \tag{2.9}$$

and where the attenuation constant $\alpha$ and the phase constant $\beta$ are the real and the imaginary parts of Eq.(2.9), respectively. The solutions of this equation for the time harmonic case at frequency $\omega$ are:

$$E_x(z) = E_o^+ e^{-\gamma z} + E_o^- e^{\gamma z} \tag{2.10}$$

where $E_o^+$ and $E_o^-$ are arbitrary amplitude constants. Then, the solutions in the time domain are:

$$\mathcal{E}_x(z,t) = E_o^+ e^{-\alpha z}\cos(\omega t - \beta z) + E_o^- e^{-\alpha z}\cos(\omega t + \beta z) \tag{2.11}$$

From Eq.(2.11) it is possible to obtain the velocity of the wave, or the phase velocity, as follows:

$$\nu_p = \frac{dz}{dt} = \frac{d}{dt}\left(\frac{\omega t - constant}{\beta}\right) = \frac{\omega}{\beta} = \frac{1}{\sqrt{\mu\varepsilon}} \tag{2.12}$$

and the wavelength $\lambda$, which is the distance between two successive maximum or minimum values of the electric wave, can be obtained considering that at any time $t$ two maxima occur in one period. Therefore, $\lambda$ can be obtained as follows:

$$(\omega t - \beta z) - (\omega t - \beta(z + \lambda)) = 2\pi$$

$$(\omega t - \beta z - \omega t + \beta z + \beta\lambda) = 2\pi$$

$$\lambda = \frac{2\pi}{\beta} \quad \text{or} \quad \beta = \frac{2\pi}{\lambda} \tag{2.13}$$

where $\beta$ is the wavenumber. For the purpose of this work, it is convenient to express the solutions of the electric field in its phasor form to simplify the calculations:

$$E_x(z) = E_o^+ e^{-\alpha z} e^{-j\beta z} + E_o^- e^{\alpha z} e^{j\beta z} \tag{2.14}$$

With this representation, frequency $\omega$, amplitude $E_o$, and phase $\beta$ are invariant in time, which enables the management of the wave solution in steady state. Therefore, the phase shift of the electric field can be referred to the $e^{j\beta z}$ term.

As mentioned in Section 2.2.1, the properties of any array can be manipulated by changing the electrical length between the elements, the current or voltage amplitude, the pattern element, or the phase excitation in each element. For phased array antennas the phase excitation variable is the most important, although the amplitude is sometimes used as well to reduce the side lobes by tapering the array excitation following a specific distribution function [3]. In this work the amplitude excitation will remain constant and the phase excitation as the sole variable. However, in order to start the analysis of the phased array antennas, let us first consider a scenario with two isotropic antennas fed with the same magnitude and phase excitation, and equidistantly distributed in a lineal array over the $yz$-plane, located symmetrically with respect to the origin of the coordinates as the reference of the phase. Figure 2.6 displays the diagram for this purpose. In order to know the total electric field ($E_T$) at point P, which is in the far-field, it is necessary to consider the electric field contribution from each of the isotropic antennas. Therefore, if the point P is at distance longer than the space between the antennas, and taking into account that the radiation trajectories from each antenna are almost the same (parallel), as it was treated in the analytical pattern multiplication section, then it can be assumed that the magnitude of the electric field from each element is affected approximately by the same attenuation. However, strictly speaking, the radiation from the antenna 1 needs to travel a little more distance than the radiation from antenna 2, which means that these

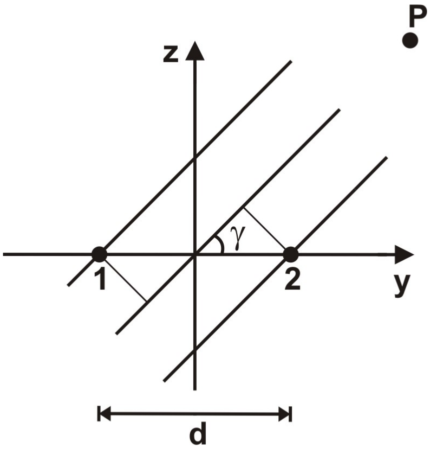

Figure 2.6: Isotropic antennas distributed equidistantly in a linear array.

radiations reach the point P with phase differences, or phase shift. The analysis can be mathematically explained as follows:

$$\vec{E}_T = \vec{E}_1 + \vec{E}_2 \tag{2.15}$$

The path length difference between both antenna 1 and antenna 2 with respect to the origin is approximately:

$$\frac{d}{2}\cos(\gamma) \tag{2.16}$$

then the radiation path length difference towards the point P between these antennas is:

$$d\cos(\gamma) \tag{2.17}$$

and to investigate the phase difference of each of the radiation paths to the point P, it is necessary to convert the length difference to a change of the phase by multiplying Eq.(2.17) by $\beta$ as follows:

$$\beta d\cos(\gamma) \tag{2.18}$$

each field can now be expressed as:

$$\begin{aligned}\vec{E}_1 &= E_o e^{-j\frac{\beta d}{2}\cos(\gamma)} \\ \vec{E}_2 &= E_o e^{j\frac{\beta d}{2}\cos(\gamma)}\end{aligned} \tag{2.19}$$

where $E_0$ is the amplitude of the field components at P, and if:

$$\Psi = \beta d\cos(\gamma) \tag{2.20}$$

each field is expressed as:

$$\begin{aligned}\vec{E}_1 &= E_o e^{-j\frac{\Psi}{2}} \\ \vec{E}_2 &= E_o e^{j\frac{\Psi}{2}}\end{aligned} \tag{2.21}$$

then the total electric field at point P from the two antennas is:

$$\vec{E}_T = E_o e^{-j\frac{\Psi}{2}} + E_o e^{j\frac{\Psi}{2}} \tag{2.22}$$

or:

$$\vec{E}_T = 2E_o \cos\frac{\Psi}{2} \tag{2.23}$$

Now if the number of elements is increased to, for example, 6 elements, it would be:

$$\vec{E}_T = 2E_o \left( \cos\frac{\Psi}{2} + \cos\Psi + \cos\frac{3\Psi}{2} \right) \tag{2.24}$$

which can easily be written in a compact expression for an infinite number of pairs of equidistantly separated antennas as:

$$\vec{E}_T = 2E_o \sum_{n=2,4,6...}^{\infty} \cos\frac{n}{4}\Psi \tag{2.25}$$

Thereby, it can be said that Eq.(2.25) is the expression of the total electric field, where the expression in the summation is the Array Factor (AF). With this mathematical analysis it is clear that the contribution of the phase of the electric field from each antenna at point P is different, because of the relative position that each element has with respect to P. Then, if the phase of each element is managed to create a specific radiation pattern, considering both the position of any point P in the space and the phase variation in the feed network at each element, it is possible to produce constructive and destructive interference among the electric waves in such a way as to steer the main beam to different directions.

Now with this analysis, it is plausible to consider an array capable of electronically steering the main beam to any desired angle by just manipulating the phase excitation. The scenario shown in Figure 2.7 can be considered for this purpose. Figure 2.7 shows an array of $n$ elements geometrically distributed over a straight line. These antennas are fed with the same amplitude excitation $|E_1| = |E_2| = |E_n| = 1$, and with equal phase difference ($\delta$) among the adjacent elements, as well as the distance ($d$) between them.

The total electric field ($E_T$) at point P can be obtained by the addition of all the

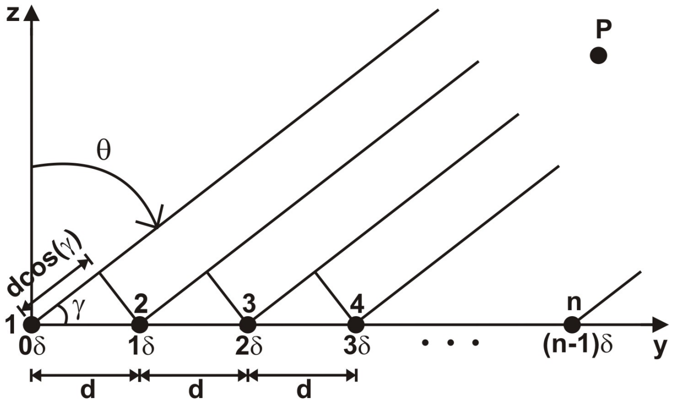

Figure 2.7: Linear array of isotropic antennas with progressive phase excitation.

electric fields from each element as follows:

$$\vec{E}_T = \vec{E}_1 + \vec{E}_2 + ... + \vec{E}_n \tag{2.26}$$

In the scenario of Figure 2.6, Eq.(2.20) shows that $\Psi$ is the expression for the phase shift caused by the path length difference only. In this scenario (Figure 2.7) $\Psi$ would include the phase shift caused by the path length difference plus the phase excitation ($\delta$) from the feeding network. Therefore, the phase excitation can be used to adjust the relative phase shift, in order to radiate maximum power towards P. For instance, considering antenna 1 as the reference in the origin, $\delta$ is the phase excitation in antenna 2 used to compensate the delay that the electric wave from antenna 1 suffers towards P, due to the difference in the path length between them. Therefore the value of $\delta$ in antenna 2 should be exactly the phase difference, which means that $\delta = -\beta d \cos(\gamma)$, in order to reach P with the same phase as antenna 1. Furthermore, in antenna 3, $\delta$ should be the double of the phase shift compensation, due to the double of the path length difference with respect to antenna 1, and in the same progressive manner for the rest elements. Consequently, $\Psi$ can be defined as:

$$\Psi = \beta d \cos(\gamma) + \delta \tag{2.27}$$

or as:

$$\Psi = \beta d \sin(\theta) + \delta \tag{2.28}$$

considering that $\theta$ and $\gamma$ are complementary angles. Then, the electric field from each element can be expressed as:

$$\begin{aligned}\vec{E}_1 &= 1e^{j0}; \\ \vec{E}_2 &= 1e^{j\Psi}; \\ \vec{E}_3 &= 1e^{j2\Psi}; \\ \vec{E}_n &= 1e^{j(n-1)\Psi};\end{aligned} \tag{2.29}$$

where the expression for the total electric field at point P is:

$$\vec{E}_T = 1 + e^{j\Psi} + e^{j2\Psi} + ... + e^{j(n-1)\Psi} \tag{2.30}$$

which in a more compact form can be expressed as:

$$\vec{E}_T = \sum_{1}^{N} e^{j(n-1)\Psi} \tag{2.31}$$

In order to obtain a simple expression, Eq.(2.30) can be multiplied by $e^{j\Psi}$:

$$\vec{E}_T e^{j\Psi} = e^{j\Psi} + e^{j2\Psi} + ... + e^{jn\Psi} \tag{2.32}$$

and if Eq.(2.32) is subtracted from Eq.(2.30), it is obtained:

$$\vec{E}_T(1 - e^{j\Psi}) = 1 - e^{jn\Psi}$$

or:

$$\vec{E}_T = \frac{1 - e^{jn\Psi}}{1 - e^{j\Psi}} \tag{2.33}$$

which can be rewritten as:

$$\vec{E}_T = \frac{-e^{jn\frac{\Psi}{2}}}{-e^{j\frac{\Psi}{2}}} \left( \frac{e^{jn\frac{\Psi}{2}} - e^{-jn\frac{\Psi}{2}}}{e^{j\frac{\Psi}{2}} - e^{-j\frac{\Psi}{2}}} \right)$$

then, the expression for the total electric field is:

$$\vec{E}_T = e^{j\xi} \left( \frac{\sin\left(n\frac{\Psi}{2}\right)}{\sin\left(\frac{\Psi}{2}\right)} \right); \qquad \xi = (n-1)\frac{\Psi}{2} \tag{2.34}$$

which in this case the expression in Eq.(2.34) is the same as that of the Array Factor of the elements in Figure 2.7, considering that the exponential has modulus unity. When $\Psi = 0$, Eq.(2.34) is indeterminate so that for this case $|\vec{E}_T|$ must be obtained as the limit of Eq.(2.34) as $\Psi$ approaches zero. Thus, it is necessary to calculate the limit as follows:

$$|\vec{E_T}| = \lim_{\Psi \to 0} \left( \frac{\sin\left(n\frac{\Psi}{2}\right)}{\sin\left(\frac{\Psi}{2}\right)} \right) = \lim_{\Psi \to 0} \left( \frac{\cos\left(n\frac{\Psi}{2}\right)\left(\frac{n}{2}\right)}{\cos\left(\frac{\Psi}{2}\right)\left(\frac{1}{2}\right)} \right) = n \tag{2.35}$$

The maximum value that $|\vec{E_T}|$ can attain is $n$. Thereby, when $\Psi$=0 it means that all the waves arrive in phase at point P, and maximum power is delivered.

In consequence, it is possible to electronically steer the main beam by controlling the phase excitation from the feeding network at each element. This can be visualized in the following example: to steer the main beam at $\gamma = 60°$ or $\theta = 30°$, and have maximum magnitude of the electric field in that direction, the value of $\delta$ must be found where $\Psi = 0$. Using the expressions (2.27), (2.28) and considering $d = \lambda_0/2$, it is possible to find $\delta$ as follows:

$$0 = \beta d \cos(\gamma) + \delta$$

or:

$$0 = \beta d \sin(\theta) + \delta$$

$$0 = \left(\frac{2\pi}{\lambda_0}\right)\left(\frac{\lambda_0}{2}\right)\cos(60°) + \delta$$

or:

$$0 = \left(\frac{2\pi}{\lambda_0}\right)\left(\frac{\lambda_0}{2}\right)\sin(30°) + \delta$$

$$\delta = -\pi/2 \tag{2.36}$$

This result means that the difference in the phase excitation between adjacent antennas has to be 90°. In other words, if antenna 1 is fed with 0°, antenna 2 should be with −90°, antenna 3 with −180°, and so on. In order to see the electric field pattern of six isotropic antennas equidistantly distributed, Figure 2.8 presents its polar plot considering the origin as the reference for both distance and phase reference as shown in the figure. This example demonstrates that phased array antennas have the potential to steer the beam electronically, and the advantage of manipulating this feature towards the benefit of many telecommunication system. However, there are many challenges that have to be addressed in phased array antennas systems in order to provide good performance for telecommunication systems. For example, in Figure 2.8 it can be seen that some side lobes appear due to the inclination of the main beam, which could affect one purpose of the array of avoiding interference from certain directions, if these lobes are big enough to receive undesirable signals. There is also the challenge of steering the beam dynamically

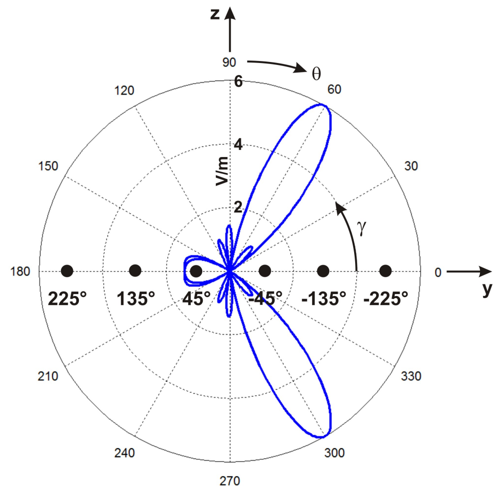

Figure 2.8: Electric field of a linear array of 6 isotropic antennas with steered beam.

at high speed, which means scanning the space from 0° to 180° in azimuth, and 0° to 90° in elevation, considering that there is no a cost-effective system for this purpose [11–13].

### 2.2.6 Planar Array Analysis

Up to now, the analysis of the Array Factor from $n$ elements in a linear array has been developed. In this section the analysis of $m$ by $n$ elements in a planar array are the subject of examination in order to obtain the corresponding expression to the Array Factor. For this purpose, it is necessary first to explain the 3-dimensional analysis. According to [1] and to the rectangular array of Figure 2.9, $\gamma$ is the angle between the axis of the array ($x$- or $y$-axis) and the radial vector from the origin to the observation point P.

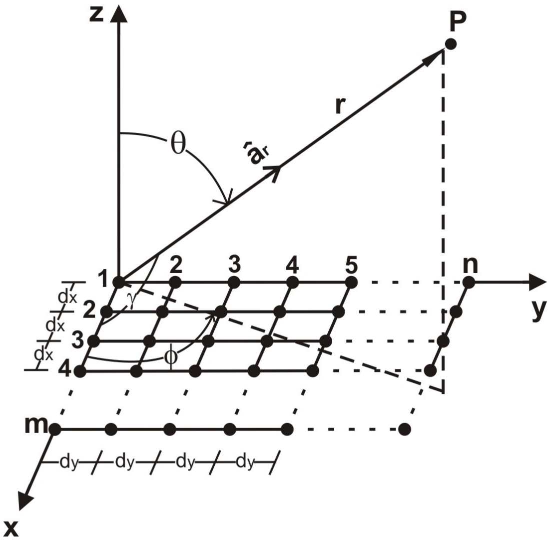

Figure 2.9: Rectangular Array.

The angle $\gamma$ can be obtained from the dot product of a unit vector along the axis of the array with a unit vector directed to the observation point P. Therefore, the planar array has to be studied as a sequence of linear arrays along and parallel to any of the axes ($x$ or $y$). Hence, considering first an array along the $y$-axis, the angle can be mathematically expressed as:

$$\cos\gamma = \hat{a}_y.\hat{a}_r = \hat{a}_y.(\hat{a}_x \sin\theta\cos\phi + \hat{a}_y \sin\theta\sin\phi + \hat{a}_z \cos\theta) = \sin\theta\sin\phi \tag{2.37}$$

and if the array is along the $x$-axis, the expression would be:

$$\cos\gamma = \hat{a}_x.\hat{a}_r = \hat{a}_x.(\hat{a}_x \sin\theta\cos\phi + \hat{a}_y \sin\theta\sin\phi + \hat{a}_z \cos\theta) = \sin\theta\cos\phi \tag{2.38}$$

Applying this analysis to the particular case of the planar array where the elements are along an axis, such as the $y$-axis explained in the previous section (Figure 2.7), $\Psi = \beta d \sin\theta\sin\phi$, where $\phi = 90°$ and thus the result would be exactly the same as the expression written in Eq.(2.28), without considering the phase excitation $\delta$. Nevertheless, to derive the array factor for the planar array shown in Figure 2.9, it is necessary to initially consider $m$ elements along the $x$-axis. The array factor can be written according to Eq.(2.31) as:

$$AF_x = \sum_{1}^{M} I_m e^{j(m-1)(\beta d_x \sin\theta\cos\phi + \delta_x)} \tag{2.39}$$

where $I_m$ is the excitation coefficient at each element, $d_x$ is the spacing between the elements along the $x$-axis, and $\delta_x$ is the progressive phase excitation at each element. Consequently, if $n$ such arrays are placed next to each other along the $y$-axis, with $d_y$ as the distance between them, and progressive phase excitation $\delta_y$ at each element as well, the array factor of the entire planar array can be expressed as the product of the array factors ($AF_x AF_y$) of both axes as follows:

$$AF_x AF_y = I_m \sum_{1}^{M} e^{j(m-1)(\beta d_x \sin\theta\cos\phi + \delta_x)} I_n \sum_{1}^{N} e^{j(n-1)(\beta d_y \sin\theta\sin\phi + \delta_y)} \tag{2.40}$$

where according to Eq.(2.28), $\Psi_x = \beta d_x \sin\theta\cos\phi + \delta_x$ and $\Psi_y = \beta d_y \sin\theta\sin\phi + \delta_y$. Therefore the normalized form of the planar array factor according to Eq.(2.34) can be expressed as:

$$AF = \left(\frac{1}{M}\frac{\sin\left(m\frac{\Psi_x}{2}\right)}{\sin\left(\frac{\Psi_x}{2}\right)}\right)\left(\frac{1}{N}\frac{\sin\left(n\frac{\Psi_y}{2}\right)}{\sin\left(\frac{\Psi_y}{2}\right)}\right) \tag{2.41}$$

This general analysis gives the fundamental elements to design rectangular arrays able to electronically steer their main beams toward any point in space.

### 2.2.7 Fundamental Parameters

Up to this point there are enough elements to understand how the electric fields from an array interfere at any point P in the space, by considering the geometrical distribution of the elements to obtain the Array Factor. A way of manipulating the phase excitation of these elements in order to have maximum radiation at that point has also been explained. Hence, the possibility to create electronically steerable beams by dynamically changing the phase excitation from the feeding network. However, in order to take advantage of this technique for different communication systems, it is necessary to evaluate the performance of the array by considering some fundamental parameters of the system. These practical parameters and specifications such as directivity, gain, beamwidth, bandwidth, side lobes, scanning loss, array size, and time-delays are essential to determine the scanning performance of the phase array system. In the next subsections is described the general way to evaluate these parameters according to [3], [1].

#### 2.2.7.1 Beamwidth

The half-power beamwidth at broadside for a linear array and for a planar array in its principal plane of scan is:

$$BW_{-3dB} = \frac{0.886 B_b \lambda_0}{L} \, rad \tag{2.42}$$

where $B_b$ is the broadening factor when tapering the amplitude by using different distributions of the feeding network, and which has unity value when the array is fed uniformly. Moreover, $L = Nd$ where $N$ is the number of elements separated by the distance $d$ for a linear array, or in the principal scan plane of a rectangular array of length L in the plane of scan. This expression changes a little when the main beam is scanned to any angle $\theta$ in space, because the pattern is displaced from broadside and the beamwidth is not constant in angle space, since it increases with scan angle according to the next equation:

$$BW_{-3dB} = \sin^{-1}(u_0 + 0.443 B_b \lambda_0 / L) - \sin^{-1}(u_0 - 0.443 B_b \lambda_0 / L) \, rad \tag{2.43}$$

where $u_0 = \sin\theta$. Figure 2.10 shows the variations of the beamwidth with respect to different normalized array sizes. For a large number of elements (N) in an array, the beamwidth from Eq.(2.43) increases approximately as $1/\cos\theta$.

#### 2.2.7.2 Directivity

The expression for the directivity of an array with uniform feeding amplitude at broadside in terms of its area is:

$$D_{max} = \frac{4\pi A}{\lambda_0^2} \tag{2.44}$$

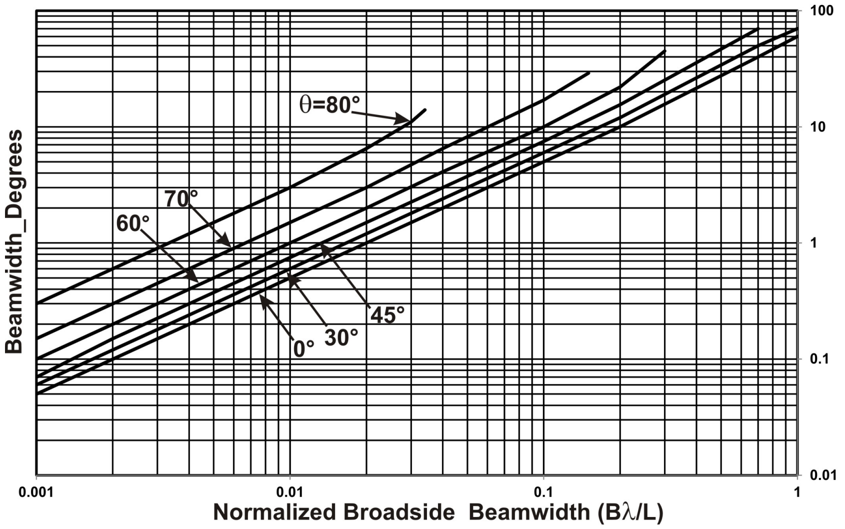

Figure 2.10: Beamwidth variation with scan.

where $A = L_x L_y$, $L_x = Nd_x$, and $L_y = Nd_y$. If both the aperture efficiency ($\varepsilon_A$) and the scan loss ($\cos\theta$) are considered, then the actual directivity for a large scanned aperture array is:

$$D_0 = \frac{4\pi A}{\lambda_0^2}\varepsilon_A \cos\theta \tag{2.45}$$

### 2.2.7.3 Gain and Scan loss

The expression for the gain of any antenna is related to its directivity by including the efficiency and the matching loss effects in the element as follows:

$$G = \varepsilon_L(1 - |\Gamma|^2)D_0 \tag{2.46}$$

where $\varepsilon_L$ is the efficiency loss, and $\Gamma$ is the reflection coefficient at the input terminal. The scan loss is not easy to predict because of the mutual impedances that exist between the elements, therefore there are some assumed scan dependences of the form $(\cos\theta)^n$, as shown in Figure 2.11, where it can be seen the expected scan loss for different steered angles.

### 2.2.7.4 Side lobes

All the lobes or peaks in the radiation pattern which are not the main beam, or the lobes with the highest directivity, are side lobes. The side lobes vary with the number of elements ($n$) and the spacing ($d$) between them in the array. In order to investigate where the side lobes occur in the radiation pattern of a linear array, it is necessary to present

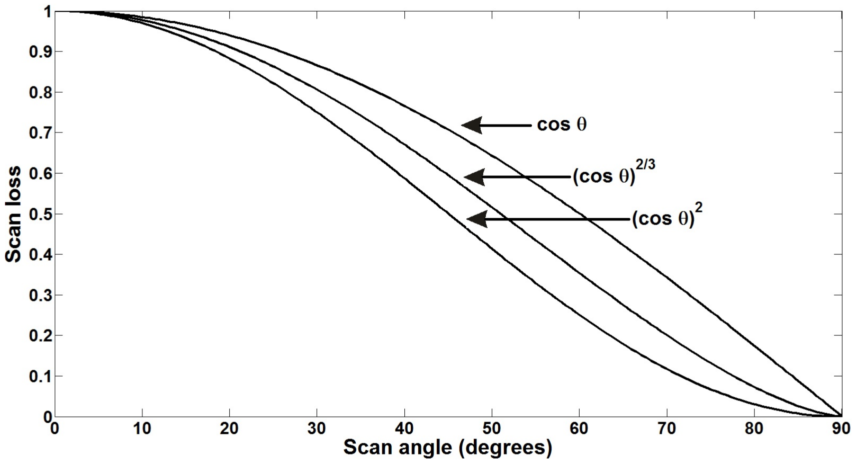

Figure 2.11: Typical scan loss curves.

first the normalized expression of Eq.(2.34) as follows:

$$\vec{E}_T = \left( \frac{\sin\left(n\frac{\Psi}{2}\right)}{\sin\left(\frac{\Psi}{2}\right)} \right)$$

The maximum value of Eq.(2.34) occurs when $\Psi = 0$, which means that $\gamma = 90^\circ$ (or $\theta = 0^\circ$). Then the maximum field intensity is $n$ times the field of one element, in the orthogonal direction of the plane that contains the antennas, because all the radiations from the elements arrive in phase, and this particular radiation is called Broadside. However, Eq.(2.34) will also have zeros at certain values of $\Psi$, corresponding to nulls in the radiation pattern, which are related to the side lobes of the array, because they are approximately midway between adjacent nulls. $\vec{E}_T$ is zero when:

$$n\frac{\Psi}{2} = p\pi \tag{2.47}$$

for $p = 1, 2, 3, etc.$ Therefore:

$$\cos\gamma = \frac{2p\pi}{n\beta d}$$

or:

$$\sin\theta = \frac{2p\pi}{n\beta d}$$

Then the first side lobe or the second maxima of the radiation pattern occurs when the numerator of $\vec{E}_T$ is maximum if:

$$\frac{n}{2} = (2m+1)\frac{\pi}{2} \tag{2.48}$$

for $m = 1, 2, 3, etc.$ Then the magnitude of the first side lobe is:

$$\frac{1}{\sin\left(\frac{\Psi}{2}\right)} = \frac{1}{\sin\left(\frac{3\pi}{2n}\right)} \tag{2.49}$$

Considering the approximation of the $\sin\left(\frac{3\pi}{2n}\right) \simeq \frac{3\pi}{2n}$ for a large value of $n$, and the normalized magnitude relative to the main lobe ($n$), it is obtained:

$$\frac{2}{3\pi} = 0.212 \tag{2.50}$$

which means that the first side lobe does not depend at all on the number of elements $n$, and that its magnitude is approximately $13.5\,dB$ below the main peak. Nevertheless, the rest of the side lobes depend on the number of elements and the spacing between them. In order to know how many of them are in an array pattern, the polynomial form of Eq.(2.30) can be considered as follows:

$$\vec{E}_T = (1 + Z + Z^2 + ... + Z^{n-1}); \quad \text{where} \quad Z = e^{j\Psi} \tag{2.51}$$

so this polynomial has $(n-1)$ roots or nulls, and according to Eq.(2.33) can be expressed Eq.(2.51) as:

$$\vec{E}_T = \left|\frac{Z^n - 1}{Z - 1}\right| \tag{2.52}$$

Then the null points are the roots of Eq.(2.52) excluding the $Z = 1$ root for $\Psi = 0$ ($\gamma = 90°$ or $\theta = 0°$) the main beam. On the complex plane, all these roots lie on the unit circle and divide it into $n$ equal parts. For example, considering the same scenario from Section 2.2.5 of an array of 6 elements, the unit circle is divided into 6 equal parts as shown in Figure 2.12.

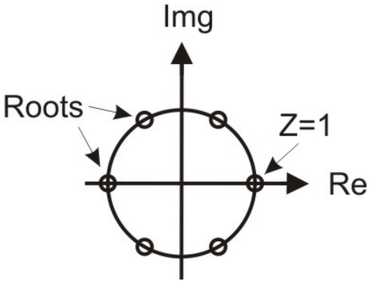

Figure 2.12: Unit circle with the roots of the polynomial.

According to Figure 2.7, as $\gamma$ goes from 0° to 180° for the half of the radiation pattern (the other half goes from 180° to 360°, by symmetry), then:

$$-1 < \cos\gamma < 1 \tag{2.53}$$

$$-\frac{2\pi d}{\lambda_0} < \Psi < \frac{2\pi d}{\lambda_0} \tag{2.54}$$

and if considering that the spacing between the antennas is $d = \lambda_0/2$, the range values of $\Psi$ are:

$$-\pi < \Psi < \pi \tag{2.55}$$

Therefore, the visible nulls of $\Psi$ in the complex plane, corresponding to the 6 elements are:

$$\Psi = -\pi, \quad -2\pi/3, \quad -\pi/3, \quad \pi/3, \quad 2\pi/3, \quad \pi; \tag{2.56}$$

whereas from Eq.(2.20) the values for $\gamma$ are obtained as follows:

$$\gamma = 180^\circ, \quad 131.8^\circ, \quad 109.4^\circ, \quad 70.5^\circ, \quad 48.1^\circ, \quad 0^\circ; \tag{2.57}$$

Hence the radiation pattern is shown in Figure 2.13, where the nulls correspond to the values of $\gamma$, and the number of side lobes are four. For arrays with scanned beams at different angles distinct to the broadside, there is a criterion for the maximum element spacing at frequency ($f_0$) in order to avoid substantial side lobes [3]. The condition is:

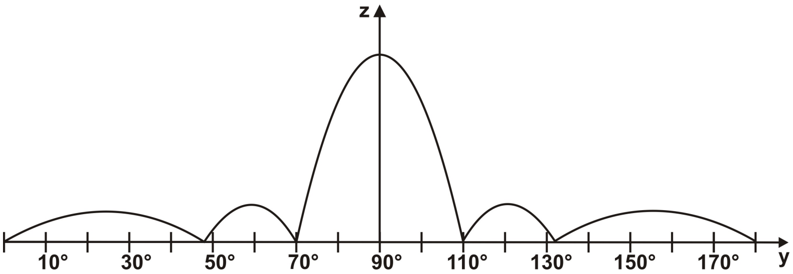

Figure 2.13: Radiation pattern.

$$\frac{d}{\lambda_0} \leq \frac{1}{1+\sin(\theta)} \tag{2.58}$$

where $\lambda_0$ is the wavelength in free space and $\theta$ is the given angle in the space.

#### 2.2.7.5 Bandwidth

As reported by [1], the bandwidth of an antenna is the range of frequencies in which the antenna presents acceptable performance in agreement with some specific standard of operation. The bandwidth can be considered to be the range of frequencies, on either side of a centre frequency, where the antenna characteristics such as input impedance, radiation pattern, beamwidth, polarization, side lobe level, gain, directivity, beam direction, and radiation efficiency are within an acceptable value of those at the centre frequency. However these characteristics do not necessary vary in the same manner, or can be critically affected by the frequency. Therefore, the specifications for the bandwidth are set for the particular application. In this work, the bandwidth will be obtained from the range of frequencies in which the magnitude of the gain or the directivity of the main beam is not lower than $-3\,dB$ with respect to the highest value at the frequency of operation.

Additionally, according to [3] it is important to consider that the bandwidth of an array is often restricted by using phase shifters other than those based on time-delay networks. It is also stated that as the array increases its size, the narrower the bandwidth becomes, as well as increasing the scanned angle of the main beam.

#### 2.2.7.6 Array Size

One of the main parameters that determines the size of an array is the required gain for the specific application. For the case of passive or active transmitting arrays, an important element to take into account is the Effective Isotropic Radiated Power (EIRP). If the arrays are large enough to guarantee approximately the same power distribution at each element, this term can be obtained as follows:

Transmitting passive array:

$$EIRP = N\varepsilon_L P_{in}(D_{cell})(1-|\Gamma|^2) \tag{2.59}$$

where $\varepsilon_L$ is the loss efficiency which accounts for the dissipative loss in both the feeding network and phase shifters. $D_{cell}$ is the directivity of one cell of a periodic array and is defined as:

$$D_{cell} = \frac{4\pi}{\lambda_0^2}(d_x d_y)\cos\theta \tag{2.60}$$

Transmitting active array:

$$EIRP = N^2\varepsilon_L P_{amp}(D_{cell})(1-|\Gamma|^2) \tag{2.61}$$

where $P_{amp}$ is the amplifiers output power.

For the case of receiving arrays, the antenna gain-to-noise-temperature $(G/T_s)$ is a figure of merit in the characterization of the reception gain in terms of the effective antenna noise temperature. For real antennas, the noise temperature is obtained by considering the noise from the radiation pattern $(T_B)$, and from the dissipative losses within the antenna and transmission lines $(T_a)$, as shown in Figure 2.14, where $T_A$ is the antenna

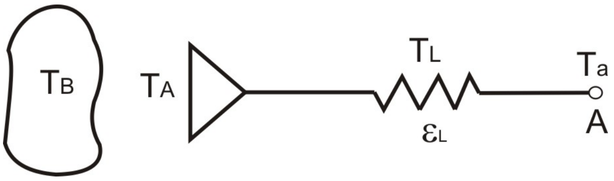

Figure 2.14: Real antenna noise temperature model.

noise temperature, $T_L$ is the noise temperature of the lossy line, and point $A$ where the antenna noise is measured. Therefore, the $G/T_s$ ratio can be obtained using the following expressions:

Receiving passive array:

$$\begin{aligned} G &= D_0 \varepsilon_L (1 - |\Gamma|^2) \\ T_a &= \varepsilon_L T_A + T_0(1 - \varepsilon_L) \\ T_s &= T_a + (F_R - 1)T_0 \end{aligned} \tag{2.62}$$

Receiving active array:

$$\begin{aligned} G &= D_0 (1 - |\Gamma|^2) \\ T_a &= T_A \\ T_s &= (F - 1)T_0 + T_a \end{aligned} \tag{2.63}$$

where $\varepsilon_L$ is the network loss, $T_0$ is the room temperature and equivalent to $T_L$, $F_R$ and $F$ are the noise figure of the passive and active array receivers, respectively. The expression to obtain the $G/T_s$ ratio for both cases is:

$$G/T_s = G\,dB - 10 \log T_s \quad dB/K \tag{2.64}$$

Another important factor to consider for the gain of an array is the loss caused by transmission lines from the feeding network. These losses limit the overall gain of the array, even if the number of elements increases linearly. For an array with $N$ square elements, with distance $d$ in either direction, and feeding each element by equal length transmission lines of $(N^{1/2} - 1)d$, the maximum array gain is:

$$G = \frac{4\pi A}{\lambda_0^2} 10^{-(d/\lambda_0)(N^{1/2}-1)(\alpha_{dB/\lambda_0})/10} \tag{2.65}$$

where $\alpha_{dB/\lambda_0}$ is the attenuation loss of the transmission line in decibels per wavelength. This formula does not include losses due to the power dividers, and assumes that all elements are matched. Figure 2.15a shows gain curves for passive arrays with different number of matched elements separated at distance $d = 0.5\lambda_0$ for various values of attenuation. Figure 2.15b shows the $G/T_s$ ratio for passive and active receiving arrays with the same line attenuation factors used in Figure 2.15a.

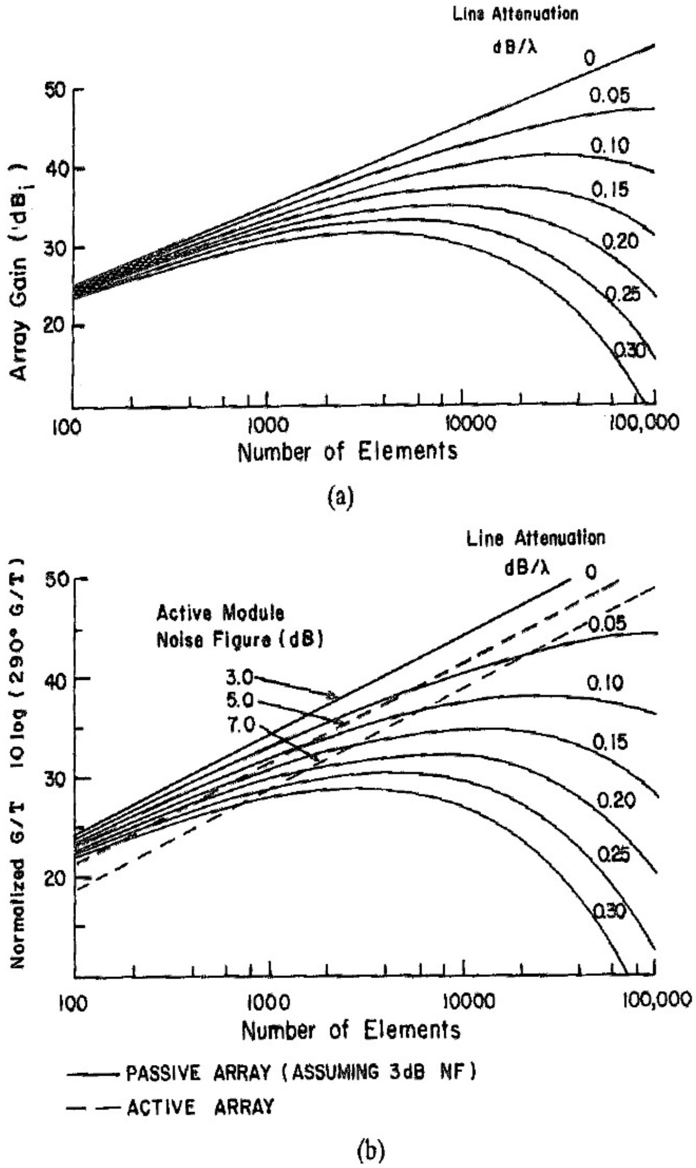

Figure 2.15: Gain and $G/T_s$ limitations due to circuit losses:(a) passive array gain; (b) passive and active array $G/T_s$ [3].

In both graphs it can be seen that gain is limited if line losses are not negligible. Then, line attenuation should be considered when an array is designed for a specific gain value. Additionally, if the progressive phase excitation is controlled by using digital phase shifters with $P$ bits and $2^P$ states separated by phase steps of $2\pi/2^P$, then extra losses and extra increase of the side lobe level have to be considered as well within the performance of the array. Figure 2.16 shows the average side lobe levels, according to the number of bits and elements in the array.

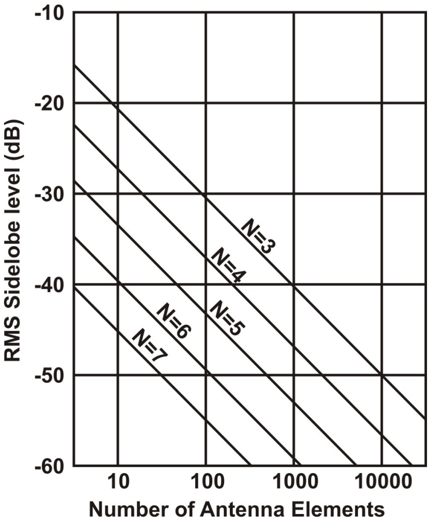

Figure 2.16: RMS side lobe levels due to N-bit phase-shift quantization.

There is an approximate expression to determine the minimum number of elements versus the scan coverage [3], taking into account the condition stated in Eq.(2.58), for the maximum allowed element spacing to avoid the excitation of side lobes. This expression is:

$$N_{min} = \frac{L}{\lambda_0}(1 + \sin\theta) \tag{2.66}$$

where L is the length of the array.

#### 2.2.7.7 Time-Delay

In section 2.2.1 it was said that phase shifters are the electronic devices responsible for delivering the required progressive phase at each element to generate the steering of the main beam. Therefore, one of the possible designs used to enhance the bandwidth of the array is the implementation of time delay paths. Some of the main disadvantages of these time-delays are the large cost they can generate when multiple discrete networks are required, mainly due to the highly complex switching network involved in the system. Additionally the current lack of effective low-loss switches able to reduce the overall size, and thus the cost of the system. However, it is desirable to find effective networks and simple switches able to solve the main disadvantages of these time-delays, and profiting their main benefits such as maintaining the main beam at a constant angle for all the range of frequencies available on the specific application.

Time-delays are very simple to implement because they use transmission lines to retard the signals in order to compensate the time difference with respect to a reference signal, and add all of them in phase. Considering a simple linear array with uniform amplitude excitation, as that used throughout this chapter for expedient analysis, the equivalent phases ($\delta_n$) at each element are:

$$\delta_n = -\frac{2\pi}{\lambda_0} n d_y \cos\gamma \quad \text{or} \quad \delta_n = -\frac{2\pi}{\lambda_0} n d_y \sin\theta \tag{2.67}$$

which need to vary linearly with frequency:

$$\delta_n = -2\pi n \frac{f_0}{c} d_y \sin\theta \tag{2.68}$$

The inserted time delay produced by the incremental lengths of transmission lines ($l_n = n d_y \sin\theta$) can be obtained as:

$$\tau_n = -\frac{n d_y \sin\theta}{c} = \frac{l_n}{c} \tag{2.69}$$

which can be positioned behind each element or subarray of elements, by switching different sections for the required delays. The phase shift inserted by the length of line $l_n$ is:

$$\delta_n = \frac{2\pi l_n}{\lambda_0} \tag{2.70}$$

In this work, time-delays or digital phase shifters made of microstrip lines will be the subject of analysis and design to prove the effectiveness of RF microelectromechanical systems (RF-MEMS) switches when they become monolithically integrated with the reconfigurable phased array antenna presented in Chapter 4. These switches will be studied in more detail in the next chapter.

## 2.3 Microstrip Antennas

In the field of Microwave Engineering, transmission lines are designed to provide good propagation of the electromagnetic waves, where power loss and wave purity are some of the aspects that determine the effectiveness of the lines. Most of the properties of the transmission lines depend on the specifications of the application, such as the amount of power, frequency of operation, characteristic impedance, wave propagation modes, phase velocity, propagation constant, and the type of technology that will be used for their fabrication and integration with the system. Microstrip is the name given to a type of planar transmission line able to be integrated with microwave RF circuits on the same board, that has been used not only as a transmission line but for the design of different circuit components such as filters, couplers, resonators, and for one of the most important aspects of this work: antennas [37] [3].

The shape of the microstrip antenna consists of a thin metallic strip line ($t \ll \lambda_0$, where $\lambda_0$ is the wavelength in free space) on the top side of a substrate with the height of a small fraction of the wavelength ($0.003\lambda_0 < h < 0.05\lambda_0$), and with dielectric constant in the range of $2.2 < \varepsilon_r < 12$ [1]. It is common to name the shape of the antenna as the patch, which has width $W$ and length $L$. The bottom side of the substrate is completely covered with a flat metal and is called the ground plane. Figure 2.17 displays one of the typical designs of a square microstrip antenna, where the lines of the electric field can be seen at the edges of the patch along its length and width.

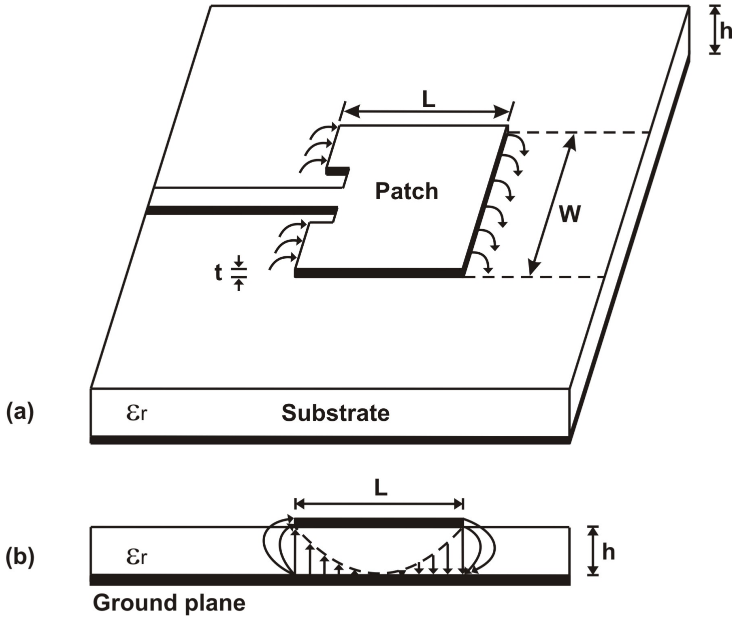

Figure 2.17: Microstrip antenna; (a) Top view. (b) Side View.

Microstrip antennas have different characteristics that provide potential advantages to many communications systems. One of the key benefits is their low cost of fabrication based on lithographic techniques in Printed Circuit Boards (PCB). This characteristic allows their integration with either Hybrid or Monolithic Microwave Integrate Circuits (MMIC), where their physical dimensions, in terms of height and weight, permit low profile construction to meet the system requirements, when size is a key parameter. Other important features are based on their electromagnetic characteristics such as their versatile design to get the desired resonant frequency of operation, characteristic impedance, polarization, and radiation pattern. However, microstrip antennas also have some disadvantages. Some of the most important are their relatively narrow bandwidth, lower efficiency, poorer polarization purity, poorer scan performance, low handing power, and spurious radiations from their feeding networks [1]. Nevertheless, these disadvantages can be reduced if an optimized design is performed. For example, to approach the narrow bandwidth issue, it is necessary to chose the correct dielectric in terms of its height and its relative dielectric constant ($\varepsilon_r$).

There are many areas of application for microstrip antennas. They have been widely used for wireless communications systems such as WLAN and WiMAX networks [38], [39], [40], and also for point-to-point communications [41]. Physical space on aircraft, spacecraft, and satellites is very valued and for that reason microstrip antennas have been used recently [42], [43], [44]. Other fields like medical science have used microstrip antennas for different sensory applications [45].

### 2.3.1 Analysis of Microstrip Antennas

According to [1], there are many methods of analysis for microstrip antennas, but just three models are the most popular. These are the *Transmission Line*, *Cavity*, and *Full-wave Models*. In this work only the first two are presented in order to have a set of formulas and theoretical basis, to design different configurations and evaluate the performance of the antennas, for the experiments developed and presented in the next chapters.

Additionally, taking into account that microstrip antennas are basically microstrip lines, with the shape of the antenna on top of the substrate, it is convenient to approach the current analytical techniques of microstrip lines to use them for the analysis of the antennas, in order to have good approximation of their electromagnetic characteristics. Therefore, the Approximate Electrostatic Solution [37] is presented as well to complement the analysis of the *Cavity Model* in order to obtain the propagation wave modes and the resonant frequencies of the microstrip antennas. The Approximate Electrostatic Solution considers the propagation of electromagnetic fields on the lines as quasi-TEM waves, like those propagating on transmission lines with two conductors. Then, this solution gives a good analysis to determine the phase velocity, propagation constant, and characteristic impedance of the microstrip lines. This solution along with the *Cavity Model* are presented first in the next section, followed by the *Transmission Line Model*, which gives an easy set of formulas to design antennas for the desired frequencies of operation, and a good physical insight into how the patches work.

#### 2.3.1.1 Approximate Electrostatic Solution

Most of the analysis of the electrostatic solution and the *Cavity Model* is based on the theory and derivations presented in [37] and [1]. Also, the derivations for the solution of some of the equations presented on these analyses have been solved in this section.

The geometry of a microstrip line presents the majority of its electric field lines in the dielectric region, concentrated between the metallic strip and the ground plane, but also a small fraction of them are presented in the air above the substrate. For this reason microstrip lines cannot support pure Transverse Electromagnetic (TEM) wave, making the analysis a little more complex compared with other planar transmission lines, such as the strip line, where the fields are on an homogeneous medium, instead of two. Figure 2.18 presents the geometry and the field lines of a micrsotrip line, where fringing of the electric field is noticeable at the edges of the line.

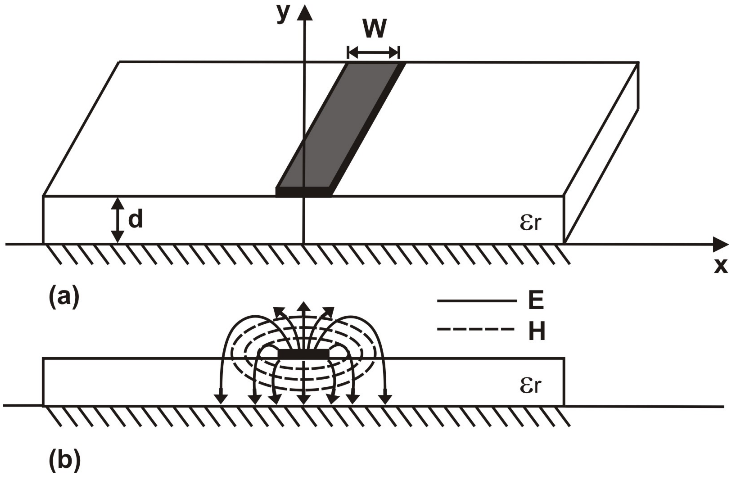

Figure 2.18: Microstrip line; (a) Geometry. (b) Electric and Magnetic fields.

If the dielectric substrate is very thin compared with the wavelength on the medium ($d \ll \lambda_g$), it is possible to consider the propagation of the electromagnetic waves through the microstrip line as quasi-TEM, which means they behave very similarly to the TEM waves on a transmission line with two conductors. This assumption is based on the fact that most of the field lines are concentrated in the centre of the conductor, allowing reduction of the geometry of the line from the sides by truncating the substrate with conducting walls without affecting the inside fields. Therefore, the microstrip line is treated as a line with two conductors, such as the strip line, but with an adjustment analysis of its fields due to the air-dielectric boundaries. Then, good approximations of the phase velocity, propagation constant, and characteristic impedance can be obtained by considering the transverse fields as quasi static fields. The phase velocity is calculated by:

$$v_p = \frac{c}{\sqrt{\varepsilon_e}} \tag{2.71}$$

where $c$ is the speed of light in the free space and $\varepsilon_e$ is the effective dielectric constant ($1 < \varepsilon_e < \varepsilon_r$) in the medium. The propagation constant is expressed as:

$$\beta = k_0\sqrt{\varepsilon_e} \tag{2.72}$$

where $k_0$ is the propagation constant in free space, defined as $k_0 = \omega\sqrt{\mu_0\varepsilon_0}$. In order to know how to calculate the effective dielectric constant and characteristic impedance, it is necessary to understand the behaviour of the fields on the microstrip lines, then it is important first to understand the propagation of the TEM waves on a transmission line by presenting their general Maxwell's Equations solution. Thus, considering time-harmonic fields with $e^{j\omega t}$ dependence in a cylindrical transmission line and boundaries parallel to the axis of propagation z-axis ($e^{-j\beta z}$), as shown in Figure 2.19, the electric and magnetic fields are defined in Eq.(2.73) and (2.74), respectively.

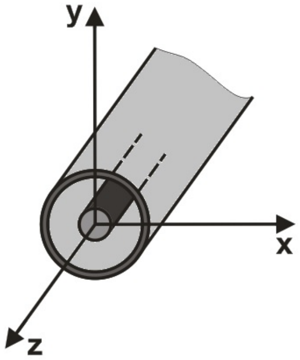

Figure 2.19: Transmission line with two conductors.

$$\vec{E}(x,y,z) = (\vec{e}_x(x,y) + \vec{e}_y(x,y) + \vec{e}_z(x,y))e^{-j\beta z} \tag{2.73}$$

$$\vec{H}(x,y,z) = (\vec{h}_x(x,y) + \vec{h}_y(x,y) + \vec{h}_z(x,y))e^{-j\beta z} \tag{2.74}$$

Where $\vec{e}_x(x,y), \vec{e}_y(x,y)$ and $\vec{h}_x(x,y), \vec{h}_y(x,y)$ represent the transverse electric and magnetic field components ($\vec{e}_T, \vec{h}_T$), respectively, while $\vec{e}_z(x,y)$ and $\vec{h}_z(x,y)$ are the longitudinal electric and magnetic field components propagating in the $+z$ direction. Assuming that the transmission line is source-free ($\rho = 0$) and lossless, Maxwell's Equations in phasor form are:

$$\nabla \times \vec{E} = -j\omega\mu\vec{H} \tag{2.75}$$

$$\nabla \times \vec{H} = j\omega\varepsilon\vec{E} \tag{2.76}$$

where the wave or Helmholtz equation for the electric field ($\vec{E}$) is:

$$\nabla^2\vec{E} + \omega^2\mu\varepsilon\vec{E} = 0 \tag{2.77}$$

considering that $\nabla \cdot \vec{E} = 0$ because $\rho = 0$. A similar equation can be written for $\vec{H}$ as follows:

$$\nabla^2\vec{H} + \omega^2\mu\varepsilon\vec{H} = 0 \tag{2.78}$$

TEM waves are characterized by $E_z = H_z = 0$. Then the Helmholtz wave equation for $E_x$ is:

$$\frac{\partial^2 E_x}{\partial x^2} + \frac{\partial^2 E_x}{\partial y^2} + \frac{\partial^2 E_x}{\partial z^2} + k^2 E_x = 0 \tag{2.79}$$

where $k = \omega\sqrt{\mu\varepsilon}$ is called the wavenumber. Due to the $e^{-j\beta z}$ dependence of the fields:

$$\frac{\partial^2 E_x}{\partial z^2} = -\beta^2 E_x \tag{2.80}$$

and because the cutoff wavenumber ($k_c = \sqrt{k^2 - \beta^2}$) is zero for the TEM waves, considering that $k^2 = \beta^2$, the Helmholtz wave equation for the electric transverse fields can be reduced as follows:

$$\frac{\partial^2 E_x}{\partial x^2} + \frac{\partial^2 E_x}{\partial y^2} = 0 \tag{2.81}$$

$$\frac{\partial^2 E_y}{\partial x^2} + \frac{\partial^2 E_y}{\partial y^2} = 0 \tag{2.82}$$

and these equations can be written in a compact way as:

$$\nabla_T^2 \vec{e}(x, y) = 0 \tag{2.83}$$

where:

$$\nabla_T^2 = \frac{\partial^2}{\partial x^2} + \frac{\partial^2}{\partial y^2}$$

is known as the Laplacian operator for the two transverse dimensions. Then it can be said that the transverse electric fields $\vec{e}_T(x, y)$ satisfy the Laplace equation. Thus, the same applies for the magnetic field $\nabla_T^2 \overline{h}(x, y) = 0$. Therefore, if the transverse fields satisfy the Laplace equation, it is possible to say that they behave as quasi static fields. For the electrostatic case, the electric field can be expressed as the gradient of a scalar potential function ($\Phi(x, y)$) like:

$$\overline{e}_T(x, y) = -\nabla_T \Phi(x, y) \tag{2.84}$$

where:

$$\nabla_T = \left(\frac{\partial}{\partial x}\right)\hat{x} + \left(\frac{\partial}{\partial y}\right)\hat{y}$$

is the transverse gradient operator in two dimensions. Since $\nabla_T \times \vec{e} = -j\omega\mu H_z = 0$, it can be said that $\Phi(x, y)$ also satisfies the Laplace equation:

$$\nabla_T^2 \Phi(x, y) = 0 \tag{2.85}$$

Knowing, then, that the electric field in the microstrip line can be considered as quasi static, it is possible to develop the electrostatic solution to find the effective dielectric constant and the characteristic impedance. Furthermore, it is necessary to solve the

Laplace equation of the potential function, according to the boundary conditions shown in Figure 2.20.

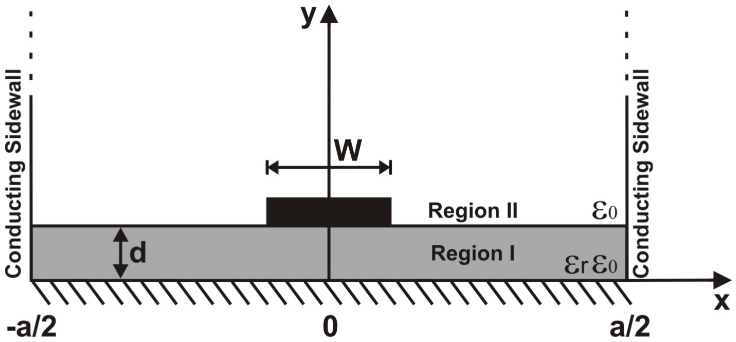

Figure 2.20: Microstrip line and conducting sidewalls.

$$\frac{\partial^2 \Phi}{\partial x^2} + \frac{\partial^2 \Phi}{\partial y^2} = 0 \quad |x| \leq \frac{a}{2} \quad 0 \leq y \leq \infty \tag{2.86}$$

with boundary conditions:

$$\begin{aligned} \Phi(x,y) &= 0 \qquad & x = \pm\frac{a}{2} \\ \Phi(x,y) &= 0 \qquad & y = 0, \infty \end{aligned}$$

Using the method of separation of variables, it is possible to solve the partial differential of Eq.(2.86). So, the first step is to propose a function with two variables:

$$\Phi = X(x)Y(y)e^{-j\beta z} \tag{2.87}$$

then if the proposal function of Eq.(2.87) is substituted in Eq.(2.86), and derivations are done, it follows that:

$$\Rightarrow X''Ye^{-j\beta z} + Y''Xe^{-j\beta z} = 0 \tag{2.88}$$

now, the equation is arranged in separable variables:

$$\frac{X''}{X} + \frac{Y''}{Y} = 0 \tag{2.89}$$

and it is possible to equate Eq.(2.89) to a constant in order to find the solution:

$$\frac{X''}{X} = -\frac{Y''}{Y} = -k^2 \tag{2.90}$$

considering first the equation for the $X$ variable:

$$\begin{gathered}\frac{X''}{X} = -k_x^2 \\ \Rightarrow X'' + k_x^2 X = 0\end{gathered} \tag{2.91}$$

the solution of which is:

$$X = C_1 e^{-jk_x x} + C_2 e^{jk_x x} \tag{2.92}$$

where $C_1$ and $C_2$ are constants. Knowing that:

$$\sin(k_x x) = \frac{e^{jk_x x} - e^{-jk_x x}}{2j}; \qquad \cos(k_x x) = \frac{e^{jk_x x} + e^{-jk_x x}}{2}$$

the solution can be written as:

$$X = A\sin(k_x x) + B\cos(k_x x) \tag{2.93}$$

where $A$ and $B$ are just constants. Because there are two regions, the even function is just considered as the solution:

$$X = B\cos(k_x x) \tag{2.94}$$

Applying the boundary conditions for $\Phi(x, y) = 0$ when $x = \pm\frac{a}{2}$:

$$X = B\cos\left(k_x\left(\frac{a}{2}\right)\right); \qquad \begin{aligned}\frac{k_x a}{2} &= \frac{\pi}{2} + \pi n \\ \Rightarrow k_x &= \frac{\pi}{a}(1 + 2n)\end{aligned}$$

then the solution for $X$ is obtained by:

$$X = B\cos\left(\frac{m\pi}{a}x\right); \quad k_x = \frac{m\pi}{a}; \quad m = 1, 3, 5, 7..\text{odd numbers} \tag{2.95}$$

Now considering the equation for $Y$:

$$\begin{gathered}\frac{y''}{y} = k_y^2 \\ \Rightarrow \quad y'' - k_y^2 Y = 0\end{gathered} \tag{2.96}$$

the solution of which is:

$$X = C_3 e^{-k_y y} + C_4 e^{k_y y} \tag{2.97}$$

with $C_3$ and $C_4$ as constants. Knowing that:

$$\sinh(k_y y) = \frac{e^{k_y y} - e^{-k_y y}}{2} \qquad \cosh(k_y y) = \frac{e^{k_y y} + e^{-k_y y}}{2}$$

the solution can be written like:

$$Y = C\sinh(k_y y) + D\cosh(k_y y) \tag{2.98}$$

where $C$ and $D$ are constants. Applying the boundary conditions for $\Phi(x, y) = 0$ when $y = 0$, it follows that:

$$0 = C(0) + D \quad \text{then} \quad D = 0;$$

and the solution for $Y$ is:

$$Y = C\sinh\left(\frac{m\pi}{a}y\right); \quad k_y = \frac{m\pi}{a}; \quad m = 1, 3, 5, 7\ldots\text{odd numbers} \tag{2.99}$$

Then the final solution for $\Phi$ in the region I is:

$$\Phi_I(x, y) = \overline{A}\cos\left(\frac{m\pi}{a}x\right)\sinh\left(\frac{m\pi}{a}y\right); \qquad m = 1, 3, 5, 7\ldots\text{odd numbers} \tag{2.100}$$

where $\overline{A}$ is a constant. Due to the fact that there are two regions by the air-dielectric interface, the potential must be continuous at $y = d$ and the solution for both regions must satisfy the boundary conditions. Then, the solution for the region II is:

$$\Phi_{II}(x, y) = \overline{B}\cos\left(\frac{m\pi}{a}x\right)\sinh\left(\frac{m\pi}{a}d\right)e^{-\frac{m\pi}{a}(y-d)}; \quad m = 1, 3, 5, 7\ldots\text{odd numbers} \tag{2.101}$$

with $\overline{B}$ as a constant. Therefore the solution for the two regions can be written as follows:

$$\Phi(x, y) = \begin{cases} \sum_{m=1}^{\infty} A_m \cos(\frac{m\pi}{a}x)\sinh(\frac{m\pi}{a}y) & 0 \le y \le d; \\ \sum_{m=1}^{\infty} A_m \cos(\frac{m\pi}{a}x)\sinh(\frac{m\pi}{a}d)e^{-\frac{m\pi}{a}(y-d)} & d \le y < \infty. \end{cases} \tag{2.102}$$

where $A_m$ is a constant and which can be found by obtaining the charge density on the strip. Then, the electric field has to be defined first from $E_y = -\partial\Phi/\partial y$:

$$E_y = \begin{cases} -\sum_{m=1}^{\infty} A_m \left(\frac{m\pi}{a}\right)\cos(\frac{m\pi}{a}x)\cosh(\frac{m\pi}{a}y) & 0 \le y < d; \\ \sum_{m=1}^{\infty} A_m \left(\frac{m\pi}{a}\right)\cos(\frac{m\pi}{a}x)\sinh(\frac{m\pi}{a}d)e^{-\frac{m\pi}{a}(y-d)} & d \le y < \infty. \end{cases} \tag{2.103}$$

The surface charge density on the strip at $y = d$ is:

$$\begin{aligned} \rho_s &= D_y(x, y = d^+) - D_y(x, y = d^-) \\ &= \varepsilon_0 E_y(x, y = d^+) - \varepsilon_0\varepsilon_r E_y(x, y = d^-) \\ &= \varepsilon_0 \sum_{m=1}^{\infty} A_m \frac{m\pi}{a}\cos\left(\frac{m\pi}{a}x\right)\left(\sinh\left(\frac{m\pi}{a}d\right) + \varepsilon_r\cosh\left(\frac{m\pi}{a}d\right)\right) \end{aligned} \tag{2.104}$$

which looks like a Fourier series in $x$. An approximation of the charge density by uniform distribution is:

$$\rho_s(x) = \begin{cases} 1 & |x| < \frac{W}{2}; \\ 0 & |x| > \frac{W}{2}. \end{cases} \tag{2.105}$$

and equating (2.105) to (2.104), by considering the orthogonality of $\cos(\frac{m\pi}{a}x)$, then:

$$A_m = \frac{4a\sin(\frac{m\pi W}{2a})}{(m\pi)^2\varepsilon_0\left(\sinh(\frac{m\pi}{a}d) + \varepsilon_r\cosh(\frac{m\pi}{a}d)\right)} \tag{2.106}$$

The voltage of the metallic strip relative to the ground plane is:

$$V = -\int_0^d E_y(x=0,y)dy = \sum_{m=1}^{\infty} A_m \sinh\left(\frac{m\pi}{a}d\right) \tag{2.107}$$

and the total charge per length on the centre is:

$$Q = \int_{\frac{-W}{2}}^{\frac{W}{2}} \rho_s(x)dx = W\left(\frac{C}{m}\right) \tag{2.108}$$

then the static capacitance of the microstrip line per unit length defined as $C = Q/V$ is:

$$C = \frac{W}{\sum_{m=1}^{\infty} \frac{4a\sin(\frac{m\pi W}{2a})\sinh(\frac{m\pi}{a}d)}{(m\pi)^2\varepsilon_0\left(\sinh(\frac{m\pi}{a}d)+\varepsilon_r\cosh(\frac{m\pi}{a}d)\right)}} \tag{2.109}$$

Finally, to find the effective dielectric constant, it is necessary to evaluate Eq.(2.109) by considering two cases. The first one for $C$ when $\varepsilon_r \neq 1$ and equal to the value of the dielectric of the substrate. The second for $C_o$ when $\varepsilon_r = 1$. Then $\varepsilon_e$ can be evaluated by the ratio of:

$$\varepsilon_e = \frac{C}{C_o} \tag{2.110}$$

and the characteristic impedance can be evaluated by:

$$Z_0 = \frac{1}{\upsilon_p C'} = \frac{\sqrt{\varepsilon_e}}{cC'} \tag{2.111}$$

where $c$ is the speed of light and $C'$ is the capacitance per unit length calculated by Eq.(2.109). The wavelength inside the microstrip is approximately evaluated by:

$$\lambda_g = \frac{\lambda_0}{\sqrt{\varepsilon_e}} \tag{2.112}$$

Up to this point, the electrostatic solution has been used to find an approximate evaluation of the phase velocity, propagation constant, effective dielectric constant, and characteristic impedance of the microstrip line as a first insight into the analysis of the microstrip antennas. However, in order to know the propagation wave modes, resonant frequencies, and an approximate sketch of the electric and magnetic patterns of the patches, it is necessary to complement the analysis by introducing the Cavity Model which, as its name suggests, considers the region between the patch and the ground plane as a cavity bounded by electric conductors above and below it, and by magnetic walls along the perimeter of the patch to simulate an open circuit. This is an approximate method which complements the analysis started by the electrostatic solution.

The Cavity Model implies that variations of the electric field along the height, or distance $d$, are constant because $d \ll \lambda_g$. This statement is based on the assumption that the fringing of the fields along the edges of the patch are very small and are not considered in the analysis. Then, the field lines of the electric field are orthogonal to the surface of the patch and only Transverse Magnetic (TM) field modes are obtained in this solution, like the ones found on waveguides of one conductor (E-waves). Therefore, the volume behind the patch is considered as the volume that exists in a rectangular wave guide, loaded with the respective dielectric constant $\varepsilon_r$ as shown in Figure 2.21.

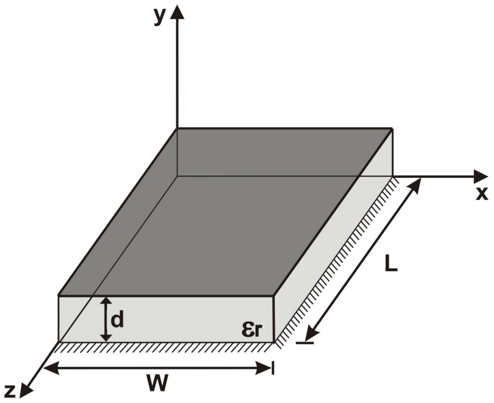

Figure 2.21: Microstrip patch as rectangular wave guide.

A potential vector (as in the electrostatic solution) is used to find the field configurations, assuming that the substrate is truncated at the edges of the patch, which must satisfy the Helmholtz wave equation:

$$\nabla^2 A_y + k^2 A_y = 0 \tag{2.113}$$

the general solution of which is obtained using the method of separation of variables, similar to the one used before for $\Phi(x, y)$ in Eq.(2.86). The solution is:

$$A_y = [A_1 \cos(k_x x) + B_1 \sin(k_x x)][A_2 \cos(k_y y) + B_2 \sin(k_y y)][A_3 \cos(k_z z) + B_3 \sin(k_z z)] \tag{2.114}$$

considering all the boundary conditions delimited by the cavity:

$$\begin{aligned} E_z(y'=0, 0 \leq z' \leq L, 0 \leq x' \leq W) = E_z(y'=d, 0 \leq z' \leq L, 0 \leq x' \leq W) = 0 \\ H_z(0 \leq y' \leq d, 0 \leq z' \leq L, x'=0) = H_z(0 \leq y' \leq d, 0 \leq z' \leq L, x'=W) = 0 \\ H_x(0 \leq y' \leq d, z'=0, 0 \leq x' \leq W) = H_x(0 \leq y' \leq d, z'=L, 0 \leq x' \leq W) = 0 \end{aligned}$$

The prime coordinates $(x', y', z')$ are used to represent the fields within the cavity. From the boundary conditions of $E_z$, $B_1 = 0$, from $H_z$, $B_3 = 0$, and from $H_x$, $B_2 = 0$, then the solution for $A_y$ is:

$$A_y = A_{mnp} \cos(k_x x') \cos(k_y y') \cos(k_z z') \tag{2.115}$$

where $A_{mnp}$ are the amplitude coefficients of each $mnp$ mode. The wavenumbers are:

$$k_x = \left(\frac{m\pi}{W}\right); \qquad k_y = \left(\frac{n\pi}{d}\right); \qquad k_z = \left(\frac{p\pi}{L}\right); \tag{2.116}$$

where $m, n, p$ represent, respectively, the number of half-cycle field variations along the $x, y, z$ directions, with $m = n = p = 0, 1, 2, ...$ but $m = n = p \neq 0$.

Since the wavenumbers are subject to the constraint equation:

$$k_x^2 + k_y^2 + k_z^2 = \left(\frac{m\pi}{W}\right)^2 + \left(\frac{n\pi}{d}\right)^2 + \left(\frac{p\pi}{L}\right)^2 = k_r^2 = \omega_r^2 \mu\varepsilon \tag{2.117}$$

the resonant frequency for the cavity can be obtained by:

$$(f_r)_{mnp} = \frac{1}{2\pi\sqrt{\mu\varepsilon}} \sqrt{\left(\frac{m\pi}{W}\right)^2 + \left(\frac{n\pi}{d}\right)^2 + \left(\frac{p\pi}{L}\right)^2} \tag{2.118}$$

although in practical circumstances $d$ is small and cannot be considered. The dominant wave mode is the one that is propagated over the lowest possible frequency, assuming that for almost all microstrip antennas $d \ll L$, $d \ll W$ and $L > W > d$, then $TM^y_{001}$ is the dominant mode:

$$(f_r)_{001} = \frac{1}{2L\sqrt{\mu\varepsilon}} = \frac{\upsilon_0}{2L\sqrt{\varepsilon_r}} \tag{2.119}$$

where $\upsilon_0$ is the speed wave of light in free space.

However, if $W > L > d$ the dominant mode is the $TM^y_{100}$ the resonant frequency of which is given by:

$$(f_r)_{100} = \frac{1}{2W\sqrt{\mu\varepsilon}} = \frac{\upsilon_0}{2W\sqrt{\varepsilon_r}} \tag{2.120}$$

The tangential electric field along the side walls of the cavity for the $TM^y_{001}$ and $TM^y_{100}$, respectively, are shown in Figure 2.22.

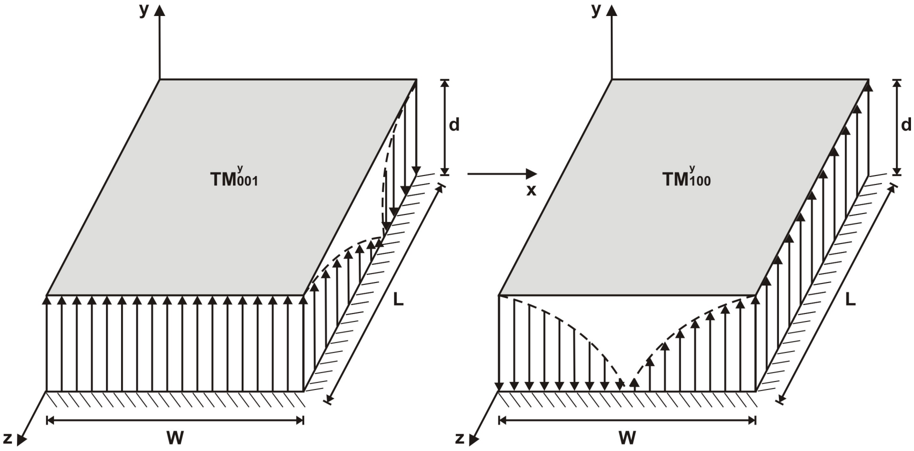

Figure 2.22: Field modes for the rectangular patch antenna.

The field component expressions for the electric and magnetic fields within the substrate are obtained considering that $TM^y_{001}$ is the dominant mode. Then the fields can be expressed as:

$$E_y = E_0 \cos\left(\frac{\pi}{L} z'\right) \tag{2.121}$$

$$H_x = E_0 \sin\left(\frac{\pi}{L} z'\right) \tag{2.122}$$

$$E_x = E_z = H_y = H_z = 0$$

where $E_0 = -j\omega A_{001}$ and $H_0 = (\pi/\mu L)A_{001}$. Finally, Figure 2.23 shows the broadside patterns of the electric and magnetic fields, in both the E- and H-planes, respectively, of the rectangular patch antenna.

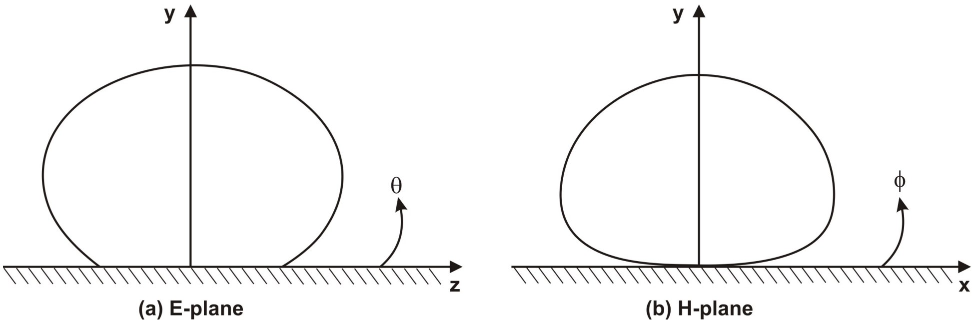

(a) E-plane (b) H-plane

Figure 2.23: Typical E-and H-plane patterns of the microstrip patch.

By complementing the analysis with the Cavity Model it is possible to better understand the behaviour of the electric and magnetic fields, propagating through the dielectric of the microstrip antennas, and the effects that these have for the radiation of the patch, giving a tool to evaluate the performance of the experiments presented in the next chapters for the reconfigurable phased array antennas.

#### 2.3.1.2 Transmission Line Model

For the design of microstrip antennas, the Transmission Line Model is considered the easiest because of its simplicity of application. It presents a set of formulas to find the approximate dimensions of the patches for the desired frequency of operation. These formulas are presented next according to [1]. This model assumes that the patch antenna can be represented by two radiating slots, each of width $W$ and height $h$ (or $d$), separated by a low impedance transmission line of length $L$ as shown in Figure 2.24.

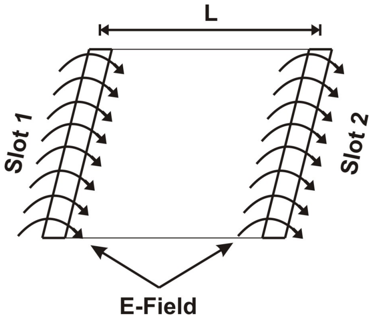

Figure 2.24: Two radiating slots model of a rectangular microstrip antenna.

One of the most important considerations in this model is the effect that the fringing of the fields has at the edges of the patch, contrary to the analysis developed in the previous section (Electrostatic and Cavity Models), because fringing influences the resonance frequency of the patch, which is one of the main parameters for the design. The fringing effects exist because the dimensions of the patch are finite along the length and width, and because the field lines travel among two different media while they are propagating through the line with different permittivity (air-dielectric interference). For the principal E-plane ($yz$-plane), fringing is a function of the dimensions ratio $L/h$ and the dielectric constant $\varepsilon_r$. For most of the micrsotrip antennas $L/h \gg 1$ and $W \gg h$, which means that fringing is reduced and most of the lines reside in the substrate. Although fringing is small, it makes the patch antenna look electrically longer than its physical dimensions. Since some of the waves travel in the substrate and some in the air, an effective dielectric constant $\varepsilon_e$ is introduced, which varies with frequency and which value is relatively close to $\varepsilon_r$ if $\varepsilon_r \gg 1$.

In order to find the dimensions of the patch for the desired frequency of operation ($f_r$), using a specific substrate with dielectric constant $\varepsilon_r$ and height $h$, there are a set of formulas to find the width $W$, length $L$, effective dielectric constant $\varepsilon_e$, and input impedance $Z_{in}$ from this model of analysis. Then, an expression to find $W$ for the desired resonant frequency is:

$$W = \frac{c}{2f_r}\sqrt{\frac{2}{\varepsilon_r + 1}} \tag{2.123}$$

where $c$ is the speed of light in free space. The effective dielectric constant $\varepsilon_e$ can be found using the next expression:

$$\varepsilon_e = \frac{\varepsilon_r + 1}{2} + \frac{\varepsilon_r - 1}{2}\left(1 + 12\frac{h}{W}\right)^{-\frac{1}{2}} \tag{2.124}$$

where $h = d$, taking into account the diagrams of the last section. The length of the patch antenna ($L$) is calculated by:

$$L = \frac{c}{2f_r\sqrt{\varepsilon_e}} - 2\Delta L \tag{2.125}$$

where $\Delta L$ is the correction factor of the length due to fringing effects, calculated by:

$$\Delta L = 0.412h\left(\frac{(\varepsilon_e + 0.3)(\frac{W}{h} + 0.264)}{(\varepsilon_e - 0.258)(\frac{W}{h} + 0.8)}\right) \tag{2.126}$$

Once the effective dielectric constant has been calculated, the wavelength propagating inside the substrate ($\lambda_g$) can be obtained by:

$$\lambda_g = \frac{\lambda_0}{\sqrt{\varepsilon_e}} \tag{2.127}$$

The input impedance of the patch is obtained from an equivalent circuit of the two slots, where each slot is represented by a parallel admittance $Y$ with conductance $G$, and susceptance $B$, as shown in Figure 2.25.

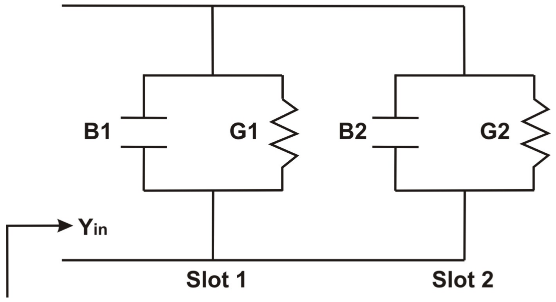

Figure 2.25: Equivalent circuit transmission line method.

Therefore the admittance of slot 1 is $Y_1 = G_1 + B_1$ and $Y_2 = G_2 + B_2$ for the slot 2. Since slot 1 is equal to slot 2, it is possible to assume that:

$$Y_1 = Y_2, \quad G_1 = G_2, \quad B_1 = B_2;$$

where the conductance $G_1$ can be obtained by solving the next integration:

$$G_1 = \int_0^{\pi} \left( \frac{\sin(\frac{k_0 W}{2}\cos(\theta))}{\sqrt{120\pi}\cos\theta} \right)^2 \sin^3(\theta) d\theta \tag{2.128}$$

with asymptotic values:

$$G_1 = \begin{cases} \frac{1}{90}\left(\frac{W}{\lambda_g}\right)^2 & W \ll \lambda_g; \\ \frac{1}{120}\left(\frac{W}{\lambda_g}\right) & W \gg \lambda_g. \end{cases} \tag{2.129}$$

The total input impedance of the patch is obtained when admittance of slot 2 is transferable to the input of the circuit at slot 1. If the length of the patch is around $\lambda_g/2$, the transformed admittance ($\overline{Y}_2$) of slot 2 becomes:

$$\overline{Y}_2 = \overline{G}_2 + j\overline{B}_2 \approx G_1 - jB_1 \tag{2.130}$$

then, the total resonant input admittance becomes real and is obtained by:

$$Y_{in} = Y_1 + \overline{Y}_2 = 2G_1 \tag{2.131}$$

As a consequence the resonant input impedance is also real:

$$Z_{in} = \frac{1}{Y_{in}} = R_{in} = \frac{1}{2G_1} \tag{2.132}$$

However for the precise calculation of the resonant input resistance, the mutual impedances between the two slots need to be considered by changing Eq.(2.132) for:

$$R_{in} = \frac{1}{2(G_1 \pm G_{12})} \tag{2.133}$$

where the mutual conductance is calculated by:

$$G_{12} = \int_0^{\pi} \left( \frac{\sin(\frac{k_0 W}{2}\cos(\theta))}{\sqrt{120\pi}\cos\theta} \right)^2 J_0(k_0 L \sin\theta)\sin^3\theta d\theta \tag{2.134}$$

with $J_0$ as the first kind order zero modified Bessel function. For typical microstrip antennas, the mutual conductance is small and good approximation for $R_{in}$ can be obtained with the only calculation of the conductance $G_1$ from Eqs.(2.128) and (2.129). There is an effective technique to match the resonant input resistance of the patch with the impedance ($Z_c$) of a microstrip line, by using an inset feed recessed a distance $z_0$ from the edge of the slot 1, as shown in Figure 2.26.

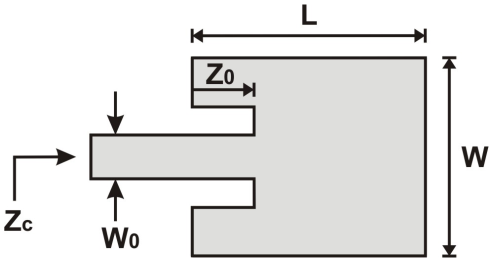

Figure 2.26: Patch with inset feed line.

The characteristic impedance of the microstrip feed line is given by:

$$Z_c = \begin{cases} \frac{60}{\sqrt{\varepsilon_e}} \ln\left(\frac{8h}{W_0} + \frac{W_0}{4h}\right) & \frac{W_0}{h} \leq 1; \\ \frac{120\pi}{\sqrt{\varepsilon_e}\left(\frac{W_0}{h}+1.393+0.667\ln\left(\frac{W_0}{h}+1.444\right)\right)} & \frac{W_0}{h} > 1. \end{cases} \tag{2.135}$$

where $W_0$ is its width. If $G_1/Y_c \ll 1$, where $Y_c = 1/Z_c$, the resonant input resistance of the inset feed can be calculated by:

$$R_{in}(z = z_0) = \frac{1}{2(G_1 \pm G_{12})} \cos^2\left(\frac{\pi}{L} z_0\right) \tag{2.136}$$

but given that $G_{12}$ is very small compared with $G_1$, Eq.(2.136) becomes:

$$R_{in}(z = z_0) = \frac{1}{2G_1} \cos^2\left(\frac{\pi}{L} z_0\right) \tag{2.137}$$

which is a good approximation for designing purposes, as demonstrated in Chapter 4 when presenting the performance of the different designs of microstrip antennas. A plot of the normalized value of Eq.(2.136) is shown in Figure 2.27. Up to this point two models

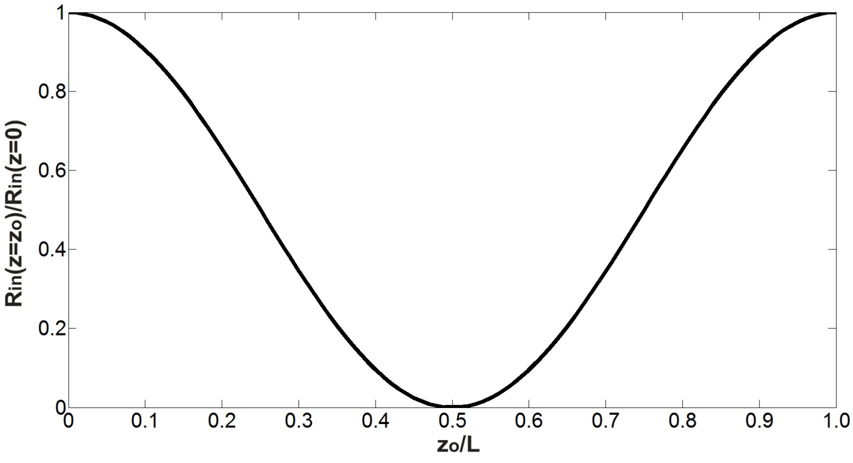

Figure 2.27: Normalized input resistance.

for the electromagnetic analysis and design of microstrip antennas have been presented as part of the Section 2.3.1. These models provide the necessary tools to design and verify the performance of microstrip antennas that are used as the main elements of the reconfigurable phased array antennas presented in Chapter 4.

## 2.3.2 Feeding and Impedance Matching Techniques

In the field of telecommunications systems, standard values for the input and output impedance are 50Ω or 75Ω for matching different transmission lines such as cables, connectors, and devices used on communication systems. Microstrip antennas were primarily designed to be integrated with planar technology like RF microwave circuits, which typically have output impedance of 50Ω. Therefore, it is important for the antennas to present 50Ω as input impedance for their implementation with circuits of this nature.

There are many configurations to feed microstrip antennas but, according to [1], microstrip line, coaxial probe, aperture coupling, and proximity coupling are the most popular. These configurations are presented in Figure 2.28.

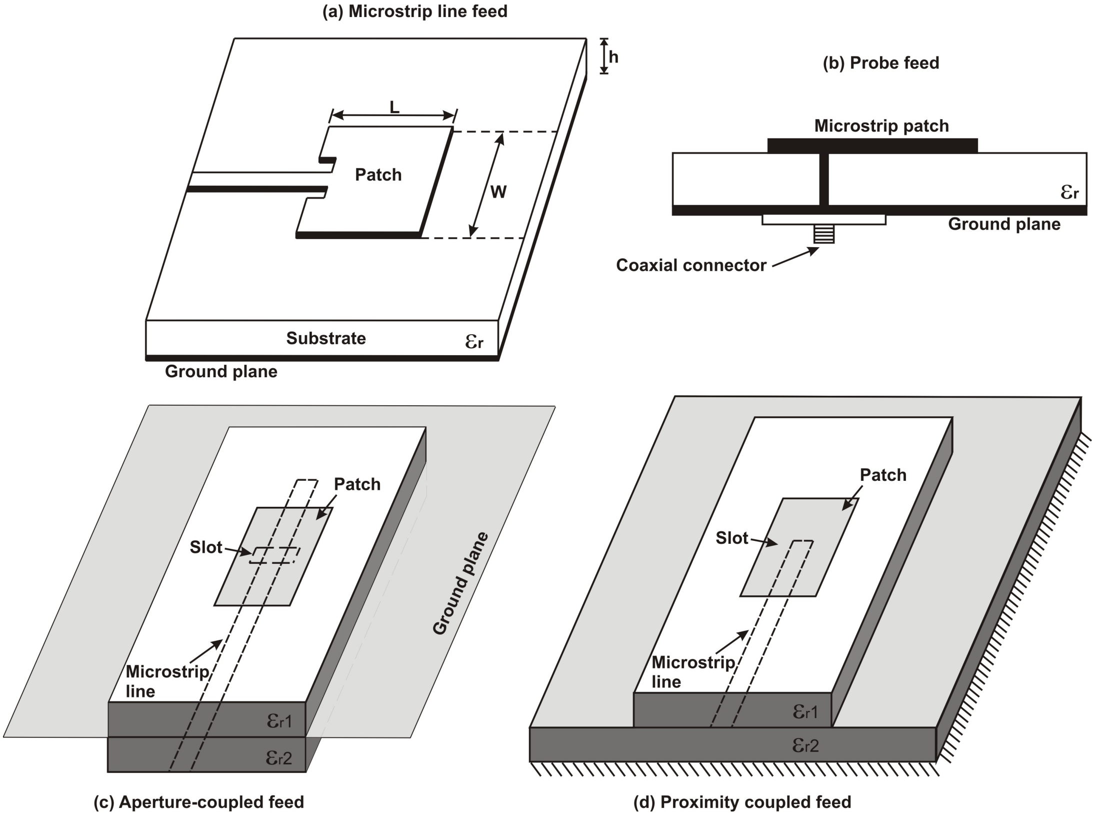

Figure 2.28: Different feed techniques of microstrip antennas.

In this work, the microstrip line configuration was selected to create the feeding network of the physical designs presented in Chapter 4, considering that this is the only configuration that allows monolithic integration of the RF-MEMS on the lines that comprise the digital phase shifters of the phased array antennas. Three different line configurations of microstrip lines are presented: the quarter-wave transformer, the T-junction power divider, and the stub. These are used in the reconfigurable phased array antennas to guarantee power distribution and impedance matching.

#### 2.3.2.1 The Quarter-Wave Transformer

The quarter-wave transformer is a simple transmission line circuit able to match any real load with a transmission line for a specific frequency of operation. This transformer can be designed using progressive sections in a precise manner in order to improve the match between the line and the load. Also, it can be used to obtain broader bandwidth for a small range of frequencies. To analyse how the transformer works, a simple circuit employing the quarter-wave transformer is shown in Figure 2.29.

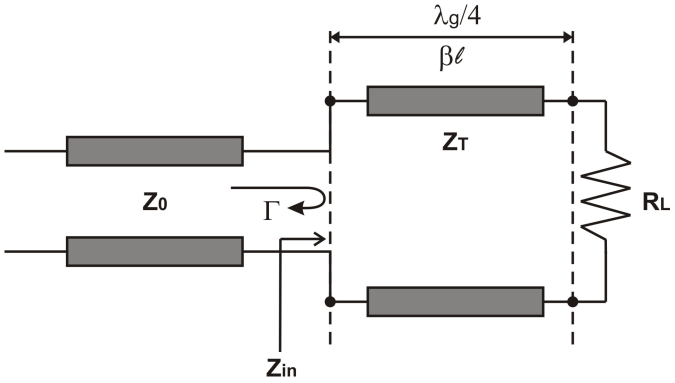

Figure 2.29: Quarter-Wave Transformer in a line.

This circuit presents a resistance load $R_L$, and a feed line with real characteristic impedance $Z_0$, where values are considered to be known. The purpose is to use the quarter-wave transformer ($Z_T$) to match both impedances. The electric length of the transformer is $\lambda_g/4$, and is intended to produce no reflection power to the feed line for good matching, which means the reflection coefficient must be zero ($\Gamma = 0$). According to [37], the reflection coefficient is defined as:

$$\Gamma = \frac{V_0^-}{V_0^+} \tag{2.138}$$

where $V_0^-$ is the reflected wave voltage and $V_0^+$ is the incident wave voltage. Considering that the input impedance ($Z_{in}$) of the transmission line shown in Figure 2.29 is given by:

$$Z_{in} = Z_T \frac{R_L + jZ_T \tan(\beta\ell)}{Z_T + jR_L \tan(\beta\ell)} \tag{2.139}$$

where $\beta\ell = (2\pi/\lambda_g)(\lambda_g/4) = \pi/2$, and by obtaining the limit when $\beta\ell \to \pi/2$:

$$Z_{in} \lim_{\beta\ell \to \pi/2} = Z_T \frac{\frac{R_L}{\tan(\beta\ell)} + jZ_T}{\frac{Z_T}{\tan(\beta\ell)} + jR_L}$$

the result is:

$$Z_{in} = \frac{Z_T^2}{R_L}$$

and to guarantee $\Gamma = 0$, then it must be that $Z_{in} = Z_0$ which provides the equation to find the impedance of the quarter-wave transformer as:

$$Z_T = \sqrt{Z_0 R_L} \tag{2.140}$$

#### 2.3.2.2 The T-Junction Power Divider

The T-junction power divider circuit is arranged in T configuration where each side constitutes one port of the power divider. This three port network is implemented over different types of transmission lines to distribute the input power to its other two ports for power division or for power combination. Over planar transmission technology, such as microstrip lines, this circuit is shaped on the top strip line, as shown in Figure 2.30.

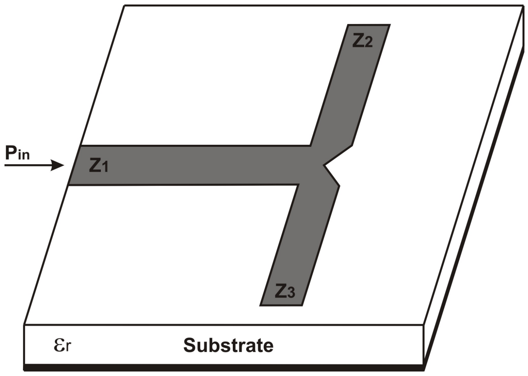

Figure 2.30: Microstrip T power divider.

According to [37], the T power divider shown in Figure 2.30 can be modelled as a junction of three transmission lines with a parallel susceptance $B$, generated by fringing effects and higher order modes produced in the junction between the three ports. This representation considers that transmission lines are lossless and must be matched to the input line of characteristic impedance $Z_1$, as shown in Figure 2.31.

Following circuit theory, in order for $Z_1$ to be matched with $Z_2$ and $Z_3$, it is necessary that:

$$Y_{in} = jB + \frac{1}{Z_2} + \frac{1}{Z_3} = \frac{1}{Z_1} \tag{2.141}$$

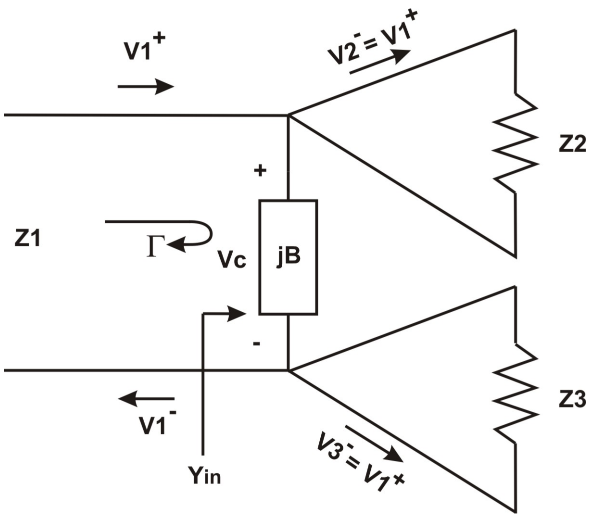

Figure 2.31: Transmission line circuit of the T-power divider.

but to simplify the analysis it is considered that these lines are lossless or with very low loss; then, the characteristic impedances are real and the Eq.(2.141) is reduced to:

$$\frac{1}{Z_2} + \frac{1}{Z_3} = \frac{1}{Z_1} \tag{2.142}$$

In order to know the power $P$ at each load or port, it is necessary to solve the following derivation considering the voltage at each line as follows:

$$\begin{aligned} V_1 = V_1^+ + V_1^- \quad \text{but } \ \Gamma = 0 \quad &\Rightarrow V_1^- = 0; \\ V_2^- &= V_C = V_1^+; \\ V_3^- &= V_C = V_1^+, \end{aligned}$$

taking into account that the input power to the matched divider is:

$$P_{in} = P_1 = \frac{1}{2}\frac{|V_C|^2}{Z_1} \tag{2.143}$$

the output powers are:

$$P_2 = \frac{|V_1^+|^2}{2Z_2} \tag{2.144}$$

$$P_3 = \frac{|V_1^+|^2}{2Z_3} \tag{2.145}$$

where $V_C = V_1^+$. In order to find the output characteristic impedances so that the power is equally divided in a 2:1 ratio, then:

$$\begin{aligned} P_2 &= \frac{1}{2}P_{in} \\ \frac{|V_1^+|^2}{2Z_2} &= \frac{1}{2}\frac{|V_C|^2}{2Z_1} \\ \Rightarrow Z_2 &= 2Z_1 \end{aligned}$$

and the same applies for $P_3$:

$$\begin{aligned} P_3 &= \frac{1}{2}P_{in} \\ \Rightarrow Z_3 &= 2Z_1 \end{aligned}$$

which means that by considering, for example, a $50\Omega$ input feed line, a $3\,dB$ split line can be obtained with output lines of $100\Omega$. Therefore, equal distribution of the input power is divided into the two ports. Also, the impedances of the output ports can be managed for different ratios of power distribution, rather than the 2:1 ratio.

#### 2.3.2.3 Single Stub Tuning

The single stub is a matching technique that uses either an open or short circuited length of transmission line, connected either in series or parallel with the transmission feed line at a certain distance from the load according to [37]. There are two adjustable parameters, one is the distance $d$ from the load to the stub position, and the other is the value of the susceptance $B$ or reactance $X$, for either parallel or series stubs, respectively, as shown in Figure 2.32.

For the parallel stub, which is the easiest to fabricate in microstrip form, the purpose is to chose $d$ so that at the position of admittance $Y$, it is of the form $Y_0 + jB$, which means the real part of the admittance $Y_L$ is matched with $Y_0$ because of length $d$. Then, to compensate the imaginary part $jB$ at that position, the length of the stub is selected in order to have $-jB$, where the width of the stub is the same as the transmission line, in case the fabrication is on microstrip form. For the series stub case, the procedure is the same but for impedances instead of admittances, this means to select $d$ so that at the position of the impedance $Z$, it is of the form $Z_0 + jX$, then the reactance of the stub is chosen as $-jX$ for the final matching of the load. The proper length of the stub will provide any desired value of susceptance or reactance, where the difference in lengths of an open or short circuited stub is $\lambda_g/4$. There are two methods to calculate the solutions for parallel or series stub tuning, these are either using the Smith chart or developing the analytical derivations. In this work, the Smith chart solution has been chosen because it is fast, intuitive, and effective for experimentation. The development

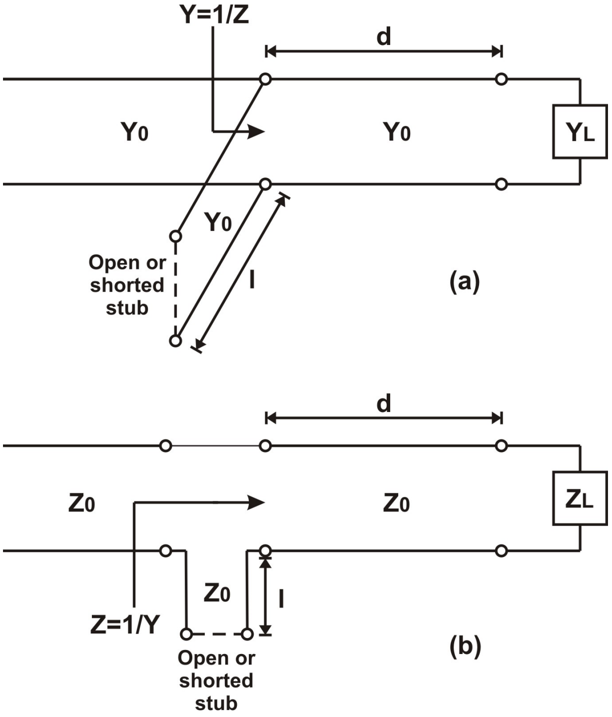

Figure 2.32: Single stub circuits. (a) Parallel stub. (b) Series stub.

of different solutions using this technique is presented in Chapter 4 for different scenarios with impedance matching issues.

The feeding and matching techniques presented so far are used to develop all the designs presented in Chapter 4, in order to achieve the representative architecture of reconfigurable microstrip phased array antenna suitable for monolithic integration of RF-MEMS.

## 2.4 Possible Applications of Phased Array Antennas

In recent years, demand for more broadband communications services has been growing, especially on the mobile market, where the fourth generation of mobile cellphones are now able to process more Internet data to cope with different high speed multimedia services. Then, technology trends and research communities involved in the commercial field of Telecommunications are focused on developing new ways to improve the effectiveness of the network systems, in terms of capacity and coverage, where mobility and cost are some of the key factors to be considered [46].

### 2.4.1 Satellite Communications: Ku-Band

Satellite communications have the potential to play an important role in this new mobile culture, because of their advantageous features such as large coverage areas, wide bandwidth for high throughput data, and broadcast communication for fixed and mobile users [47]. Currently, satellites provide different services like broadcasting of information, weather images, General Position System (GPS), phone services, and Earth observing in general. However, most of the geostationary satellites (GEO) around the planet provide Direct Broadcast Satellite (DBS) services in the Ku-band frequencies (10.9 - 12.75 GHz). Video broadcasting is the most popular service in this band, where the Digital Video Broadcast over Satellite version (DVB-S) presents a feasible service for both video and packet data traffic [48]. Therefore, wider communication around the world can be possible if there is full interaction between satellite systems and terrestrial networks, using part of the data traffic as protocol control. Then other services besides video, such as Internet and voice, can be offered within the rest of the traffic. This integration suggests the improvement of the network infrastructure for both satellites and terrestrial systems. From the satellite systems side, one of the main challenges is to create simple devices able to communicate with the satellite while the user is in motion, considering that mobility is becoming more important in these days for communication.

Services on the Ku-band have been extensively exploited for land fixed users, such as TV broadcast received by small dish antennas placed on the roof of houses. Nevertheless, the exploitation of these services for mobile users has been less adopted [49]. A strong reason for that is the current lack of effective land mobile satellite terminals able to track the satellite links while they are in motion.

As presented in Section 2.2, one of the main advantages of phased array antennas is their capability to electronically steer the main beam to the desired direction. Thus, phased array antennas are good candidates to solve the tracking demands of the mobile terminals. Also, they have already been widely studied for radar communications systems, since they have been used for ground, ship, air, and space applications [4].

There are three commercial sectors where compact and cost-effective platforms with phased array antennas, as the front-end terminals, can make an impact on the market. These sectors are: trains, cars, and planes. According to [13], there are specific parameters for such platforms. These requirements are: relatively low cost, small size, and conformal shape. Besides those, power loss is another important factor, because at lower rates, it can be possible to make the design suitable for other sectors like mobile cellphones or space devices. From the analysis presented in [50], [51], [52], [53], it is possible to identify some of the main requirements for land mobile platforms to receive Ku-band satellite links:

- Operating frequency: 10.7 - 12.75 GHz

- Polarization: linear
- G/T: $\sim 6\,\mathrm{dB/K}$, (Figure-of-Merit; G,T: system gain, noise temperature)
- Gain: $\sim 30\,dBi$
- Operation: Rx-only
- Aperture size: 20cm in diameter (EU), 30cm (USA)
- Height: <5cm
- Estimated manufacturing price for the entire system: <1500 euros
- Scan range: 20° - 60° in elevation from horizon, 0° - 360° in azimuth

The above requirements suggest compact and low cost production of the platform. The technology involved in the design of the phased array antennas (front-end of the platform) plays an important role to satisfy these requirements. The use of high integration technologies, such as Monolithic Microwave Integrated Circuits (MMIC) on standard manufacturing process, are desirable for these purposes. Also, the relatively short wavelengths ($\lambda_0 = 25mm$) in the Ku-band frequencies makes possible the design of small size antennas. Therefore, one possible design for phased array antennas is the use of microstrip antennas, as the main elements of the array, and using the design of low-loss phase shifters with microstrip lines in order to monolithically integrate them on a single platform, without compromising the good performance of the system.

For instance, according to Figure 2.15a for a passive $N$ square array with elements separated $0.5\lambda_0$ in $x$ and $y$ directions, approximately 300 microstrip antennas would be essential to satisfy the required gain of $30\,dBi$ of the system. This means that a square array of approximately $18 \times 18$ elements is necessary. Then, if the array is designed for the frequency of interest at 12.5 GHz ($\lambda_0 = 24\,mm$), the spacing between the elements in either direction ($d_x$ and $d_y$) is 12 mm, and the overall size of the array would be approximately $20\,cm \times 20\,cm$. Therefore, it would be possible to design compact platforms using microstrip antennas.

According to [16], if phased array antennas use true-time delay phase shifters, with Radio Frequency-microelectromechanical systems (RF-MEMS) switches, new generation of intelligent base stations with beam scanning capabilities and pattern nulling for high interference can be designed. RF-MEMS and digital phase shifters are presented in detail in the next section, as part of the background for the designs developed in this work. Low cost production can be achieved by using the standard manufacturing process of Printed Circuit Boards (PCB), where the small size and conformal shape are satisfied by choosing an appropriate design for both microstrip antennas and phase shifters on PCB, and where good performance can be achieved by monolithically integrating the RF-MEMS switches on the phase shifters for the whole system.

### 2.4.2 Motivation

A possible solution to satisfy the cost-effective and size requirements for mobile satellite terminals can be achieved if a suitable design of phased array antennas with RF-MEMS phase shifters presents good performance for this application. However, as stated in the Introduction of this work, the challenge is to find an alternative design and a cheap technique for manufacturing RF-MEMS switches on PCBs with promising performance.

Other applications are possible if the design of the switch presents good performance. For instance, satellites services in the Low Earth Orbit (LEO) for L-band (1 - 2 GHz) or S-band (2 - 4 GHz) frequencies are considered to be more effective for the quality of the services, although the available bandwidth is small. This is because LEO satellites are closer to the Earth than GEO satellites, then less attenuation and less power is required. However, tracking systems are more complex because they are moving faster and unsynchronized with the movement of the Earth, whereas GEO satellites seem to be steady, making the tracking systems to be required just for the mobile receiver terminals as mentioned before. Nevertheless, once the design has been proved for the Ku-band, it can be adjusted and improved for faster tracking at those frequencies.

Another possible application is for higher frequencies instead, up to the Ka-band frequencies (20 - 30 GHz) for GEO satellites as well. In this band bi-directional services are more likely to present better performance than the Ku-band because of the current available bandwidth. This means the possibility for the user to interact with the satellite by exchanging information (up-link and down-link) and share information with users around the globe at the same time. This would allow interactive networks between satellites systems and mobile networks on Earth as explained before. Then the phased array antenna would need to be redesigned for higher frequencies, and ensure that RF-MEMS present good performance and linearity at those frequencies.

## 2.5 Summary

The main aim of this chapter is to present the general background of phased array antennas in order to be familiar with their essential characteristics and with their way of operation. Therefore, the definition, classification, analysis, and the fundamental parameters of phased array antennas have been presented. The electromagnetic analysis has been developed from the basics of two isotropic antennas only to the analysis of planar arrays. This procedure aims to understand how the Array Factor is obtained, and how the phase excitation from the feeding network is able to modify the direction of the main beam at the desired direction, without physically moving the array. This characteristic is the most important for the purpose of this work. Fundamental parameters have been also presented to have the essential elements to measure and evaluate the performance of the reconfigurable phased array antennas presented in Chapter 4, in order to decide weather or not the antennas proposed here are suitable for the aim of this project.

Microstrip antennas have been found to be the best option as the main elements for the reconfigurable phased array antennas. This has been selected according to the size and cost-effective requirements for the possible application of this work. Therefore, methods for both the analysis of the main electromagnetic characteristics, and the design of square microstrip antennas have been presented. The Electrostatic Solution, Cavity and Transmission Line Models have been developed by presenting most of their derivations, in order to better understand the behaviour of the electromagnetic fields, radiation, and input impedance of the microstrip antennas. Also a set of formulas to design square microstrip antennas for the desired frequency of operation and input impedance has been introduced. Additionally, some of the most popular feeding and impedance matching techniques have been explained for either a single or an array of antennas. This background explains why the patches radiate, how antennas for the desired frequency of operation can be designed, and which techniques can be used to provide power distribution to an array. This provides the tools to design and evaluate the performance of the microstrip antennas to employ them as the main elements for the reconfigurable phased array antennas.

Finally a promising application of phased array antennas on Satellite Communications has been analysed, according to the technological trends on mobile communications, and to the current state of the satellite systems. The ultimate goal is to realise a full electronically reposition of the antennas radiation at an efficient cost, in order to target the market for different satellite bands like the Ku- and Ka-bands. An important aspect of this work is to offer a good contribution in the way of finding the best device for this application by using different techniques and technologies. As mentioned in [16], recent advances in SiGe and CMOS technologies have resulted in high performance and highly dense phased array chips, where semiconductor switches present high linearity and power handling. However applications like steerable receive-only terminals for satellite communications are ideally suited for RF-MEMS, because neither silicon nor GaAs technologies can meet their requirements. This is why the next chapter is dedicated to RF-MEMS. Another important aspect of this work is to find a cheap manufacturing process for RF-MEMS on PCBs to have full integration with both, phase shifters and microstrip antennas, and obtain good performance of the phased array antennas for one of the current most popular bands in the satellites systems: Ku-band.

# Chapter 3

# Background of RF-MEMS and Digital Phase Shifters

## Contents

## 3.1 Introduction

In the field of Radio Frequency (RF) engineering, where all the systems are involved in transmitting or receiving radio waves, developing effective RF switches able to work in the radio frequency spectrum is crucial for the good performance of the systems. These RF switches have been extensively used on communication networks, satellites, instrumentation, radar systems, mobile technology, and signal routing over different electronic circuit configurations. However, the search for the ideal switch design continues in an attempt to make the most of these systems, and to expand its application to other areas. The ideal behaviour of an RF switch occurs when it has virtually no insertion loss ($R_{on} = 0\Omega$), very high isolation ($C_{\text{off}} = 0fF$) over a wide frequency range, high linearity, high-power handling, and almost no DC power consumption [16]. For microwave circuit designs, two switches have been commonly used based on semiconductor technology: the p-i-n diode and Gallium Arsenide (GaAs) FET switch. Advances in HEMT and CMOS transistors have also presented high-performance chips for the same purpose. However, all these devices have not reached a desirable standard for many applications [14]. RF-microelectromechanical systems (RF-MEMS) switches are devices that use mechanical movement of tiny structures to achieve a short or an open circuit in an RF transmission line. Because of their nature of operation, RF-MEMS have demonstrated to be a good alternative switch thanks to their better performance at these frequencies [15].

The aim of this chapter is to present the general background of RF-MEMS. Thus, characteristics, models and guidelines for designing RF-MEMS are explained, along with the state-of-the-art of this technology. The operability of digital phase shifters is also described in order to show how these devices can be benefited using RF-MEMS. Most of the background presented in this chapter has been taken from [14], but complementary information and analysis from other sources is appropriately referenced when required.

## 3.2 Types of RF-MEMS

RF-MEMS operate by the physical movement of either a very small cantilever or a bridge over a transmission line to get an open or short circuit for frequencies up to 50 GHz. RF-MEMS have two main components: the mechanical and the electrical sections, and can be classified accordingly. In terms of the mechanical or actuation part, RF-MEMS can be actuated using electrostatic, magnetostatic, piezoelectric or thermal forces. The switches can move vertically (most common) or laterally, depending on their layout. From the electrical perspective, they can be placed either in series or shunt configuration, and have metal-to-metal or capacitive contacts between the beam and the transmission line. Figure 3.1 displays the two most common configurations of the switches actuated by electrostatic force.

Series switches can also be classified depending on their configuration on the transmission line (t-line). These are the inline or the broadside series switches. Actuation of the inline switch occurs in the same plane as the t-line, therefore the switch must have a continuous metal path from its anchor to the contact region since the RF signal passes by the entire switch. The actuation of the broadside switch results in a perpendicular plane of the t-line, and its contact is composed of two regions due to the outside position of the anchor from the t-line. Figure 3.2 shows these two configurations of the series

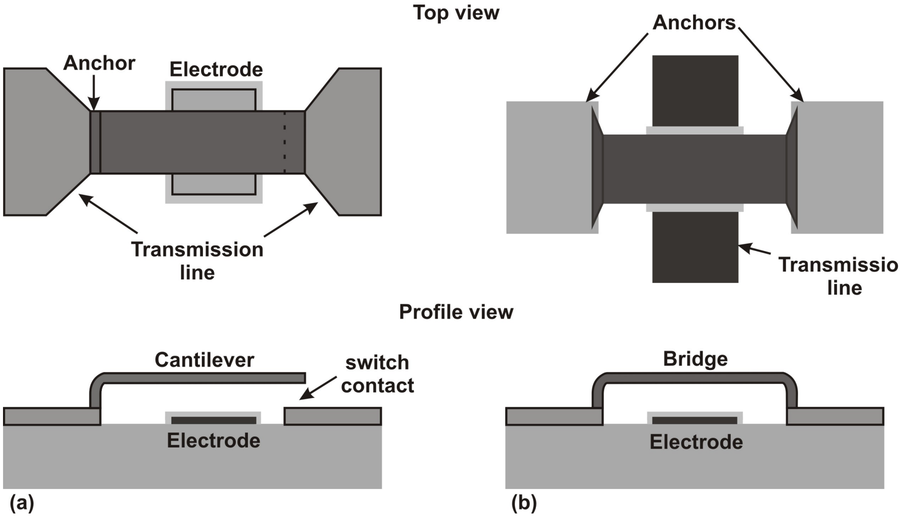

Figure 3.1: Electrostatic RF-MEMS. (a) Series switch. (b) Shunt switch.

RF-MEMS. For both configurations, the open circuit on the microwave line is created when the switch is in the up-state position, also known as the open- or *off-state*. The short circuit is generated when the beam goes down due to the electrostatic force to touch the t-line, known as the down-state position, or as the closed- or *on-state*. This chapter concentrates the analysis solely on the inline series cantilever RF-MEMS switches with vertically electrostatic actuation, where the electrostatic force is created by an isolated electrode beneath the cantilever to conduct a metal-to-metal contact. These particular switches are also known as DC-contact RF-MEMS switches [14], and have been selected in this work because of their easy configuration to operate with microstrip lines.

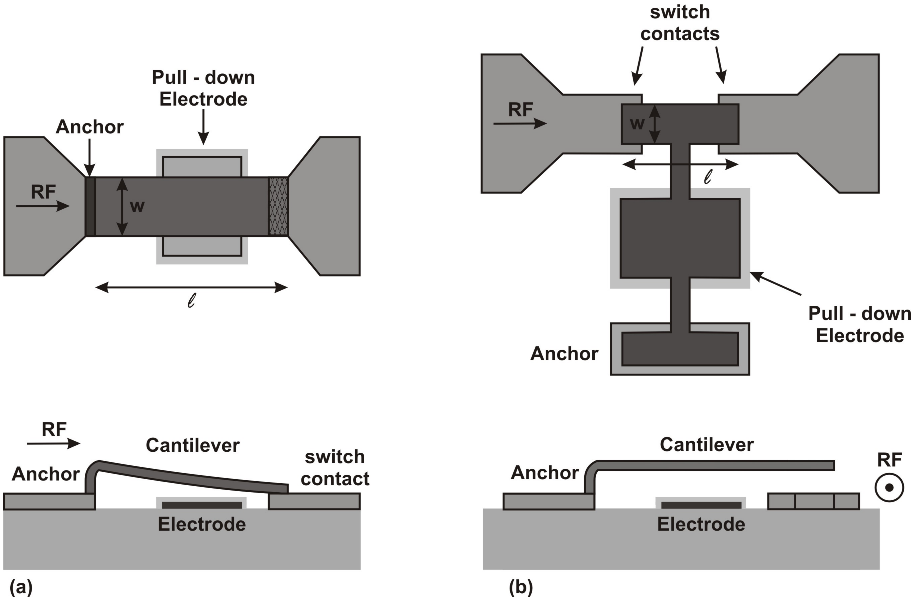

Figure 3.2: DC-contact RF-MEMS switches. (a) Inline series. (b) Broadside series.

## 3.3 Current Characteristics of RF-MEMS

The development of RF-MEMS was made with the view of improving the performance of p-i-n diodes and GaAs FET transistors since these were the first solutions from the semiconductor industry to replace the bulky and expensive electromechanical relays used in the past on different RF systems, and especially for phase shifters. According to [15], [14], from 2001 to 2003, the RF-MEMS technology using semiconductor techniques for their fabrication, demonstrated better RF switches than the traditional ones because of their nearly ideal performance as mechanical relays. At that time, electrostatic RF-MEMS demonstrated high reliability from 0.1-100 GHz, under wafer-scale manufacturing techniques. Since that moment, electrostatic RF-MEMS became the most common type of switches under investigation in order to find the best alternative for p-i-n diodes and FET transistors. In the process of trying to prove that RF-MEMS were better, good results and comparisons were charted, as can be seen in Table 3.1 by comparing each switch technology.

| **Parameter** | **RF-MEMS** | **PIN** | **FET** |
|---|---|---|---|
| Voltage (V) | 20-100 | ±3-5 | 3-5 |
| Current (mA) | 0 | 3-20 | 0 |
| Power consumption (mW) | 0.05-0.1 | 5-100 | 0.05-0.1 |
| Switching time | 1-300$\mu$s | 1-100ns | 1-100ns |
| $C_{\text{off}}$(series)(fF) | 1-6 | 40-80 | 70-140 |
| $R_s$(series)($\Omega$) | 0.5-2 | 2-4 | 4-6 |
| Capacitance ratio | 40-500 | 10 | n/a |
| Cutoff frequency(THz) | 20-80 | 1-4 | 0.5-2 |
| Isolation(1-10GHz) | Very high | High | Medium |
| Isolation(10-40GHz) | Very high | Medium | Low |
| Isolation(60-100GHz) | High | Medium | None |
| Loss(1-100GHz)(dB) | 0.05-0.2 | 0.3-1.2 | 0.4-2.5 |
| Power handling(W) | $< 1$ | $< 10$ | $< 10$ |
| Third-order intercept point (dBm) | +66-80 | +27-45 | +27-45 |

Table 3.1: Performance comparison of electrostatic RF-MEMS, PIN, and FET switches.

Table 3.1 shows some of the most important parameters that have to be taken into account for the proper operation of a switch. It is clear that some of the features of the RF-MEMS, such as their high isolation, low losses, and very low power consumption, are better than those of the p-i-n diodes and FET switches. Isolation in RF-MEMS is better than the other switches because of their very low capacitance values ($C_{\text{off}}$ or $C_{up}$) in the *off-state*. Their low losses are generated by the very low series resistance values ($R_s$) in the *on-state*. And their power consumption is very low because of the practically zero current required for their actuation. In short, these features are better due to the nature of operation of RF-MEMS. For instance, in the *off-state* air is the dielectric in the capacitor created between the beam and the transmission line over the contact area, which causes the capacitance to be very low. For the actuation of the beam, the electrostatic force is enough to move the beam to its down position because of the very low mass of the bridge or cantilever, and then metal-to-metal contact is generated between the beam and the t-line, creating a contact resistance $R_{on}$ with very low values, which as a result contributes to the very low insertion loss of the switch.

Recent advances in SiGe and CMOS technologies have resulted in high performance and highly dense phased array chips [16], [54], which seems they have virtually eliminated RF-MEMS, and hence also GaAs p-i-n diodes and FET switches, from this area of application. However, most of the essential characteristics of the RF-MEMS render them still today a better alternative to p-i-n diodes, GaAs FETs, silicon on insulator (SOI) or on sapphire (SOS) transistor switches for a range of different applications, such as Satellite Communications (SATCOM) systems where low power consumption, low insertion loss, and high linearity switches are required. In this area of application receive-only phased array antennas are crucial, and they are also significant for the purpose of this work. The most important characteristics of RF-MEMS according to [16] are:

1. **Very High Figure of Merit:** The Figure of Merit (FoM) is defined as FoM=$1/2\pi$ $R_{on}C_{\text{off}}$, and is about 10-20 THz, which implies that $C_{\text{off}} \sim 10\, fF$ and $R_{on} \sim 1-2\Omega$. This means that RF-MEMS offer much higher isolation ($> 20dB$), low insertion loss ($\sim -0.1dB$), or both for a wide range of frequencies.

2. **Very High Linearity:** Metal-to-metal contact switches are very linear if $R_{on} = 1-2\Omega$. The typical values of the intermodulation products are: $IP2 > 120dBm$ and $IP3 > 75dBm$. The second- and third-harmonic distortion is also very small, around $-90dBc$ at an input power of $20dBm$.

3. **Very Low Power Consumption:** Electrostatic actuation switches require 30-90V but they do not consume any current. However, if the RF-MEMS are intended to be used on cellphones, for example, the power consumption of the up converter voltage has to be included.

4. **Integration on Different Substrates:** RF-MEMS are mostly fabricated using surface micromachining techniques, or on SOI membranes. Then they can be fabricated on virtually any carrier, including glass and quartz, silicon, low-temperature ceramics, or GaAs wafers for a wide range of applications on microwave frequencies. Low cost in the manufacturing process is one of the key factors to expand their use in commercial applications.

However some of the main current disadvantages of RF-MEMS are:

1. **Relative low speed:** As shown in Table 3.1, the switching speed of most of the RF-MEMS is around 1-300$\mu$s whereas semiconductor switches are faster up to 100$ns$. Certainly, high speed switches are needed for some specific applications.

2. **Power Handling:** Extinction is one of the main problems when the switch is in contact with the t-line, specially if the RF power is high. Most of the RF-MEMS cannot handle more than 20-50mW.

3. **High Voltage Drive:** Electrostatic switches require relatively high voltage to actuate, and for many applications an up converter is needed on the system.

4. **Reliability:** Mature RF-MEMS industry has offered switches of 0.1-10 billion cycles. However many systems require switches with 20-200 billion cycles.

5. **Packaging:** RF-MEMS need to be packaged in inert atmospheres (nitrogen, argon, etc.) and in very low humidity, for hermetic seals. This process is one of the main factors that have rendered RF-MEMS too expensive and unable to compete in the market. However, new switches without packaging have been developed with promising performance to overcome this requirement.

6. **Cost:** Ideally RF-MEMS can be fabricated on different low cost wafers or substrates but an extra cost needs to be added due to the packaging and due to the up-converter voltage chip for some applications. Recently cost of a Single Pole Double Throw (SPDT) is around US$100, whereas semiconductor switches are around US$0.30-0.60.

Fortunately, most of the main disadvantages of RF-MEMS related to the process of fabrication have already been addressed and current investigation is still in progress. For instance, power handling has been solved by using different metals to make the metal-to-metal contacts more durable, like the reliable designs of DC-contact RF-MEMS switches presented in [18], [19]. However cost and full integration of the switches for certain applications is still one of the main problems in the RF-MEMS industry. If a good switch design can be developed, preserving the advantages of the RF-MEMS, and solving most of the issues in the manufacturing process for full integration and low cost, many areas of applications could benefit. This is why the aim of this work is to address this problem by proposing a new manufacturing technique of RF-MEMS on PCB substrates, aiming at the low price of the product, and the complete integration with microstrip phased array antennas, in order to get equal or better performance of the system compared with the current ones.

Recent analysis of the state-of-the-art of RF-MEMS made in [16] has shown areas in which RF-MEMS have been eliminated because of the low cost and high performance of semiconductor switches. However, other applications have been highlighted as well suited for RF-MEMS, where neither silicon nor GaAs technologies can meet their requirements. For instance, cost in cell phone front-ends has been the major problem for RF-MEMS, therefore SP4T semiconductor switches of around US$0.12-0.16 have been the choice of this area, as well as others such as WLAN networks and cell-phone base stations. Nevertheless potential areas for RF-MEMS are: Automated test equipment, wideband instrumentation, switching matrices and digital attenuators, and others that are closely related to the aim of this work:

1. **Satellite Switching Networks:** The switching matrix in a satellite is used for signal routing, beam manipulations, and redundancy switches for back-up amplifiers, specially on the receive and low power circuit portions. Then RF-MEMS can well benefit this part of a satellite.

2. **Defense Systems:** Wideband receivers/transmitters in the 0.1-6 GHz and 2-18 GHz bands use different SPNT switches. Also true-time delay phase shifters are still best done by using switched transmission lines because of the better isolation, insertion loss and linearity of RF-MEMS, compared with the ones built using p-i-n diodes or FET switches.

3. **Intelligent Base-Station Antennas:** This is the application that would most directly benefit from this project, because it suggests that RF-MEMS can be used for a new generation of intelligent base stations with beam scanning capabilities and pattern nulling for avoiding interference. RF-MEMS with their high linearity, high isolation and very low insertion loss are a strong candidate to develop such an application.

Consequently, there is a promising future for RF-MEMS in many applications. Factors such as reliability, cost, and full integration are the current most critical aspects to be considered.

## 3.4 Design of RF-MEMS

The design of RF-MEMS switches involves the mixing of different specialized areas where each one is equally important to become successful with a reliable product. However two of them are the most important at the beginning of the design of either a cantilever or a bridge switch. These two are: the mechanical and the electromagnetic models. For instance, the mechanical analysis allows to calculate most of the forces involved, and to know the critical characteristics of the switch. Then, it is possible to decide whether or not the physical model predicts a reliable design. The important aspects to be considered at this stage are: whether the switch will break or not, and whether the applied electrostatic force is enough for the correct actuation. The electromagnetic analysis allows to find the equivalent circuit of the switch over the transmission line in order to decide whether or not it will present good behaviour as an open or short circuit for the desired range of frequencies. Then, the compromise process of these two models starts by modifying the original design along with the available fabrication techniques, to finally obtain a reliable model.

### 3.4.1 Mechanical Modeling

The following expressions for the mechanical modeling of cantilever RF-MEMS have been taken from [14]. The first step to understand the mechanical operation of cantilever RF-MEMS is to obtain the spring constant $k\,[N/m]$, which is basically the factor that relates the linear deflection of the beam, $\Delta g\,[m]$, when an external force $F\,[N]$ is applied. The expression is:

$$F = k\Delta g \tag{3.1}$$

The spring constant is related to the stiffness of the cantilever, which accounts for the material Young's modulus $E\,[Pa]$ and the moment of inertia $I\,[m^4]$ when a concentrated vertical load is applied to the cantilever. If the distributed force ($\xi$) applied over the cantilever is uniform, as shown in Figure 3.3a, the spring constant is given by:

$$k_a = \frac{2E\mathrm{w}}{3}\left(\frac{t}{l}\right)^3 \tag{3.2}$$

where w is the width, $l$ the length, and $t$ the thickness of the cantilever. For a force distributed from $x$ to $l$ on the cantilever, as shown in Figure 3.3b, the spring constant is given by:

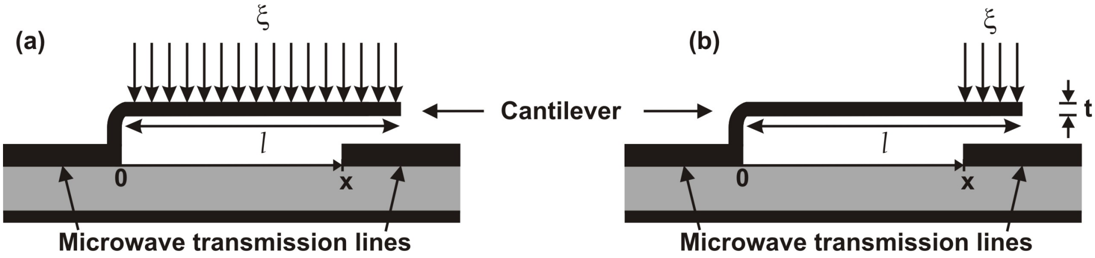

Figure 3.3: Cantilever with Different Distributed Loads. (a) Uniform. (b) Concentrated.

$$k_c = 2E\mathrm{w}\left(\frac{t}{l}\right)^3 \frac{1-(x/l)}{3-4(x/l)^3+(x/l)^4} \tag{3.3}$$

During the building process of the cantilever, particularly when the thin-film is deposited, an unwanted stress gradient can appear in the normal direction of the beam due to the different residual stress ($\sigma$ as a function of thickness in z-direction) between the top and the bottom layer of the cantilever. This stress gradient generates the bending of the cantilever in positive or negative curvatures. Figure 3.4 shows all the possible bending scenarios due to the differences in the magnitude of the residual stress. Ideally all the residual stress on a cantilever is released because it is not fixed at one end, and the spring constant should not have any residual component. However the stress gradient appears particularly when the film of the beam is deposited at different stages, or because it is composed of two or more different materials.

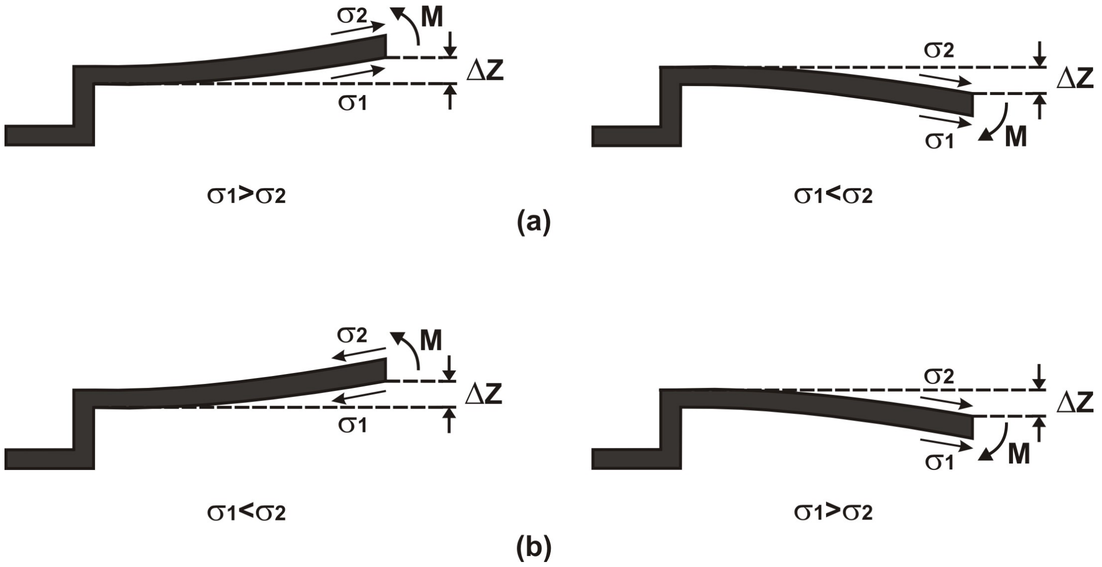

Figure 3.4: Effect of stress gradient on beam curvature for (a) compressive stress and (b) tensile stress.

## 3.4.2 Electrostatic Actuation

The electrostatic force used to actuate the cantilever beam is the same as the one that exists on the plates of a capacitor. An electrostatic force can be induced on the cantilever by creating an electrical potential difference where the positive charges are in the electrode and the negatives on the beam, or vice versa, in order to have an electric field to produce the force. By simply applying a voltage $V$ between the cantilever and the pull-down electrode, the beam is actuated. This electrostatic analysis considers a good approximation of the electric force by modeling the beam over the pull-down electrode as a parallel-plate capacitor. Although it is considered that the real capacitance is around 20-40% larger due to fringing fields, the model provides a good understanding of how the electrostatic force works. This approximation considers that the width of the cantilever is w, and the width of the pull-down electrode is $W$, with distance or gap $g$ between these

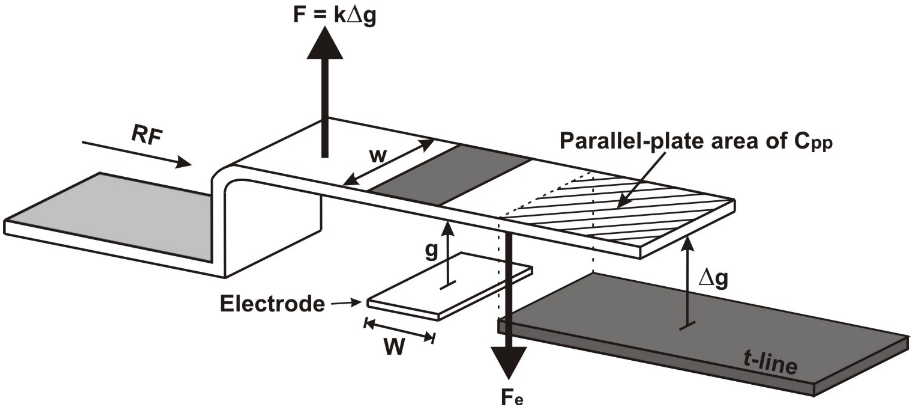

Figure 3.5: Cantilever RF-MEMS switch with isolated pull-down electrode.

two parallel plates, as shown in Figure 3.5. The parallel plate capacitance between the cantilever and the pull-down electrode is given by:

$$C \simeq \frac{\varepsilon_0 W \mathrm{w}}{g} \simeq \frac{\varepsilon_0 A}{g} \tag{3.4}$$

The electrostatic force is found by considering various expressions such as $Fe = qE/2$, $C = q/V$, $E = V/g$, where $q$ is the charge, $E$ the electric field, and by considering that the power is delivered to a time-dependent capacitance. Therefore the expression for the induced electric force is:

$$F_e \simeq \frac{1}{2}V^2\frac{dC(g)}{dg} \simeq -\frac{1}{2}\frac{\varepsilon_0 W \mathrm{w} V^2}{g^2} \tag{3.5}$$

Eq.(3.5) does not consider the effect of a possible dielectric layer between the cantilever and the pull-down electrode. The electrostatic force is approximated as being evenly distributed across the beam section above the electrode. Then, in order to find the required voltage $V$ that breaks the mechanical restoring force $F$, which is related with the stiffness of the metal, and which goes in opposite direction to the electric force $F_e$, as shown in Figure 3.5, it is necessary to equate Eq.(3.5) to $F = k\Delta g$, for the spring constant that is associated with the distance moved under the location of the force. Then, we have that:

$$\frac{1}{2}\frac{\varepsilon_0 W \mathrm{w} V^2}{g^2} \simeq k\Delta g \tag{3.6}$$

where the electrostatic force is independent of the voltage sign and far away from the required force for the resonant frequency of the cantilever (free vibration). Solving Eq.(3.6) for the voltage $V$ we have that:

$$V \simeq \sqrt{\frac{2k}{\varepsilon_0 W \mathrm{w}} g^2 \Delta g} \tag{3.7}$$

When the voltage source is applied and uniformly increased, the electric force is incremented due to an accumulation in the charge. Therefore, the gap is decreased simultaneously, which in turn, increases the capacitance and thus the charge and the electric field, causing the beam to be unstable at $(2/3)\Delta g$, and to collapse to the down position. This happens because the electric force becomes bigger than the restoring mechanical force until the total collapse of the beam. There is an expression to find the *pull-down voltage* at which the cantilever reaches the $(2/3)\Delta g$ and collapse, given by:

$$V_p \simeq V(2\Delta g/3) \simeq \sqrt{\frac{8k}{27\varepsilon_0 W \mathrm{w}}\Delta g^3} \tag{3.8}$$

Typical values of the *pull-down voltage* for cantilever switches are considered to go from 20 to 100V as presented in Table 3.1, however values up to 120V are also common. The value of the required voltage is directly linked with each particular design, because it depends on the stiffness, shape, and dimensions of the beam. Thus, the electrostatic force needs to be strong enough to break the restoring mechanical force, and make the cantilever touch the transmission line. The value of the contact resistance $R_{on}$ is directly related to the strength of the contact force. In general, the force at the contact areas is considered to be around 30-60% of the electric force. The better the contact is, the better the insertion loss becomes with values of $R_{on} \sim 1 - 2\Omega$.

### 3.4.3 Electromagnetic Modeling

For an ideal series switch when no bias voltage is applied (up-state or *off-state*) the isolation is infinite, whereas the insertion loss is zero when the bias voltage is applied (down-state or *on-state*). Typical values of isolation for ideal switches are considered to be around -20 to -30dB at 20 GHz, and for good low insertion loss around -0.2 at 0.1 to 40 GHz. The purpose of the electromagnetic analysis of RF-MEMS is to give an overview on how to model the capacitance, resistance, and inductance of the switch, and how to acquire a good approximation of the general RLC circuit from either the measured or simulated S-parameters. This model estimates that the *off-state* capacitance is composed of a series capacitance $C_s$ between the t-line and the metal switch, and of a parasitic capacitance $C_p$ between the ends of the t-line as shown in Figure 3.6a. Then, a general expression for the *off-state* capacitance of a switch with one contact is obtained by:

$$C_{\text{off}} = C_s + C_p \tag{3.9}$$

The series capacitor $C_s$ is mainly composed of a parallel-plate area between the t-line and the cantilever region that is exactly above this section of the t-line ($C_{pp} = \varepsilon_0 A/\Delta g$, see Figure 3.5), and a fringing component which is around 30-60% of this $C_{pp}$. For the

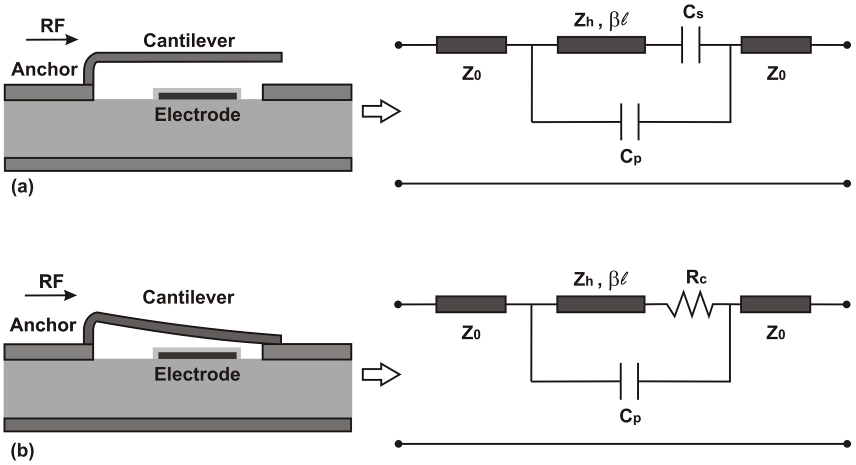

Figure 3.6: General circuit model of a inline DC-contact RF-MEMS series with one contact. (a) Up-State. (b) Down-State.

parasitic capacitance $C_p$, an extra factor has to be taken into account due to the fringing capacitance of the electrode. This factor can be negligible it is $40 - 60\mu m$ away from the t-line. Good typical values for $C_{\text{off}}$ have been found to be around $2 - 6fF$ for switches with height of around $1.5 - 3\mu m$, line width of $30 - 40\mu m$, an electrode separation around $40 - 60\mu m$, and a t-line gap of $60 - 100\mu m$. Then, very high isolation results can be obtained at microwave frequencies with these capacitance values. However the isolation of the switches also depends on many other factors such as the type of the substrate used, the shape and dimensions of the beam, and the losses involved in the entire switch.

There are three components for the series switch resistance ($R_s$) of the DC-contact RF-MEMS in the *on-state* position according to this model, and to Figures 3.6b and 3.7. The first one is due to the cantilever itself, which can be determined by calculating the

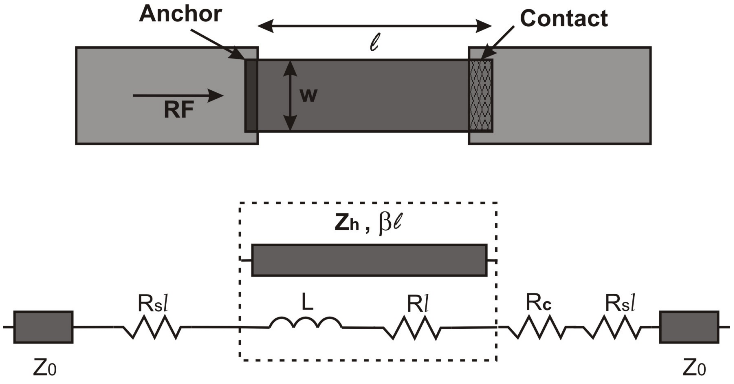

Figure 3.7: General circuit model for the series switch in the down state.

loss ($\alpha$) of a t-line of the same dimensions as the cantilever, and then by obtaining the equivalent series resistance $R_l$ from the following expression:

$$\alpha = \frac{R_l/\ell}{2Z_0} Np/m \tag{3.10}$$

where $\ell$ is the length of the cantilever, and $Z_0$ the characteristic impedance of the line. The second one is due to the loss of the t-line section by obtaining the equivalent resistance $R_{sl}$ from Eq.(3.10), in the same way as $R_l$ was obtained. Finally, the contact resistance $R_c$ that depends on the size of the contact area, the applied electric force, and the quality of the metal-to-metal contact must be added. Therefore the final expression for the series switch resistance is:

$$R_s = R_c + 2R_{sl} + R_l \tag{3.11}$$

The series resistance is considered to be dominated by $R_c$, and typical values are around $1 - 2\Omega$ depending on the contact area and the applied force. The loss of a RF-MEMS series switch can be calculated by using $R_s$ from the equation above, and by using this expression: $P_{loss} = I_s^2 R_s$, where $I_s$ is the current on the switch, or by using the measured or simulated S-parameters where $Loss = 1 - |S_{11}|^2 - |S_{21}|^2$, where $S_{11}$ is the reflection coefficient and $S_{21}$ the transmission coefficient.

In order to obtain the equivalent series inductance $L$ for the *on-state*, as shown in Figure 3.7, this electromagnetic analysis suggests modelling the cantilever alone by a high-impedance t-line section $Z_h$, of length $\ell$, width w, and effective dielectric constant $\varepsilon_e$, where its electromagnetic parameters are obtained from any microwave software able to simulate the piece of t-line suspended $g\ \mu m$ above the substrate. Hence, it is possible to model the cantilever by a series inductance given by:

$$L = \frac{Z_h \beta \ell}{\omega} = \frac{Z_h \ell}{\nu_p} \quad \text{for} \quad \ell < \frac{\lambda_g}{12} \tag{3.12}$$

where $\nu_p$ is the phase velocity of the high-impedance t-line calculated by: $\nu_p = c/\sqrt{\varepsilon_e}$. Typical values are considered to be around 30-80 pH for designs of $\ell = 60 - 100\mu m$ and $g = 1 - 2\mu m$. This high-impedance t-line section is used as well to better investigate a model of the RF-MEMS switch in the *off-state*, along with the *off-state* capacitance ($C_{\text{off}} = C_s + C_P$) presented in the general circuit diagram of Figure 3.6a. More analysis about this model is presented in Chapter 5, from the examination of the RF-MEMS results. Once there is a general way to obtain the capacitance, resistance, and inductance of a DC-contact RF-MEMS in series, it is possible to estimate the RLC circuit of the switch if the S-parameters are known. In order to calculate a good estimation of the isolation, the high-impedance t-line used to model the cantilever is neglected and the parameter is obtained by:

$$S_{21} = \frac{2j\omega C_{\text{off}} Z_0}{1 + 2j\omega C_{\text{off}} Z_0} \tag{3.13}$$

where $\omega = 2\pi f$, and $Z_0$ is the characteristic impedance of the t-line. If $S_{21} \ll -10dB$ and $2\omega C_{\text{off}} Z_0 \ll 1$ it is possible to calculate the isolation faster by:

$$|S_{21}|^2 \sim 4\omega^2 C_{\text{off}}^2 Z_0^2 \tag{3.14}$$

Then, it is straightforward to derive the *off-state* capacitance $C_{\text{off}}$ by solving Eq.(3.14) from the S-parameter values. For the equivalent series impedance $(Z_s)$ in the *on-state*, $R_s$ can be extracted from:

$$Z_s = R_s + j\omega L \tag{3.15}$$

and if $\omega L \ll R_s$, it can be assumed that $Z_s = R_s$, then the series switch resistance can be obtained from the value of the reflection coefficient at low frequencies ($f \leq 3GHz$) by:

$$|S_{11}|^2 = \left(\frac{R_s}{2Z_0}\right)^2 \tag{3.16}$$

For high frequencies the *on-state* inductance can also be extracted from the $S_{11}$ parameter. For this case, the reflection coefficient is fitted to an RL model with either the t-line or the $L$ controlling the response at high-frequencies. Therefore, if $\omega L \gg R_s$, it results that $Z_s = j\omega L$, and the inductance is obtained from:

$$|S_{11}|^2 = \left(\frac{\omega L}{2Z_0}\right)^2 \tag{3.17}$$

It is considered that accurate values for $L$ are obtained from 20-50 GHz, taking into account that this inductance includes both the switch and t-line segments. This electromagnetic model is very useful in Chapter 5 for the analysis of the simulated and measured results of RF-MEMS , when presenting the equivalent circuit of the switch for both states. This analysis allows to start from a general representation of the electromagnetic behaviour of the switch, to the particular representation of the switch design presented in Chapter 5.

### 3.4.4 Design Guidelines for RF-MEMS

As stated at the beginning of Section 3.4, the design of RF-MEMS requires expertise on different very specialized areas. The mechanical and electromagnetic models are a very good start for the primary switch design. However, sometimes the original design of the RF-MEMS needs to be modified according to the available and reliable fabrication techniques. This is because other factors can arise during the fabrication process, as, for instance, those related to the mechanical behaviour of the metals, such as the presence of residual stress, or the stability of the beam, to name a few. Recent analysis in [16] has summarized a list of general design guidelines according to the latest successful developed RF-MEMS. These guidelines are presented here as a reference for the designing and building of the DC-contact RF-MEMS cantilever switch of this work:

1. **Actuator Design:** The cantilever must be able to deliver high contact and release forces of around $100-1000\mu N$, under all stress conditions such as the residual stress and stress gradients. Also under a wide temperature range.

2. **Packing:** Only hermetic and clean packages result in reliable switches. Normally, packaging is developed under high temperatures around $280-500°C$ and after flushing the switch cavity with Nitrogen or Argon for cleaning. Therefore, the switch has to be able to support high temperatures without presenting deformation or bending.

3. **Contact Metallurgy:** Hard metal contacts require a relatively large contact force ($> 400\mu N$) to result in a $R_{on}$ of $1-2\Omega$. Ruthenium (Ru) and hardened gold compounds such as AuNi, AuCo, etc. are now extensively used because pure gold (Au) has resulted in low contact forces ($< 50\mu N$) due to its softness, high adhesion coefficient, and low melting temperature. This step of the design is very important to ensure a relatively high power handling at the contact area.

4. **Dielectric Charging:** The cantilever should be designed with a minimum of dielectric regions, and ensuring low electric fields across the dielectric layers if any, to eliminate dielectric charging effects.

5. **Creep:** Metal cantilevers suffer from creep effects due to the stress induced in the switch, and this tends to lower the spring constant, the actuation voltage, and can result in long term failure. Typical reliable switches have shown low stress less than 30-40MPa.

6. **RF Design:** This step requires the use of advanced electromagnetic simulators to know and ensure the success of the main parameters, such as the insertion loss, isolation, and return loss of the entire RF environment of the switch.

The intention of these guidelines is to lead the model to a reliable switch from the beginning of its design, to its fabrication process.

## 3.5 Latest RF-MEMS Designs

The purpose of this section is to present some of the current developments of reliable RF-MEMS switches from both the industrial and research sectors, in order to have a general reference for the design and analysis of the results of the RF-MEMS switches developed in this work.

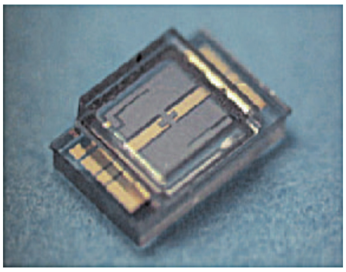

Figure 3.8: The SPDT Omron switch [17].

Figure 3.8 shows a single pole double throw (SPDT) switch created by Omron [17] based on Silicon on Insulator (SOI) technology, comprised of a glass and silicon substrate with wafer-to-wafer packing. The movable silicon membrane of this switch has two thin metal contacts of around $0.5\mu m$ of thickness, $200\mu m$ of length, and $50\mu m$ of width. This Omron switch presents insertion loss of $-1dB$, high isolation of $-40dB$ up to 10 GHz, and contact resistance of $1\Omega$. Other cantilever switch designs, like the one made by Radant [18], are fabricated using a thick layer of gold ($7-9\mu m$), with a length of $75\mu m$ and width of $30\mu m$, using hard metal contacts on a high resistivity silicon substrate as shown in Figure 3.9. This single pole single throw (SPST) cantilever switch presents an isolation of $-20dB$ with an *off-state* capacitance of $20fF$, insertion loss of $-0.4dB$ with a

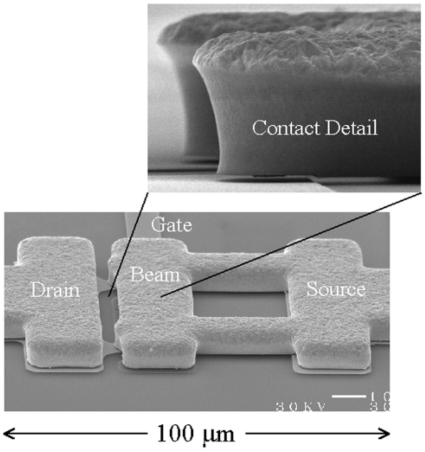

Figure 3.9: Radant cantilever RF-MEMS [18].

switch resistance of $3-4\Omega$, and 90 V for actuation, at 10 GHz. One of the disadvantages of this Radant switch is the need to add bond wires on its terminals to connect it to the RF board.

The University of California-San Diego (UCSD) has developed a high-force metal-contact Au thick ($7-10\mu m$) cantilever [19], of $155\mu m$ of length and $130\mu m$ of width employing Au-Ru contacts, on a high resistivity silicon substrate without using any hermetic package as shown in Figure 3.10. This UCSD RF-MEMS presents an isolation of $-18dB$ with $C_{\text{off}} = 24fF$, insertion loss better than $-1dB$ with contact resistance $R_s = 0.6-1\Omega$, at 10 GHz.

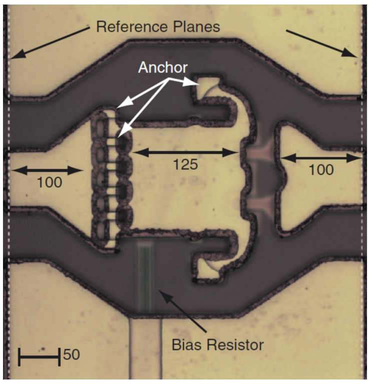

Figure 3.10: University of California-San Diego RF-MEMS switch [19].

Other designs of RF-MEMS have been investigated in the literature [14], [15], [16], [55], [56], [57], [58], [59], [60], [61] in order to have a fuller picture of extant cantilever switches. Based on the analysis of the different configurations presented here, a general range of the dimensions that comprise the design of a cantilever was identified. For instance, the length ($l$) of the cantilever was found to go from $70\mu m$ to $250\mu m$, the width ($w$) from $30\mu m$ to $140\mu m$, the thickness ($t$) from $0.6\mu m$ to $10\mu m$, and the height or gap ($\Delta g$), between the cantilever and the miscrostrip line, from $0.8\mu m$ to $6\mu m$. That there is such an ample range in the dimensions of a switch is because every particular structure of a cantilever depends on the specific actuation, and on the particular configuration for which it is intended to work. This survey of different designs of cantilevers does not represent all the possible dimensions of a switch of this type, but it represents a good reference for this work, taking into account designs that were developed for a similar purpose. All these designs were performed in order to present good mechanical and electromagnetic behaviour according to their specific application.

## 3.6 RF-MEMS Phase Shifters

There are two particular aspects that make phase shifters the most critical devices in phased array antennas. First, phase shifters are responsible for giving each array element the relative phase to electronically steer the beam. Second, there is a potential opportunity to improve the entire system by increasing the effectiveness of the phase shifters, exploiting the advantages of RF-MEMS switches over the p-i-n diodes or FET transistors, as explained before. Then, phase shifters can result in lower losses, wider bandwidth, power reduction, and full integration with the array. For instance, as [14] explains, it is possible to eliminate one or two amplifier stages in a T/R chain if the average loss of a 3-bit RF-MEMS phase shifter is around -0.9 dB at 10 to 14GHz. Therefore it would be possible to get an improvement of 3 to 4 dB over comparable on-wafer designs using GaAs FET switches, which in turn would translate to a 6 to 8 dB improvement in a two-way telecommunication system by reducing 20 to 100mW per element at X- to V-band frequencies. Thus, RF-MEMS phase shifters would be able to eliminate up to 50 to 75% of the T/R modules in large phased array configurations like the one presented in Figure 3.11.

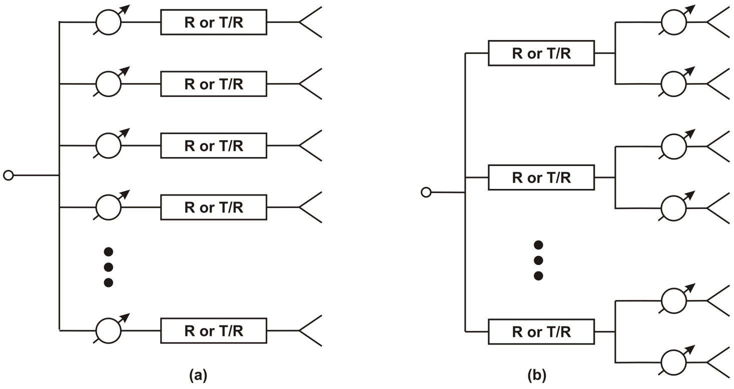

Figure 3.11: (a) A standard phase array. (b) A RF-MEMS base phase array.

Phase shifters can be classified based on their design. These can be either analog or digital phase shifters. Analog phase shifters result in a continuously variable phase shift from 0 to 360°, whereas digital phase shifters provide a discrete set of phase delays frequently built using switches. Also, phase shifters can work either by providing constant phase versus frequency, or linear phase versus frequency. The constant-phase designs are best fabricated using switched networks or loaded-line techniques. Linear-phase designs are frequently used in true-time delay phased arrays by implementing switched delay lines for wide bandwidth.

The easiest way to implement digital phase shifters is by using this switched delay-line technique, over different configurations as shown in Figure 3.12. As the name suggests,

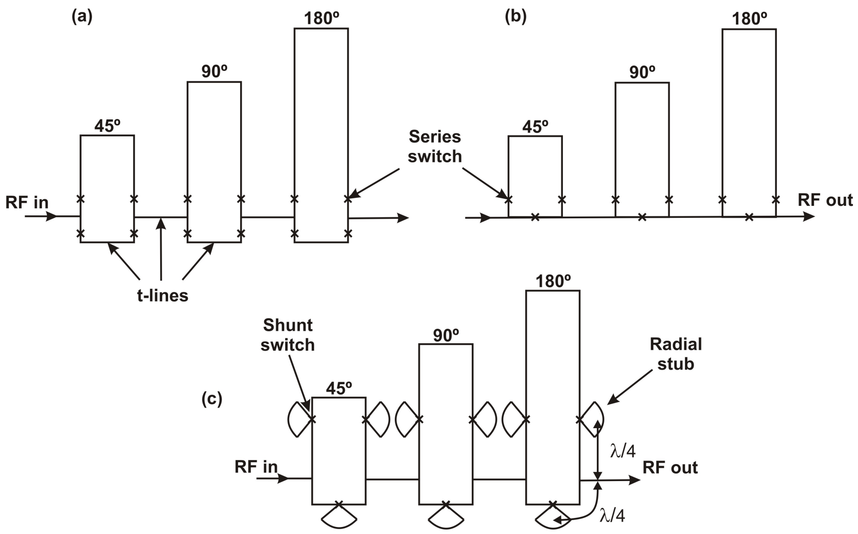

Figure 3.12: (a,b) Switched-line phase shifters with series switch, and (c) shunt switch configurations.

digital phase shifters are based on different delay bits or delay transmission lines, where the phase shift is obtained by switching the required number of bits. For instance, every delay bit is implemented separately and a N-bit phase shifter is obtained by using a succession of different bit values as presented in Figure 3.12. These digital phase shifters can be fabricated using series or shunt RF-MEMS switches over different types of transmission lines, but commonly over microstrip or coplanar waveguide (CPW) lines. For series switches in microstrip line designs with isolated electrodes, no DC-blocking capacitors are needed between the RF-MEMS. Also, due to the high isolation of the switches, the design can be implemented by using 3-switches (Figure 3.12b) instead of 4-switches (Figure 3.12a). For shunt switches on microstrip lines, their anchors need to be connected to the ground plane, using either via-holes or $\lambda_g/4$ open stubs. When via-holes are used, the t-line is physically grounded when the switch is down, whereas by using stubs, the t-line is virtually grounded resulting in a resonance at the desired frequency according to the dimensions of the stubs. The radial shape of the stubs shown in Figure 3.12c is used to improve the bandwidth compared with straight low-impedance stubs.

The biasing of RF-MEMS is achieved by using different circuit configurations depending on the type of switch and line implemented on the design, as presented in Figure 3.13. The most important aspect to highlight from these diagrams is the complexity reduction of the circuits, by contrasting the biasing circuit configurations of the p-i-n diode (Figure 3.14a) and the FET transistor (Figure 3.14b) with the RF-MEMS switches. The p-i-n diodes require both positive and negative voltages, more current, and evidently more space. FET transistors are equally simple for biasing as RF-MEMS but they suffer from a relatively high insertion loss and no linearity above 6 GHz. However FET switches still

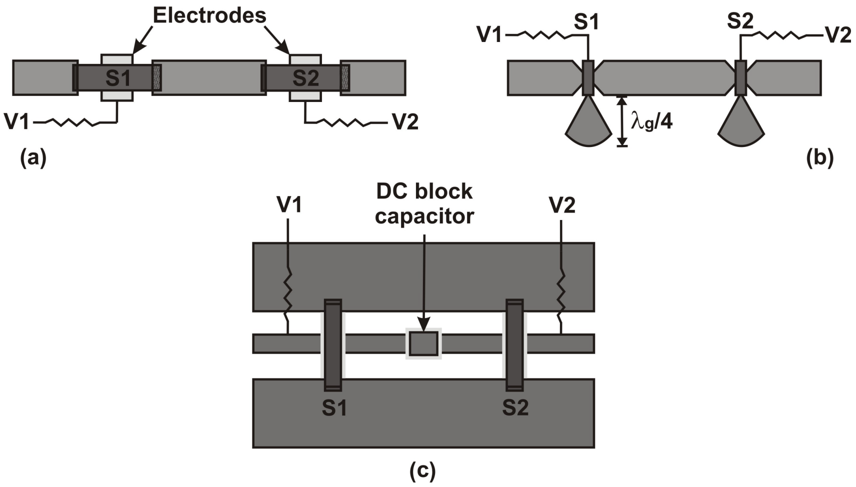

Figure 3.13: Bias configuration for microstrip (a) series switches, (b) shunt switches, and (c) CPW shunt switches.

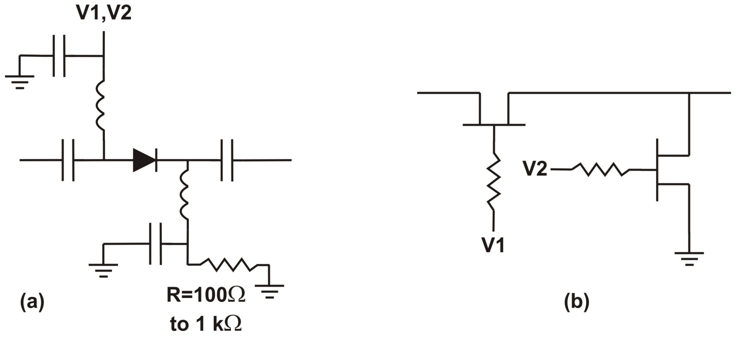

Figure 3.14: Bias configuration for (a) p-i-n diode, and (b) FET switch.

provide a good cost-performance ratio, considering that RF-MEMS still need to reduce their cost of production, and refine their monolithic full-integration option on microwave circuits to beat the other switches. As mentioned before, this work will focus only on DC-contact RF-MEMS cantilever switch designs in series on microstrip lines. Therefore, different aspects related to the electrostatic actuation, like the position, dimension, and isolation of the pull-down electrode is analysed in Chapter 5 along to the simulated and measured results of the RF-MEMS design developed in this work. An example of a DC-contact RF-MEMS phase shifter using the switched delay line technique is the one developed by The Rockwell Science Centre [14] as presented in Figure 3.15. This microstrip switched-line phase shifter is a 4-bit DC-40 GHz built on a $75\mu m$-thick GaAs substrate. The series switches have $C_{\text{off}} = 2fF$ and $R_s = 1 - 1.5\Omega$, resulting in a very high isolation up to 50 GHz, with average insertion loss of -2.2 dB at X-band (8-12GHz).

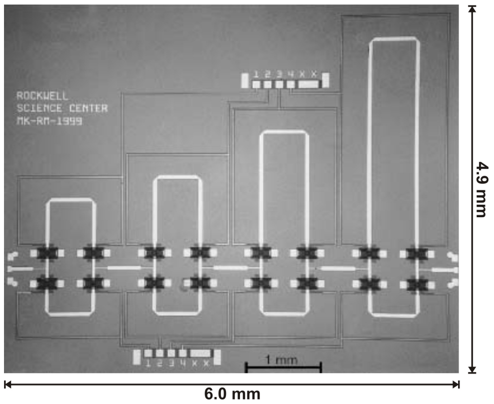

Figure 3.15: Rockwell DC-40-GHz switched-line phase shifter [14].

## 3.7 Summary

The aim of this chapter was to present the most relevant information about RF-MEMS in order to understand their way of operation, their promising better features (compare with the most common switches used for some specific applications), the general models used for their design and analysis, the main issues on their fabrication process, and the state-of-the-art of this switch technology. It is important to point out that there is a large amount of information about RF-MEMS nowadays, however most of the background and models of analysis of RF-MEMS exposed in this chapter have been taken from one particular book [14], for the particular case of a DC-contact RF-MEMS cantilever switch in series on microstrip lines. Also, complementary information from different articles that has been considered important for the aim of this work, such as the analysis of the state-of-the-art of RF-MEMS made on [16], have also been included.

Furthermore, this chapter has shown the description, classification, characteristics, main parameters, models of design and analysis, and the current possible applications of RF-MEMS, where p-i-n diodes, FETs, SiGe, and CMOS technologies are not able to meet the requirements of these applications. Also, a recent analysis of the state-of-the-art of RF-MEMS has been presented to point out the different applications where RF-MEMS have been identified as well suited, such as receive-only intelligent base station antennas with beam scanning capabilities using true-time delay phase shifters, which is closely related to the main aim of this project.

Also, some of the current issues and challenges of RF-MEMS have been detected, where cost, full-integration, and reliable performance are the critical factors that have limited the complete exploitation of RF-MEMS in the market. Therefore, general design guidelines have been exposed as a reference to this work, with the aim of proposing a new cheap manufacturing technique for RF-MEMS switches on PCBs, in order to have full integration with the phase array antennas by implementing digital phase shifters on microstrip technology, and contributing to the research of a reliable switch. Then, a general background of digital phase shifters using the switched delay-line technique has been explained in order to understand their operability, and how RF-MEMS can benefit the effectiveness of these devices to enhance the entire system. Next chapters present the designs, simulations, measurements, and analysis of the results of both the reconfigurable microstrip phased array antennas and RF-MEMS, based on the background presented here and in Chapter 2.

# Chapter 4

# Reconfigurable Microstrip Phased Array Antennas

## Contents

## 4.1 Introduction

In Chapter 2 the analysis of the general background of phased array antennas was carried out in order to investigate their way of operation. The derivation of some of their fundamental parameters was presented as well, to evaluate their performance. Additionally, different models for the analysis and design of microstrip antennas were demonstrated. In Chapter 3, the general background of the switched delay-line technique was presented in order to design microstrip digital phase shifters with RF-MEMS. The purpose of the background is to have the elements to design a representative architecture of reconfigurable microstrip phased array antenna, suitable for the monolithic integration of RF-MEMS on the same PCB, in order to electronically steer the main beam. Therefore, the aim of this chapter is to present the procedure followed to achieve such architecture. The evaluation of the performance of this reconfigurable phased array is based on the theoretical background, and on the validation of the simulations that demonstrate good agreement with the measurements.

The design and simulation processes, along with the measured parameters such as reflection coefficient ($S_{11}$), input impedance ($Z_{in}$), gain ($G$), beamwidth ($BW_{-3dB}$), side lobe level ($SLL$), and bandwidth ($BW$) are presented for the frequency of interest of 12.5 GHz. Also, the reconfigurability of the phased array antennas is investigated, analysing the performance of the array when the beam is steered to different positions in the H-plane. In this work, an antenna is considered to be good if it presents acceptable values in its main parameters, in agreement with a standard of operation. For instance, the main resonant frequency of an antenna is found if the magnitude of the reflection coefficient is $\leq -15dB$ at that frequency. Then, it is possible to say there is acceptable matching of impedances between the antenna and the feeding source. The evaluation of the fundamental parameters of an antenna is discussed in the analysis of the results of the radiation pattern, comparing the values of the measurements with the simulations for each specific parameter.

In this chapter the simulations, measurements, and analysis of the results of different designs of microstrip phased array antennas are presented, describing the procedure and analysis developed in each design to achieve the final architecture of reconfigurable phased array antenna. Thus, Section 4.2 discusses the methodology used to design, simulate, and measure different architectures of antennas. Sections 4.3 presents the design and analysis of the main element of the phased array. This design is explained in more detail, considering it as the departing point to understand the process applied to the rest of the designs. Section 4.4 presents the analysis of the performance of four microstrip antennas. Section 4.5 presents the design and evaluation of the performance of the four antennas with feeding network. Section 4.6 describes the design and performance of the digital phase shifter. Finally, Section 4.7 presents the analysis of the performance of the reconfigurable phased array antennas.

## 4.2 Design and Verification

One of the key benefits that makes microstrip antennas the best option for the aim of this project is their low cost and their versatile fabrication based on PCB technology. Therefore, the model used to design microstrip antennas on PCB substrates, alongside to the simulation and validation processes that have been employed for all the designs of this work, are presented next.

### 4.2.1 Design

In order to design microstrip antennas many aspects have to be considered. First, there are different parameters that characterize an antenna, but two are the most important for designing. These two parameters are: the desired frequency of operation, related to the reflection coefficient ($S_{11}$), and the desired input impedance ($Z_{in}$) that the antenna should present when excited. Once these two parameters have been selected, the type of substrate, the shape of the antenna, and the feeding technique need to be decided.

In this project, the frequency of operation and the input impedance are 12.5 GHz and 50Ω, respectively, for all the antenna designs presented here. Rogers 4003c has been chosen as the main substrate because of its low loss ($\tan\delta = 0.0027$), and good performance at high frequencies, with relative dielectric permittivity ($\varepsilon_r$) of 3.55, double-sided 17$\mu m$-thick copper, and 0.813 mm substrate height ($h$) [62]. Rectangular shape microstrip antennas with inset feed technique, quarter wave transformer, and T-junction power divider are used to feed the different arrays. Parallel open stubs have been used for better matching of the input impedance of the arrays with the 50Ω SMA connectors used as the source probes. The background of all these feeding and matching techniques has been presented in Chapter 2.

Once the general parameters have been chosen, it is possible to start with the design of the microstrip antennas. The Transmission Line Model has been chosen as the initial designing method because of its simplicity and versatility of application. As was explained in Chapter 2, this model has a set of formulas to find the dimensions and the input impedance of the patches for the desired frequency. Therefore, this model is employed for designing the main patch element that all the different designs of antennas have in this work.

### 4.2.2 Simulation

All the simulations carried out for the different designs of antenna have been developed in CST Microwave Studio ®. With this simulator it is possible to investigate most of the main parameters of the antennas at the range of frequencies of interest, by looking at the results allocated in different categories of the simulator. For instance, the 1D-results present the graphical representation of the magnitude of the S-parameters and the parameters related to them. Therefore, parameters such as the resonant frequency (or the reflection coefficient, $S_{11}$), input impedance ($Z_{in}$), and standing wave ratio (SWR) are possible to be obtained. The 2D-results include all the available monitors for different parameters such as the electric and magnetic fields, surface current, electric energy density, and power flow. The 3D-results are basically the representation of the radiation pattern in different coordinate systems like the cartesian, polar, and spherical systems. Then, different parameters such as gain (G), directivity (D), radiation efficiency, beamwidth ($BW_{-3dB}$), bandwidth (BW), side lobe level (SLL), and the direction of the main beam can be obtained.

CST Microwave Studio applies the Finite Integration Technique (FIT) [63] as the numerical base method to investigate the electromagnetic behaviour of any device under test (DUT). This technique applies and solves the integral form of the Maxwell's Equations to the DUT, by taking into account different aspects such as the electric and magnetic characteristics of all the materials that integrate the device, and the boundary conditions of the device. The analysis can be developed by applying different possible solvers on either time or frequency domain. This simulator employs a spatial discretization technique to divide the shape of the DUT into cells or cuboids in order to have geometric flexibility and suitable conditions for the application of the FIT technique. This spatial discretization is developed by applying a general mesh, which is defined according to the range of frequencies of interest, type of solver, boundary conditions, materials, and shape of the device. The accuracy of this method depends on different aspects but mainly on the number of meshcells, or on the amount of lines per wavelength in which each cell has been divided. In general, this is an overview of how CST Microwave Studio works for investigating the electromagnetic behaviour of different structures like antennas.

### 4.2.3 Experimental Validation

In order to validate the results obtained from all the designs of antennas analysed in the simulator, these were built on Rogers 4003c boards employing PCB manufacturing techniques. Specifically, a photomask and a developer were used to selectively remove part of the photoresist coated on one side of the board, and to preserve the remaining photoresist to protect the copper featuring the design of the antenna. Subsequently, the unprotected copper is removed using a wet etching technique. Then, the layout of the antenna remains on the board. Two different scenarios were performed to measure the main parameters of the physical antennas. The first one (scenario 1) was set to obtain the reflection coefficient ($S_{11}$), the input impedance ($Z_{in}$), the standing wave ratio (SWR), and the bandwidth of the resonant frequency ($BW_{-10dB}$), defined in this work as the range of frequencies in which the $S_{11}$ is below $-10dB$, considering that the loss of an antenna is low in this range. Therefore, once different designs of antennas were built, the first step was to connect each design to a Network Analyser (NA), and particularly to the Vector Analyser ZVB-20, to measure the S-parameters as shown in Figure 4.1.

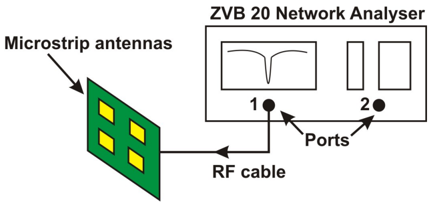

Figure 4.1: Measurement scenario of the $S_{11}$ parameter of the antennas with the NA.

Figure 4.1 shows the settings for the connection of the different antennas developed in this work. In this configuration, an antenna is connected to the 50Ω port 1 of the network analyser by a RF cable. Then, the network analyser is calibrated first with the RF cable for the frequency range of 10 to 14 GHz. Thus, the magnitude of the $S_{11}$, SWR, and the $BW_{-10dB}$ are obtained straightforwardly from the screen of the NA by selecting the appropriate measurement. The $Z_{in}$ of the antennas is obtained by looking at the value of the $S_{11}$ over the Smith Chart mode of the NA. This way of measuring the input impedance is based on the following analysis:

According to [37] the scattering parameters of a two-port network (Figure 4.2) are given by the relationship between the amplitudes of the incident voltage waves on each port $V_1^+$ and $V_2^+$, and the amplitudes of the reflected voltage waves $V_1^-$ and $V_2^-$, as given by:

$$\begin{bmatrix} V_1^- \\ V_2^- \end{bmatrix} = \begin{bmatrix} S_{11} & S_{12} \\ S_{21} & S_{22} \end{bmatrix} \times \begin{bmatrix} V_1^+ \\ V_2^+ \end{bmatrix}$$

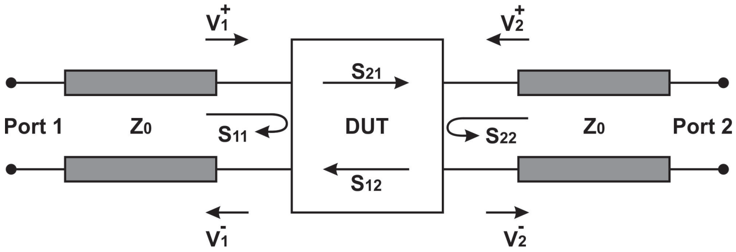

Figure 4.2: Analysis of the S-parameters of a two-port network.

where the scattering parameters are the $S_{ij}$ elements. A specific element of the [S] matrix is determined as:

$$S_{ij} = \left(\frac{V_i^-}{V_j^+}\right)_{V_k^+=0, \quad \text{for} \quad k \neq j} \tag{4.1}$$

which means that $S_{ij}$ is found by exciting port $j$ with an incident wave of voltage $V_j^+$, and measuring the reflected wave amplitude, $V_i^-$, coming out of port $i$. The incident waves on all ports except the $jth$ port are set to zero, which means that all ports should be terminated in matched loads to avoid reflections. Then, $S_{21}$ is the transmission coefficient $T$ from port 1 to port 2, and $S_{11}$ is the input reflection coefficient $\Gamma$ seen looking into port 1 when port 2 is terminated in matched load, or for a one port network, such as the scenario presented in Figure 4.3, for the measurement of the input impedance of an antenna. Then, according to Eq.(4.1) the $S_{11}$ parameter is defined as in Eq.(4.2).

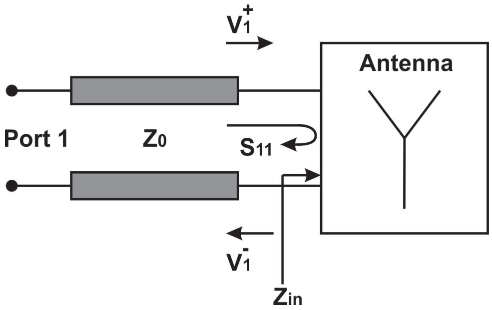

Figure 4.3: Analysis of the $S_{11}$ parameter of one port.

$$S_{11} = \left(\frac{V_1^-}{V_1^+}\right)_{V_2^+=0} \tag{4.2}$$

If the antenna presents an input impedance $Z_{in}$ to an incident wave of voltage, the input reflection coefficient with load $Z_{in}$ is:

$$\Gamma = \frac{Z_{in} - Z_0}{Z_{in} + Z_0} \tag{4.3}$$

where $Z_0$ is the characteristic impedance of the transmission line connected to the antenna. Therefore, by rearranging Eq.(4.3) to find $Z_{in}$ in terms of $\Gamma$, this results in:

$$Z_{in} = \frac{Z_0(1+\Gamma)}{1-\Gamma} \tag{4.4}$$

where $\Gamma = S_{11}$. Then the input impedance of the antenna can be obtained by simply measuring the reflection coefficient. Thus, the network analyser employs this single measurement of the S-parameters to determine the corresponding impedance by using the expression of Eq.(4.4). Consequently, by simply looking at the Smith Chart of the network analyser, which represents the normalized input impedance of the antenna with respect to $Z_0$, or $50\Omega$, at the desired frequency, it is possible to measure the input impedance of the antenna. Then, the antenna presents $50\Omega$ of input impedance at 12.5 GHz if the normalized value at that frequency in the Smith Chart is very close to unity, considering that the input impedance of the RF cable is $50\Omega$ as well, due to the previous calibration of the system.

The second scenario (scenario 2) involves the measurements of the radiation pattern, beamwidth ($BW_{-3dB}$), bandwidth (BW), side lobe level (SLL), and gain (G) of the antennas. These measurements were performed inside an anechoic chamber in order to avoid reflections and interferences of the interested RF signals from other bodies in the environment, and to obtain a better approximation of the exact parameters of the antennas. For these measurements it was necessary to set the network analyser in a full two-port mode in order to measure the radiated energy from the microstrip antennas (transmitter) to a waveguide horn antenna (receiver), investigating the magnitude of the transmission coefficient or the $S_{21}$ parameter, according to the arrangement of connections presented in Figure 4.4. From Figure 4.4 it is possible to see that port 1 of the network analyser is connected by a RF cable to the microstrip antennas. These antennas are set on a turntable that rotates in a discrete number of steps by a synchronous electric motor from $0°$ to $180°$, in order to obtain the magnitude of the $S_{21}$ parameter at all these different positions for the frequency range of 10 to 14 GHz. These antennas are fixed on an aluminium plate to have physical support while the turntable moves. The antenna positioned at the left side of the anechoic chamber, at approximately 2.6 m, is a waveguide horn broadband antenna (EMCO Model 3115, covering the frequency range of 1 to 18 GHz), able to receive the transmitted energy from the microstrip antennas. This horn antenna is connected to the port 2 of the network analyser by another RF cable. With this measurement setup it is possible to obtain the magnitude of the power of the $S_{21}$ parameter at different positions for the desired frequency range. The radiation pattern of the microstrip antennas was obtained by plotting the magnitude of the power of the $S_{21}$ at 12.5 GHz against the angle position of the antennas in either cartesian or polar coordinate systems.

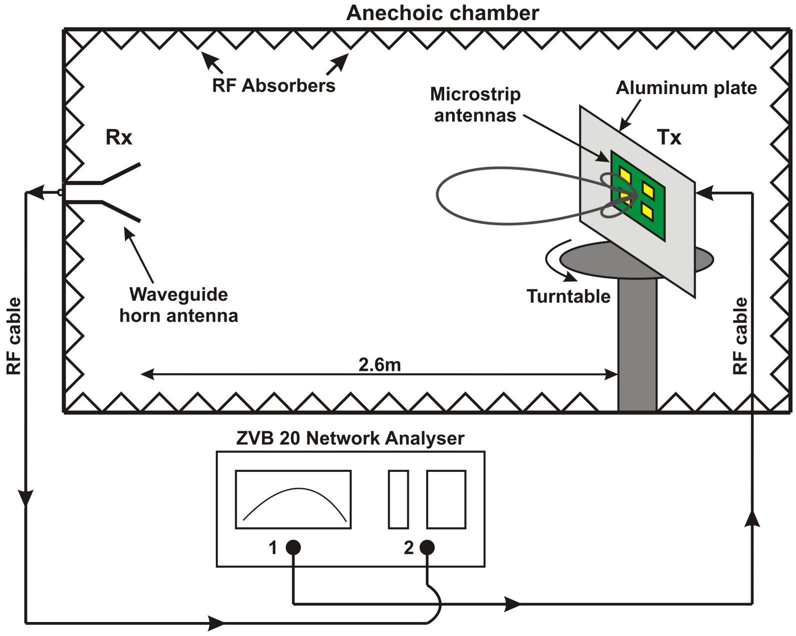

Figure 4.4: Measurement scenario of the S-parameters inside the Anechoic Chamber.

The beamwidth ($BW_{-3dB}$) was obtained by investigating the angle range in which the magnitude of the power of the main beam was $3dB$ below its maximum value. In this work, the bandwidth ($BW$) was obtained by examining the frequency range in which the magnitude of the $S_{21}$ was $3dB$ below its value at 12.5 GHz. The side lobe level (SLL) was measured only for the antennas with steered main beam, considering that the main side lobe appears in the same plane of the main beam when the entire pattern is displaced from broadside, and that there is a rotation restriction of the antennas on the turntable from 0° to 180°. The gain of each antenna was obtained using three elements: one antenna of known gain as the *Reference Gain*, another one that may or may not be of known gain, and the last one the antenna under test. Figure 4.5 shows this scenario in sequence.

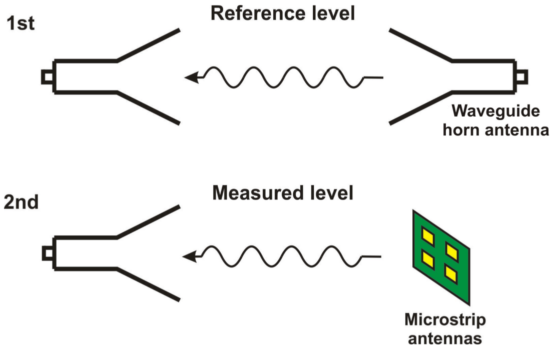

Figure 4.5: The sequence of the process to measure the gain.

The first step is to measure a *Reference Level* of gain by placing the waveguide horn antenna, or the one of known gain (13.2 dBi at 12.5 GHz), in the aluminium plate of Figure 4.4 with straight line of sight with the antenna of unknown gain (placed in the left side of the anechoic chamber) to measure the magnitude of the $S_{21}$ parameter. Once this value has been obtained, the second step is to replace the waveguide horn antenna by the microstrip antennas in order to measure the $S_{21}$ parameter as well, to obtain the *Measured Level*. Once this is done, it is possible to use the following expression to obtain the gain of the antenna under test:

$$\text{G dBi} = \text{Reference Gain dBi} + (\text{Measured Level dB - Reference Level dB}) \qquad (4.5)$$

In words, using the expression of Eq.(4.5) it is possible to investigate the gain of the microstrip antenna by finding the change of the magnitude of the $S_{21}$ by replacing one antenna of known gain with another of unknown gain. This is why it is not necessary to know the gain of the horn antenna placed in the left side of the anechoic chamber, because it only helps to obtain the value of the magnitude of the transmission coefficient at the desired frequency. Photographs of the real antennas used to obtain the measurements inside the anechoic chamber are presented in Figure 4.6.

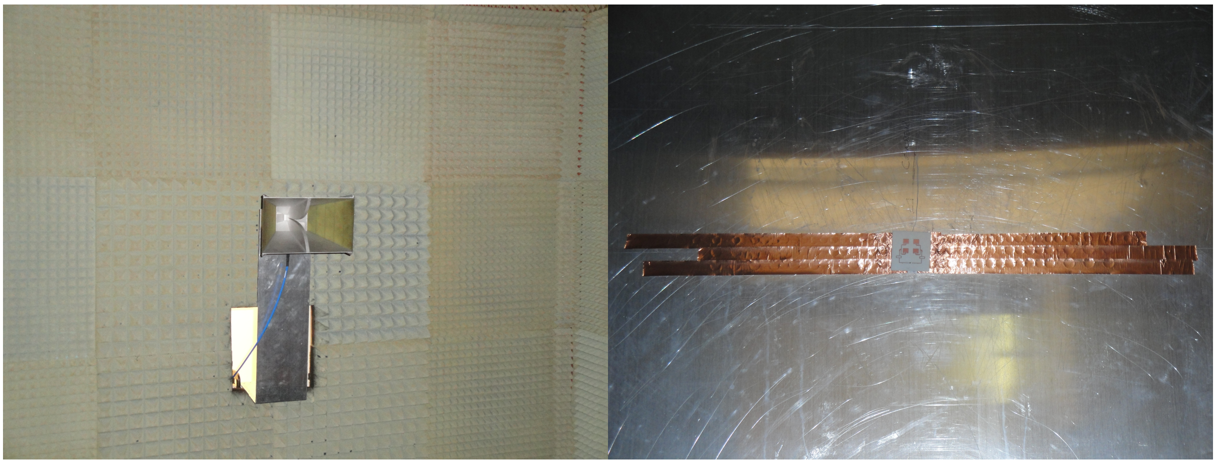

Figure 4.6: Antennas inside the Anechoic Chamber. Waveguide horn antenna (left), and microstrip phased array antenna (right).

## 4.3 Design of the Main Element

The design and simulation of the main element of the reconfigurable phased array antennas is presented in this section. The discussion of the simulation of this antenna is used as the starting point to show the procedure followed for the simulation of the rest of the antennas of this work. This simulation is explained in detail, showing the steps used to obtain the main parameters of the antenna. Specific analysis related to each particular design is presented in the sections dedicated to it, such as the evaluation of matching impedance of the feeding network, or the radiation performance of the antennas.

In order to find the dimensions of the patch antenna (Figure 4.7) on the Rogers 4003c board for the desired frequency of operation at 12.5 GHz, and for the required input impedance of 50Ω, the set of formulas of the Transmission Line model presented in Chapter 2 are used. The derivations developed to obtain all these parameters are presented next. The first parameter to obtain is the width ($W$) of the patch by using Eq.(2.123):

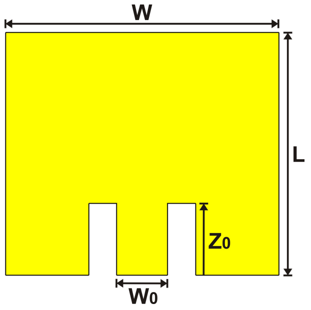

Figure 4.7: Design of the microstrip patch antenna.

$$W = \frac{\left(3 \times 10^{8}\, \frac{m}{s}\right)}{(2)(12.5 \times 10^{9}\, Hz)} \sqrt{\frac{2}{3.55+1}} = 7.9\, mm$$

The effective dielectric constant is found by using Eq.(2.124):

$$\varepsilon_e = \frac{3.55+1}{2} + \frac{3.55-1}{2} \left[1 + 12 \left(\frac{0.813 \times 10^{-3} m}{7.9 \times 10^{-3} m}\right)\right]^{-\frac{1}{2}} = 3.13$$

In order to find the length ($L$) of the patch, first it is necessary to consider the correction factor due to the fringing effects by using Eq.(2.126):

$$\Delta L = (0.412)(0.813 \times 10^{-3} m) \left(\frac{(3.13+0.3)(9.71+0.264)}{(3.13-0.258)(9.71+0.8)}\right) = 0.38\, mm$$

then $L$ is obtained by Eq.(2.125):

$$L = \frac{3 \times 10^{8}\, \frac{m}{s}}{(2)(12.5 \times 10^{9}\, Hz)\sqrt{3.13}} - 2(0.38 \times 10^{-3}) = 6\, mm$$

The wavelength propagating inside the Rogers substrate for 12.5 GHz is obtained by Eq.(2.127):

$$\lambda_g = \frac{0.024\, m}{\sqrt{3.13}} = 13.5\, mm$$

The input conductance ($G_1$) at the edge of the patch antenna with dimensions $W$ and $L$ is approximated using the asymptotic values of Eq.(2.129). Then by considering that $W < \lambda_g$, the expression to obtain $G_1$ is:

$$G_1 = \frac{1}{90}\left(\frac{7.9\,mm}{13.5\,mm}\right)^2 = 0.0038\,S$$

then an approximation to the real part of the input impedance of the patch ($R_{in}$) is given by Eq.(2.132):

$$R_{in} = \frac{1}{2(0.0038)} = 131\,\Omega$$

The input impedance at the edge of the patch is not suitable for the purpose of exciting the antenna with an impedance source of 50Ω. Therefore, it is necessary to use one of the available feeding techniques presented in Chapter 2 to match this impedance. The inset feed technique allows to match the resonant input resistance of the patch with a 50Ω microstrip line. This inset feed line is recessed towards the centre of the patch a distance $z_0$ from the edge of the patch, to drop down the value of the impedance. Therefore, the value of the recessed distance $z_0$ can be calculated using Eq.(2.137), considering that $G_1/Y_c << 1$, where $Y_c = 1/50\Omega$ is the admittance of the microstrip line, and assuming that the mutual conductance $G_{12}$ of the patch is very small. Then the expression to find $z_0$ with $R_{in} = 50\Omega$ is:

$$50\Omega = (130.9)\cos^2\left(\frac{\pi}{6\times 10^{-3}\,m}z_0\right)$$

where 50Ω is achieved when $z_0 = 1.73\,mm$. Finally the width $W_0$ of the microstrip line that matches the input impedance of the patch is obtained by using Eq.(2.135) and by taking into account that $W_0/h > 1$:

$$Z_c = \frac{120\pi}{\sqrt{3.138}\left(\frac{W_0}{0.813mm} + 1.393 + 0.667\ln\left(\frac{W_0}{0.813mm} + 1.444\right)\right)}$$

where $Z_c$ is approximately 50Ω if $W_0$ is $1.66\,mm$.

### 4.3.1 Simulation

Once the dimensions of the patch antenna have been obtained for both the desired frequency of operation at 12.5 GHz and the input impedance of 50Ω, the next step is to draw the patch in CST Microwave Studio and set all the required parameters to properly investigate the main electromagnetic parameters.

This simulator has a user-friendly graphic interface. Most of the required parameters involved in any simulation environment can be modified by using the options in the tool bar. The first step for drawing the patch is to set in the simulator all the materials involved in the design. Copper and hydrocarbon/ceramic dielectric substrate of the Rogers 4003c board are the elements that comprise the antenna. These materials can be found in the library of the simulator where different parameters of their electric, magnetic, mechanic and thermal characteristics are shown. However, some of them need more attention because they should match the values of the specific PCB board that it is used for the physical design. The most important parameters that need to be rectified are: the electric conductivity ($\sigma = 5.8 \times 10^7\ S/m$) and permeability ($\mu = 1$) of the copper, and tangent loss ($\tan\delta = 0.0027$), relative dielectric permittivity ($\varepsilon_r = 3.55$), and permeability ($\mu = 1$) of the dielectric material of the Rogers 4003c board. The loss tangent ($\tan\delta$), along with the dielectric permittivity, is a very important parameter of the dielectric material because it is the one that quantifies the dissipation of the electromagnetic energy or the losses of the electromagnetic field in the substrate. In order to define $\tan\delta$, it is important to consider the electric displacement current density ($\vec{J_d}$) and the electric conduction current density ($\vec{J_c}$), which are present in a metal-dielectric medium. According to [64] these two parameters are defined as follows:

$$\vec{J_d} = j\omega\varepsilon'\vec{E}$$
$$\vec{J_c} = \sigma\vec{E}$$

where $\omega$ is the wavenumber, $\varepsilon' = \varepsilon_r\varepsilon_0$, and loss tangent is seen to be the ratio of these two currents, or an angle in a complex plane as follows:

$$\tan\delta = \frac{\sigma}{\omega\varepsilon'}$$

In words, the definition of $\tan\delta$ means that there is a good dielectric if $\sigma \ll \omega\varepsilon'$, or a good conductor if $\sigma \gg \omega\varepsilon'$. Then to keep the losses low, $\tan\delta$ of the dielectric of the Rogers board is very low.

Once all the parameters of the materials have been established, it is possible to draw the square shape of the patch with the inset feed line, considering all the dimensions that were calculated before. The easiest way to feed the physical design of the antenna is by using a coaxial connector (SMA type) from the back of the patch, presented in Chapter 2 as one of the possible feeding techniques. Therefore, to simulate this configuration, a discrete port of 50Ω is chosen. This connector is situated between the edge side of the inset microstrip line, where the patch presents 50Ω of input impedance, and the ground plane. Figure 4.8 shows the 3D design of the patch on the Rogers board, where $t$ is the thickness of the copper ($17\mu m$) and $h$ the height (0.813 mm) of the dielectric of the

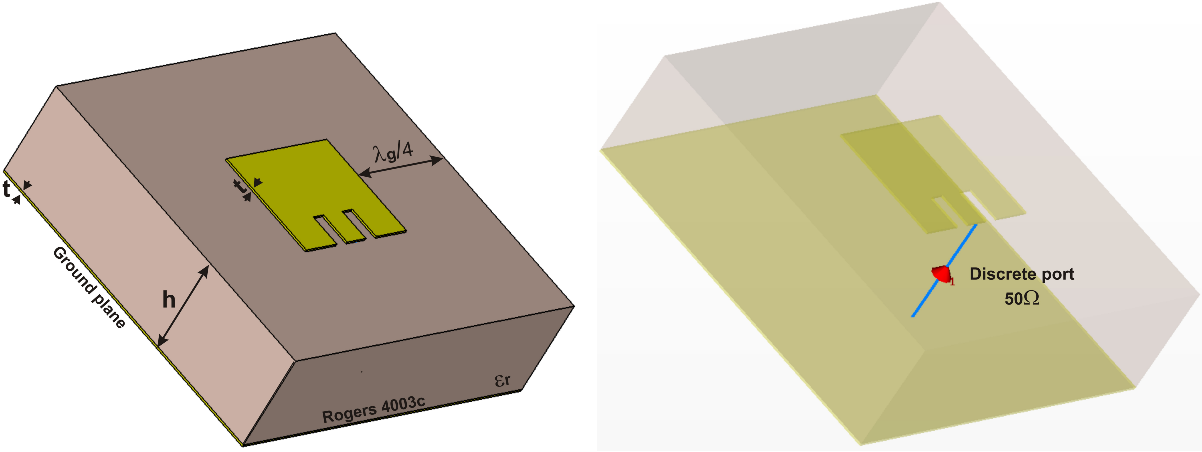

Figure 4.8: 3D design of the antenna (left), and position of the probe feed (right).

substrate, and the position of the discrete port that excites the antenna.

Once the design of the antenna has been created in the simulator, it is time to define all the settings for the simulation such as the excitation signal, frequency range, boundary conditions, mesh, and field monitors. The latter helps to investigate different parameters like the electric and magnetic fields, surface current, bandwidth, or energy distribution on the patch. The signal used to excite the antenna by the discrete port is a Gaussian modulated sine wave covering the range of frequencies of interest. This signal allows the approximation of the impulse response of the antenna, nearly isolating the response for the frequency of the sine wave of 12.5 GHz. Figure 4.9 shows the excitation signal employed for all the designs of antennas simulated in this work.

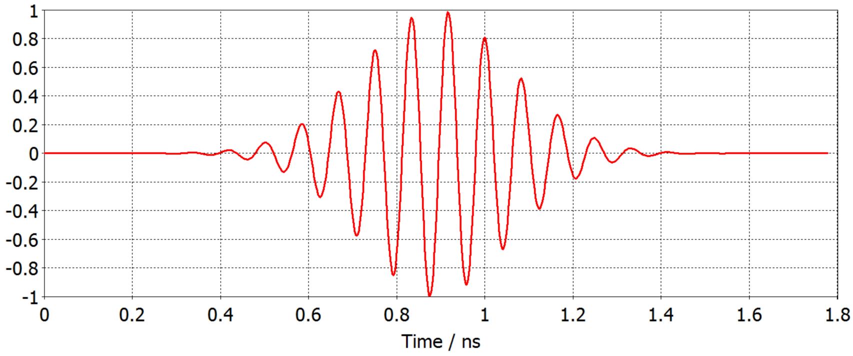

Figure 4.9: Excitation signal of the simulator.

The boundary conditions are set for free space, which means there is open space in all directions around the antenna. Then, the plot of the radiation pattern, along with the parameters related to it, are investigated in the far-field. The mesh applied to the design is directly related to the frequency range of interest (10 to 14 GHz), because the simulator divides the design into cells according to the lines per wavelength selected in the properties of the mesh.

The field monitors are chosen in order to investigate the electromagnetic parameters that are important for the analysis of the antenna. For example, the magnitude and behaviour of the electric field can be examined at different positions from the design, by selecting the position of a reference plane, which can also be set inside the substrate to identify the propagation modes of the electric field.

After all the settings for the simulation have been established, the type of solver has to be selected. Transient and Frequency Domain solvers have been the two solvers used in the simulations of all the different designs of this work. Transient solver is the time domain solver capable of investigating the S-parameters and the field patterns at different frequencies and positions of an antenna. According to the CST documentation [65], this solver stimulates the antenna through the defined port using the broadband signal presented in Figure 4.9. Therefore, it calculates the development of the fields through time, by investigating the transmission energy between the ports and the open space.

Hence, it is possible to develop the first simulation of the antenna. All simulations presented in this work were performed following sufficient computational iterations where steady state solutions were obtained. Figure 4.10 shows the magnitude of the $S_{11}$ parameter in decibels versus the frequency range.

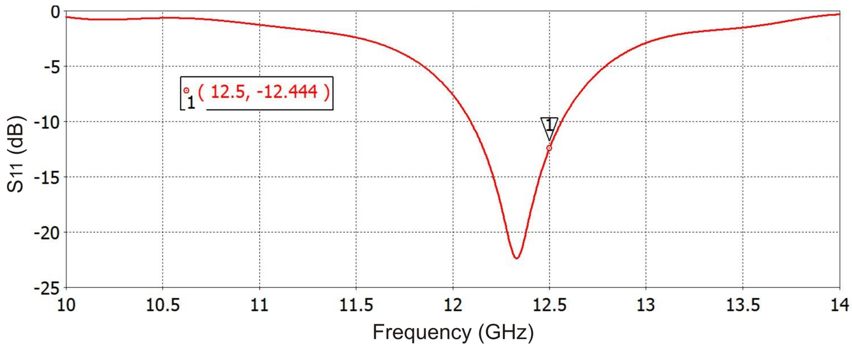

Figure 4.10: Magnitude of the $S_{11}$ of the patch antenna with the theoretical dimensions.

It is important to mention that the magnitude of the S-parameters in the simulator gives the power ratio involved in the network for each parameter. For instance, the magnitude of the $S_{11}$ is the ratio of the power reflected to the incident power. As it can be seen in Figure 4.10, there is one peak below $-20\,dB$ in the frequency range of 10 to 14 GHz. This result suggests that there is one fundamental resonant frequency of the patch at these frequencies because the reflection coefficient is below $-15\,dB$. This agrees with the standard established before, which specifies that an antenna is good when the resonant frequency is equal or below this value. The low value of the reflection coefficient indicates that most of the excited energy from the port is delivered to the antenna. However, this peak is not situated at the desired frequency of operation of 12.5 GHz because at this frequency the input impedance of the antenna is not purely real of 50Ω, hence there is no good impedance matching with the source port. Therefore, an optimization of the dimensions of the antenna was developed in order to change its input impedance in order to get the peak exactly at that frequency. There are two ways to optimize the design. One is using the optimization option of the simulator which modifies the dimensions of the patch according to a defined target. The target for this scenario is the lowest value of the $S_{11}$ parameter at 12.5 GHz. The other way is by modifying manually the dimensions and simulate the design every time a new value is defined. For simplicity, for this antenna, the manual optimization was selected by first modifying the main dimensions ($W$ and $L$) that can potentially modify the resonant frequency of the antenna. After evaluating the change of the $S_{11}$ parameter with the modification of the parameters, $W$ was identified as the main parameter responsible for the change of the resonant frequency. However, a small variation of the width $W_0$, and the distance $z_0$ of the inset microstrip line were also changed. The length $L$ was the only dimension that remained with its original value. The optimum values are: $W = 6.75\,mm$, $W_0 = 1.26\,mm$, and $z_0 = 1.78\,mm$. Figure 4.11 shows the magnitude of the $S_{11}$ with the optimum dimensions of the patch.

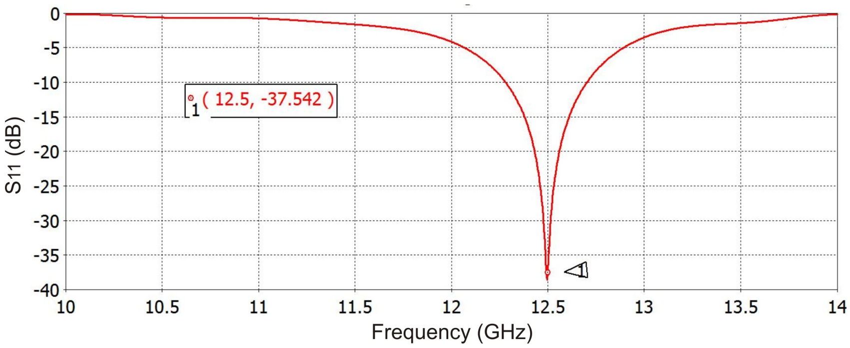

Figure 4.11: Magnitude of the $S_{11}$ of the patch antenna with optimum dimensions.

It also shows that the reflection coefficient at 12.5 GHz is around $-37.5\,dB$, which means very low power is rejected from the antenna. It means that around 99% of the possible transferable power from the source reaches the antenna. It also suggests that the input impedance of the patch is very close to 50Ω. In order to verify the value of the input impedance, Figure 4.12 shows the Smith Chart for the frequency range of interest. The value of the input impedance of the antenna at 12.5 GHz is $(48.7 - 0.34j)\Omega$. With this result, and especially from the value of the real part, it is possible to say that a 50Ω SMA coaxial connector can be matched to the antenna. However, it is necessary to analyse the effect of the imaginary part because its negative value suggests the existence of a parasitic capacitance at that frequency.

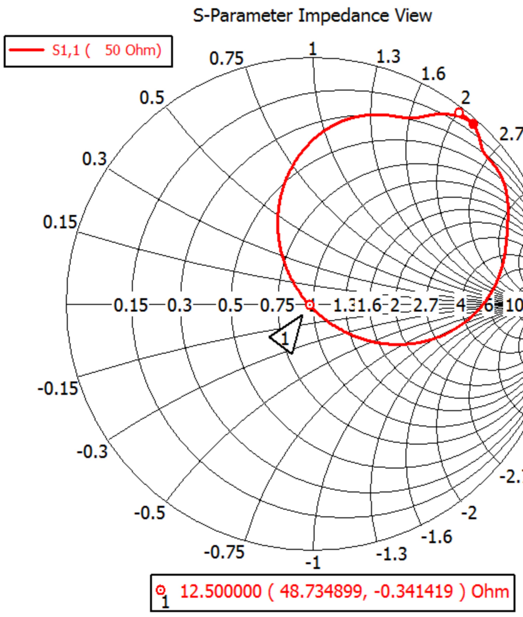

Figure 4.12: Smith Chart normalized at 50Ω.

The associated capacitance to the imaginary part is obtained as follows:

$$C = \frac{1}{j\omega Z_c} = \frac{1}{j2\pi(12.5 \times 10^9\,Hz)(-0.34j)} = 37.4\,pF$$

where $Z_c$ is the imaginary part of the impedance. The associated capacitance is 37.4 pF. This value is small and it will not significantly affect the matching of the connector to the antenna. The Standing Wave Ratio (SWR) is defined as the ratio of the maximum and minimum incident voltage waves, taking into account the magnitude of the reflection coefficient. These incident waves are defined as:

$$V_{max} = V_0^+ + |\Gamma| V_0^+$$
$$V_{min} = V_0^+ - |\Gamma| V_0^+$$

then the Standing Wave Ratio, also called voltage SWR, is obtained by:

$$VSWR = \frac{V_{max}}{V_{min}} = \frac{1 + |\Gamma|}{1 - |\Gamma|} \tag{4.6}$$

This parameter is important because it helps to investigate if there is good coupling between a transmission line and a load. For instance, if $\Gamma = 0$ the value of the VSWR is 1, and the maximum possible transferable energy is delivered to the load, which means there is good coupling. However, if $\Gamma = -1$ or $\Gamma = 1$ for a short or open circuit, respectively, the value of the VSWR goes to infinity, and no energy is delivered because the wave is

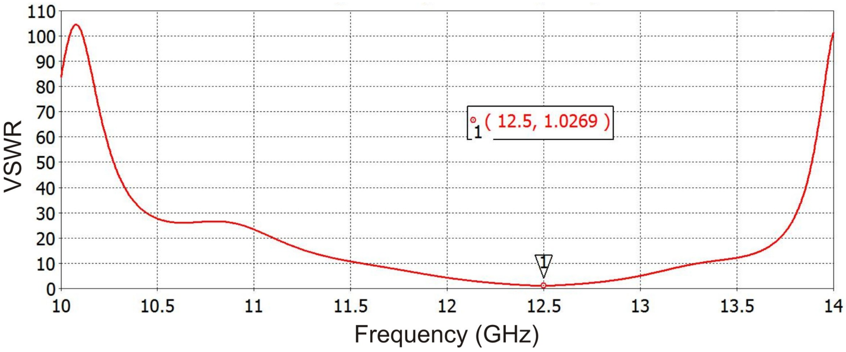

Figure 4.13: Voltage Standing Wave Ratio of the microstrip antenna.

stationary in the line. Figure 4.13 shows the graph of the VSWR versus frequency for the microstrip antenna. The value of the VSWR of the patch is 1.02 which confirms the good matching of the antenna with the port. Once two of the most important parameters have been proved to be at the desired values ($S_{11}$ and $Z_{in}$), it is time to investigate the performance of the antenna by obtaining the rest of the main parameters. The bandwidth of the resonant frequency ($BW_{-10\,dB}$) is presented in Figure 4.14. It can be seen that $BW_{-10\,dB}$ goes from 12.28 to 12.70 GHz, which means a bandwidth of 420 MHz. Another very important electromagnetic parameter is the radiation pattern. From the plot of the radiation pattern in different coordinate systems it is possible to obtain the gain, radiation efficiency, bandwidth, beamwidth, side lobe level, and the direction of the main beam of the antenna. Figure 4.15 shows the 3D plot of the radiation pattern in spherical coordinates. This plot shows the space distribution dependence in the far-field of the strength of the power radiated from the antenna expressed in dBi. The common expression used to identify the far-field distance for antennas physically larger than a half-wavelength of the radiation that they emit is [1]:

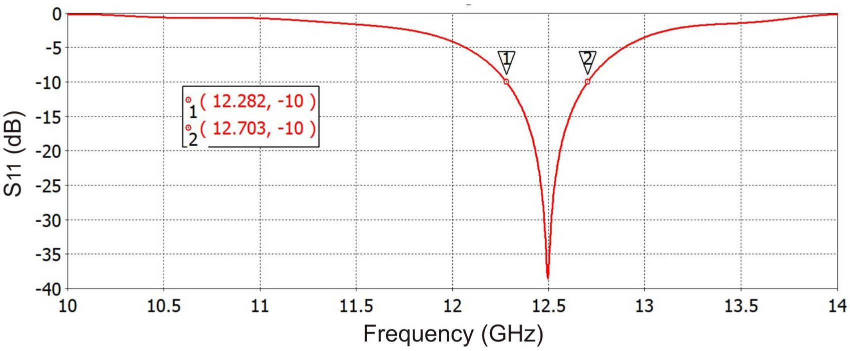

Figure 4.14: Bandwidth of the $S_{11}$ below $-10\,dB$.

$$d_f = \frac{2D^2}{\lambda_0} \tag{4.7}$$

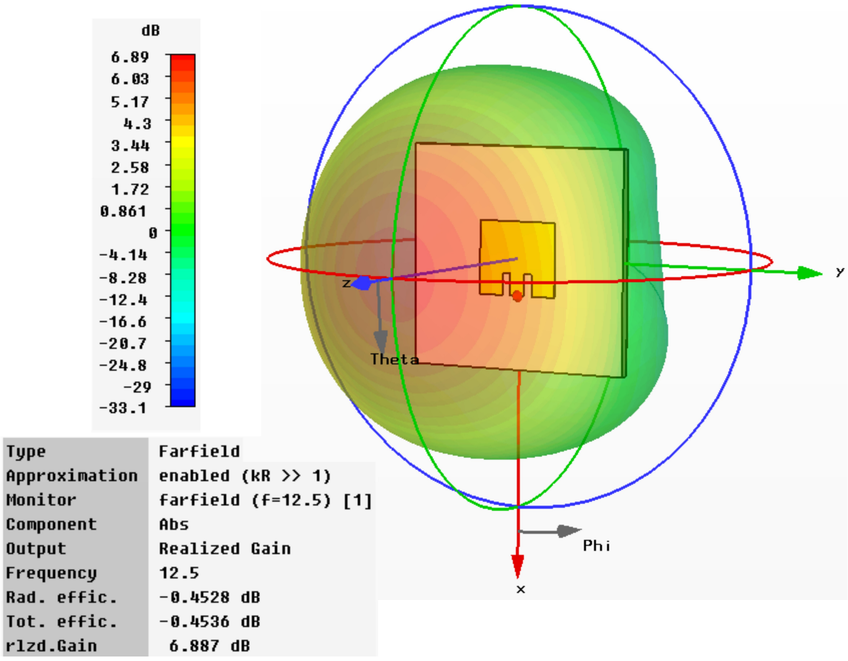

| | |
|---|---|
| Type | Farfield |
| Approximation | enabled (kR >> 1) |
| Monitor | farfield (f=12.5) [1] |
| Component | Abs |
| Output | Realized Gain |
| Frequency | 12.5 |
| Rad. effic. | -0.4528 dB |
| Tot. effic. | -0.4536 dB |
| rlzd.Gain | 6.887 dB |

Figure 4.15: Radiation pattern of the path antenna: spherical coordinates system.

where D is the maximum dimension of the antenna. Then, the plot of the radiation pattern of Figure 4.15 is for a distance longer than 3.8 mm, considering that the biggest dimension of the patch is 6.75 mm. The maximum radiated power is pointing out along of a normal vector from the patch, which means the antenna is radiating at broadside. If the radiation pattern is cut by the xz-plane and seen from the y-axis, it is possible to identify the E-pattern, as the one presented in the analysis of the field components of a microstrip antenna in Chapter 2 (Figure 2.23). In the same manner, if the radiation pattern is cut by the yz-plane and seen from the x-axis, the H-pattern is identified as well. The magnitude of the gain is approximately $6.8\,dBi$, and it is defined as the ratio of the power radiated per unit solid angle to the accepted or input power of the structure multiplied by a $4\pi$ factor. This means it includes the impedance mismatch loss. The radiation efficiency is $-0.45\,dB$, and it is defined as the ratio of the power radiated $P_{rad}$ to the accepted power in the antenna $P_{in}$ in decibels. The bandwidth is obtained by considering the standard established before, as the frequency range where the magnitude of the main beam is $3\,dB$ below its value at 12.5 GHz. Then the bandwidth is 1.25 GHz, from 11.85 to 13.1 GHz.

The radiation pattern can be represented in other coordinate systems, like the polar and cartesian, to better investigate its characteristics. Figure 4.16 presents the radiation pattern in polar (top) and cartesian (bottom) plots. For instance, by looking at the pattern in the polar system, it is easy to see the values of different parameters like the beamwidth and the direction of the main beam on a magnitude/angle scale. The type of the cartesian system used in this simulator allows the projection of the polar plane over

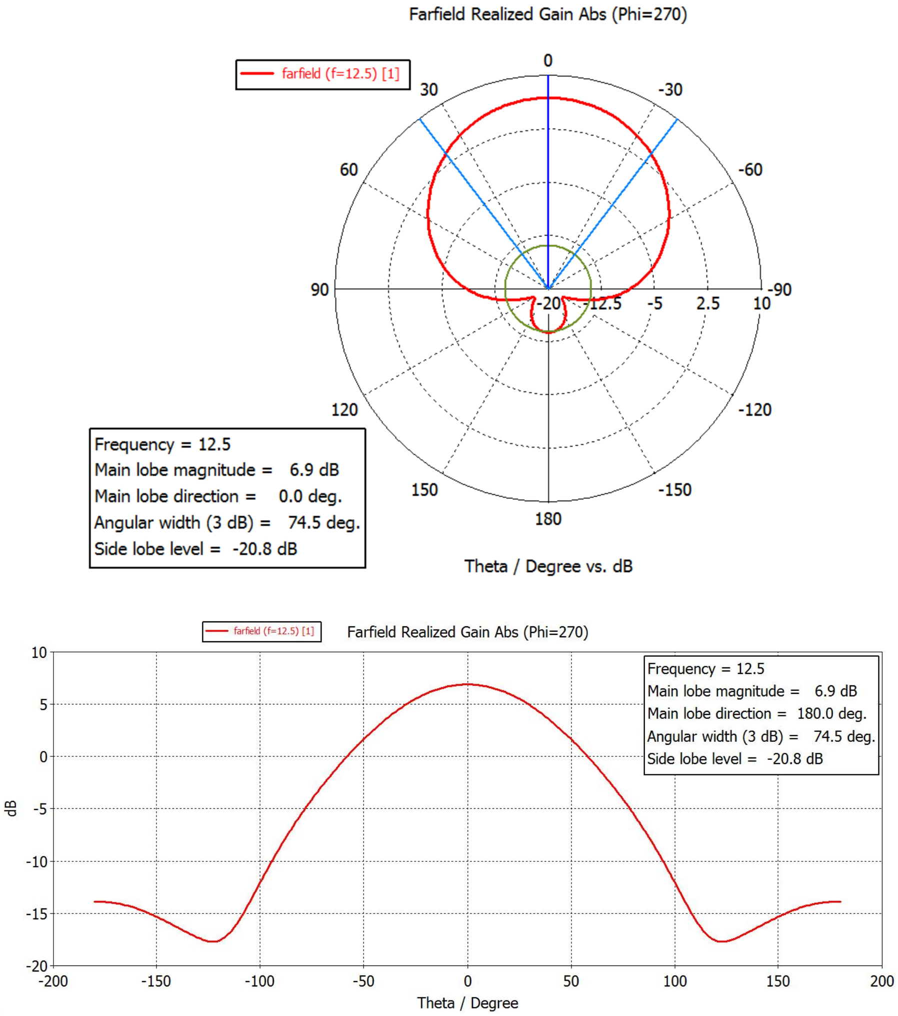

Figure 4.16: Radiation pattern of the patch antenna: Polar plot (top); Cartesian plot (bottom).

the positive region of the rectangular plane to better visualize the pattern, especially the magnitude of the side lobes. The illustration of the radiation pattern in both coordinate systems is plotted by considering that $\phi$ is fixed at certain angle to obtain the projection by seeing into the pattern from the x-axis. From the polar plot it is possible to obtain both the beamwidth ($BW_{-3\,dB}$) angle of 74.5°, and the direction of the main beam at 0° of the patch. The beamwidth is defined as the angle between two directions of the pattern, where the power of the radiation is $3\,dB$ below its maximum magnitude of the main beam. The side lobe level is also shown in this plot, where the green circle in the middle is used to easily identify the magnitude of the main (biggest) side lobe. The side lobe level (or side lobe ratio) is defined as the ratio of the power of the minor lobe with maximum intensity to the power of the main lobe. Therefore the side lobe level is easily calculated by subtracting the magnitudes in decibels, which means the magnitude of the side lobe

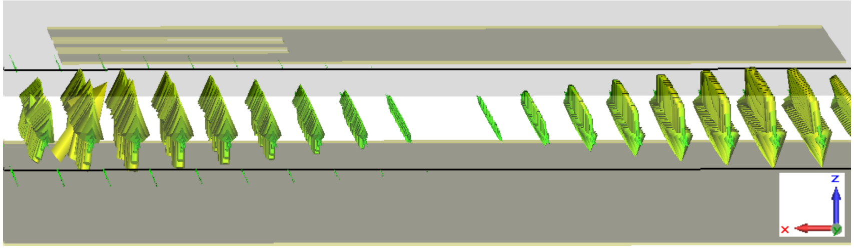

Figure 4.17: Behaviour of the Electric field inside the dielectric.

minus the magnitude of the main beam. However a better representation is displayed in the cartesian plot, where the value of this parameter is approximately $-20.8\,dB$.

From the field monitors of the simulator it is possible to see the behaviour of the electric field generated either inside or outside the patch at certain distance. Figure 4.17 displays the behaviour of the electric field inside the dielectric of the Rogers board, where the variation of the field demonstrates the propagation mode along the x-axis. According to the analysis developed in Chapter 2 about the propagation of the dominant wave mode, it is possible to say that $TM^z_{100}$ is the mode seen in Figure 4.17 for the propagation of the E-field within the substrate along the x-axis. Figure 4.18 shows the electric field at 6 mm away from the surface of the patch. From this plot it is possible to say that the antenna is radiating with linear polarization due to the orientation of the electric field parallel to length $L$ of the patch. Then, the xz-plane is identified as the E-plane, and the yz-plane as

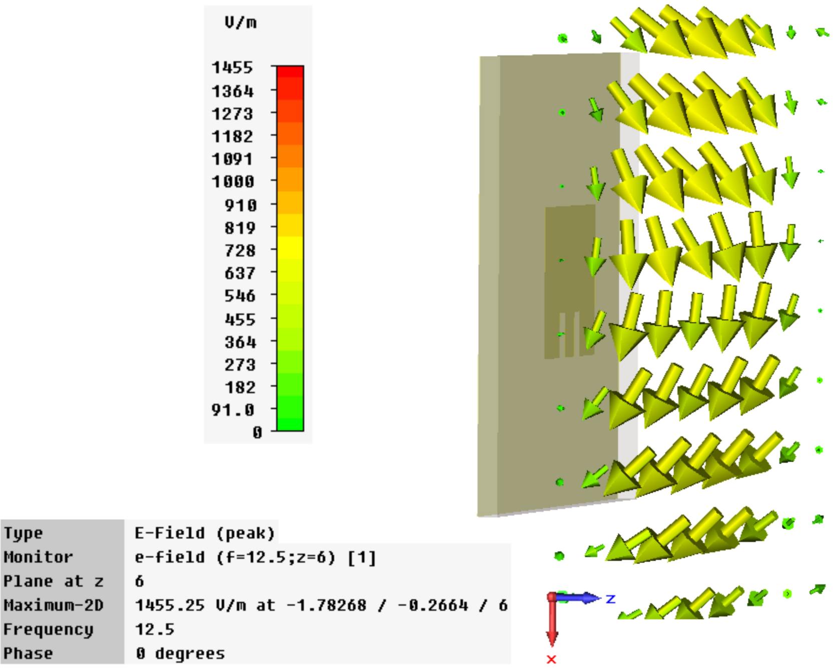

| | |
|---|---|
| Type | E-Field (peak) |
| Monitor | e-field (f=12.5;z=6) [1] |
| Plane at z | 6 |
| Maximum-2D | 1455.25 V/m at -1.78268 / -0.2664 / 6 |
| Frequency | 12.5 |
| Phase | 0 degrees |

Figure 4.18: Orientation of the radiated E-field of the antenna.

the H-plane. The strength of the E-field is demonstrated by the size of the vectors using arrows, where the biggest concentration of the field is situated at broadside of the antenna. It is also possible to observe that as long as the vectors move away from the centre (in front of the patch) to the sides of the path, they bend following the curvature pattern of the E-field. Another important characteristic that can be investigated from the field monitors is the distribution of the currents on the patch. Figure 4.19 shows the distribution of the currents generated in the structure of the antenna. According to [1] when the patch is energized, a charge distribution is generated on the upper and lower surfaces of the patch, and on the surface of the ground plane as well. The movement of these charges creates the currents on the structure. This situation is visible in Figure 4.19 where most of the density of the currents is in the lower surface of the patch and in the upper part of the ground plane, both more concentrated in the centre. This concentration suggests that the higher magnitude of the current is at the centre, and the higher magnitude of the voltage is at the edges of the patch.

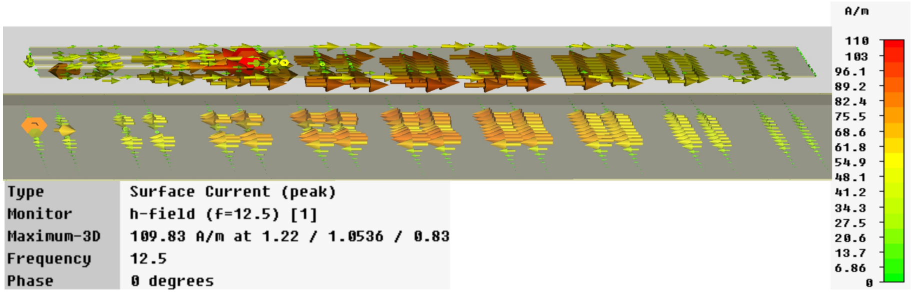

```
Type          Surface Current (peak)
Monitor       h-field (f=12.5) [1]
Maximum-3D    109.83 A/m at 1.22 / 1.0536 / 0.83
Frequency     12.5
Phase         0 degrees
```

Figure 4.19: Distribution of the currents on the antenna.

Up to this point the design and simulation processes of the main element of the reconfigurable microstrip phased array antennas have been developed. A detailed explanation of the steps involved in the simulation to investigate the main parameters of the antenna has been presented as well. This simulation is used as the departing process to develop the simulations of different designs of antennas. Then, the particular aspects of each design are discussed and analysed in the next sections.

## 4.4 Analysis of the Relative Separation of an Array of Four Microstrip Antennas

Once the main element of the reconfigurable phased array antennas has been designed and simulated, it is time to set the configuration of an array to combine the beams from each antenna, optimize the performance, and tune the parameters of the overall array for the desired frequency at 12.5 GHz.

### 4.4.1 Design

In this work, an array of 2 x 2 antennas was selected (Figure 4.20), considering it as the most basic configuration of a planar array. The elementariness of the configuration was chosen taking into account the aim of this work, which is to design a representative phased array antenna in order to prove their reconfigurability based on RF-MEMS switches that can be monolithically integrated on the same PCB board, and to demonstrate the good performance of the entire system. In this work, a design of phased array antenna is considered as good if it satisfies the standard of operation established before for a microstrip antenna, in terms of the $S_{11}$ and $Z_{in}$, and if it demonstrates an electronic change of the main beam with good radiation performance by evaluating some of its parameters such as the gain, beamwidth, and side lobe level. Therefore, the planar array of four elements presented in Figure 4.20 is considered as the reference design to create and to investigate the steering of the main beam when all the individual beams are combined in a constructive and destructive electromagnetic manner. Once a first analysis of the scanning performance has been done in this section, digital phase shifters will be implemented within the feeding network to investigate the overall performance in further sections.

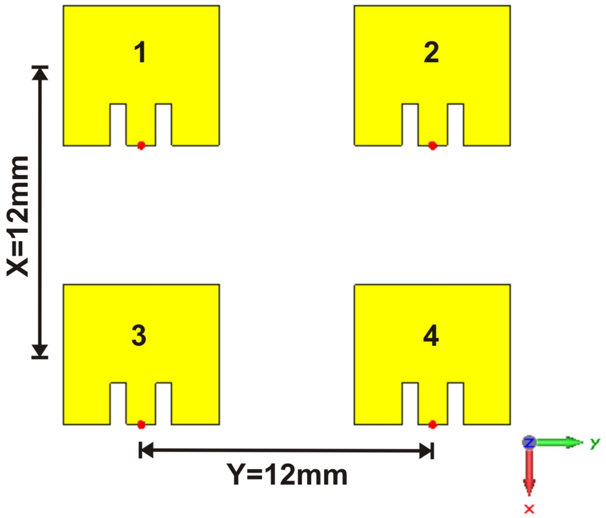

Figure 4.20: 2 x 2 microstrip antenna array.

### 4.4.2 Analysis

The relative distance between the antennas plays an important role because it is one of the possible controls to modify the overall pattern of the array. According to the background in Chapter 2 about these controls, by changing the separation of the elements it is possible to modify the gain and the shape of the radiation pattern. Therefore, in this section the analysis of the relative separation of the elements is presented in order to obtain the possible maximum magnitude of the gain with the lowest side lobe level of the radiation pattern of the array. Part of this analysis process was developed using the optimization option of the simulator with X and Y as the centre-to-centre distance variables, and G and SLL as the target parameters with maximum and minimum magnitudes, respectively. The process of the analysis was divided into two main scenarios. The first one consisted of analysing the radiation pattern with main beam at both broadside and at approximately 30° steered in the H-plane, by modifying the distance of the antennas in Y direction, or in the H-plane, and by leaving the distance in X direction fixed at $0.5\lambda_0$. The beam was steered to 30° in the H-plane because this allows simplification of the design of the digital phase shifter used in the phased array explained and presented in further sections. The values of a series of different parameters such as the reflection coefficient ($S_{11}$), isolation, gain (G), directivity (D), side lobe level (SLL), beamwidth ($BW_{-3dB}$), and radiation efficiency (RE) were obtained for the analysis of the performance of the array based on them. The isolation of the antennas was evaluated by selecting the transmission coefficient with the maximum magnitude for each specific separation. This means the isolation was investigated by observing the biggest transfer of power from one antenna to another.

The second scenario consisted of analysing the radiation pattern with main beam at both broadside and at approximately 30° steered in the H-plane as well, but this time modifying the distance of the antennas in X direction, and leaving the distance in Y direction fixed at $0.5\lambda_0$. The excitation of each antenna is based on $50\Omega$ discrete ports placed in the same position as the one used for the simulation of the single patch shown in Figure 4.8. For the radiation pattern with main beam at broadside all the antennas were fed coherently with the same amplitude and phase of the stimulating signal by the ports. For the radiation with the main beam steered to $\sim 30°$ in the H-plane, all the antennas were fed with the same amplitude, but antennas 2 and 4 with a phase shift relative to antennas 1 and 3 in order to achieve the desired direction of the beam. For instance, a 90° phase shift was used when the separation in both Y and X was set at $0.5\lambda_0$. The reason of the applied phase shift to these two antennas is based on the results derived in Eq.(2.36) for the required phase shift $\delta$ to steer the beam at $\theta = 30°$ (or $\gamma = 60°$). Although this result was calculated for a linear array of isotropic antennas along the y-axis with a separation of $0.5\lambda_0$, it also applies for this planar array of 4 microstrip antennas taking into account the Analytical Pattern Multiplication and the Planar Array Analysis developed in Chapter 2. Then, by looking at the rectangular array of Figure 2.9, if the steering of the beam is only along the yz-plane with $\phi = 90°$, the required progressive phase shift $\delta_y$ of the signal that excites each antenna can be calculated from the next expression:

$$\Psi_y = \beta d_y \sin\theta \sin\phi + \delta_y \tag{4.8}$$

with $\sin\phi = 1$. Then this expression is reduced to $\Psi_y = \beta d_y \sin\theta + \delta_y$ and the analysis of the array is changed to a particular case of the planar array, where the progressive phase shift in the antennas along the x-axis is calculated from the next expression:

$$\Psi_x = \beta d_x \sin\theta \cos\phi + \delta_x \tag{4.9}$$

with $\delta_x = 0$ because $\cos\phi = 0$, which in turn is the same analysis as for a linear array from which the value of $\delta_y = -90°$ was obtained. This is why only antenna 2 and 4 need to be fed with either $-90°$ or $90°$ to steer the main beam at $\sim 30°$ to the right or to the left side of the z-axis, respectively. Then, the required progressive phase difference between the antennas is satisfied by taking into account that antenna 1 and 3 are fed with 0°. Figure 4.21 shows the arrangement of the progressive phase at each element for the planar array of 4 antennas with $0.5\lambda_0$ of separation in both X and Y directions. In the same manner, the phase shift was varied for the other different separations of the antennas in order to achieve the steering of the main beam at 30° in the H-plane. Also, a slight increase of the theoretical phase at each antenna was sometimes necessary in order to move the main beam to 30°. This might be related to the particular type of radiation of the microstrip antennas, to the coupling between them, and to the relatively small size of the overall array. Tables 4.1 and 4.2 show all the values obtained of the parameters for the first scenario of analysis, and Tables 4.3 and 4.4 show the results for the second one.

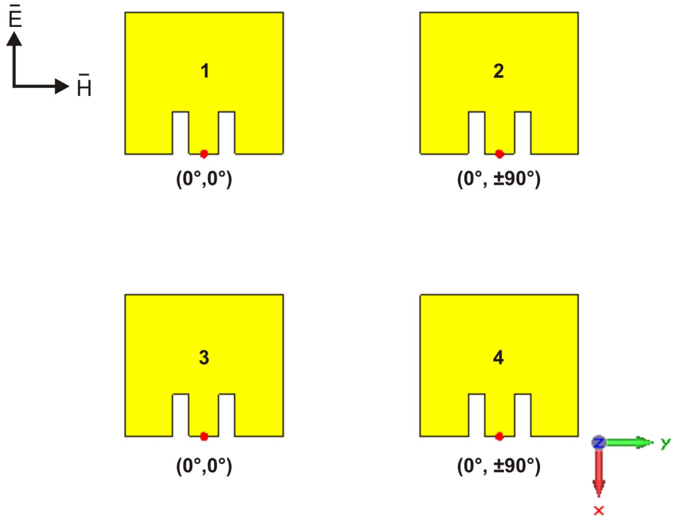

Figure 4.21: Phase shift distribution at each element.

The main analysis was carried out for relative separations longer than $0.4\lambda_0$. The main reason for this decision was the relatively high magnitude of the transmission coefficient obtained at this separation (in Y direction) of around $-10\,dB$. Therefore, in order to avoid poor isolation and strong coupling between the antennas, the initial separation for the

| **Separation** | **$S_{11}$ dB** | **isolation dB** | **Gain dBi** | **D dB** | **SLL dB** | **$BW^{\circ}_{-3dB}$** | **RE %** |
|---|---|---|---|---|---|---|---|
| $0.4\lambda_0$ | -23.54 | -10.63 | 10.78 | 11.12 | -31.4 | 52.3 | 94.49 |
| $0.5\lambda_0$ | -38.70 | -15.92 | 11.48 | 11.84 | -31.4 | 45.4 | 93.52 |
| $0.52\lambda_0$ | -41.60 | -16.70 | 11.63 | 11.99 | -31.3 | 44.0 | 93.58 |
| $0.55\lambda_0$ | -40.16 | -17.82 | 11.80 | 12.18 | -31.2 | 42.4 | 93.29 |
| $0.6\lambda_0$ | -42.19 | -19.60 | 12.08 | 12.50 | -25.4 | 39.8 | 92.83 |
| $0.65\lambda_0$ | -42.30 | -21.13 | 12.31 | 12.76 | -20.3 | 37.5 | 92.25 |
| $0.7\lambda_0$ | -41.70 | -22.50 | 12.49 | 12.97 | -16.9 | 35.4 | 91.60 |

Table 4.1: Results changing the distance in the H-plane with fixed $0.5\lambda_0$ distance in E-plane and main beam at broadside.

| **Separation** | **$S_{11}$ dB** | **isolation dB** | **Gain dBi** | **D dB** | **SLL dB** | **$BW^{\circ}_{-3dB}$** | **RE %** |
|---|---|---|---|---|---|---|---|
| $0.4\lambda_0$ | -23.54 | -10.63 | 9.29 | 10.40 | -5.5 | 46.4 | 87.55 |
| $0.5\lambda_0$ | -38.70 | -15.92 | 9.39 | 10.04 | -3.2 | 43.1 | 88.55 |
| $0.52\lambda_0$ | -41.60 | -16.70 | 9.48 | 10.04 | -3.0 | 42.4 | 89.63 |
| $0.55\lambda_0$ | -40.16 | -17.82 | 9.39 | 9.89 | -2.4 | 41.4 | 90.15 |
| $0.6\lambda_0$ | -42.19 | -19.60 | 9.35 | 9.78 | -1.8 | 39.9 | 91.13 |
| $0.65\lambda_0$ | -42.30 | -21.13 | 9.14 | 9.53 | -0.8 | 38.3 | 91.68 |
| $0.7\lambda_0$ | -41.70 | -22.50 | 9.10 | 9.47 | -0.39 | 36.9 | 92.06 |

Table 4.2: Results changing the distance in the H-plane with fixed $0.5\lambda_0$ distance in E-plane and main beam at $\sim 30°$.

| **Separation** | **$S_{11}$ dB** | **isolation dB** | **Gain dBi** | **D dB** | **SLL dB** | **$BW^{\circ}_{-3dB}$** | **RE %** |
|---|---|---|---|---|---|---|---|
| $0.4\lambda_0$ | -32.10 | -15.57 | 10.36 | 10.76 | -23.4 | 43.9 | 95.34 |
| $0.5\lambda_0$ | -38.70 | -15.92 | 11.48 | 11.84 | -31.4 | 45.4 | 93.52 |
| $0.52\lambda_0$ | -36.50 | -15.94 | 11.69 | 12.05 | -32.3 | 45.7 | 93.28 |
| $0.55\lambda_0$ | -34.36 | -16.06 | 11.92 | 12.27 | -32.9 | 46.1 | 92.74 |
| $0.6\lambda_0$ | -33.89 | -16.25 | 12.20 | 12.58 | -26.3 | 46.8 | 91.72 |
| $0.65\lambda_0$ | -29.54 | -16.16 | 12.35 | 12.74 | -22.8 | 47.4 | 91.51 |
| $0.7\lambda_0$ | -28.50 | -16.00 | 12.34 | 12.76 | -20.5 | 48.0 | 91.49 |

Table 4.3: Results changing the distance in the E-plane with fixed $0.5\lambda_0$ distance in H-plane and main beam at broadside.

| **Separation** | **$S_{11}$ dB** | **isolation dB** | **Gain dBi** | **D dB** | **SLL dB** | **$BW^{\circ}_{-3dB}$** | **RE %** |
|---|---|---|---|---|---|---|---|
| $0.4\lambda_0$ | -32.10 | -15.57 | 8.31 | 8.75 | -2.5 | 43.3 | 91.03 |
| $0.5\lambda_0$ | -38.70 | -15.92 | 9.39 | 10.04 | -3.2 | 43.1 | 88.55 |
| $0.52\lambda_0$ | -36.50 | -15.94 | 9.63 | 10.31 | -3.2 | 43.0 | 88.45 |
| $0.55\lambda_0$ | -34.36 | -16.06 | 9.90 | 10.65 | -3.2 | 42.9 | 87.67 |
| $0.6\lambda_0$ | -33.89 | -16.25 | 10.48 | 11.34 | -3.7 | 42.9 | 85.76 |
| $0.65\lambda_0$ | -29.54 | -16.16 | 10.83 | 11.79 | -3.6 | 42.7 | 85.09 |
| $0.7\lambda_0$ | -28.50 | -16.00 | 11.22 | 12.23 | -4.0 | 42.8 | 84.35 |

Table 4.4: Results changing the distance in the E-plane with fixed $0.5\lambda_0$ distance in H-plane and main beam at $\sim 30°$.

analysis was set at $0.5\lambda_0$ for both directions. Nevertheless the results of the parameters at $0.4\lambda_0$ are shown for comparison purposes. Also a little modification of the width $W$ of the antennas, from 6.75 mm to 6.7 mm with $0.5\lambda_0$ separation in both directions, was done before the whole analysis process started. This modification was performed in order to improve the value of the $S_{11}$ parameter of the entire array. This slight change suggests the coupling between the antennas when they are together in an array. Thus, the width has been reduced to ameliorate such coupling, and to maintain the $S_{11}$ at the lowest magnitude for the resonant frequency of the array at 12.5 GHz.

Once these two factors were considered, the optimum separation distances for the radiation pattern with the main beam at broadside for both scenarios were obtained, using the optimization option of the simulator. However, the optimum distances with main beam steered at 30° for both scenarios were obtained by manually simulating the array for the different separations. This situation is attributed to the fact that it was not possible to use the optimization option to change the separation and to steer the main beam of the antennas at the same time. This is why all the results of the parameters for all the scenarios are presented in different tables to discuss and explain the criterion used to select the best separation of the antennas, in order to achieve the targets established before. The optimization of the simulator showed that $0.52\lambda_0$ is the best distance of Y for the highest gain with the lowest SLL of the radiation pattern, taking into account the radiation efficiency factor of the antennas as well. This value can be verified by looking at the values of G and SLL on Table 4.1, where the best options are $0.5\lambda_0$, $0.52\lambda_0$, and $0.55\lambda_0$ because these three are the ones that present the lowest SLL with almost the same gain. However $0.52\lambda_0$ is the one that presents the best radiation efficiency with 93.58 %.

By looking at Table 4.2 with the results for the main beam at 30°, either $0.5\lambda_0$ or $0.52\lambda_0$ are the best options because these two are the ones with the lowest SLL, without considering the value of $0.4\lambda_0$. The highest gain is for $0.52\lambda_0$ with $9.48\,dBi$, however the lowest side lobe level is for $0.5\lambda_0$ with $-3.2\,dB$. Nevertheless the RE is better for $0.52\lambda_0$ with 89.63 %, along with the values of the isolation and the $S_{11}$. Therefore, $0.52\lambda_0$ has been selected as the best option for the distance Y investigated so far.

The same analytical process was made for the second scenario with X as the variable and Y fixed at $0.5\lambda_0$. The optimum value showed from the optimization of the simulator with radiation at broadside was $0.5\lambda_0$. Looking at Table 4.3 the best choice of distance is between $0.5\lambda_0$, $0.52\lambda_0$, and $0.55\lambda_0$, considering that these three are the ones with the lowest SLL and with almost the same gain. All these three values present very similar results. However $0.5\lambda_0$ is the one that presents better radiation efficiency with 93.52 %. Also by looking at Table 4.4 with the results for the main beam at 30°, these three distances present the same SLL and almost the same gain. Therefore, the best option was again selected by considering the best value of the radiation efficiency where $0.5\lambda_0$ is the best with 88.55 %. Thus, $0.5\lambda_0$ has been selected as the best option for the distance X.

Once the relative separations between the antennas have been selected based on the last analysis, with $Y = 0.52\lambda_0$ and $X = 0.5\lambda_0$, it is time to investigate the S-parameters and the radiation performance of this particular array. Figure 4.22 presents the magnitude of the S-parameters versus the frequency range of 10 to 14 GHz. From Figure 4.22 it is possible to see that the magnitudes of the $S_{11}$, $S_{22}$, $S_{33}$, and $S_{44}$ behave in the same manner for the entire frequency range with a main peak of around $-40\,dB$ at 12.5 GHz. Therefore, it is possible to say that the main resonant frequency of the array is at this frequency. Looking at the magnitudes of the transmission coefficients, the biggest values are for $S_{34}$ (or $S_{43}$, because they are reciprocal) with $-16.7\,dB$ and for $S_{21}$ with almost the same magnitude at around $-17\,dB$. The next lower magnitude is for $S_{31}$ and $S_{42}$ with around $-20\,dB$, and the lowest are for $S_{41}$ and $S_{32}$ with around $-26\,dB$. With these results the biggest magnitudes of the transmission coefficients are for the antennas that are in a side-by-side configuration (antenna 1 with 2, and antenna 3 with 4) compared with the ones that are in a collinear configuration (antenna 1 with 3, and antenna 2 with 4), and with the antennas in cross configuration (antenna 1 with 4, and antenna 2 with 3) which show the lowest magnitudes. According to [1], this can be attributed to the mutual effects that exist between elements of any array, and the easiest way to explain this is by looking at the relative position of the antennas with respect to the radiated source, where the antennas with larger incident energy, or transferred power, are the ones placed in the direction of maximum radiation. For instance, for this particular planar array the biggest transmission coefficients between the elements were obtained between the antennas 1 and 2, and between antennas 3 and 4, from their respective $S_{21}$ and $S_{43}$ parameters. This situation can be explained by looking at the radiation pattern shown in Figure 4.23, where antenna 1 is the only that has been excited.

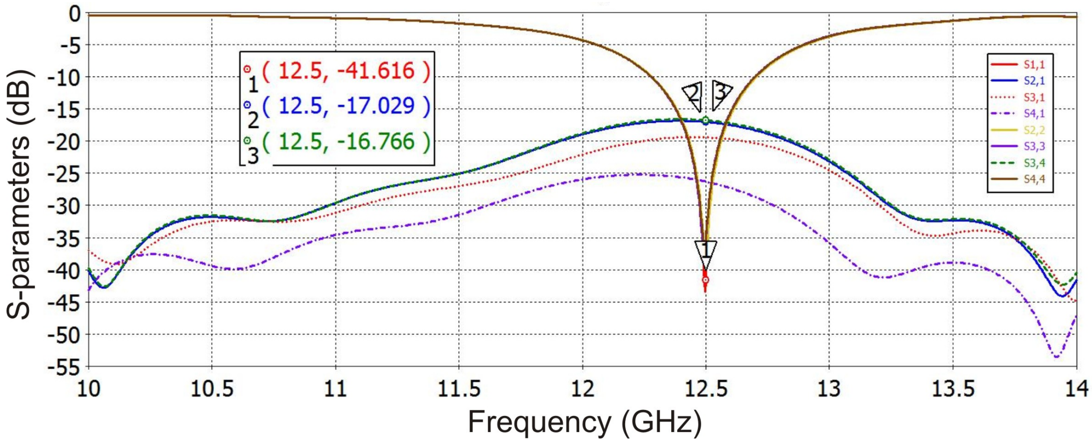

Figure 4.22: S-parameters of the array.

This pattern has been plotted in linear scale in order to better perceive the direction

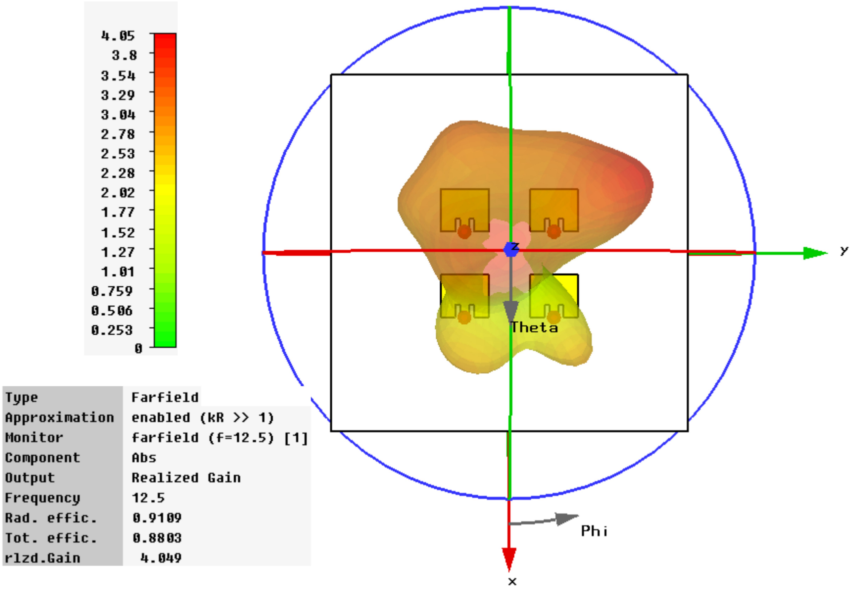

| | |
|---|---|
| Type | Farfield |
| Approximation | enabled (kR >> 1) |
| Monitor | farfield (f=12.5) [1] |
| Component | Abs |
| Output | Realized Gain |
| Frequency | 12.5 |
| Rad. effic. | 0.9109 |
| Tot. effic. | 0.8803 |
| rlzd.Gain | 4.049 |

Figure 4.23: Radiation pattern of the array when only antenna 1 is excited.

of the radiation and to support the next analysis. In Figure 4.23 it is possible to see

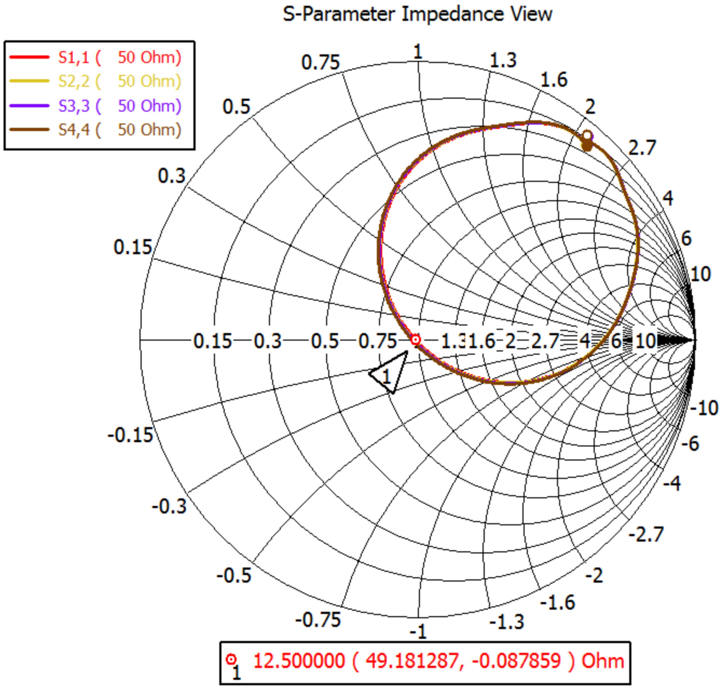

Figure 4.24: Input impedance of the four antennas.

that most of the power radiated from antenna 1 is in the direction of antenna 2, whereas lower radiation can be seen in the direction of antenna 3, and the lowest in the direction of antenna 4. The same behaviour happens if antenna 3 is the only one excited, in which case the antenna 4 is the more affected because it is in the direction of maximum radiation.

This is why $S_{21}$ and $S_{34}$ are the parameters with the biggest magnitudes, followed by $S_{31}$ and $S_{42}$, and finally the $S_{41}$ and $S_{32}$. The input impedance of the four antennas are shown in the Smith Chart of Figure 4.24.

All the antennas show good match with the $50\Omega$ discrete ports used to excite each antenna. This is because the value of all the input impedances are $(49.1, -0.08j)\,\Omega$ at 12.5GHz, with small imaginary part. The good matching of the antennas could be anticipated by the low magnitude of the reflection coefficients presented before. Also, the value of the VSWR supports the good coupling of the antennas with a value of 1.01. The bandwidth of $S_{11}$ below $-10\,dB$ goes from 12.28 to 12.7 GHz, which means a bandwidth of 420 MHz. This value is the same as the one obtained for the single patch antenna presented in the previous section. Neither the plot of the VSWR nor the one for the $BW_{-10\,dB}$ have been presented this time because they are not relevant for the demonstration of these parameters. The radiation pattern of the entire array in the far-field is observed in Figure 4.25. The 3D plot of the radiation pattern shows that the magnitude of the gain is approximately $11.6\,dBi$, and the radiation efficiency is $-0.28\,dB$. Comparing the obtained gain of $6.9\,dBi$ from a single patch, an improvement of around $4.7\,dBi$ was attained from the array, instead of the expected $6\,dBi$ of four antennas. This is because of the losses in the substrate. Then, the gain was approximately increased 3 times instead of 4 times. The radiation efficiency was slightly improved as well, due to the better magnitude of the reflection coefficients of the array. It was not possible to obtain the bandwidth of the array because this option is not available in the simulator when there is more than one antenna excited with multiple source ports defined for each element. Nevertheless this situation is only presented for this particular design.

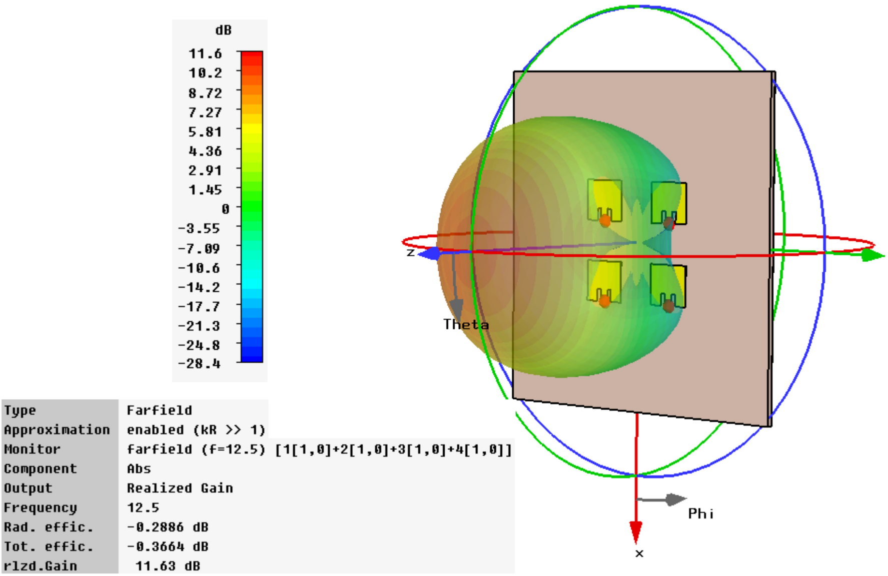

| | |
|---|---|
| Type | Farfield |
| Approximation | enabled (kR >> 1) |
| Monitor | farfield (f=12.5) [1[1,0]+2[1,0]+3[1,0]+4[1,0]] |
| Component | Abs |
| Output | Realized Gain |
| Frequency | 12.5 |
| Rad. effic. | -0.2886 dB |
| Tot. effic. | -0.3664 dB |
| rlzd.Gain | 11.63 dB |

Figure 4.25: 3D radiation pattern of the array.

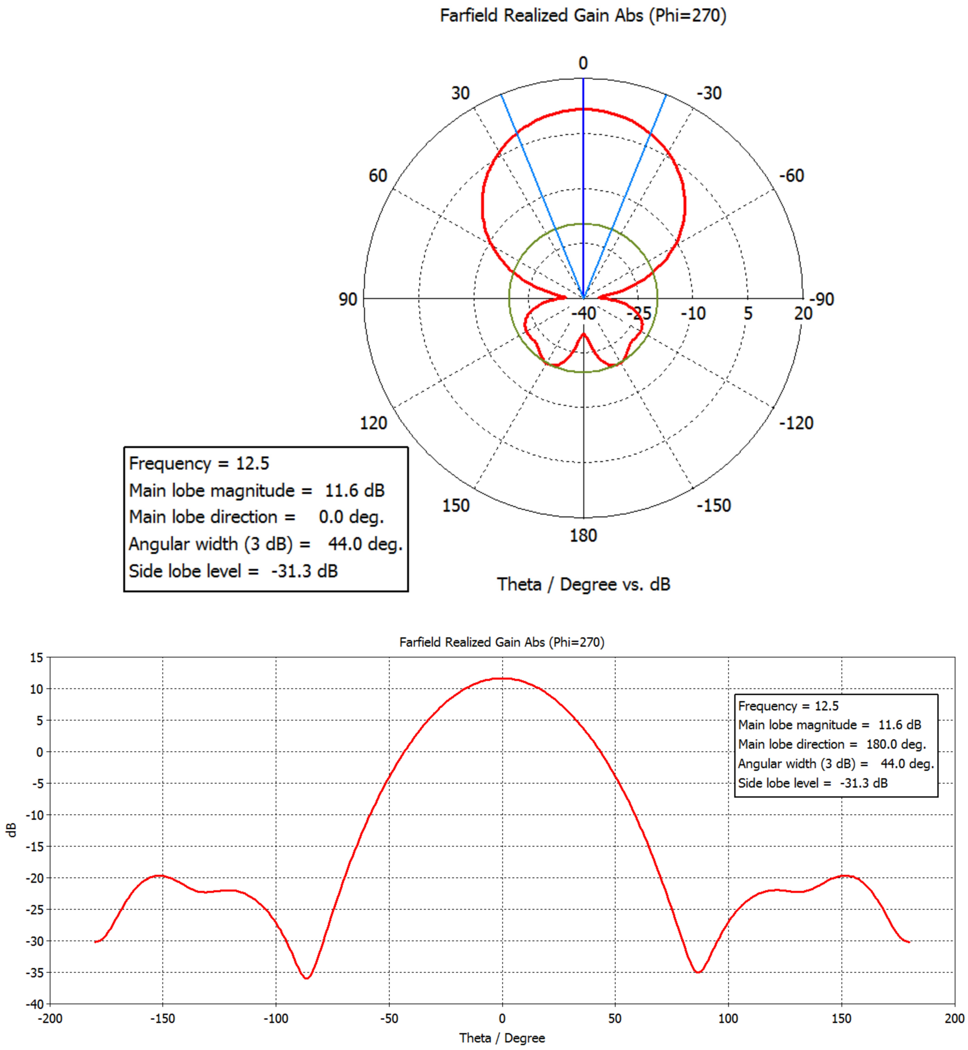

Figure 4.26: Radiation pattern of the array: Polar plot (top); Cartesian plot (bottom).

In order to investigate the beamwidth ($BW_{-3dB}$), direction of the main beam, and the SLL of the array, the radiation pattern is presented in both polar (top) and cartesian (bottom) plots in Figure 4.26. The angle of the $BW_{-3dB}$ shown in the polar plot is 44° with the direction of the main beam at 0°. This angle is narrower than the one obtained from the patch antenna. According to [3], the beamwidth and the side lobe level of an array are governed by the type of feeding network and the type of distribution used for the excitation of the elements. In agreement with Eq.(2.42), it is also possible to say that the more elements in an array there are, the narrower the beamwidth becomes. However it is important to mention that this might only apply when the number of elements of an array is increased following the same geometric distribution of the original design, with the same type of antenna, and with the same type of excitation source. This is why the beamwidth of the array became narrower than the one of the patch, because both have been excited with isolated discrete ports, and only the number of elements has been increased. The SSL of the array is $-31.3\,dB$ which is around $-10\,dB$ lower than the one from the patch antenna. This value is lower than the patch because the magnitude of the difference between the main side lobe and the main beam (gain) of the array is bigger than the patch.

Up to this point the analysis of the radiation pattern at broadside has been shown based on the main parameters obtained from the simulations. In order to evaluate these results, the theoretical expressions presented in Chapter 2 for an approximate estimation of the gain, beamwidth, bandwidth, and position of the side lobes of an array with radiation at broadside can be used in order to have a reference, and determine if the values from the simulations are close to the expected ones. It is important to mention that most of the theoretical expressions used to obtain these parameters were derived assuming that the antennas of the array are small rectangular surfaces that radiate only from the top side of the elements. This means with zero pattern for the region behind their surface, which for practical purposes, can be considered as equivalent to microstrip antennas. This is why the values obtained from these expressions should be considered only as guides. This is valid for this analysis taking into account that the purpose is to provide practical expressions for useful results of the array, in order to have a reference value instead of an ideal one, which would require a derivation of the exact electromagnetic model of the elements, which is beyond the scope of this chapter. The gain of an antenna is calculated using the expression of the Eq.(2.46). This considers the directivity of the antennas at broadside $D_{max}$. Then, the first step is to calculate this term using Eq.(2.44) as follows:

$$D_{max} = \frac{4\pi A}{\lambda_0^2} = \frac{(4\pi)(1.04)\lambda_0^2}{\lambda_0^2} = 13.12 \tag{4.10}$$

for $A = L_x L_y$, where:

$$L_x = N d_x = (2)(0.5\lambda_0) = \lambda_0$$
$$L_y = N d_y = (2)(0.52\lambda_0) = 1.04\lambda_0$$

Once the directivity has been calculated, the gain is derived as follows:

$$G = \varepsilon_L (1 - |\Gamma|^2) D_0 = (1)(0.99)(13.12) = 13.1 \tag{4.11}$$

where the value of $\varepsilon_L$ is considered to be for a lossless network with value 1, and where the magnitude of the reflection coefficient is taken from the simulated results presented before. Then the magnitude of the gain in decibels is $11.7\,dBi$. The beamwidth $(BW_{-3dB})$

of the design is calculated by the expression of the Eq.(2.42) as follows:

$$BW_{-3dB} = \frac{0.886 B_b \lambda_0}{L} = \frac{0.886\lambda_0}{1.04\lambda_0} = 0.848 \text{ rad} = 48.6^\circ \tag{4.12}$$

with $B_b = 1$ because the array is fed uniformly, and with $L = Nd_y$, where $N = 2$ and $d_y = 0.52\lambda_0$. The number of antennas is considered as two because this is the number of antennas that are in the direction of the y-axis, where the principal plane of scan is for the phased array antennas that are presented later, and the value which will help to investigate the change of the beamwidth when steering the main beam. The position of the side lobes of the radiation pattern in the yz-plane seen from the x-axis, are calculated according to the analysis of the side lobes for an array of isotropic antennas developed in Chapter 2, and by using the expression of Eq.(2.54) as follows:

$$-\frac{2\pi d_y}{\lambda_0} < \Psi < \frac{2\pi d_y}{\lambda_0} = -1.04\pi < \Psi < 1.04\pi \tag{4.13}$$

where the visible values of $\Psi$ in the complex plane are $-\pi$ and $\pi$, and correspond to the two antennas in y-axis. Then, based on the expression: $\Psi = \beta d_y \cos\gamma$, the values for $\gamma$ that correspond to these values of $\Psi$ are: 164.1° and 15.9°, respectively, which are the two nulls of the radiation pattern. Then, in order to compare the position of these nulls with the format of the cartesian plot of the simulator with 0° as the centre, Figure 4.27 shows the expected pattern of the radiation by subtracting 90° from the values of the nulls, then the position of the nulls are set at $-74.1^\circ$ and 74°, respectively. It is important to mention that the chart of Figure 4.27 only presents an estimation of the radiation pattern on the cartesian plot, because the background analysis of these parameters was developed for isotropic antennas instead of microstrip antennas. Also, the difference in distance between the peak of the main beam to the peak of the main side lobes does not represent the real proportion of the magnitudes, only the possible shape of the pattern according to the position of the nulls. A theoretical estimation of the side lobe level can be obtained by plotting the expression of Eq.(2.34) with $n = 2$ and $d = 0.52\lambda_0$ and calculating the

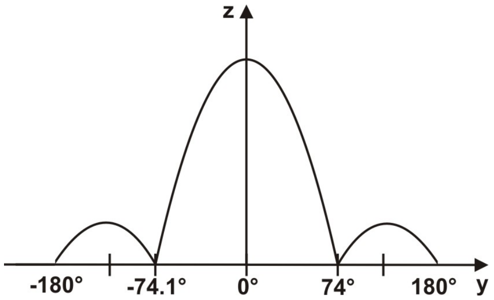

Figure 4.27: Expected radiation pattern of the array in the cartesian plot.

difference in magnitude of the main beam with the main side lobe. This value is around $-24\,dB$ and is used only as a reference.

The bandwidth of the array is obtained from the simulations and measurements that are presented later for the physical design in accordance to the criterion specified before, which determines the range of frequencies in which the magnitude of the gain of the main beam is $3\,dB$ below its highest value at 12.5 GHz. Table 4.5 presents the simulated and the theoretical values of the parameters obtained so far, in order to contemplate both results. The observed agreement of the results of Table 4.5 indicates the good approximation of the simulated results with the ones obtained from the analytical expressions. The position of the side lobes observed in Figure 4.27 can be compared with the cartesian plot of Figure 4.26 (bottom), where one of the nulls is positioned approximately at $-86°$ and the other at $87°$. Based on the similar positions of the nulls on both plots, it is possible to say that the radiation pattern of a physical design should be close to these two. The good agreement of the simulated and theoretical parameters of the array when radiating at broadside suggests the certainty of the first stage of the process, that of the validation of the simulations. All this analysis has been developed by evaluating the parameters of the array with main beam at broadside. However, it is important to investigate the variation of these parameters when the main beam is steered towards certain angles in space, and more particularly to approximately $30°$ in the H-plane. The steering of the main beam was performed by feeding all the antennas with the same amplitude but with a phase shift of $\sim 94°$ at antenna 2 and 4, according to the analysis explained at the beginning of this section, and taking into account that $Y = 0.52\lambda_0$. In order to start with the analysis of the radiation pattern, Figure 4.28 displays the 3D plot of the pattern with the main beam steered at $29°$.

| | $\boldsymbol{G}$ **dBi** | $\boldsymbol{BW^{\circ}_{-3dB}}$ | **SLL dB** |
|---|---|---|---|
| **Simulated** | 11.6 | 44.0 | -31.3 |
| **Theoretical** | 11.7 | 48.6 | ∼-24.0 |

Table 4.5: Simulated and theoretical results of the array.

As can be seen in Figure 4.28 the gain of the main beam is around $9.48\,dBi$, which implies a decrease of the magnitude of about $2.12\,dBi$ compared with the gain of the antennas radiating at broadside. This situation is due to the scan loss that affects the steering performance of any phased array system, as mentioned in the section of Fundamental Parameters in Chapter 2. This and all the variations of the parameters caused by the steering of the main beam will be analysed at the end of this section, after presenting all the results from the simulations, and after calculating the parameters from the theoretical expressions. A main side lobe is also identified from the 3D plot due to the steering of the main beam. In order to better perceive the magnitude of this side lobe,

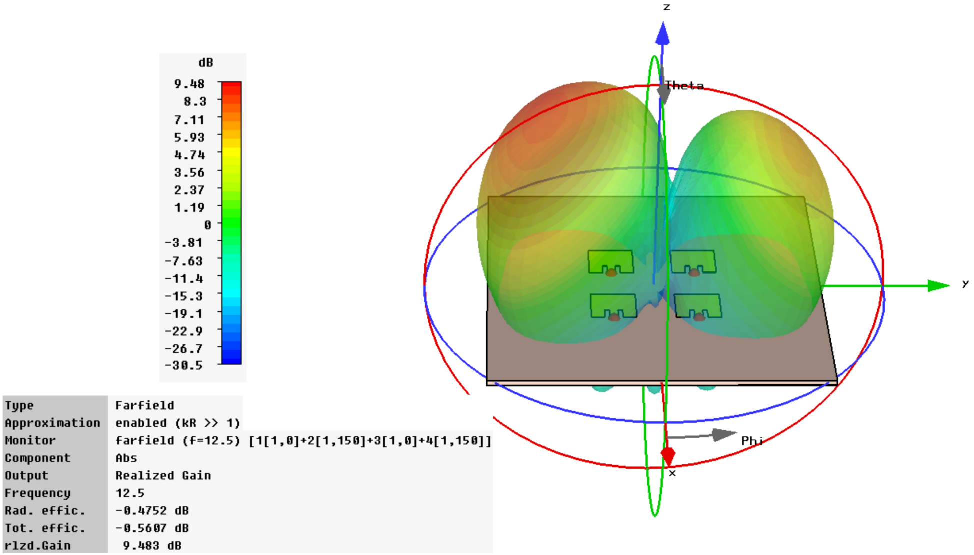

| | |
|---|---|
| Type | Farfield |
| Approximation | enabled (kR >> 1) |
| Monitor | farfield (f=12.5) [1[1,0]+2[1,150]+3[1,0]+4[1,150]] |
| Component | Abs |
| Output | Realized Gain |
| Frequency | 12.5 |
| Rad. effic. | -0.4752 dB |
| Tot. effic. | -0.5607 dB |
| rlzd.Gain | 9.483 dB |

Figure 4.28: 3D radiation pattern of the array with main beam at $\sim 30°$.

Figure 4.29 presents the radiation pattern in polar and cartesian plots. The beamwidth, direction of the main beam, and the side lobe level are presented as well.

As can clearly be seen in both plots from Figure 4.29 the main side lobe has been increased due to the steering of the main beam at 29°, where the SLL is $-3\,dB$. This situation affects the resolution of the scanning when distinguishing between two adjacent radiating sources in the space, because as long as the main side lobe increases its magnitude, more interference can be received from other undesirable sources. Nevertheless, the relative high magnitude of the SLL of this particular array is due to the small size of the array. If the array becomes larger by adding more elements following the same geometric distribution and feeding technique, as in the array of four elements, the gain of the main beam will become bigger and the effect of the main side lobe will be reduced significantly.

In order to clarify this point, Figure 4.30 shows the polar plot of the radiation pattern of an array of 16 elements (four by four) with the main beam steered at 29°. As shown in Figure 4.30 the SLL is $-10.4\,dB$ with a gain of $16.6\,dBi$, and beamwidth angle of 26.9°. Although the magnitude of the main side lobe of the array of 16-elements maintains almost the same value as the one from the array of 4-elements at approximately $6\,dB$, the SLL has been improved for the largest array because of the increase of the gain of about $7.1\,dBi$. It can also be observed that the other side lobes have increased their magnitude, although it is below the main one. If the purpose is to reduce these side lobes, different techniques can be applied. For instance, according to [3] by tapering the array excitation in order to excite the elements of the centre more strongly than those near the edge of the array, it is possible to significantly reduce the side lobes of an array. However, the impact of the SLL over the demonstration of the steering of the main beam with RF-MEMS is not critical

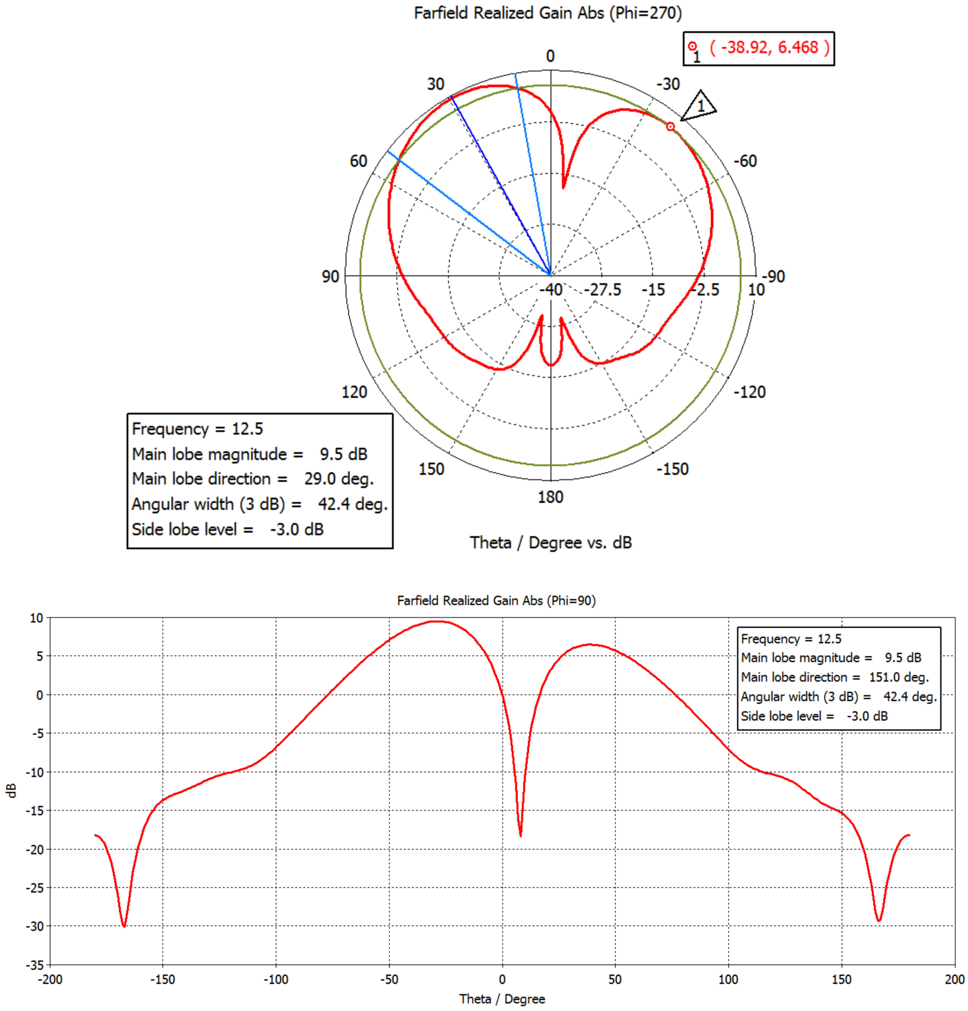

Figure 4.29: Radiation pattern of the array with main beam at 29°: Polar plot (top); Cartesian plot (bottom).

for the aim of this work. This is why a simple array of four antennas has been selected. Another parameter that has also been modified with the increase of size of the array is the beamwidth. Its value has been reduced to around one half of the beamwidth of the array of four antennas (see Figure 4.26). This means that most of the radiated power is concentrated in a thinner beam. In order to investigate the effect that the steering of the main beam has over the gain, directivity, and beamwidth calculated from the theoretical expressions, the derivation of these are presented. The gain of the antenna is affected by the scan loss that any phased array suffers because of the mutual impedances that exist between the elements, then an approximation of the gain can be calculated by assuming some scan dependences of the form $(\cos\theta)^n$, according to the graphs of the typical scan loss presented before, in Figure 2.11. Taking into account the simplest dependence of the form $\cos\theta$, in order to calculate the gain, it is necessary first to calculate the directivity

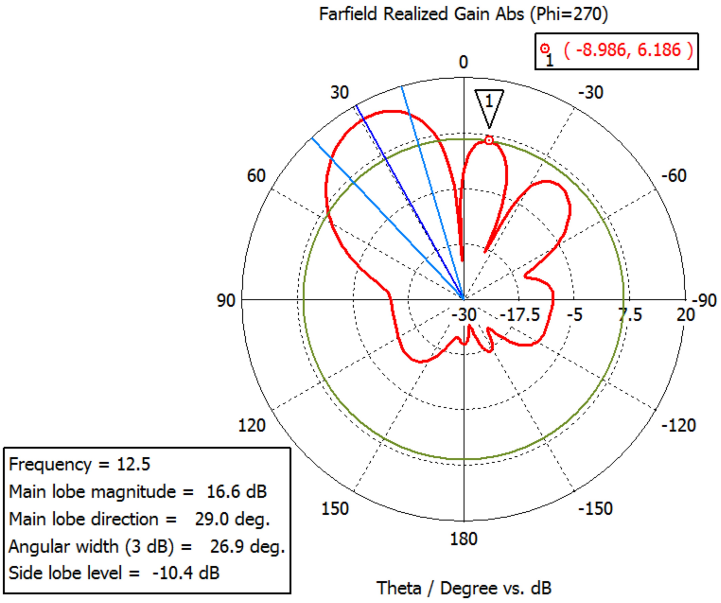

Figure 4.30: 3D radiation pattern of the array of 16 elements with main beam at ∼ 30°.

as it was obtained for the antennas radiating at broadside, but by adding the scan loss factor as follows:

$$D_0 = \frac{4\pi A}{\lambda_0^2}\varepsilon_A \cos\theta = \frac{(4\pi)(1.04)\lambda_0^2}{\lambda_0^2}\cos(30^\circ) = 11.36 \tag{4.14}$$

considering that $\varepsilon_A = 1$, which is the aperture efficiency. Once the directivity has been calculated, the gain is calculated as follows:

$$G = \varepsilon_L(1 - |\Gamma|^2)D_0 = (1)(0.99)(11.36) = 11.35 \tag{4.15}$$

with $\varepsilon_L = 1$ for a lossless network. Then the magnitude of the gain in decibels is 10.55 $dBi$. The beamwidth of the scanned beam is calculated from the expression of Eq.(2.43) as follows:

$$BW_{-3dB} = \sin^{-1}(0.523 + 0.424) - \sin^{-1}(0.523 - 0.424) = 1.14\ rad = 65.5^\circ \tag{4.16}$$

Table 4.6 presents the simulated and theoretical results of the parameters with the main beam steered at ∼ 30°. Although the values from the theoretical expressions are different

| | $G$ dBi | $BW^\circ_{-3dB}$ | SLL dB |
|---|---|---|---|
| **Simulated** | 9.48 | 42.4 | -3.0 |
| **Theoretical** | 10.55 | 65.5 | - |

Table 4.6: Simulated and theoretical results of the array with main beam at ∼ 30°.

from the ones obtained with the simulations, both show the effect caused by the steering of the main beam. This effect is more notable in the magnitude of the gain, since a decrease in its magnitude was expected compared to the one at broadside. The expected change in the beamwidth was a broader angle than the one at broadside, however, a narrower beam was obtained in the simulations. The gain suffered a decrease in more than $1\,dBi$, if the simulated value is considered as the closest to the real one. According to the typical scan loss curves of Figure 2.11, and calculating the ratio of the gain with steered main beam of $9.48\,dBi$ to the gain of the one at broadside of $11.6\,dBi$, the linear ratio is about 0.61, which suggests that the calculation of the gain should have been done assuming a scan dependence of around $(\cos\theta)^{13/5}$, instead of $\cos\theta$, considering that this function is the one that contains the required 0.68 of scan loss at 30° to obtain a similar magnitude of the simulated gain. Contrary to expectations, the beamwidth instead of presenting a wider angle according to the results of Eq.(4.16), it slightly reduces its width of $\sim 1.5°$, as part of the simulations. It seems possible that this result is due to the relative small size of the array. From the simulations of the array of 16-elements both with radiation at broadside and with main beam steered, only a slight increase of the beamwidth was found from 25° to 26.9°, respectively. This time it was not possible to calculate a theoretical value for the side lobe level because the plot of the radiation pattern of four isotropic antennas with steered beam in the direction of the scanning plane (yz-plane) could not show the magnitude of the main side lobe. This situation is attributed again to the size of the array. With this last analysis of the simulated and the theoretical results of the parameters of the antennas with main beam steered, the second part of the first stage of the process of the validation of the simulations has been done.

The analysis developed in this section has allowed to obtain the relative separation between the elements in order to have a good trade-off between gain and side lobe level of the array. This trade-off represents part of the main aim of the analysis of this section. This has been developed from the evaluation of the results of the electromagnetic parameters obtained with the simulator. The selected array has been evaluated by proving the expected behaviour of its parameters based on the background presented in Chapter 2, and by comparing some of its results with the ones obtained from the single antenna. Also the presentation and analysis of the radiation pattern of the array at broadside and at $\sim 30°$ steered in the H-plane, represents the other part of the main aim of this section. The purpose is to show the expected behaviour that the physical designs of reconfigurable phased array antennas should present, once the feeding network and the digital phase shifters are implemented. Then, this first analysis of the scanning performance represents a reference for further comparisons. Therefore, based on the results obtained, especially from the investigation of the steering of the main beam, it is possible to say that this array is a good initial design to start implementing the appropriate feeding network, phase shifters, and RF-MEMS to demonstrate a similar behaviour of the steering of the beam. It is important to mention that the selection of this particular array does not mean it is the best of its type, but a good one to demonstrate the performance of the array when steering the main beam. In order to present the sequence followed to find the good architecture of reconfigurable phased array antenna, the next section presents the array that has been analysed here but with a feeding network to develop the second stage of the process for the validation of the simulations, based on the measurements of a physical design.

## 4.5 Array Antennas with Feeding Network

In the analysis presented in the last section each antenna was excited by a $50\Omega$ discrete port situated exactly at the edge side of the inset transmission line, where the antenna presents $50\Omega$. This feeding technique was used because it was the simplest way to energize each antenna for the purpose of that analysis. However, in order to build a physical design of this array of four antennas and measure its parameters, it is necessary to create a feeding network able to match all the antennas with a common SMA coaxial connector source of $50\Omega$. Then the validation of the simulated design can be carried out by demonstrating the agreement between the simulated and measured results.

### 4.5.1 Design

As shown in Chapter 2, there are different feeding techniques to excite microstrip antennas, where the probe feed and microstrip line are the simplest to implement in a physical design. The probe feed technique has already been simulated when the antennas were excited using discrete ports as explained in the last section. The microstrip line technique is an easy method that allows the matching of all the elements of an array by designing the appropriate network. Therefore, the combination of both techniques has been selected to design the feeding network for the array. In order to create an appropriate feeding network with an equal power distribution, and a good matching of the four antennas at the frequency of operation of 12.5 GHz, different microstrip line configurations have been used in order to implement the quarter wave transformer and the T-junction power divider techniques.

Figure 4.31 shows the array of four antennas with the feeding network used to excite all the antennas. The composition of this feeding network started with the design of the four required quarter wave transformers, represented with the segment of lines $\overline{ab}$, $\overline{cd}$, $\overline{ef}$, and $\overline{gh}$, to match the $50\Omega$ input impedance of the antennas with $100\Omega$ microstrip lines, that are used to match antenna 1 with 3, and antenna 2 with 4, by the segment of lines $\overline{bf}$

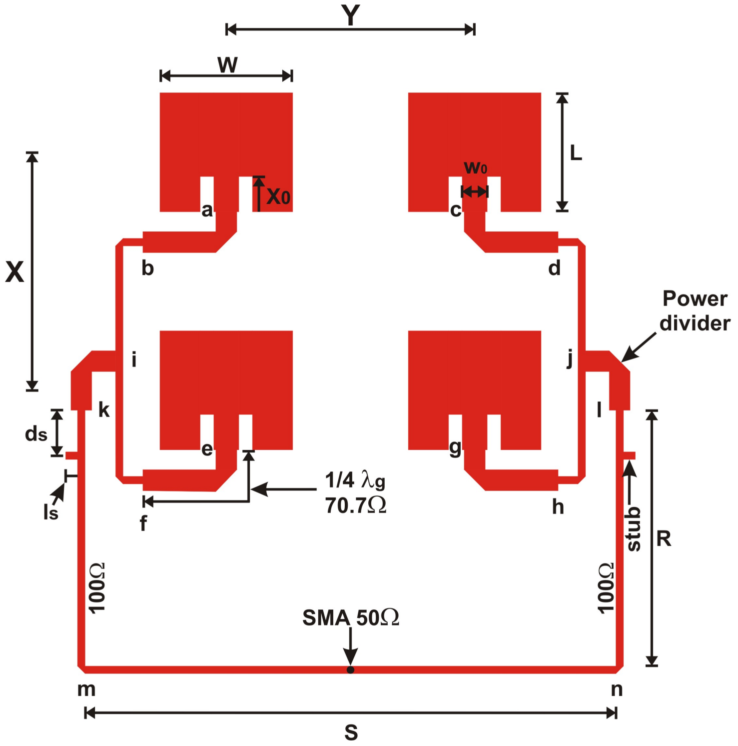

Figure 4.31: Antenna array with feeding network. Quarter wave transformers: $\overline{ab}$, $\overline{cd}$, $\overline{ef}$, $\overline{gh}$; 100Ω transmission lines: $\overline{bf}$, $\overline{dh}$, R, S; T-power dividers: $\overline{ik}$, $\overline{jl}$.

and $\overline{dh}$, respectively. Based on the theoretical analysis of the quarter wave transformer presented in Chapter 2, the impedance of the required transformers is obtained from this expression:

$$Z_T = \sqrt{Z_0 R_L} = \sqrt{(100)(50)} = 70.7\Omega \tag{4.17}$$

where 100Ω is the impedance of the lines that need to be matched through the quarter wave transformers with the 50Ω that each antenna presents as the real part of its input impedance. In order to find the dimensions of microstrip lines with different specific impedances over the Rogers 4003c board for the frequency of operation at 12.5 GHz, two simulators were used (TXLINE and CST) to obtain an approximation of the dimensions of the line for the required impedance. Thus, the dimensions for the microstrip line of the quarter wave transformers with 70.7Ω were calculated, obtaining a length of $\sim 3.6\,mm$ and a width of $\sim 0.9\,mm$. The length of the transformers represents one quarter of the wavelength that propagates into the dielectric ($\lambda_g$) of the Rogers board. Then, it is possible to prove this value by considering that $\lambda_g$ was calculated before for the design of the patch antenna, where the value obtained was 13.5 mm, which is approximately four times the value of the length calculated for the transformers. Once these dimensions were calculated, a simulation of the four antennas with the segment of the lines was developed in CST to prove that 100Ω of input impedance was obtained exactly at the end side of each line, or at points b, d, f and h, for each antenna, respectively. As shown in Figure 4.31, the microstrip lines of the transformers were bent 90° to the outside of the array in order to save space and to avoid a potential interference of the lines with the antennas. Based on the results of the simulation, an optimization for the dimensions of the transformers was developed in order to obtain the required 100Ω exactly at the end side of each line. A series of manual simulations were performed by changing the width and the length of the lines in order to achieve the desired input impedance at 12.5 GHz. The optimum value for the length of the transformers is 4.68 mm and 1.06 mm for the width.

Once all the transformers have been matched with the antennas and optimized for the required input impedance, 100Ω microstrip lines with 0.38 mm of width and 13.62 mm of length were placed from point b to f, and from point d to h, to match antenna 1 with 3, and antenna 2 with 4, respectively. The optimum width of all the 100Ω lines used for this network was obtained using the simulators in the same manner as it was performed for the calculation of the dimensions of the transformers.

In order to equally distribute the power from the main source to the four antennas, microstrip T power dividers were implemented by creating a three transmission line junction exactly in the middle point of segments $\overline{bf}$, and $\overline{dh}$, with i and j as the centre points, respectively. According to the theoretical analysis of the T power divider presented in Chapter 2, and more particularly the example presented to find the impedance of the input line that equally distributes the power in a 2:1 ratio, a 50Ω input feed line is required to split the power into two 100Ω loads or lines. Considering that segments $\overline{bi}$ and $\overline{fi}$ are the 100Ω loads or ports of one of the power dividers, a microstrip line with $\sim 50\Omega$ was initially matched to equally distribute the power to antenna 1 and 3. The same situation was applied for segments $\overline{dj}$ and $\overline{hj}$ to equally distribute the power to antenna 2 and 4. Therefore, segments $\overline{ik}$ and $\overline{jl}$ represent the power dividers at each side of the array.

An optimization was also developed for these two power dividers in order to get 100Ω of input impedance exactly at points k and l for 12.5 GHz by modifying the dimensions of the lines. For instance, it was observed that by changing the width of the power dividers the input impedance changed, whereas the change in the length produced a shift of the frequency in which 100Ω was obtained. Therefore the optimum values for the width of the power dividers was 1.05 mm and 3.15 mm for the length, considering that the lines were bent 90° down to save space and to easily match the antennas. These dimensions are very similar to the ones obtained for the transformers because the power dividers were used both to split the power to the antennas and to transform the 50Ω presented at points i and j to 100Ω at k and l, respectively. The impedance values at these last points were obtained in order to prepare the antennas for coupling any 100Ω lines to fully match all the antennas, or for coupling switched-line digital phase shifters to steer the main beam and match all the antennas in order to finally have an architecture of reconfigurable phased array antenna. Nevertheless, to start investigating the performance of this array, two microstrip lines of 100Ω and distance R of 12.9 mm ($\sim \lambda_g$) where matched at points k and l, respectively, to translate the input impedance of 100Ω at points m and n. Then, another line of length S of 27.5 mm was added to match the four antennas completely. Finally, the method of the power divider was again applied in order to split the power to the two 100Ω lines, using the probe feed technique with a 50Ω SMA connector placed exactly in the middle of the segment of line S.

Once all the antennas were completely matched, a first simulation of the array with the feeding network was developed in order to investigate the electromagnetic parameters of the design. The value of the input impedance ($Z_{in}$) obtained was $(49.5 + 2.08j)\Omega$ at the point of the lowest magnitude of the $S_{11}$ with -33.4 dB at 12.4 GHz. These results indicate a small impedance mismatch between the array and the 50Ω SMA connector. Therefore two small open-circuited microstrip lines set in parallel to the feeding network were used as stubs to solve the mismatch issue.

According to the theoretical analysis of a single stub in Chapter 2, there are two adjustable parameters to place a stub. One is the distance $d$ from the load to the position of the stub on the line, and the other is the length $l$ of the stub to obtain the required susceptance $jB$ that compensates the imaginary part of the load. In order to have an equal distribution of the power from the 50Ω source, only the real part of the input impedance of 100Ω should be seen in either side of the lines that are joined at the SMA connector. When necessary, a stub may be added to compensate the imaginary part. Thus, another simulation was developed eliminating one of the two 100Ω lines of the design to excite only two antennas from either the left or the right side of the array, and to investigate the input impedance so that one part did not interfere with the other. The input impedance obtained was $Z_L = (101 + 10.2j)\Omega$, which indicates there was an imaginary part.

According to the circuit configuration of the parallel stub presented in Figure 4.32, the basic idea of placing a stub at distance $ds$ from the load is to see into the line the admittance $Y$ of the form $Y_0 + jB$. Then, the susceptance of the stub is chosen as $-jB$

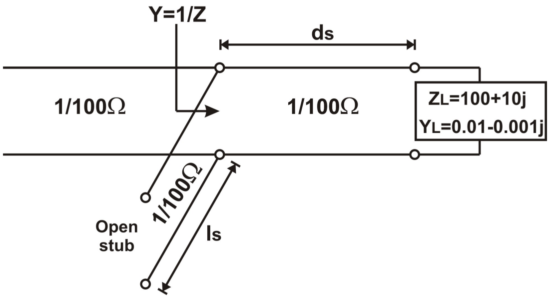

Figure 4.32: Circuit configuration of the parallel stub on the line.

in order to compensate the imaginary part of the admittance. If, for practical purposes, the input impedance is considered to be $Z_L = (100 + 10j)\Omega$ or $Y_L = (0.01 - 0.001j)S$ as the load of the circuit configuration of the stub (as shown in Figure 4.32), it is not necessary to calculate the distance $ds$ because the real impedance of the load is equivalent to that of the transmission line where the stub will be placed. This means the form of the admittance $Y$ seen into the line is already of the form $Y_0 - jB$, where $Y_0$ is the same as the real part of $Y_L$, and where $jB = -j0.001$. Therefore, the only distance to calculate is the length of the stub $ls$, in order to compensate the imaginary part of the admittance with a susceptance value of $0.001j$. According to [37] the impedance of a parallel stub behaves as a capacitor if its length $ls < \lambda_g/4$, and as an inductor if $\lambda_g/4 < ls < \lambda_g/2$. Therefore, based on the required positive value of the susceptance ($0.001j$) for the compensation of the impedance, a stub less than $\lambda_g/4$ is required. As explained in Chapter 2, there are two solutions to calculate the parameters of a stub: the Smith Chart and the analytic method. The Smith Chart solution is the simplest and the fastest, taking into account that the normalized input impedance (or load) is of the form $Z_{LN} = 1 + 0.1j$ and the normalized input admittance of the form $Y_{LN} = 1 - 0.1j$. Then, by following the solution explained in [37] to find the length of the susceptance $0.1j$, the length of the stub has to be around $0.016\lambda_g$, where $\lambda_g$ is approximately 15 mm for a $100\Omega$ line on Rogers 4003c. Then the length $ls$ of the stub is around 0.24 mm, and the position of the stub over the line can virtually be at any distance from the load. Once the length of the stubs was calculated, arbitrary distances $ds$ from points k and l, for each side of the antenna, were set close to the end side of the lines of the power dividers as an initial test. It is important to mention that the parameters of the stubs obtained so far are only approximations of the real parameters. Hence, they have been used as starting point for an optimization process to find the optimum values of the stubs to better match the impedance of the source with the antennas. This optimization was developed using the optimization option of the simulator, with the length $ls$ and distance $ds$ of the stubs as the variables, and with the lowest magnitude of the $S_{11}$ at 12.5 GHz as the main target of the optimization. The optimum parameters of the stubs obtained are $ls = 0.6\,mm$ and $ds = 2.29\,mm$.

### 4.5.2 Simulation and Measurement Results

Once the optimum values of the distance $ds$ and length $ls$ of the stubs were obtained from the simulations, the next step was to investigate and evaluate the rest of the parameters of the array, and to build the design in order to validate the simulations based on the measurements. Figure 4.33 shows a picture of the physical design of the array alongside a pound coin to contrast its size. In order to have a better arrangement for the analysis of the results, both the simulated and measured results are presented next, along with their pertinent examination.

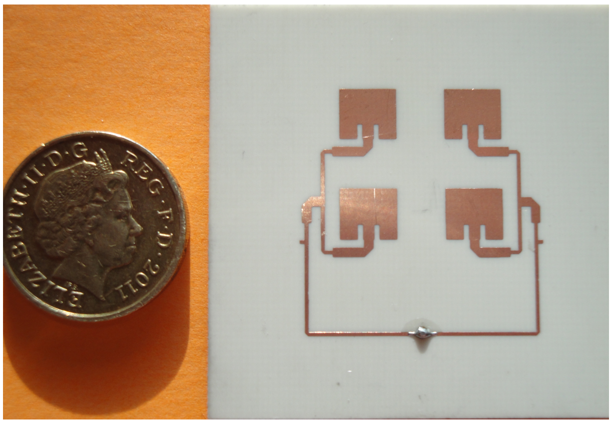

Figure 4.33: Physical design of the array with feeding network.

Based on the two scenarios described in Section 4.2.3 about the settings for the measurement of all the parameters of the antennas, the simulated and measured results involved in the first scenario (scenario 1) are presented next, followed by the results of the parameters involved in the second scenario (scenario 2). Figure 4.34 presents the graph of both the simulated and measured results of the $S_{11}$ parameter for the frequency range of 10 to 14 GHz. As shown in Figure 4.34, there is a very good agreement between the simulated and measured values of the reflection coefficient, because of the very similar behaviour of both in the frequency range. Both graphs present the lowest magnitude at 12.5 GHz, where the measured value is around $-28\,dB$. This result indicates that only 0.15% of the possible transferable power from the source is reflected and the rest is delivered to the array, which for practical purposes, shows a very good matching. In order to compare and analyse the rest of the results obtained in the scenario 1 of the measurements, Table 4.7 shows the values of the simulated and measured parameters. The value

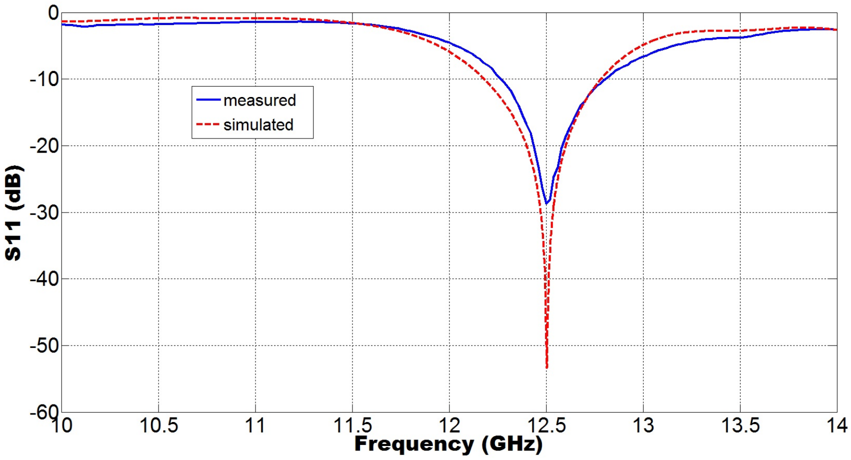

Figure 4.34: Simulated and measured result of the $S_{11}$.

| | $S_{11}$ dB | $Z_{in}$ Ω | VSWR | $BW_{-10dB}$ |
|---|---|---|---|---|
| **Simulated** | -46.4 | 50+0.47j | 1 | 600 MHz |
| **Measured** | -28.2 | 48.4-3.4j | 1 | 540 MHz |

Table 4.7: Parameters in the scenario 1 of the measurements of the array with feeding network.

of the measured input impedance, close to 50Ω with a small imaginary part, was already expected due to the measured magnitude of the $S_{11}$ parameter. In order to observe the behaviour of the input impedance along the frequency range under investigation, Figure 4.35 shows the Smith Chart obtained from the simulation of the design. Looking at the Smith Chart it is clear that the input impedance of the array is 50Ω at 12.5 GHz. This finding has an important implication, as it suggests that the maximum possible transferable power from the source to the antennas has been achieved at this particular frequency of operation. This means that the feeding network is working efficiently for this particular frequency, hence the values obtained from the measurements of the $S_{11}$ and the $Z_{in}$. The good matching of the design with the source is also corroborated from the measured value of the VSWR. Finally, the difference in the bandwidth of the resonant frequency between the simulated and measured results is around 60 MHz, which for practical purposes can be considered as small, and makes it possible to say that this value presents good agreement as well.

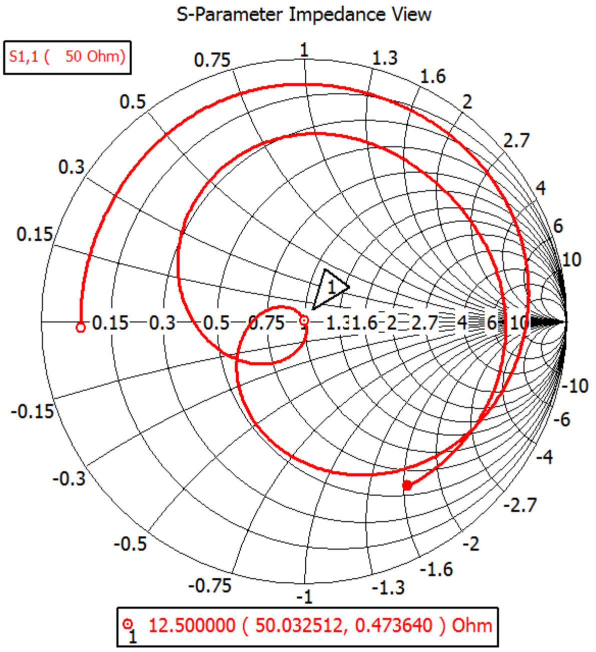

Figure 4.35: Input impedance of the array with feeding network on the Smith Chart.

The scenario 2 of the measurements includes analysis of the parameters related to the radiation pattern of the antennas. Therefore, the first part of this analysis is developed, showing a comparative table of the results obtained from the simulations and measurements. The second part presents a global comparison between the performance of this design with the one from the antennas without the feeding network based on all the results presented so far. The purpose of this second part of the analysis is to investigate the contribution of the feeding network to the array. Before presenting these two examinations, Figure 4.36 shows the 3D radiation pattern expressed in decibels, in order to have a first insight on the radiation pattern of the design.

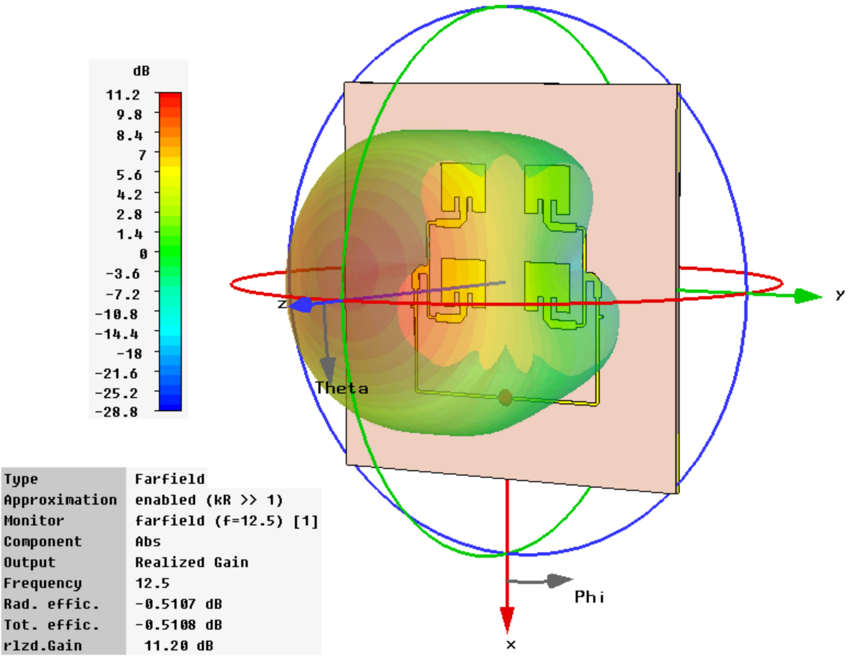

| | |
|---|---|
| Type | Farfield |
| Approximation | enabled (kR >> 1) |
| Monitor | farfield (f=12.5) [1] |
| Component | Abs |
| Output | Realized Gain |
| Frequency | 12.5 |
| Rad. effic. | -0.5107 dB |
| Tot. effic. | -0.5108 dB |
| rlzd.Gain | 11.20 dB |

Figure 4.36: 3D radiation pattern of the array with feeding network.

Comparing this radiation pattern with the one obtained from the array without feeding network (Figure 4.25), it is clear that the pattern is affected by the presence of the network of microstrip lines in the same plane as the antennas. Although the gain of both patterns is very similar ($\sim 11\,dBi$), the pattern with the feeding network is wider in both x- and y-directions. This is attributed to the contribution that the radiation of the feeding network has over the radiation pattern of the antennas. The radiation efficiency has also changed, with a slightly worse value for the antennas with feeding network, due to the possible losses added by the microstrip lines. A more detailed analysis of the performance of the antennas with feeding network is addressed at the end of this section, once the validation of the simulations has been done, comparing the results with the measurements.

In order to begin with the first part of this analysis, Figure 4.37 presents both the normalized simulated and normalized measured radiation patterns in linear scale over the polar plot in order to investigate the direction of the main beam, and the shape of

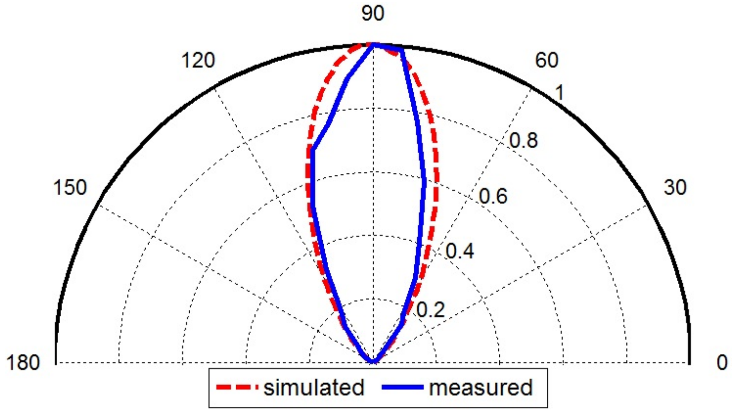

Figure 4.37: Normalized simulated and normalized measured radiation patterns in linear scale of the array with feeding network.

the patterns in an angle range of 0° to 180°. This plot must be interpreted taking into account that the magnitude of the measured pattern is normalized with respect to the highest linear magnitude of the simulated gain. This was developed in order to be able to compare the shape of both patterns in the same chart, considering that different reference levels of magnitudes were used for the simulations and measurements. The reference level of the magnitudes obtained from the measurements are presented when displaying the derivations involved in the calculation of the gain of the array. This graph shows that both patterns display a very similar shape with a slight decrease in the width for the measured pattern. All the parameters related to the radiation patterns are better analysed looking at Table 4.8 which shows the measured and simulated results. The measured magnitude of the gain presents 0.8 $dBi$ lower than the simulated one. Although the difference is considered of little significance, it is important to explain the possible cause of this inconsistency. The derivations developed to obtain the measured gain are presented:

| | $G$ dBi | $BW^{\circ}_{-3dB}$ | BW | SLL dB |
|---|---|---|---|---|
| **Simulated** | 11.00 | 45.5 | 11.9-13.2 GHz=1.3 GHz | -26.5 |
| **Measured** | 10.20 | 43 | 12.02-13 GHz=980 MHz | - |

Table 4.8: Parameters in the scenario 2 of the measurements of the array with feeding network.

$$\text{G dBi} = 13.2\,\text{dBi} + (\text{-37 dB - (- 34 dB)}) = 10.2\,\text{dBi} \tag{4.18}$$

where 13.2 $dBi$ is the gain of the waveguide horn antenna at 12.5 GHz, $-34\,dB$ is the reference magnitude measured when placing the waveguide horn antenna in front of other horn antenna of unknown gain (or red horn), and $-37\,dB$ is the measured value obtained by placing the array with the feeding network in front of the red horn antenna, exactly in the same position where the waveguide horn was set to obtain the reference magnitude. Therefore, the $0.8\,dBi$ loss in the measurements might have several possible explanations. First of all, although the copper of the design of the array has been defined as lossy metal in the simulator, and the Rogers board with its real parameters such as the permittivity and loss tangent, the environment of the simulation is ideal and most of the losses involved in the measurements of the physical designs are not included. An indicator of that is the difference of magnitude obtained for the measured $S_{11}$ of around $18\,dB$ bigger than the simulated one, which implies that the matching is not as good as in the simulation. Then all the possible losses involved in the physical design that are related with the quality of the fabrication might contribute to the inconsistency of the measured gain. Nevertheless, this discrepancy does not have an important impact on the aim of the chapter, which is to design a good architecture of phased array antenna. The simulated results of the rest of the parameters are presented in Figure 4.38 on the polar plot with decibels scale to better perceive the beamwidth and side lobe level of the array. The analysis of the results obtained for the beamwidth is not considered as relevant due to the similarity of the values obtained for both cases. Then it is acceptable to say that both results coincide. The measured narrow bandwidth of the array means that the magnitude of the main beam dropped faster with the variation of frequency than the bandwidth obtained from the simulations. The reason of this might be related to the losses involved in the physical design that are not considered on the simulated one, such as the effect that the physical substrate of the Rogers board might have in the antenna than the substrate used for the simulation.

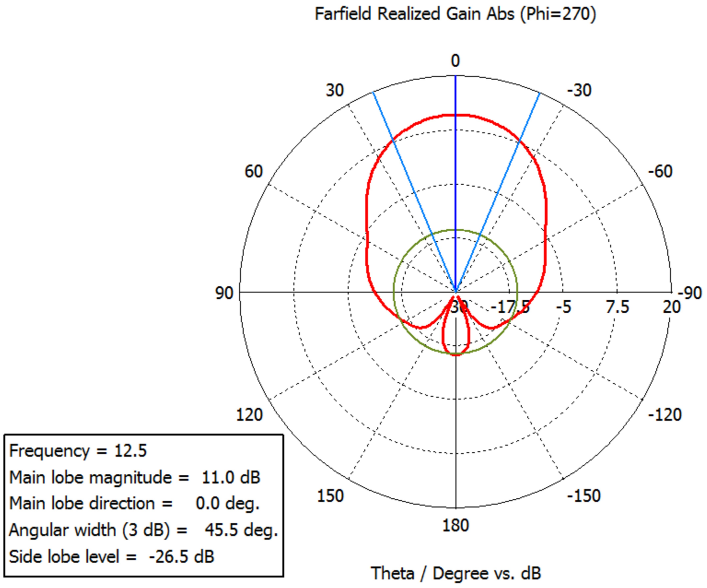

Figure 4.38: Radiation patten of the array with feeding network: Polar plot.

It was not possible to measure the magnitude of the main side lobe of this array with radiation at broadside due to the scenario used for the measurements of the radiation pattern over the turntable for an angle range of 0° to 180°. However an estimation of its value can be obtained based on the value of the magnitude of the main beam at 90° and on the value of its sides at either 0° or 180°. This estimation should nonetheless be taken with caution, considering that side lobes are bigger than the lowest magnitude of the main beam. This possibility has been considered once a plot in MATLAB of the radiation at broadside of four isotropic antennas distributed in the same manner as the array of microstrip antennas has been developed, which shows very low side lobes close to the lowest magnitude of the main beam. Hence, only as a reference, the difference of the measured magnitudes of the main beam with $-36.6\,dB$, and approximately $-70\,dB$ for 0° and 180°, is around $-33.4\,dB$. This might suggest that the side lobe level is around $-30\,dB$. It is acceptable to say that there is a good agreement between the simulated and measured results based on the explanation of the factors that might cause the difference between the values of some of the simulated parameters and the measured results. Also, based on all the results obtained so far, it is convincing to say that the process followed up to this point for the development of the simulations and for the measurements has shown a valid method in order to continue on the path to find a good architecture of phased array antenna.

Concerning the effect that the feeding network has over the performance of the array, it is acceptable to compare the simulation results of the parameters of the array with feeding network, with the simulation results of the array without it, given that the simulations of the physical design have already been validated. This is also by considering the lack of measured results for the array without feeding network. Then, contrasting the results of both designs for the $S_{11}$, $Z_{in}$, VSWR, and $BW_{-10\,dB}$, it is notable that all of them present acceptable values, taking into account that these parameters mainly depend on the accuracy of the matching of the design with the source. Then for practical purposes, if both present input impedance of $50\Omega$, and reflection coefficient lower than $-15\,dB$, no further analysis is required. The $BW_{-10\,dB}$ is the only parameter that has presented a slight change, with an increase of around 180 MHz. This change means that the entire design is less selective at 12.5 GHz than the design without feeding network, because the addition of microstrip lines on the design implies extra parasitic elements that might not have resonant frequency at 12.5 GHz, and then might modify the reflection coefficient.

In order to investigate this, Figure 4.39 presents the graph of the $S_{11}$ parameter of the feeding network in which the antennas were replaced by $50\Omega$ resistors as the loads of the network. The substitution of the antennas for real loads of $50\Omega$ was developed in order to isolate the effect of the inductances and capacitances of the antennas on the reflection coefficient. As shown in Figure 4.39, the magnitude of the reflection coefficient

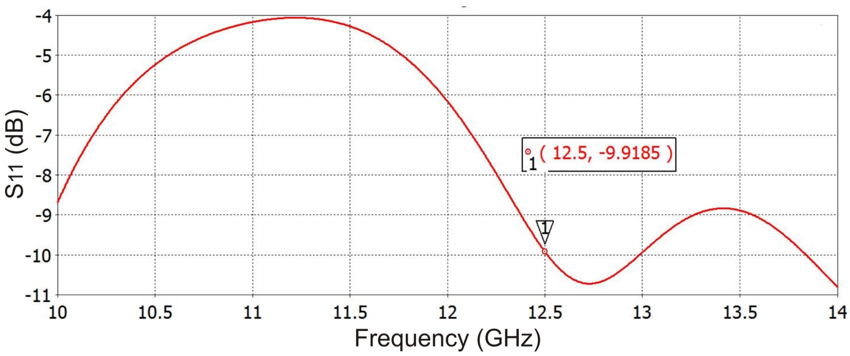

Figure 4.39: Reflection coefficient of the feeding network.

is $\sim -10\,dB$ at 12.5 GHz which means that around 10 % of the power from the source is reflected. Then, this might change the behaviour of the reflection coefficient of the entire design of the array with the feeding network, and its bandwidth as well.

Comparing the radiation patterns of both designs, and the parameters related with them, it is clear that the width of the radiation pattern of the array with feeding network is wider in x- and y-directions, as it was mentioned before due to the presence of the feeding network. This effect is shown in Figure 4.40, which features the radiation pattern expressed in linear scale, caused only by the feeding network of the design. The radiation pattern of the feeding network was obtained by keeping the 50Ω resistors as the loads instead of the antennas, in order to only get the radiation from the network. The direction of the biggest magnitude of this pattern are on the left and right sides of the z-axis, and on the positive direction of the x-axis. Therefore, it can be argued that most of the

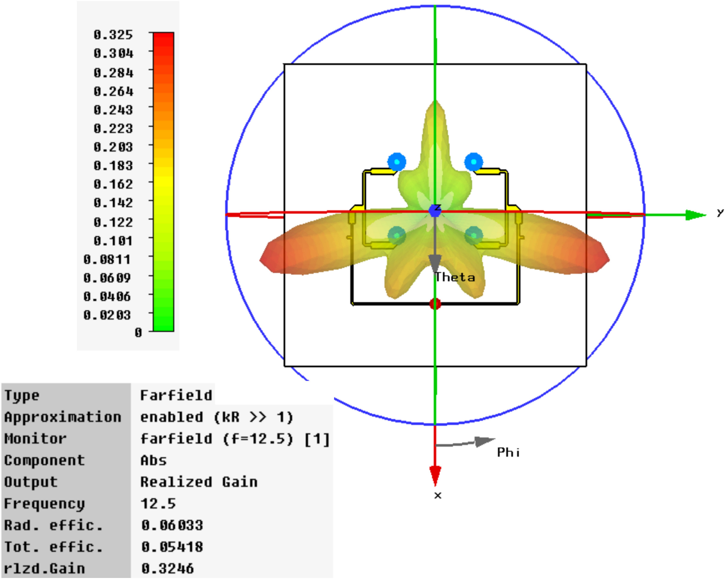

| | |
|---|---|
| Type | Farfield |
| Approximation | enabled (kR >> 1) |
| Monitor | farfield (f=12.5) [1] |
| Component | Abs |
| Output | Realized Gain |
| Frequency | 12.5 |
| Rad. effic. | 0.06033 |
| Tot. effic. | 0.05418 |
| rlzd.Gain | 0.3246 |

Figure 4.40: 3D radiation pattern of the feeding network.

effect of the feeding network over the radiation pattern is on these directions. According to [66] typical discontinuities in width or direction of microstrip lines produce a significant radiation, however in order to minimise this effect mitred bends, curves and Y junctions can be used. This is why mitred bends were used in every corner of the feeding network of the array to reduce part of the radiation. The most important effect of the feeding network over the parameters is on the magnitude of the gain, where a decrease of around $0.6\,dBi$ was obtained comparing the simulated results of both designs. This is caused by the losses of the microstrip lines. In order to have an estimation of the losses generated from the feeding network, the expression of Eq.(2.65) can be used as follows:

$$G = \frac{4\pi A}{\lambda_0^2} 10^{-(d/\lambda_0)(N^{1/2}-1)(\alpha_{dB/\lambda_0})/10} = (13.1)(10^{(-0.5)(1)(0.1)/10}) = 12.95 \tag{4.19}$$

where $d = 0.5\lambda_0$ due to the fact that this distance is almost the same for both x- and y-directions, with $N = 4$, and with $\alpha \sim 0.1dB/\lambda_g$. Then the magnitude of the gain in decibels is $11.1\,dBi$, which is similar to the simulated value of the gain obtained for the design with feeding network. This result would support the idea that only $0.6\,dBi$ of the gain is lost because of the feeding network. However, a better conclusion is reached taking into account the measured value of the gain of the physical design of $10.2\,dBi$. Although this value includes both the possible losses related to the quality of fabrication of the design and the losses of the feeding network, it is possible to say that an average of around $1\,dBi$ of the gain is lost due to the effect of the feeding network on the design. Regarding the effect that the feeding network has on the SLL, the change from $-31.3\,dB$ to $-26.5\,dB$ is caused mainly due to the increase of the main side lobe than the change in the main beam on the physical design. This is because the main beam only changed $0.6\,dB$, whereas the side lobe varied from $-19.6\,dB$ to $-15.5\,dB$ for the design without and with feeding network, respectively, hence the change in the side lobe level.

Based on the comparison developed so far between the array with and without feeding network, it is possible to say that the feeding network does change the performance of the array but it does not represent an important issue to carry on with the design of a good architecture of reconfigurable phased array antenna to demonstrate the aim of this work. In the next section, the design of the digital phase shifter is presented in order to add it within the feeding network for the steering of the main beam. The effect of the feeding network with phase shifters is also analysed when presenting the radiation characteristics of the phased array antennas.

## 4.6 Digital Phase Shifter

Based on the background presented in Chapter 3, phase shifters are the most essential devices in phased array antennas, because they provide each element the relative phase to electronically steer the main beam. Also, there is a potential opportunity to reduce the cost and to improve the performance of the overall system by exploiting the characteristics of the RF-MEMS switches, when they are monolithically integrated on digital phase shifters. This type of phase shifter provides discrete sets of phase delays.

### 4.6.1 Design

The easiest way to implement a digital phase shifter with microstrip lines is by applying the switched delay-line technique shown in Chapter 3, and explained in the Time-Delay section of Chapter 2. According to the expressions of Eq.(4.8) and Eq.(4.9), in order to steer the main beam of the array at 30° from broadside in the H-plane, a phase difference among the adjacent elements in y-direction should be around $\sim \pm 94^\circ$, for either steering to the left or to the right side of the z-axis as demonstrated in the next derivation:

$$\delta_y = \pm \frac{(2\pi)(0.52\lambda_0)}{\lambda_0} \sin(30^\circ) = \pm 93.6^\circ \tag{4.20}$$

with $\phi = 90^\circ$ for which $\sin\phi = 1$, and $\delta_x = 0$ due to the fact that $\cos\phi = 0$. This expression is equivalent to the one presented in Eq.(2.67) with $n = 1$ to obtain the required progressive phase at each element, implementing a switched delay-line network. In order to provide this progressive phase, the design of a 1-bit microstrip phase shifter is presented next, in Figure 4.41. This digital phase shifter consists of splitting the signal into a reference path (RP) of a multiple integer of the half wavelength ($\lambda_g/2$), and into a

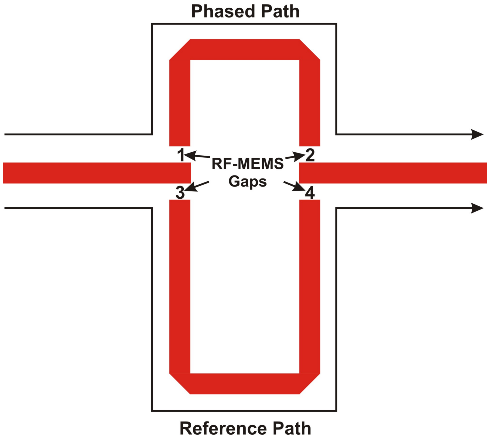

Figure 4.41: Switched-line digital phase shifter.

second path, or phased path (PP), to add or subtract a fraction of the wavelength. Then, the phase shift is obtained from the difference in electrical lengths of the paths according to the following expression:

$$\Delta\phi = \left(\frac{360^\circ}{\lambda_g}\right) \times (RP - PP) \tag{4.21}$$

then $\Delta\phi$ is the phase shift caused by the difference in delays that each path produces over the signal. Therefore, if 94° of phase shift is required to steer the main beam 30° in the H-plane, and the length of reference path is considered to be $\lambda_g$, the electrical dimension of the phased path is obtained by solving the following expression for PP:

$$94^\circ = \left(\frac{360^\circ}{\lambda_g}\right) \times (1 - PP)\lambda_g \tag{4.22}$$

Then the length of PP is approximately $0.74\lambda_g$, which means that around $\lambda_g/4$ of length difference is required between the reference path and the phased path. In order to convert the array of Figure 4.31 to a design of reconfigurable phased array antenna using this design of digital phase shifter, two of these need to be placed in the array. With two digital phase shifters in the array, one for antenna 1 and 3, and the other for antenna 2 and 4, it is possible to steer the main beam $-30^\circ$, $0^\circ$, and $30^\circ$ in the H-plane, considering that $0^\circ$ corresponds to the radiation at broadside. Thus, in order to dynamically change the beam to these three positions, Figure 4.41 shows the gaps where RF-MEMS switches will be placed to connect the appropriate delay line to provide the required phase shift for the electronic steering of the main beam.

The easiest positions to place two digital phase shifters on the array are in the locations where the $100\Omega$ lines of length $R$ are. For the demonstration of the reconfigurability of the phased array, the full set of delay lines that form a phase shifter was placed at each side of the array, even though always one of the delay lines is not connected when steering the main beam at any of the three positions. The purpose of this is to investigate the performance of the phased array only, without the RF-MEMS on the design. Once the design has been evaluated and validated, it is ready to integrate the RF-MEMS and investigate the performance of the entire system. The dimensions of the gaps for the switches were set to $300\mu m$ based on the research, analysis, and simulations of RF-MEMS presented in Chapter 5. This means that the gaps were considered to fit with the dimensions of the design of the RF-MEMS switch that is presented in the next chapter. The analysis of the evaluation and validation of the architecture of reconfigurable phased array antenna is presented in detail later, once the evaluation of the digital phase shifter has been developed with simulations.

### 4.6.2 Simulation

In order to investigate the performance of the phase shifter for each of its connections, one when the reference path is connected, labelled as RP-state, which means that gaps 3 and 4 are closed and gaps 1 and 2 are open, and the other when the phased path is connected, labelled as PP-state, with gaps 1 and 2 closed, and 3 and 4 open, the results of its main parameters from the simulations such as the $S_{11}$, $Z_{in}$, and phase shift are presented next for the frequency of operation at 12.5 GHz. Figure 4.42 shows the dimensions and configuration of the RP-state of the phase shifter based on 100Ω microstrip lines with 0.38 mm of width, and mitred bends on the corners over the Rogers board. The dimensions and shape of the phase shifter were selected based on the background presented in Chapter 3. The space between the delay lines of 2 mm was arbitrarily selected, although a trade-off between the shape and the isolation was considered. Two 100Ω discrete ports were connected at the end of the lines to investigate the S-parameters of the phase shifter. According to the result obtained in Eq.(4.22), approximately $\lambda_g/4$ of length difference is required between the reference path and the phased path to get around 94° of phase shift. Then, based on transmission line theory, and particularly on the next expression for the input impedance $Z_{in}$ of any line:

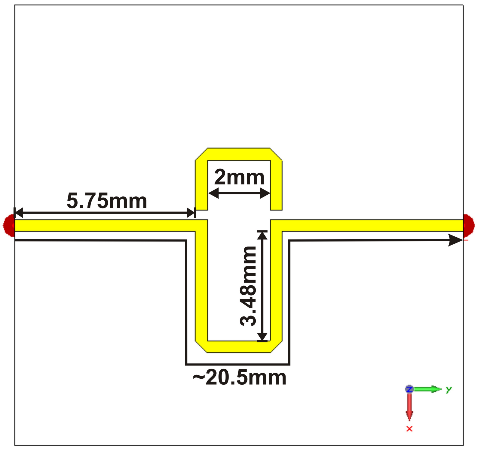

Figure 4.42: Digital phase shifter: RP-state.

$$Z_{in} = Z_0 \frac{Z_L + jZ_0 \tan \beta l}{Z_0 + jZ_L \tan \beta l} \tag{4.23}$$

where $Z_L$ is the impedance of the load, and $Z_0$ of the line, if the length of the line is increased in multiple integers (n) of $\lambda_g/2$, the input impedance remains the same but translated to another reference point. Therefore, the length of the reference path was increased from the sides following this rule, in order to be able to place the phase shifter on the array without overlapping with the antennas, and to obtain either 0° or 180° of phase shift for the transmission coefficient. According to simulations, and particularly to the phase shift that the $S_{21}$ presents, the length of the reference path is approximately 20.5 mm to obtain 180° of phase shift, as shown in Figure 4.43. The magnitude of the S-parameters for this configuration in the frequency range of 10 to 14 GHz is presented in Figure 4.44. From the graph of the S-parameters, it can be seen that the magnitude of the $S_{21}$ is around $-0.75\,dB$ at 12.5 GHz, which means that approximately 84 % of the power is transmitted from one side of the line to the other. Also, the magnitude of the $S_{11}$ is around $-18\,dB$ at the same frequency, which means that approximately 1.6 % of the power from the source is reflected. The rest of the power might be consumed because of the losses and radiation of the line. For practical purposes, it is possible to say that this configuration presents acceptable results to work at 12.5 GHz, considering that most of the power is transmitted at this frequency. The input impedance obtained from the Smith Chart of this path is $(101.1 + 25.5j)\Omega$.

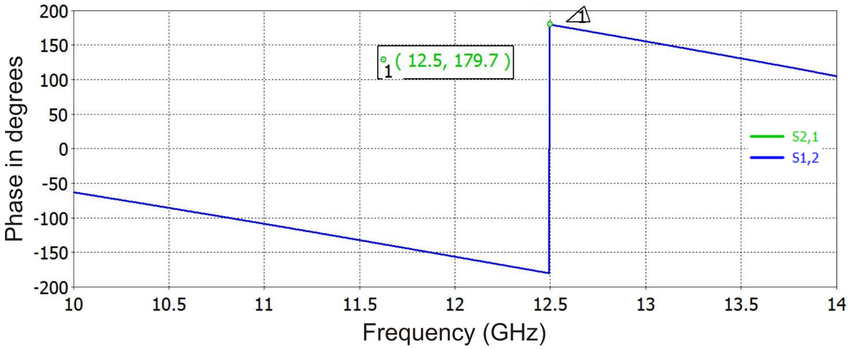

Figure 4.43: Phase shift of the $S_{21}$ for the RP-state.

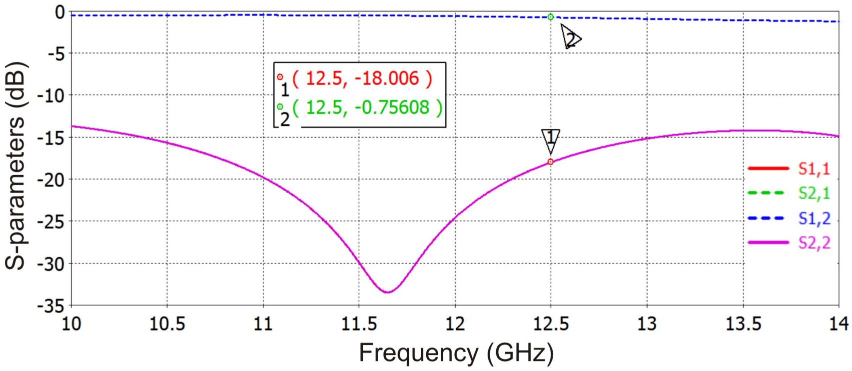

Figure 4.44: S-parameters of the phase shifter for the RP-state.

Once the RP-state of the phase shifter was simulated and evaluated, gaps 1 and 2 were connected and 3 and 4 disconnected to investigate the performance of the other state of the phase shifter. The length of the phased path is approximately 17.2 mm, as shown in Figure 4.45. Although this length does not represent the calculated 0.74 portion of the reference path, this length was obtained by manually optimizing the dimensions of the path to obtain the required 94° of phase shift, as shown in Figure 4.46. The value of the phase presented in Figure 4.46 is $-86.4°$ at 12.5 GHz. Calculating the difference of this value with the 180° obtained for the reference path, the phase shift is around 93.6°. Looking at the behaviour of the phase versus the frequency for each state, the phase of $S_{21}$ changes linearly with frequency, which proves what was stated in Chapter 3 about the linear-phase designs by using true-time delay phase shifters. The magnitudes of the S-parameters of the phase shifter on the PP-state are presented in Figure 4.47. These results show a slight improvement compared to the ones from the RP-state. This improvement may be explained by the fact that the length of the path is smaller than the one for the RP-state. Then, there are lower losses and parasitic impedances on the path. The input impedance of this path obtained from the Smith Chart is $(123.7 + 5.33j)\Omega$.

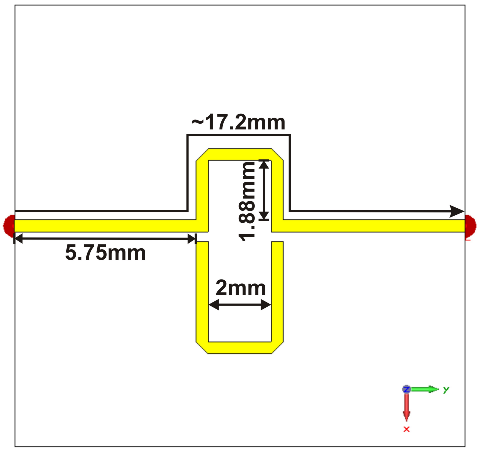

Figure 4.45: Digital phase shifter: PP-state.

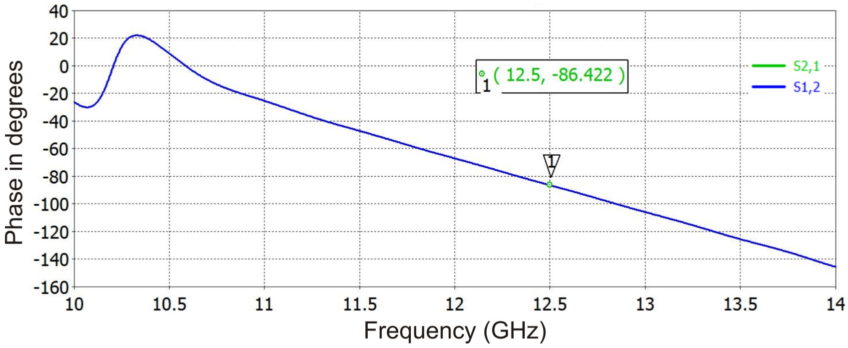

Figure 4.46: Phase shift of the $S_{21}$ for the PP-state.

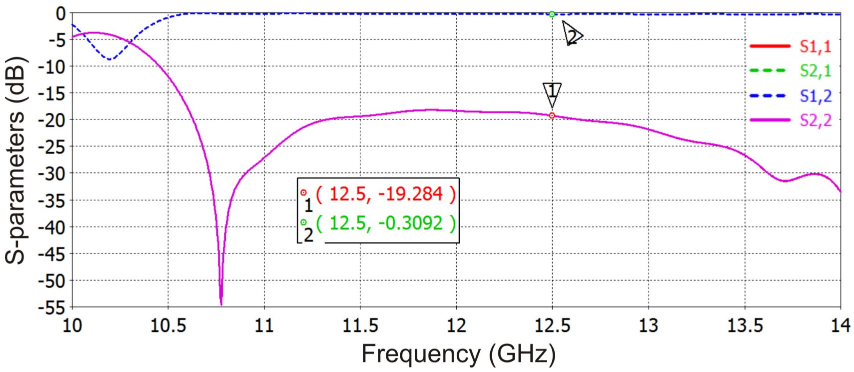

Figure 4.47: S-parameters of the phase shifter in the PP-state.

The results obtained so far from the simulations of the phase shifter must be taken with caution because these findings are not exactly the best ones. A slight variation on the phase shift and on the input impedance was found when the measurements of the physical designs of phased array antennas were obtained. This is attributed to the use of discrete ports rather than waveguide ports on these simulations. The consequence was that instead of providing 94° of phase shift, the real value is around 86°. This became plain when noting that the steering of the main beam was approximately at 27° instead of 30°. Also, the input impedances from the Smith Chart of each state are closer to only 100Ω than the ones presented with discrete ports. However, the results of these simulations are presented here because this is the design used in the physical designs. A more precise configuration could have been obtained by slightly decreasing the length of the phased path. A further explanation is provided when presenting the simulated and measured results of the reconfigurable phased array antennas in the next section. Nevertheless it is important to mention that this discrepancy is not critical, because the purpose is to obtain a good architecture of reconfigurable phased array antenna that can demonstrate whether the RF-MEMS can be monolithically integrated for good performance. This is why the value of the steered angle on the space does not represent an impediment to demonstrate this.

## 4.7 Reconfigurable Phased Array Antennas

In order to develop and investigate the performance of the reconfigurable phased array antennas, the 1-bit phase shifters were collocated in place of segments R, from the array with feeding network designed in Section 4.5, as described next.

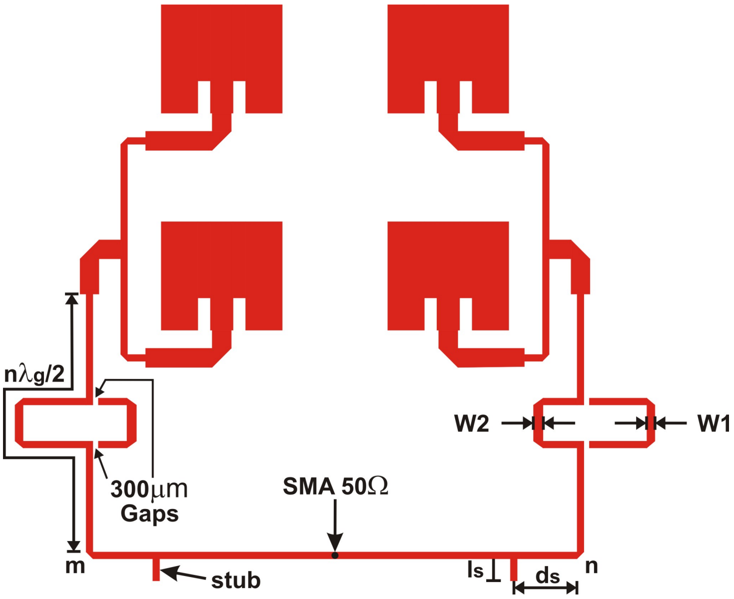

Figure 4.48: Reconfigurable phased array antenna for the steering of the main beam at ∼ 27° in the H-plane.

### 4.7.1 Design

A phase shifter was collocated at k point and another at l point, according to Figure 4.31. Figure 4.48 shows the new array design with phase shifters within the feeding network. With the connections of the phase shifters on the reconfigurable phased array antenna shown in Figure 4.48 the main beam is steered at ∼ 27° to the left side of the z-axis in the H-plane. Taking into account that one of the possible applications of these antennas is for the reception of the signals from satellites in the Ku-band, the configuration of this particular antenna means that the radiation of the source in the space is coming from the left side of the z-axis, which implies that the first antennas to receive the signal are the ones on the left. This is why the longest line of the phase shifter on the left is connected to compensate the delay that the signal suffers when arriving to the antennas on the right. This compensation is achieved by retarding the signal to synchronize it in phase with the one received in the antennas on the right. Hence the smallest line of the phase shifter on the right is connected. The reconfigurability of the phased array antennas is developed by changing the connections of the phase shifters. Then one of the next three states of the phased array can be performed:

1. State 1, which means that both phase shifters are switched to the line of 0°
2. State 2, which means that left phase shifter is switched at 0°, and right is at 86°
3. State 3, which means that left phase shifter is switched at 86°, and right is at 0°

It is important to mention that for practical identification the connection of the phase shifters at 180° has been named 0°.

Previous results of the simulations of the S-parameters showed a little mismatch when all the antennas and phase shifters were connected together, due to the disparity in the length of the microstrip lines at each side of the array caused by the connections of the phase shifters. To compensate this mismatch it was necessary to change the width of some of the phase shifter lines ($W_1$ and $W_2$), and to add two stubs in the same manner as it was done for the antenna without phase shifters of Figure 4.31. The first step to solve the mismatch was to obtain as close as possible only a real input impedance of 100Ω at points m and n, for any state. By changing the width of the segments of the phase shifters shown in Figure 4.48, it was possible to reduce part of the imaginary parts of the impedance seen at these points. Then, optimum values for $W_1$ and $W_2$ are 0.45 mm and 0.53 mm, respectively.

Once approximately 100Ω was obtained at points m and n, a couple of stubs were collocated in parallel to the microstrip line that connects the two phase shifters, and that matches all the antennas. The dimensions of these stubs were first calculated using the Smith Chart solution, as developed in the array of Figure 4.31, in order to have initial values to perform an optimization. The optimum distance $ds$ and length $ls$ of the stubs were different for each state when trying to get the best tuning at 12.5 GHz. Then, for state 1 $(0°, 0°)$ $ds = 5.3\,mm$ and $ls = 0.7\,mm$. For the state 2 $(0°, 86°)$ and 3 $(86°, 0°)$, considering that both are reciprocal, $ds = 3.5\,mm$ and $ls = 1.2\,mm$. These results show that distance $ds$ is the parameter with bigger change for each state. However the precise length $ls$ for each state allows the best tuning at 12.5 GHz. Therefore, a trade-off between the parameters of the stubs and the good performance of the reconfigurable phased array is required when switching to all the states. A simulation of the reconfigurable phased array with the optimum values for $ds$ and $ls$ for all the states is performed at the end of this section, in order to show the results of the S-parameters, and to prove that the radiation characteristics do not change even though the optimum values of the stubs for each particular state are not set on the design. This simulation is presented once the simulated and measured results of each state of the phased array with their optimum values of the stubs have been validated.

### 4.7.2 Simulation and Measurement Results (State 2)

Once the mismatch issue was solved for each state, the design of Figure 4.48 was built to measure its parameters according to the settings of the two scenarios presented in Section 4.2.3. Figure 4.49 shows a picture of the physical design. The simulated and measured results involved in the scenario 1 of the measurements are presented first, followed by

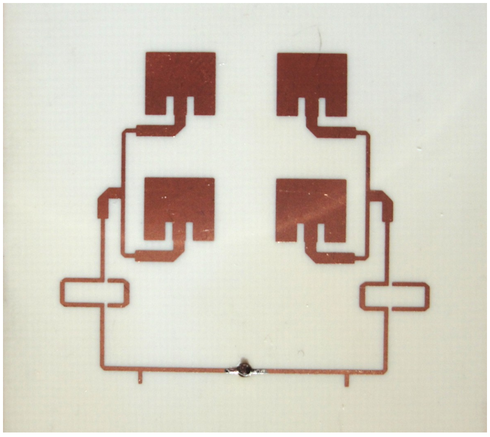

Figure 4.49: Physical design of the reconfigurable phased array antenna for the steering of the main beam at 27°.

the results of the scenario 2. All the parameters are arranged in tables contrasting their values. Figure 4.50 displays the graph of both the simulated and measured results of the $S_{11}$ for the frequency range of 10 to 14 GHz. The results of both cases show good agreement between them, with main lowest magnitude below $-25\,dB$ at 12.5 GHz for both. This means that the main resonant frequency of the physical design is at 12.5 GHz, as it was predicted from the simulations. Also, this finding proves there is good matching with the source, although one line from each phase shifter is present in the design but disconnected from the network.

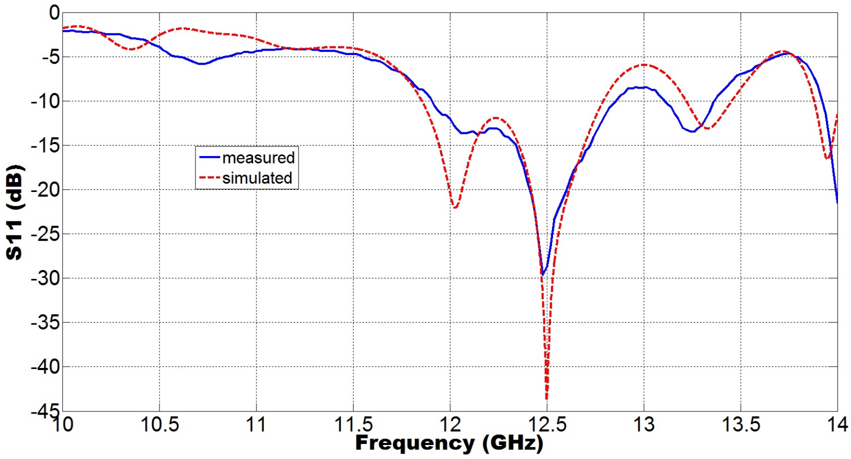

Figure 4.50: Simulated and measured results of the $S_{11}$ for the state 2 of the phased array antenna.

Table 4.9 shows the results of the simulated and measured parameters involved in the scenario 1 of the measurements. The values of all the parameters in Table 4.9 ratify the good agreement between the simulated and measured results that were already expected

| | $S_{11}$ dB | $Z_{in}\ \Omega$ | VSWR | $BW_{-10dB}$ |
|---|---|---|---|---|
| **Simulated** | -43.8 | 50.5+0.34j | 1 | 1000 MHz |
| **Measured** | -26.9 | 51.0-4.30j | 1 | 960 MHz |

Table 4.9: Parameters in the scenario 1 of the measurements of the state 2 of the phased array antenna.

from Figure 4.50. According to the measured magnitude of the $S_{11}$, only 0.20 % of the power from the source is reflected back, which means there is good matching between the array and the source. Interestingly, the relationship between the simulated and measured values of the $S_{11}$ obtained from the design of Figure 4.31 was repeated for this design of phased array. This finding is important because it supports the idea that once the magnitude of the $S_{11}$ from the simulations shows a lower value than $-40\,dB$, it might ensure the good matching and the very similar behaviour of the physical design compared with the simulated one. This idea is also supported by the values of the input impedance, VSWR, and bandwidth of the resonant frequency, which show very close results to the ones expected from the simulations, which fulfil the aim of this chapter. These findings confirm part of the validation of the simulations of the design of these antennas developed so far.

Figure 4.51 shows the behaviour of the input impedance on the Smith Chart of the phased array for the frequency range of interest. If this input impedance is compared with the one obtained for the array without phase shifters (Figure 4.35), more variations on the graph are observed because of the imbalance of the parasitic elements in the network

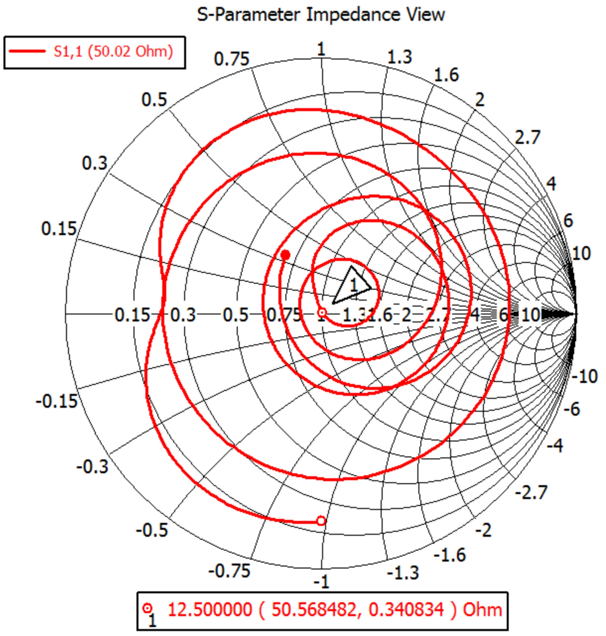

Figure 4.51: Input impedance of the state 2 of the reconfigurable phased array.

due to the connections of each phase shifter. This is due to the disparity in the length of the microstrip lines that the source connector sees at each side of the array. This situation can be an issue for the tuning of the system at 12.5 GHz because the input impedance changes rapidly due to the variation of frequency.

In order to start with the analysis of the results of the parameters related to scenario 2 of the measurements of the design, Figure 4.52 shows its 3D radiation pattern expressed in decibels. It is clear that the main beam of the radiation pattern presents an inclination to the left side of the z-axis in the H-plane. This inclination is ∼ 27° due to the connections of the state 2 of the phased array. An important side lobe is also observed on the right side due to the steering of the main beam. Figure 4.53 shows the normalized simulated and normalized measured radiation patterns over the polar plot with linear scale to observe the shape, direction of the main beam, and the side lobe level of both patterns. The measured pattern is plotted by normalizing its magnitude with respect to the highest linear magnitude of the gain obtained from the simulations, as it was done for the array without phase shifters. The shape of the measured pattern follows the predicted one with main beam pointing at ∼ 29° in the H-plane.

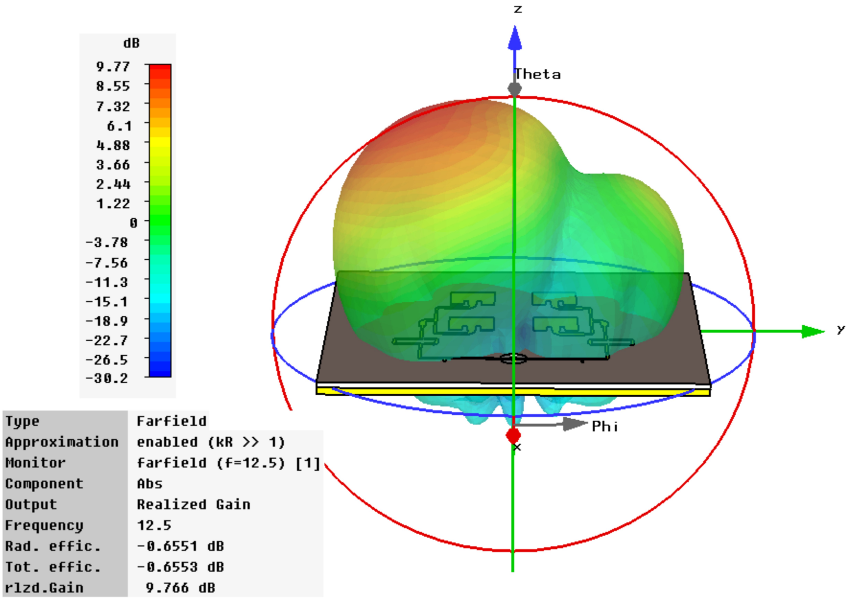

| | |
|---|---|
| Type | Farfield |
| Approximation | enabled (kR >> 1) |
| Monitor | farfield (f=12.5) [1] |
| Component | Abs |
| Output | Realized Gain |
| Frequency | 12.5 |
| Rad. effic. | -0.6551 dB |
| Tot. effic. | -0.6553 dB |
| rlzd.Gain | 9.766 dB |

Figure 4.52: 3D radiation pattern of state 2 of the reconfigurable phased array antenna.

The overall gain of the measured pattern is lower than the simulated one, due to the extra losses involved in the physical design that are not considered in the simulations. In order to better analyse the characteristics of the radiation pattern, Table 4.10 presents the results of the parameters from the simulations and measurements related with the radiation of the phased array. From the results of the magnitude of the gain, a difference of 1.5 $dBi$ is found between the simulated and measured values. A similar average difference

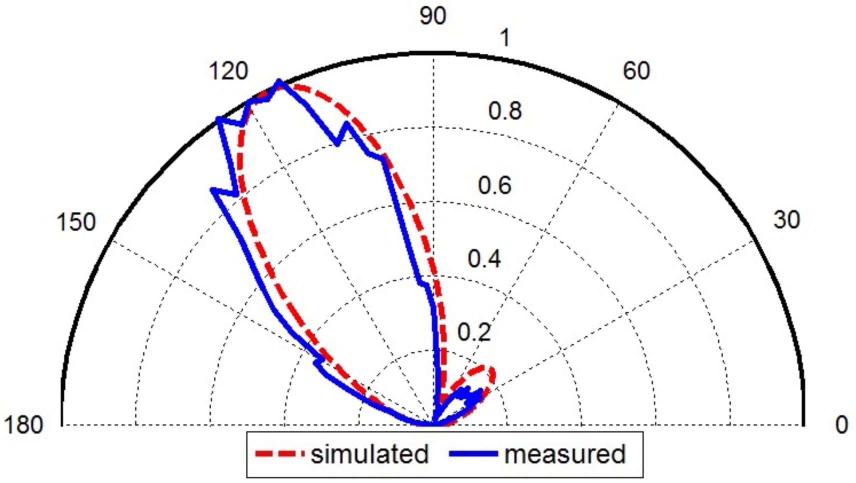

Figure 4.53: Normalized simulated and normalized measured radiation patterns in lineal scale of the state 2 of the reconfigurable phased array antenna.

| | $G$ **dBi** | $BW^{\circ}_{-3dB}$ | **BW** | **SLL dB** | $\theta^{\circ}$ |
|---|---|---|---|---|---|
| **Simulated** | 9.7 | 47.6 | 11.42-13.17 GHz=1.75 GHz | -6.7 | 27 |
| **Measured** | 8.2 | 49.0 | 12.24-13.16 GHz=920 MHz | -8.19 | 29 |

Table 4.10: Parameters in the scenario 2 of the measurements of the state 2 of the phased array antenna.

was obtained when measuring the gain of the design without phase shifters. As explained earlier, this means that the losses of the physical design are the probable cause of this difference. What is interesting about these findings is that the measurements of different designs follow a similar behaviour, with almost the same factor of discrepancy. This is also supported by the values of other results such as the beamwidth and bandwidth. However, it is not possible to say the same for the side lobe level due to lack of measurements for this parameter in the array without phase shifters. The values of the beamwidth present a slight difference with a wider angle for the measured pattern with approximately 2° of difference. This slight difference was also found in the array without phase shifters, which is considered not relevant for further analysis due to the similarity of the results. The bandwidth is also found to be narrower than the one from the simulations. Although the difference is bigger than the one obtained from the array without phase shifters, 12.5 GHz is in the range of frequencies of the bandwidth with the highest magnitude, which represents the most important point from this parameter.

Therefore, although the measured bandwidth is narrower because of the possible effect that losses of the physical design cause, this result shows that both the radiation of the antennas and the small radiation from the feeding network are combined in a way to constructively radiate for the desired frequency and direction. Figure 4.54 shows the pattern from the simulations on the polar plot to better observe the side lobe level and the beamwidth of phase array. The magnitude of the measured side lobe level is lower

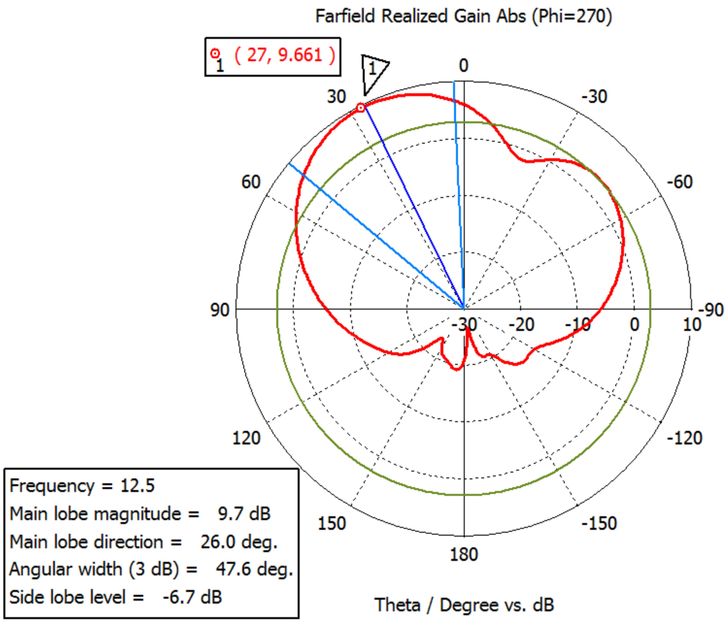

Figure 4.54: Radiation pattern of the state 2 of the reconfigurable phased array antenna: polar plot.

than the one from the simulations. This might be attributed to the loss factor that the overall magnitude of the pattern presents from the measurements. By comparing the magnitude of the main side lobe from the simulations of around $3\,dB$ with the one from the measurements of around $0.01\,dB$, the difference is bigger than the $1.5\,dB$ factor already considered from the results of the gain. The missing $1.5\,dB$ is not clear but it may be related to the accuracy of the measurements for lower magnitudes, as the one from the main side lobe, and the effect the losses might have over these levels of power. Nevertheless, the lower the side lobe level is, the better the performance becomes for the reconfigurable phased array antennas, as long as the main beam presents good magnitude. The slight mismatch on the direction of the main beam of 2° from both cases might be related to the accuracy of the measurements. This difference does not represent a critical issue for the aim of this chapter. It is important to mention that the magnitude of the main beam is virtually the same at 26° and 27°, although Figure 4.54 shows that the maximum magnitude is at 26°. This is why a marker on the pattern was collocated to show this similarity. The analysis of these results validates the other part of the simulations of the state 2 of the reconfigurable phased array antenna, as it demonstrates good agreement between the simulations and the measurements.

### 4.7.3 Simulation and Measurement Results (State 1)

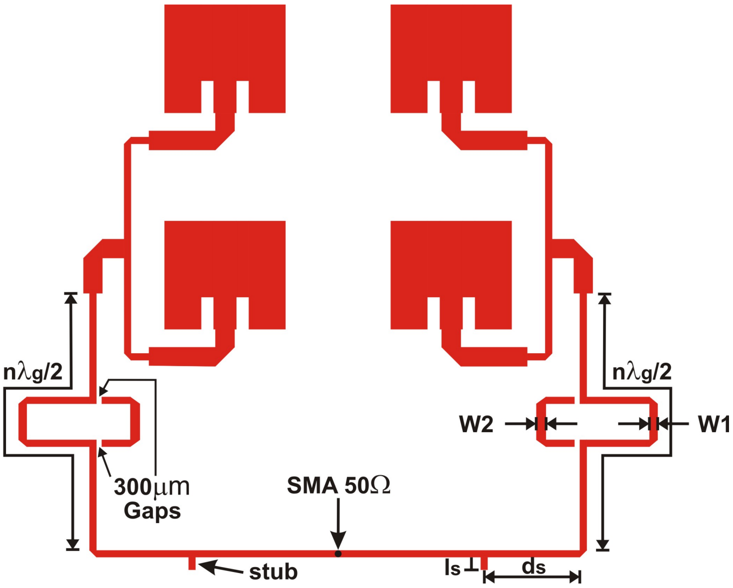

Figure 4.55: Reconfigurable phased array antenna with radiation at broadside.

Once the validation of the state 2 of the reconfigurable phased array antenna has been demonstrated, the results of the state 1 are presented next. The results of the state 3 are not presented because this configuration should be reciprocal to the state 2. The process followed for the presentation and analysis of the state 1 of the phased array is the same as the one developed for the state 2. Therefore, only the most relevant aspects of the parameters are analysed. Nevertheless all the results from the settings of the two scenarios of the measurements, along with the ones from the simulation, are presented in two tables. Figure 4.55 displays the design used in the simulator with the configuration of the connections for the state 1 of the phased array.

In Figure 4.55 it is possible to observe that in this occasion the longest lines of both phase shifters are connected to the feeding network, in order to feed with equal phase all the elements of the array, and to have maximum radiation at broadside. Figure 4.56 shows a picture of the physical design. If the photos of the two physical designs of the phased array presented so far are compared, it is possible to see the small change in the configuration of the feeding network regarding the required connections of the phase shifters for the steering of the main beam. This switching is intended to be done with the design of the RF-MEMS switch presented in the next chapter. This is why the electromagnetic analysis of each state of the reconfigurable phased array has been developed, leaving the disconnected lines of the phase shifters on the design, in order to analyse the performance of the entire system under these circumstances to simulate as close as possible a real scenario. This means that the reconfigurable design is ready for

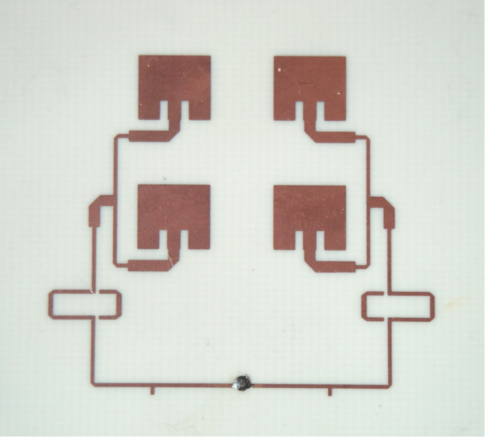

Figure 4.56: Physical design of the reconfigurable phased array with radiation at broadside.

the integration of the RF-MEMS. Figure 4.57 exhibits the graph of both the simulated and measured results of the magnitude of the $S_{11}$ for the frequency range of 10 to 14 GHz. The lowest peak on the graph for the measured $S_{11}$ seen in Figure 4.57 shows that the magnitude is $-29.2\,dB$ at 12.54 GHz. This mismatch in the frequency is due to the use of a 50Ω discrete port as the probe source rather than a 50Ω SMA connector on the simulated design. This issue was identified when the design was simulated again but with a SMA connector instead and proved to have better matching with the measurements. This means that the use of SMA connectors on the design of antennas allows a closer prediction of the behaviour of the real values. Nevertheless, this slight mismatch does not represent an important effect over the radiation characteristics of the phased array as it is demonstrated next.

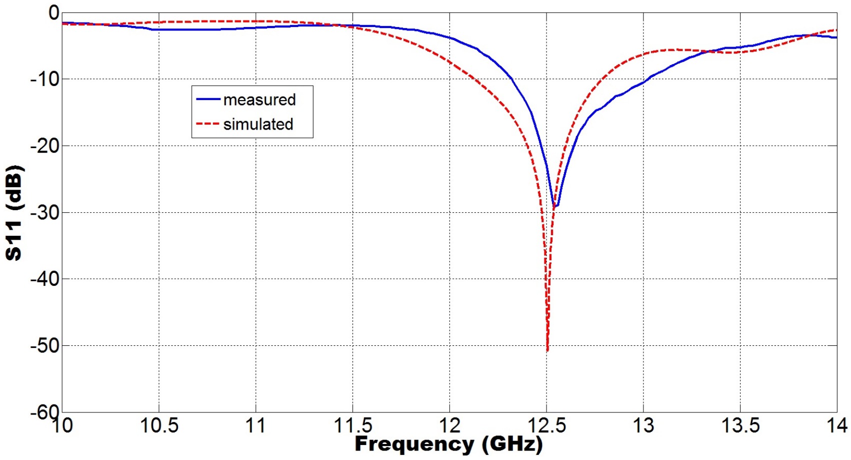

Figure 4.57: Simulated and measured results of the $S_{11}$ for the state 1 of the reconfigurable phased array antenna.

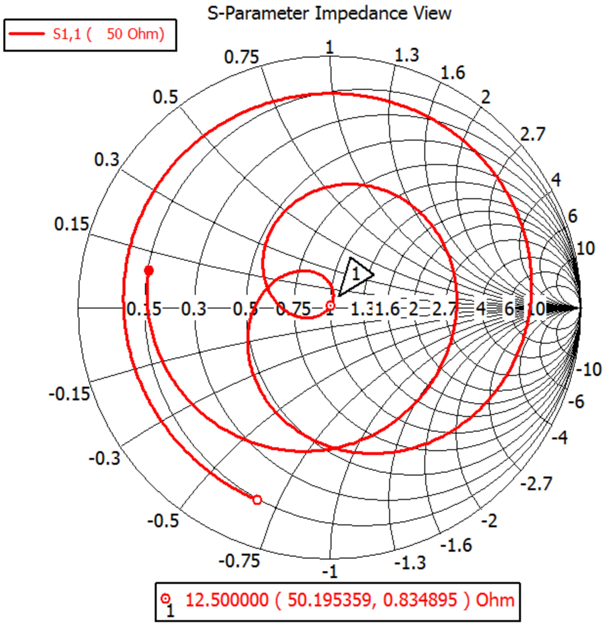

Figure 4.58: Input impedance of the state 1 of the reconfigurable phased array antenna.

Table 4.11 presents the simulated and measured parameters involved in the scenario 1 of the measurements. Comparing the results of all the parameters of the Table 4.11, it is acceptable to say that there is a good agreement between the simulations and the measurements of these parameters, although a slight mismatch was found for the resonant frequency. Figure 4.58 shows the variation of the input impedance along the frequency range of interest of this configuration. Comparing this input impedance with the one obtained from the array without phase shifter (Figure 4.35), it is clear that both input impedances behave similarly. This is due to the balance of the parasitic elements that exist at each side of the network seen from the source. Although the feeding lines of this configuration are longer than the array without phase shifters, all the antennas are fed coherently, and in phase as well. Then, only an extra loss factor might affect the power delivered to the elements due to the extension of the lines on the phase shifters.

|  | $S_{11}$ **dB** | $Z_{in}$ $\Omega$ | **VSWR** | $BW_{-10dB}$ |
|---|---|---|---|---|
| **Simulated** | -41.5 | 50.2+0.83j | 1 | 670 MHz |
| **Measured** | -29.2 | 48.4-2.4j | 1 | 700 MHz |

Table 4.11: Parameters in the scenario 1 of the measurements of the state 1 of the phased array antenna.

In order to have a first insight into the radiation pattern of the state 1 of the phased array, Figure 4.59 presents the 3D representation of the pattern. Maximum radiation at broadside is shown according to Figure 4.59 with no important side lobe on the sides of the main beam that could affect the radiation. This means that all the elements are fed

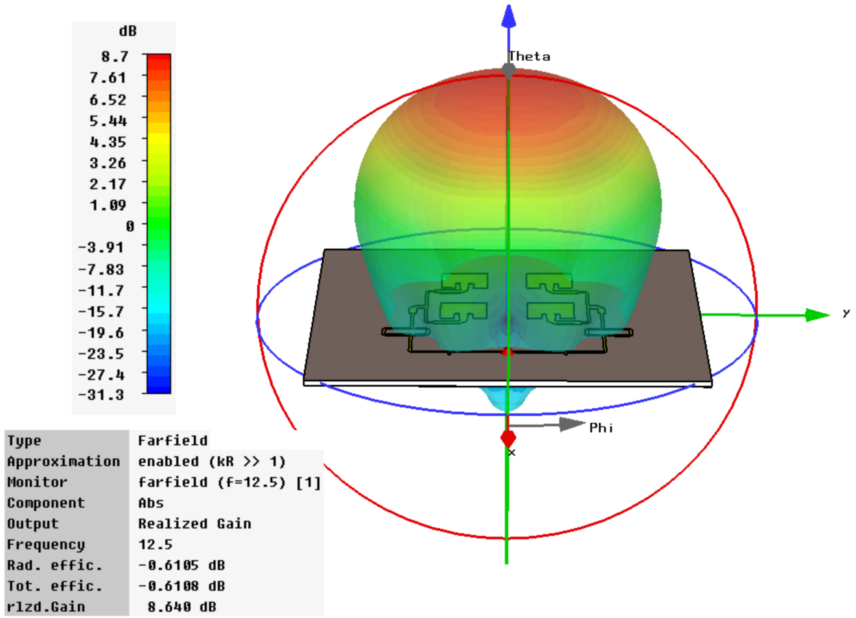

| | |
|---|---|
| Type | Farfield |
| Approximation | enabled (kR >> 1) |
| Monitor | farfield (f=12.5) [1] |
| Component | Abs |
| Output | Realized Gain |
| Frequency | 12.5 |
| Rad. effic. | -0.6105 dB |
| Tot. effic. | -0.6108 dB |
| rlzd.Gain | 8.640 dB |

Figure 4.59: 3D radiation pattern of the state 1 of the reconfigurable phased array antenna.

coherently with the same phase, as it was already predicted from the result of the input impedance seen in the Smith Chart. In order to start with the analysis of the parameters related to the pattern, Table 4.12 presents both the simulated and measured values of them. A difference of $0.4\,dBi$ in the magnitude of the gain is observed by comparing the results. This situation has already been analysed, considering that the discrepancy on the values is related to the losses of the physical design. However this difference has been the lowest value among all the designs of antennas measured so far, where $0.8\,dBi$ and $1.5\,dBi$ were identified for the array without phase shifters, and for the state 2 of the phased array, respectively. As a result, it is likely that a loss of $1\,dB$ in average is present in the measurements of the different designs of antennas. This explains the difference between the simulated and measured results.

| | **$G$ dBi** | **$BW^{\circ}_{-3dB}$** | **BW** | **SLL dB** |
|---|---|---|---|---|
| **Simulated** | 8.6 | 63.6 | 11.85-13.30 GHz=1.45 GHz | -26.2 |
| **Measured** | 8.2 | 50.3 | 12.32-13.44 GHz=1.12 GHz | - |

Table 4.12: Parameters in the scenario 2 of the measurements of the state 1 of the phased array antenna.

Figure 4.60 shows the normalized simulated and normalized measured patterns over the polar plot with linear scale showing their shape, and the narrower beam obtained from the measurements. Compared to the smaller difference obtained between the magnitudes of the gain, the beamwidth presents the highest difference among the designs of the antennas measured so far. This might be attributed to the resolution of the waveguide

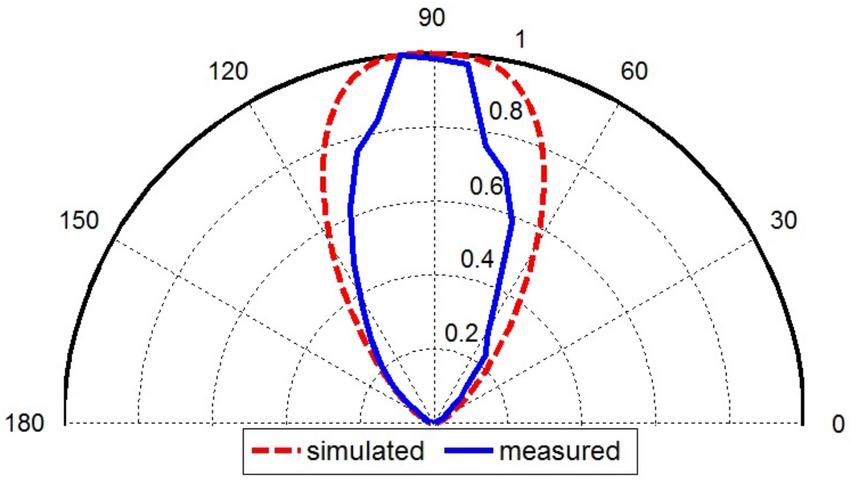

Figure 4.60: Normalized simulated and normalized measured radiation patterns in lineal scale of the state 1 of the reconfigurable phased array antenna.

horn antenna used for the measurements. According to the manual of the horn antenna, its beamwidth is around 30° at 9 GHz in the H-plane. Therefore an accuracy issue could cause the inconsistency of the measurements for a wider pattern as the one obtained from this state. Nevertheless, this deviation of around 13° of the beamwidth does not affect the identification of the main radiation at broadside, as it was predicted for the state 1 of the phased array. A narrower bandwidth was again obtained from the measurements of this state, due to the probable losses of the physical design that are not considered in the simulations. This result is significant because a very similar difference of around 300 MHz was also identified for the array without phase shifters. This implies that there is a similar loss factor in the measurements of this parameter when the antennas are radiating at broadside. The existence of a loss factor originates from the fact that there is a narrower bandwidth due to the faster drop of the main beam with the variation of the frequency, than the behaviour expected from the simulations. It was not possible to measure the magnitude of the side lobe level due to the restriction on the resolution of the turntable from 0° to 180°, where all the designs of the different antennas are set. Nevertheless, no side lobe was found in the plane of the antennas that could affect the radiation of the main beam.

Based on the good agreement observed between the simulations and measurements, and on the analysis developed for the explanation of the results of some parameters of this state of the phased array, it can be said that it was validated, and that the process followed for the simulations is an acceptable method. Therefore, taking into account that all the designs of antennas measured so far have allowed validation of the simulations, it can be said that the processes followed for both the simulations and measurements are indeed reliable methods to ensure that the designs of the reconfigurable phased array antennas presented here can conform a good architecture for the integration of the RF-MEMS switch that is presented in the next chapter.

### 4.7.4 Analysis of the Steered Beam

Once the reconfigurability of the phased array antennas has been proven and validated, it is important to clarify why the beam is steered at 27° instead of 30°. This was explained in Section 4.6 about the design of the digital phase shifter, taking into account that there is a slight variation on the phase that each phase shifter provides due to the use of a less accurate port in the simulations. Thus Figure 4.61 shows the phases of the $S_{21}$ obtained when the reference path was connected (top), and when the phased path was connected as well (bottom), considering that this time waveguide ports were used for better accuracy. Looking at the value of the phases for each connection according to the scale of the graphs, $-149°$ is obtained for the reference path, and $-63°$ for the phased path, which generates an absolute phase shift of 86°. Then, by solving the expression of the Eq.(4.8) for $\theta$, with $\phi = 90°$, as follows:

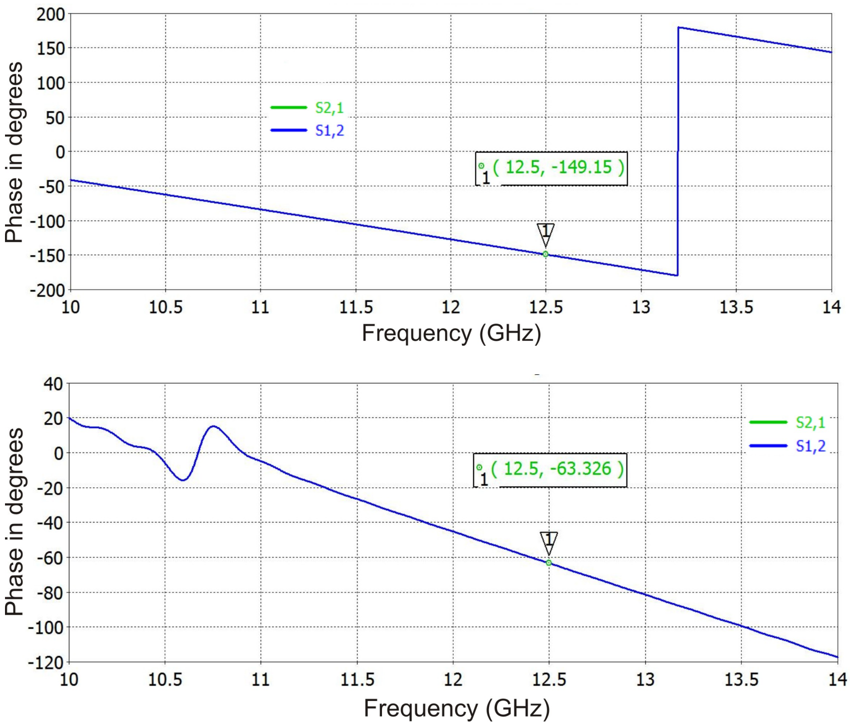

Figure 4.61: Phase shift of the $S_{21}$ for the RP-state (top), and PP-state (bottom) of the digital phase shifters.

$$\theta = \sin^{-1}\left(\frac{\pm\delta_y}{\beta d_y}\right) = \sin^{-1}\left(\frac{\pm 86°}{187.9°}\right) = \pm 27.22° \tag{4.24}$$

the direction of the beam results in $\sim \pm 27°$ in the H-plane of the antenna. This result ratifies the direction of the beam obtained for the state 2 of the reconfigurable phased array antenna. Also the magnitudes of the S-parameters for each connection of the phase shifter were improved with $-0.52\,dB$, and $-31.2\,dB$ for the $S_{21}$ and $S_{11}$, respectively, for the connection of the reference path. This means that around 89 % of the power is transmitted, and 0.07 % of the power is reflected back to the source. The rest might be lost due to the radiation and losses of the lines. For the connection of the phased path $-0.25\,dB$, and $-32\,dB$ were obtained for the $S_{21}$ and $S_{11}$, respectively. This means that around 94 % of the power is transmitted, and 0.06 % of the power is reflected back to the source. Therefore, the input impedance for each connection of the phase shifter was also changed to $(104.8 + 4.4\jmath)\Omega$, and $(104.9 + 3.7\jmath)\Omega$ for the reference and phased path, respectively. All these results indicate that a better accuracy was obtained by changing the type of port used in the simulations. This change was required for the demonstration of the mismatch obtained in the direction of the main beam at 27° instead of 30°.

### 4.7.5 Tuning for Monolithic Integration of RF-MEMS

The results presented before for each state of the phased arrays were developed by setting the optimum values of the stubs on the designs, in terms of their distance $ds$ and length $ls$, for each particular case in order to obtain the best tuning at 12.5 GHz. This was performed in order to have the best results from the simulations, and to ensure a greater likelihood of good results from the measurements. Hence the effectiveness of this procedure to validate the simulations of all the designs presented so far.

Taking into account that the process applied for the simulations ensures acceptably close results for the real world, it is now easy to develop another simulation to demonstrate that there are common optimum values for the stubs ($ds$ and $ls$) that are applicable to all the states of the reconfigurable phased arrays. This means there is a common position and length of the stubs regardless to the state of the phased array. The purpose of this is to obtain a reconfigurable phased array antenna ready for the monolithic integration of the RF-MEMS. Therefore, the common optimum values obtained from the simulation are: $ds = 3.5\,mm$ and $ls = 1.1\,mm$. Figure 4.62 shows the magnitude of the $S_{11}$ parameter obtained for each state of the reconfigurable phased array by using these common values of the stubs. In Figure 4.62 it can be seen that magnitude of the $S_{11}$ at 12.5 GHz presents a higher magnitude in all the states than the respective value obtained for each state with its particularly parameters of the stubs. This was already expected due to the required trade-off of the parameters of the stubs for a general configuration applicable to all the states. For instance, the state 1 is the more affected because it presents the highest magnitude of the $S_{11}$ of around $-18\,dB$, whereas $-41.5\,dB$ was obtained with

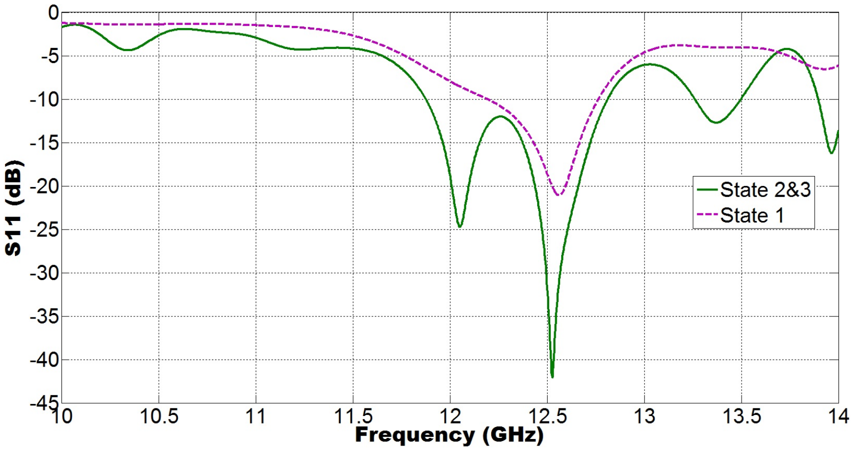

Figure 4.62: Magnitude of the $S_{11}$ for all the states of the reconfigurable phased array.

the optimum parameters of the stubs for this state. Nevertheless, this magnitude still satisfies the standard established before of $\leq -15\,dB$ for the finding of the main resonant frequency of an antenna in the range of interest. As a consequence, the values of the input impedance, VSWR, and $BW_{-10dB}$ were affected as well in all the states. The results of these parameters related with the $S_{11}$ are presented in Table 4.13 for all states. Looking at the results presented in Table 4.13, only a slight variation is found for the parameters of the state 2&3, which suggests that the radiation performance of the phased array is safe for these states. A smaller change is found for the state 1 with an increase in both the imaginary part of the input impedance and in the VSWR, and a reduction of around 100 MHz of the bandwidth of the reflection coefficient. Despite the variation on the results of these parameters for all the states, the radiation characteristics of the reconfigurable phased array antenna is not affected, as the results presented in Table 4.14 show. The radiation characteristics of the state 2 have practically not been affected in any of its parameters. For the state 1 only a slight difference in the beamwidth from 63.6°

|  | $S_{11}$ dB | $Z_{in}\,\Omega$ | VSWR | $BW_{-10dB}$ |
|---|---|---|---|---|
| **State 2&3** | -31.3 | 51.9-1.96j | 1.05 | 940 MHz |
| **State 1** | -18.5 | 53.0+11.8j | 1.26 | 570 MHz |

Table 4.13: Parameters related with the $S_{11}$ for all the states of the phased array with common values of the stubs.

|  | $G$ dBi | $BW^{\circ}_{-3dB}$ | BW | SLL dB | $\theta^{\circ}$ |
|---|---|---|---|---|---|
| **State 2&3** | 9.7 | 47.6 | 11.42-13.17 GHz=1.75 GHz | -6.7 | 27 |
| **State 1** | 8.6 | 62.9 | 11.80-13.15 GHz=1.35 GHz | -25.3 | 0 |

Table 4.14: Parameters related with the radiation pattern of all the states of the phased array with common values of the stubs.

to 62.9°, in the bandwidth from 1.45 GHz to 1.35 GHz, and in the SLL from $-26.2\,dB$ to $-25.3\,dB$ has been presented. This shows that the simulated and measured parameters of the radiation pattern of each state of the reconfigurable phased arrays maintain their good performance using these new common parameters of the stubs. This means that a representative architecture of reconfigurable microstrip phased array antenna has finally be found for the integration of the RF-MEMS. Therefore, with this architecture it is possible to electronically steer the main beam, as shown in Figure 4.63, by switching only the connections of the digital phase shifters.

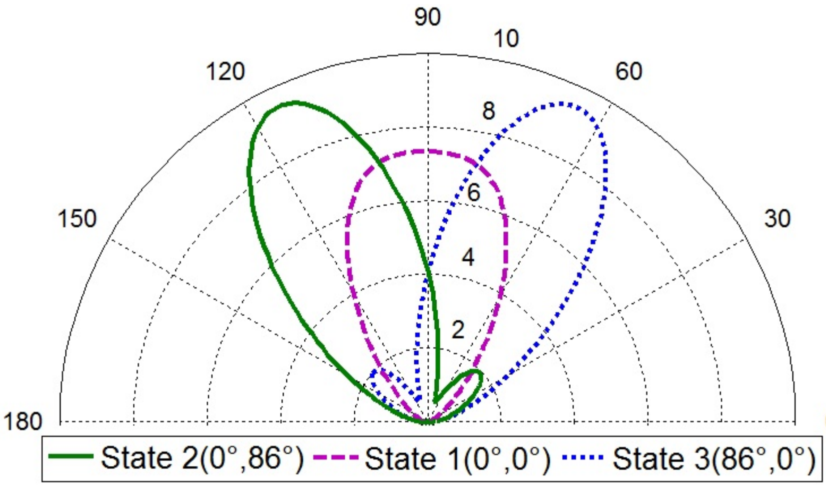

Figure 4.63: Electronically steering of the reconfigurable phased array antenna.

Now that a good architecture of reconfigurable phased array antenna has been designed, it is important to compare its radiation characteristics with the first array of four antennas without feeding network, considered as the reference design in Section 4.4. The intention is to investigate the effect of the feeding network over the radiation pattern, taking into account that in this occasion the phase shifters are within the network. Tables 4.15 and 4.16 show the values of the parameters of both designs related with the patterns for radiation at broadside, and with steered beam, respectively.

| | $G$ **dBi** | $BW^{\circ}_{-3dB}$ | **SLL dB** | $\theta^{\circ}$ |
|---|---|---|---|---|
| **Array without feeding network** | 11.6 | 44 | -31.3 | 0 |
| **Reconfigurable phased array** | 8.6 | 62.9 | -25.3 | 0 |

Table 4.15: Radiation characteristics of both the antennas without feeding network and the reconfigurable phased array at broadside.

Comparing the values of the Table 4.15, it is evident that there is an important reduction in the magnitude of the gain of about $3\,dBi$ for the reconfigurable phased array with radiation at broadside. According to the comparative analysis between the array

| | $G$ **dBi** | $BW^{\circ}_{-3dB}$ | **SLL dB** | $\theta^{\circ}$ |
|---|---|---|---|---|
| **Array without feeding network** | 9.48 | 42.4 | -3 | 29 |
| **Reconfigurable phased array** | 9.7 | 47.6 | -6.7 | 27 |

Table 4.16: Radiation characteristics of both the antennas without feeding network and the reconfigurable phased array with steered beam.

without feeding network and the array with it but with lack of phase shifters, the effect of the feeding lines over the gain was on average 1 $dBi$ of loss. Thus, it can be asserted that the specific connection of the phase shifter for the state 1 of the phased array contributes to the other 2 $dBi$ of loss. It is important to consider that the connections for the state 1 represent the longest lines connected on the design to feed the elements, which suggest a bigger loss of energy. Also the introduction of the phase shifters in the same plane of the antennas, with a couple of lines disconnected, generates some distortion on the pattern, which might affect the directivity and gain of the phased array. An indication of this distortion is the added width on the angle of the beamwidth.

However, it is somewhat surprising looking at the values of the Table 4.16, where only a slight difference on the magnitude of the gain was found for the designs with steered beam. In this case the gain of the reconfigurable phased array shows a slightly bigger magnitude than the array without feeding network, because its beam is pointing at 27°, whereas the design without feeding network is at 29°. Then, according to the scan loss that exists in any phased array from Chapter 2, this slight difference can be attributed to this factor. However this rule is not valid comparing the magnitudes of the gain of the reconfigurable phased array when radiating at broadside and with steered beam. This is because different connections of the phase shifters is needed with longer lines, which suggest the addition of more losses when radiating at broadside. Ideally the magnitude of the main beam in any direction should be the same, in order to have a balanced performance of the phased array regardless of the steering of the beam. However, due to the particular configuration and method used in this design, a difference of around 1 $dBi$ is presented between the beam at broadside and steered at 27°. Despite this difference the aim of this chapter is not affected, taking into account that the gain of the reconfigurable phased array is not a critical parameter for the purpose of this work. The rest of the parameters show good agreement, except for the values of the side lobe level from the designs with steered beam. However a better result for this parameter was obtained for the reconfigurable phased array which suggests no further analysis.

## 4.8 Conclusions

A good architecture of reconfigurable microstrip phased array antenna has been designed and measured for the frequency of operation of 12.5 GHz. The reconfigurability of the phased array has been demonstrated, measuring their radiation characteristics with main beam at 0° and $\sim 29°$ in the H-plane. The reconfigurability is performed by the implementation of two digital phase shifters that allow the electronically steering of the main beam at $-27°$, 0°, and 27° in the H-plane. The evaluation of the performance of the reconfigurable phased array has been demonstrated, by the validation of the electromagnetic parameters obtained from the simulations and ratified with the measurements, through the analysis of the performance of a sequence of different designs of antennas developed to achieve a final representative architecture.

According to the measurements, the average of some of its most important parameters such as the gain is $8.2\,dBi$, bandwidth of 1 GHz, and side lobe level of $-26\,dB$ and $-8.2\,dB$ for radiation at broadside and main beam at $\sim 29°$, respectively. An important loss factor of around $1\,dB$ was found during the measurements due to the possible losses involved in the physical designs that might be related with the quality of fabrication. The most important effect of this loss factor was over the gain, with lower magnitude, and over the bandwidth, with narrow range of frequencies.

This architecture of reconfigurable phased array antenna has proven the behaviour expected from the analysis developed for the trade-off between the gain and side lobe level of an array of four antennas without feeding network, considered as the reference design. The gain of this reference design with main beam at 29° was expected to be around $9.48\,dBi$, however if the loss factor is taken into account, the measured gain should be around $8.48\,dBi$ which is very close to the measured value of $8.2\,dBi$ of the physical design. The expected gain of the reference design with radiation at broadside was $11.6\,dBi$ so, if the loss factor is considered as well, the measured gain should be around $10.6\,dBi$. However, both the simulated and measured magnitude of the reconfigurable phased array were 8.6, $dBi$ and $8.2\,dBi$, respectively. This lower value is attributed to the required configuration of the phase shifters for this state, where the length of the feeding network is the longest for this case. Then, the energy loss is increased due to the extension of the microstrip lines for this connection, and because of the distortion that the phase shifters might generate on the radiation pattern, taking into account that they are within the feeding network in the same plane as the antennas. Although the magnitude of the reconfigurable phased array at broadside is lower than the expected from the reference design, this loss was already considered, taking into account that the reference magnitude was obtained from an ideal array without feeding network, which presents lower losses than the design with the feeding network. Despite this, it does not represent an important issue to demonstrate the steering of the main beam. In fact, this result allows to ignore the effect of the scan loss and have a similar magnitude of the gain for all the positions of the main beam, considering that the gain with main beam at $\sim 29°$ and at broadside, is around $8.2\,dBi$.

The expected side lobe level was $-31.3\,dB$ for the radiation at broadside, while the measured one was $\sim -26.5\,dB$, which for practical purposes means that the magnitude matches the expected one. For the radiation with main beam at $\sim 29°$ the side lobe level was expected to be $-3\,dB$, while the measured one was better with $-8.2\,dB$. Based on these results, it is acceptable to say that the physical design of reconfigurable phased array follows the expected behaviour from the analysis developed for the trade-off between the gain and side lobe level.

Another important finding is the good agreement between the simulations and measurements. Basically all the electromagnetic parameters, of all the physical designs developed in sequence to achieve the final architecture of reconfigurable phased array present good agreement with the measurements. The results of these parameters, such as the $S_{11}$, $Z_{in}$, VSWR, $BW_{-10dB}$, G, $BW_{-3dB}$, BW, SLL, and the direction of the main beam are suitable to demonstrate the electronically steering of the main beam with good radiation characteristics, which the results and analysis presented in this chapter have demonstrated.

The most interesting finding is the demonstration of the electronically steering of the main beam, changing the reconfigurability of the phased array by the use of digital phase shifters. This reconfigurability is performed by switching the different connections of the 1-bit digital phased shifters, to provide the required discrete phase delays to steer the main beam at the desired direction. The most value of this demonstration is the possibility to develop this switching by using RF-MEMS. The performance of this design has satisfied the main aim of this chapter, which is to obtain a good architecture of reconfigurable phased array antenna suitable for the monolithic integration of RF-MEMS on the same PCB, to demonstrate the dynamic reconfigurability of the phased array, and as a result the electronic steering of the main beam. It is important to mention that this architecture might not be the best of its type [29], [30], [31], [32], [33], [34], [35], but it is a good representative one that allows the integration of RF-MEMS, in order to demonstrate that low cost of production and good performance of the phased arrays can be achievable with this new switch technology. Therefore, in the next chapter the design, simulation, and fabrication process, along with the measurement, of a copper RF-MEMS cantilever switch are presented, in order to evaluate its performance, and to integrate it with the reconfigurable phased array to demonstrate the effectiveness of the entire system.

# Chapter 5

# DC-Contact RF-MEMS Cantilever Switch

## Contents

## 5.1 Introduction

In Chapter 4, a suitable architecture of reconfigurable microstrip phased array antenna for the monolithic integration of RF-MEMS on the same PCB has been demonstrated. The aim of this chapter is to present a novel design of a DC-contact RF-MEMS cantilever switch able to operate with the reconfigurable phased array at a frequency of 12.5 GHz. The switch is designed on a Rogers substrate in order to investigate its performance on the same PCB as that of the phased array. This chapter presents the design, simulation, fabrication, and analysis of the measurements of different switch designs.

In Chapter 3, the most relevant information about RF-MEMS was presented, highlighting their main characteristics and their potential application in different areas. Additionally, a list of general design guidelines to obtain a reliable RF-MEMS was introduced, based on the state-of-the-art of this switch technology. As stated in that chapter, the design of a faithful RF-MEMS requires expertise in different specialized areas. However, the general mechanical and electromagnetic modeling of a switch presented in Chapter 3 are a very good start for a primary design. The RF-MEMS presented here is based solely on these two models. Indeed this chapter mainly focuses on the required electromagnetic performance of this RF-MEMS, for effective operation with the reconfigurable phased array. The mechanical analysis is based on a static mechanical modeling able to demonstrate and validate the electrostatic actuation of the RF-MEMS. The mechanical simulation of the switch is used only to ensure that the cantilever does not break when switching by applying an external force. The dynamic mechanical analysis of the switch is out of the scope of this project, considering that this analysis is useful for determining the switching time when many cycles of operation are performed, and that the purpose of this chapter is to validate only a design of RF-MEMS able to demonstrate the principle of operation of an RF switch for operation with the phased array. The dynamic mechanical analysis is considered as the next stage of this project, once the electromagnetic performance of the switch has been validated.

The mechanical and electromagnetic behaviour of the switch is demonstrated by evaluating simulated results, based on the background presented in Chapter 3 and on measurements. The electromagnetic performance is analysed based on the measurements of the S-parameters of physical designs of RF-MEMS. According to the hypothesis of this project, which states that good performance and low cost of phased array antennas can be achieved by monolithically integrating reliable RF-MEMS on commercial PCBs, a cost-effective technique to fabricate these switches on PCBs needs to be developed. Therefore, the aim of this chapter is also to propose and develop a new convenient process of fabrication of RF-MEMS, using photolithography techniques for their monolithic integration with the phased array. Simulations are validated by contrasting the measurements of physical designs of RF-MEMS built with this process of fabrication.

The first part of this chapter (Section 5.2) presents the design and simulations of the mechanical and electromagnetic characteristics of the switch. Section 5.3 presents the developed fabrication process used to build the switches on the PCB, using photolithography techniques. Section 5.4 demonstrates the electrostatic actuation of some built cantilevers by contrasting the expected *pull-down voltage* with the measurements. Section 5.5 presents the measurements of the S-parameters of some built switches for both the *off-state* and *on-state*, along with the explanation of the method used to develop the measurements, and to validate the simulations. Finally, Section 5.6 presents two approximate equivalent circuits of the RF-MEMS for the characterization of each state of the switch. Additionally, the commutation quality factor (CQF) is calculated to complement the analysis of the electromagnetic performance of the switch.

## 5.2 Design and Simulation of the RF-MEMS

The RF-MEMS switch was developed considering different aspects. First, the design was conducted to connect both sides of the 300$\mu m$ gaps of the 100 $\Omega$ microstrip lines that form the switched-line digital phase shifters of the phased array. Second, based on the types of RF-MEMS presented in Chapter 3, an inline series DC-contact RF-MEMS switch was designed, based on a thin cantilever with vertical electrostatic actuation by an isolated electrode placed beneath the beam, in order to generate a metal-to-metal contact with the microstrip line (t-line).

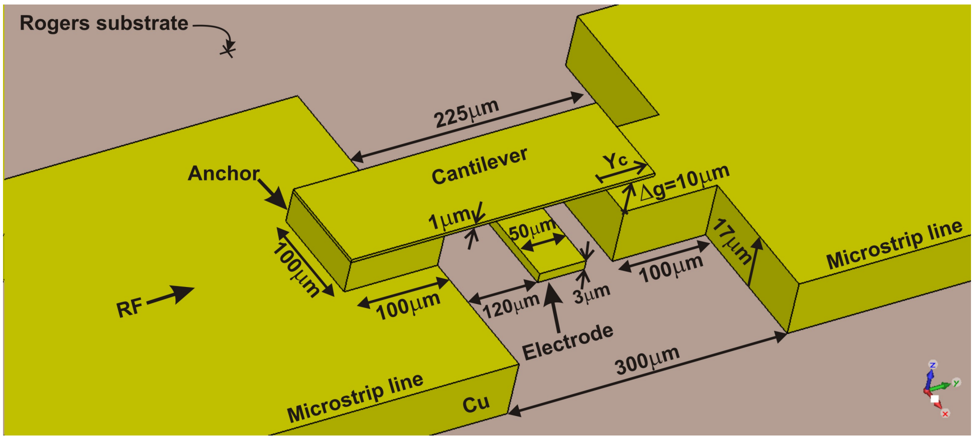

Figure 5.1: 3D view of the DC-contact RF-MEMS cantilever switch with z-axis escalated.

Third, according to the different physical dimensions of RF-MEMS investigated from the literature in Chapter 3, where the length ($l$) of the cantilevers was found to go from 70$\mu m$ to 250$\mu m$, the width ($w$) from 30$\mu m$ to 125$\mu m$, the thickness ($t$) from 0.6$\mu m$ to 10$\mu m$, and the height ($\Delta g$), between the cantilever and the miscrostrip line, from 0.8$\mu m$ to 6$\mu m$, the dimensions of the DC-contact RF-MEMS switch presented in this work were optimized in order to ensure good mechanical and electromagnetic behaviour, for both the *off-* and *on-state* over the 300$\mu m$ gap of the phase shifters. Finally, another important consideration were the resources available at the Electronics Department, which limit the physical dimensions for the fabrication of a structure to a minimum resolution of 100$\mu m$. Based on these aspects, the RF-MEMS is based on a 1$\mu m$-thick copper (Cu) cantilever, with 225$\mu m$ of length, and 100$\mu m$ of width over the Rogers 4003c substrate ($\varepsilon_r = 3.55, \tan\delta = 0.0027$ and $h = 0.813\,mm$), as shown in Figure 5.1.

The central part of the gap was reduced from the original 300$\mu m$ to 200$\mu m$, in order to decrease the length of the cantilever and the chance of breaking. This consideration was based on the mechanical and electromagnetic simulations of the design (Figure 5.1) developed in CST Microwave Studio. The purpose of the mechanical simulation is to ensure that the cantilever will not break when switching down for the connection of both sides of the transmission lines. Figure 5.2 shows the magnitude of the stress in the most critical region of the cantilever produced by switching the beam. The stress of the deformed cantilever near the anchor of the structure is around 45 MPa, which is lower than the 260 MPa of the maximum stress that the copper can withstand while being pulled [67]. It is important to mention that this value does not suggest a reliable dynamic behaviour of the switch for many cycles of actuation, but a simple demonstration of the deformation of the cantilever when a force is applied over the structure, as the electrostatic force that is intended to be used to achieve an open and a short circuit.

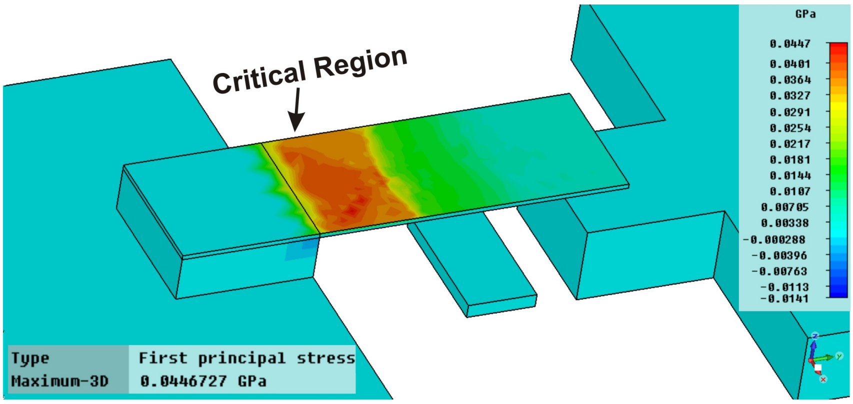

Figure 5.2: Stress on the cantilever due to the bending down of the switch.

The physical structure of the RF-MEMS goes hand in hand with the electromagnetic (RF) behaviour of the switch. This is why the reduction of the gap to $200\mu m$ needs to be evaluated taking into account the RF behaviour as well. Then a trade-off between the dimensions and the electromagnetic response of the switch is always required. Ideally a RF switch should present no insertion loss (IL), which means the value of the resistance ($R_{on}$ or $R_c$), produced between the cantilever and the transmission line in the *on-state*, should be $0\,\Omega$. It should also present very high isolation, which means the capacitance ($C_{\text{off}}$) between the cantilever and the area of contact in the *off-state* should be 0 fF. The closer to these values the resistance $R_{on}$ and the capacitance $C_{\text{off}}$ are, the better the RF performance of the switch becomes. Besides the literature review presented in Chapter 3 for a reference of the general dimensions of the cantilevers, the range of values of the isolation, insertion loss, and return loss (RL) for an acceptable RF behaviour were also identified. According to this research, the isolation is usually better than $-20\,dB$, the insertion loss is usually better than $-1\,dB$, and the return loss is usually better than $-20\,dB$, with values for $R_{on}$ that go from 1 to $7\,\Omega$, and for $C_{\text{off}}$ from 1 to 24 fF.

The range of these values relates to the technology used to fabricate the RF-MEMS. This is why these values cannot be considered as the target but solely as a general reference. Taking into account the importance of these parameters for the RF performance of the switch, the optimization of the gap between the transmission lines ($200\mu m$), the length of the cantilever ($225\mu m$), and the height ($\Delta g = 10\mu m$) between the cantilever and the area of contact (or height of the switch with respect to the t-line), were based on the RF performance obtained from the simulations of different dimensions of these parameters of the switch. Then, an electromagnetic simulation was developed for the design in Figure 5.1 with the transmission lines only, i.e. without any structure shown in Figure 5.1 except for the transmission lines with the gap in the middle.

The simulation was carried out by placing two $100\,\Omega$ ports at the ends of the $100\,\Omega$ lines in order to obtain the magnitude of the $S_{21}$ parameter for different gaps in a frequency range of 10 to 14 GHz, particularly for the frequency of interest of 12.5 GHz. Figure 5.3 shows results of the isolation of the design for gaps that go from $50\mu m$ to $300\mu m$. Based on these results, it can be seen that the bigger the gap is, the better the isolation becomes. However here is where part of the trade-off between the dimensions of the switch and the RF behaviour take place. In this case, if a big gap is selected, the length of the cantilever becomes longer as well, and the risk of breaking increases. Therefore the target was to obtain the highest possible isolation without risking the mechanical stability of the switch. This is why the decision was focused only on a gap between $200\mu m$ and $250\mu m$, considering that a gap of $300\mu m$ represents a bigger risk of breaking, and that gaps lower than $200\mu m$ do not present a good isolation, although they can have better mechanical stability.

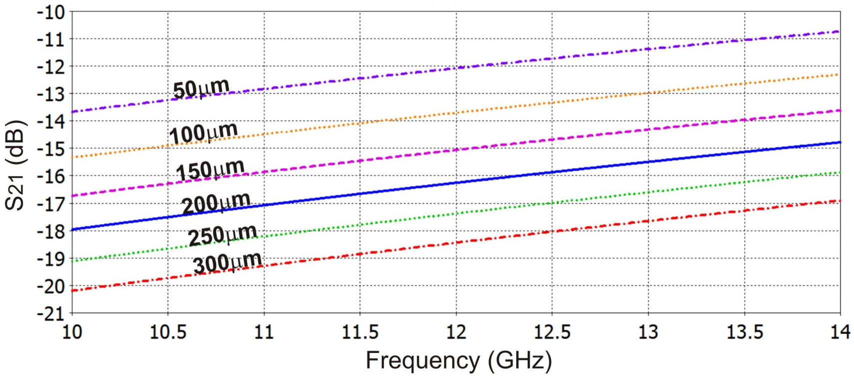

Figure 5.3: Isolation of the microstrip lines for different gaps.

Despite the fact that the gap with $250\mu m$ presents a good isolation of $-17\,dB$, the gap of $200\mu m$ with an isolation of $-16\,dB$ was chosen, taking into account that the length of the cantilever needs to be bigger than the gap selected in order to generate the metal-to-metal contact. This means that a cantilever is bigger than $200\mu m$ with a gap of this dimension. Also, based on research from the literature of physical designs of cantilevers with no more than $250\mu m$ of length, a gap of $200\mu m$ is a good option for the design of the switch in this work, considering that the length of the cantilever can have an extra $50\mu m$ of length. Although a precise mechanical analysis could have been developed to see whether cantilevers bigger than $250\mu m$ break or not, the fact that such dimensions were not found in the literature suggests that some problems might occur during the fabrication. This is why a gap of $200\mu m$ was chosen, mainly due to the uncertainty of the effectiveness of the fabrication process that was already investigated but not proved at this stage of the project. The decision was also due to the relatively small difference in the isolation of $1\,dB$ between the gaps of $250\mu m$ and $200\mu m$, and the potential risk of failure that might happen during the fabrication process of the switch for a longer cantilever.

Once the gap between the transmission lines was chosen, the other part of the trade-off was developed by optimizing the length of the cantilever, and the height $\Delta g$ in order to ensure a good RF performance of the switch. The evaluation of the electromagnetic behaviour of the switch is based on the values obtained for the isolation in the *off-state*, and on both the insertion loss and return loss in the *on-state*. This is why it is important to present the expressions to calculate these parameters. According to [37], the insertion loss is defined as:

$$IL = -20 \log |T| \; dB \tag{5.1}$$

and the return loss as:

$$RL = -20 \log |\Gamma| \; dB \tag{5.2}$$

If a two-port network is considered, as the one presented in Figure 5.4, the $S_{11}$ parameter is the input reflection coefficient $\Gamma$ seen in port 1, if port 2 is terminated in a matched load to avoid reflections. Also, the $S_{21}$ parameter is the transmission coefficient $T$ from port 1 to 2 with the matched load.

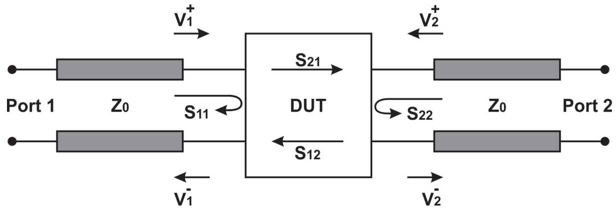

Figure 5.4: S-parameters of a two-port network.

Based on the expressions (5.1) and (5.2), the isolation of the switch can be obtained by:

$$Iso = -20 \log |T| \; dB \tag{5.3}$$

taking into account that the magnitude of the transmission coefficient for the *off-state* is expected to be lower than for the *on-state* of the switch, this can therefore be described as isolation. This expression was already used for plotting magnitudes of the $S_{21}$ obtained in Figure 5.3, as part of the analysis of the isolation for different gaps between the transmission lines.

The isolation, insertion loss, and return loss were then investigated from the S-parameters obtained by the simulation of the design of the switch shown in Figure 5.1 for both states. This design presents an optimum length of the cantilever of $225\mu m$, and a height $\Delta g$ of $10\mu m$. It shows also an electrode beneath the cantilever separated from the line of contact at $30\mu m$.

The RF performance of this switch is presented in Figure 5.5, which shows the magnitude of the S-parameters for the frequency range of 10 to 14 GHz. Figure 5.5 demonstrates that the behaviour of the switch at 12.5 GHz presents an insertion loss (IL) of around $-0.1\,dB$, and return loss (RL) of around $-38.4\,dB$ in the *on-state*. The isolation (Iso) in the *off-state* is of around $-11.6\,dB$. In order to evaluate these results, they are compared with the ones obtained from a single-pole single-throw (SPST) RF-MEMS fabricated by Radant [18] on a high resistivity silicon substrate, and with a shunt RF-MEMS fabricated on a PCB [21]. Table 5.1 compares the most important parameters of these switches with the switch obtained in this work. The switch fabricated by Radant was selected for comparison because it is a commercial RF-MEMS based on the same principle of operation as the one presented here, although the technology of fabrication is different. The shunt

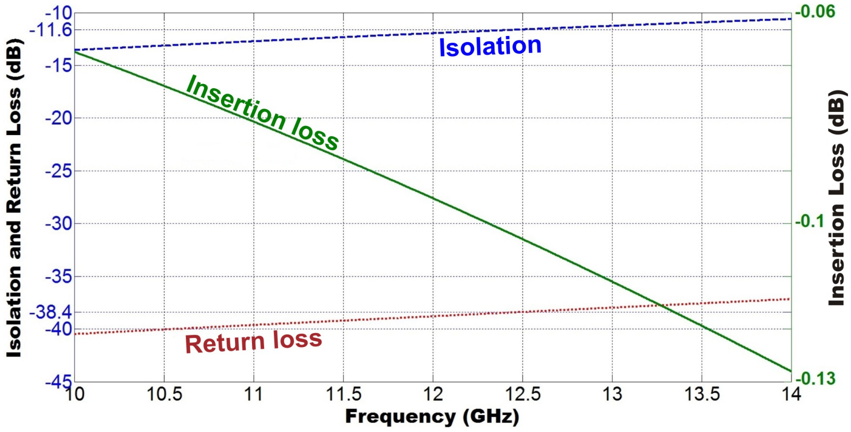

Figure 5.5: S-parameters of the RF-MEMS for both the *off-* and *on-state.*

| Technology | Isolation | Insertion loss | Return loss | Frequency |
|---|---|---|---|---|
| On silicon | -12 dB | -0.32 dB | -20 dB | 10 GHz |
| On PCB | -20 dB | -0.06 dB | -20 dB | 10 GHz |
| This work | -11.6 dB | -0.1 dB | -38.4 dB | 12.5 GHz |

Table 5.1: Comparison of different RF-MEMS.

RF-MEMS was selected because it is one of the few switches fabricated on PCB substrates found in the literature. This switch can therefore be a good reference considering that the purpose is to present and prove a convenient process of fabrication on PCB.

Based on parameters presented in Table 5.1, it is clear that both the insertion and return loss for the switch in this work are similar to that of the other switches. Although the isolation is very similar to that of Radant's switch, it presents a lower value than the one achieved on PCB. This is attributed to the particular characteristics of the Rogers 4003c substrate where the switch is designed. In fact, it is the height or thickness of the substrate which affects the isolation of the RF-MEMS as it is explained next.

In order to prove this, the RF-MEMS presented in Figure 5.1 was simulated on a thinner Rogers substrate with height of 0.203 mm, instead of the 0.813 mm of the original substrate. The other parameters of the board are the same ($\tan\delta = 0.0027$, $\varepsilon_r = 3.55$). Figure 5.6 shows the magnitude of S-parameters obtained for this design for a frequency range of 10 to 14 GHz. From Figure 5.6, it is possible to see that the isolation of the switch has been improved to $-22.6\,dB$ instead of $-11.6\,dB$ obtained in the original design. In spite of this, Rogers 4003c with $h = 0.813\,mm$ was selected because it is more effective for the performance of the reconfigurable phased array antenna than the thinner one, in terms of bandwidth and radiation efficiency. This means that the thickness of this substrate gives better results for antennas than for microwave integrated circuits. This is because the thinner the substrate is, the more concentrated the lines of the electric field become within the substrate, and less radiation is generated from the structure. Accordingly, a thick substrate is beneficial for the radiation of the antenna. Therefore, a trade-off between the performance of the phased array and of the RF-MEMS is required, based on the thickness of the substrate. This trade-off was relatively easy to solve taking into account that a thinner substrate bends more easily than a thick one, which represents

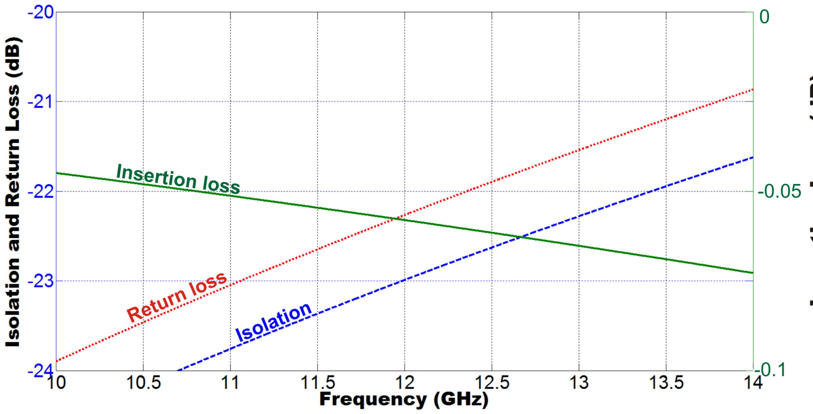

Figure 5.6: S-parameters of the RF-MEMS for both the *off-* and *on-state* with a thinner substrate.

an issue for the effectiveness of the fabrication of the switch, because of the facilities available. Although this was known a priori, this analysis is presented here in order to show that better performance of the RF-MEMS designed in this work can be achieved by simply changing the thickness of the substrate.

One way to compensate for the lower magnitude of the isolation was by increasing the height $\Delta g$, or gap of the cantilever, and by reducing the length of Yc related to the metal-to-metal area of contact with the transmission line, according to the design in Figure 5.1. This is why the height $\Delta g$ is bigger ($10\mu m$) than the ones identified in the literature. Also the length of Yc is $25\mu m$ instead of the available $100\mu m$ to cover all the area of contact. The selected height represents a potential issue for the reliability of the switch, considering that the stress produced on the cantilever while switching down is bigger than for cantilevers with lower height. In fact, the issue might be more critical for several cycles of operation, considering that metal cantilevers suffer from creep effects as explained in Chapter 3. In spite of that, this height was selected in order to have a relatively good isolation of $-11.6\,dB$, which means that only around $7\,\%$ of the power is transmitted. Good switches were indeed built with this height, and proper actuation was demonstrated for several cycles of operation. This is better explained in Section 5.4 where the electrostatic actuation of the switch is demonstrated. Based on the considerations and analysis made from the simulations of this design of RF-MEMS, this switch is considered to be suitable for the monolithic integration with the reconfigurable phased array antenna due to its good performance at microwave frequencies. However the validation of these simulations is required. Further analysis is presented based on the measurements obtained from some physical switches built with the fabrication process presented in the next section.

## 5.3 Fabrication Process

The fabrication technique developed in this work for the building of the switch was created based on the photolithography techniques explained in [14,21,22,25,68–70]. However, the examination of other processes, like the ones presented in [34, 59, 61, 71], for either the fabrication of shunt RF-MEMS or cantilevers with sacrificial layers different from the one used in this work, helped to understand the general stages involved in the fabrication of RF-MEMS. The achievement of an effective fabrication process to build switches suitable for measuring both the electrostatic actuation and S-parameters was obtained from the fabrication of a simple cantilever. The performance of various experiments to build the first successful switches allowed the improvement of the fabrication process itself. The purpose of the fabrication of a simple cantilever on the Rogers substrate was to prove the effectiveness of the process, and static stability of the cantilever. This means proving that the cantilever is fixed and stable, without applying any external force. The process flow of this first fabrication is described in sequence in Figure 5.7.

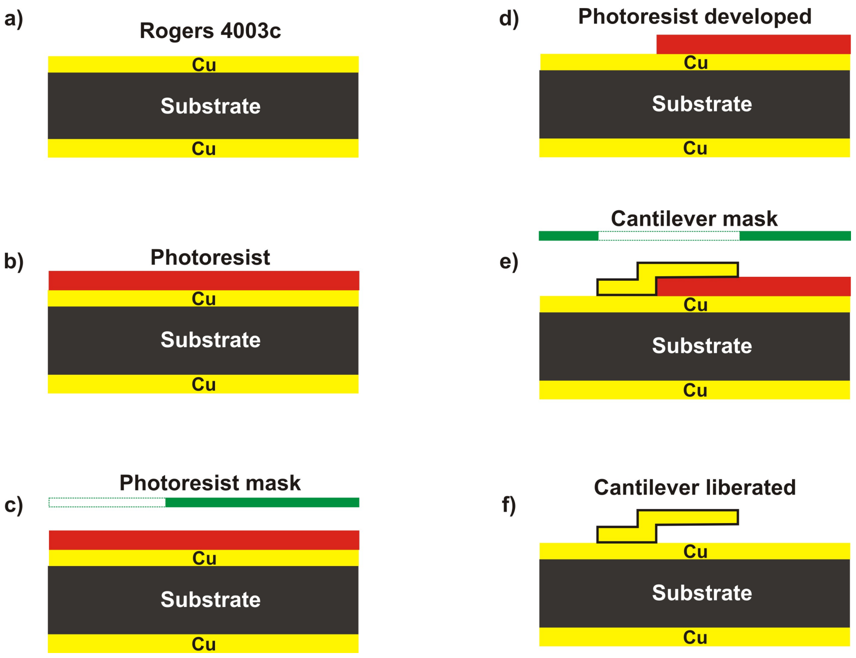

Figure 5.7: Fabrication process flow used for the building of the first cantilever.

This figure shows the lateral view of all the sequential steps involved in the fabrication of the cantilever on the Rogers substrate. The process begins with the 0.813 mm-thick Rogers 4003c substrate, with double-side $17\mu m$-thick standard copper cladding (Figure 5.7a). The first step is the spin-coating of the AZ9260 photoresist on the top of the copper of the board to form the sacrificial layer. The optimum speed to obtain a layer with thickness between $8 - 10\mu m$ was investigated in several experiments. This speed is around 2900 rpm for 1 min (Figure 5.7b). Next, the substrate with photoresist is put in the oven for 120 s at $110°C$. Then, part of the photoresist is exposed with UV light for 33 s ($\sim 900mJ/cm^2$), using a transparent black mask to block the light in the area where the photoresist is required to remain (Figure 5.7c). Thus, the exposed photoresist is developed with the AZ400K chemical for 1 min, obtaining the shape of a step (Figure 5.7d). Next, the cantilever is formed by depositing copper to obtain a $1\mu m$ thin film on the top of the sacrificial layer. The deposition is performed using a thermal evaporation technique. The shape of the cantilever is created by using a mask with a hole with the overall length of the switch. This means both the cantilever and the anchor are formed by the deposition of the copper through the hole on the mask (Figure 5.7e). Finally, the cantilever is liberated by wet-etching the sacrificial layer using acetone or P1316 stripper (Figure 5.7f).

Different issues during the process were identified. For instance, the good alignment of the masks, and both the material and resolution of the mask used for creation of the cantilever during the deposition of the copper, should be considered as a potential improvement for this process. Also, the optimization of the process of liberation of the cantilever represents a critical step in obtaining a successful switch. Despite these issues, this process allowed demonstrating of the working principle of RF-MEMS by the fabrication of different switches, taking into account that every experiment was an opportunity to be more accurate, despite the difficulties in some of the steps of the process.

Figure 5.8 shows photos of some of the steps involved in the process. The top left photo shows the patterned photoresist on the right side of the copper layer. This means that only the right side is covered with photoresist, as described in Figure 5.7d. The top right photo shows the shape of the deposited copper for the formation of a cantilever. This cantilever has not been liberated yet, this is why the photoresist beneath the cantilever is visible as described in Figure 5.7e. In this photo, it is possible to observe the anchor of the cantilever as well, which is at different height compared to the cantilever. At the bottom of Figure 5.8, it is possible to see one liberated cantilever (bottom left), and the demonstration of its physical displacement, using a needle to push down the cantilever (bottom right). The photo on the left bottom demonstrates the mechanical equilibrium of the cantilever, considering that it did not collapse. This means that the weight of

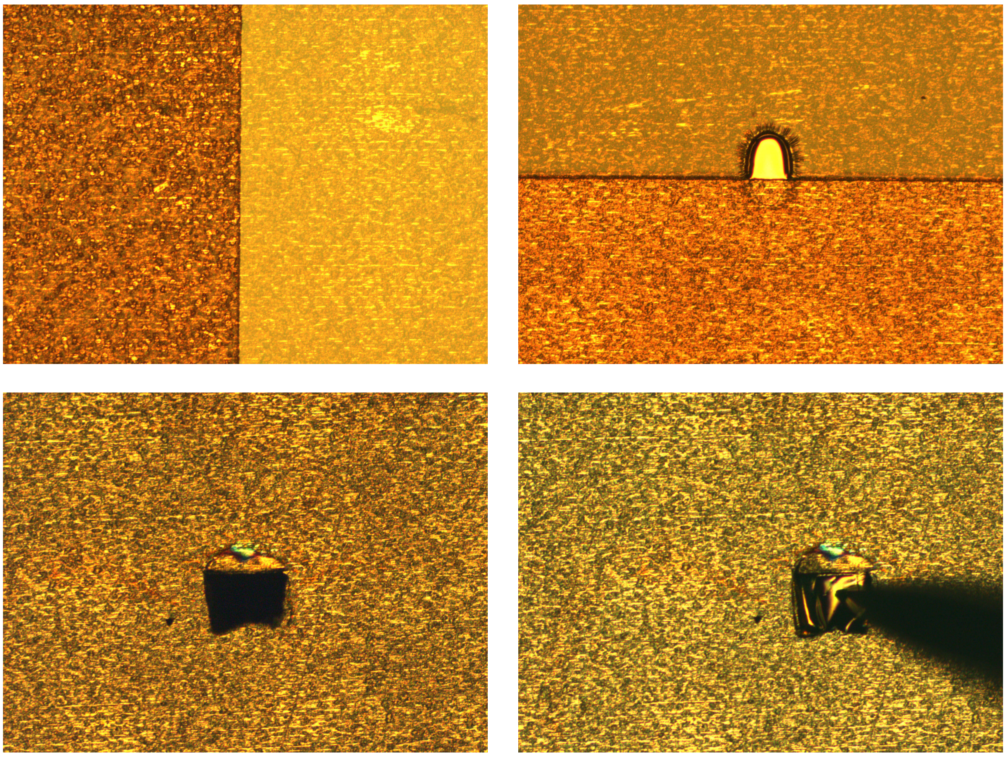

Figure 5.8: Photoresist patterned (top left), cantilever not liberated (top right), cantilever liberated (bottom left), and cantilever actuated (bottom right).

the cantilever is held by the anchor, allowing the static stability of the structure. The physical manipulation with a needle shown in the bottom right of the photo was done to demonstrate that the cantilever was completely liberated, and that it was able to switch with an external force without breaking down. This was carefully performed in order to avoid breaking the cantilever, and to demonstrate a few cycles of switching. No more than 10 manipulations were applied, considering that few actuations ware enough to prove the mechanical switching. Using the same process, other switches were fabricated during this and other experimentations. It is clear from the photos at the bottom that the shape of the cantilever was not the expected one. This and other issues were improved every time an experiment was performed. However others remain as important factors that need to be enhanced for the fabrication of a reliable switch.

Once the aptness of the fabrication process was demonstrated, the next task was to demonstrate the electrostatic actuation of the switch, for which was required to insert an electrode in the design. The initial conditions of the substrate in the fabrication process described in Figure 5.7 were not suitable for this demonstration, taking into account that the electrostatic actuation is generated by the attraction of opposite charges between the cantilever and the electrode, and that the physical contact between the top copper of the substrate with the anchor of the switch does not allow this effect. Therefore an initial substrate with an electrode crossing half of the top part of the substrate was used. This would have implied the need for wet-chemical etching part of the $17\mu m$ copper layer of the top of the substrate. However, this copper is thicker than what can be obtained with the photoresist. The solution was to completely remove this copper layer and deposit a new thinner one. Thus, the initial conditions of the fabrication process were changed as described in Figure 5.9.

Comparing this fabrication flow with the one described in Figure 5.7, the only difference is the use of an extra mask at the beginning of the process to deposit a thin layer of copper of $0.5\mu m$, in the half side of the substrate to form the electrode (Figure 5.9a). The thinness of the copper layer was selected in order to maintain the flatness on the top of the photoresist, taking into account that this time two different height surfaces needed to be covered with the photoresist. The rest of the steps of the flow remained identical.

This fabrication process was performed and different switches were obtained, similar to the one presented in the SEM images of Figure 5.10. These SEM images show one of the first successful switches actuated with electrostatic force. It is possible to see a flat cantilever suspended $8\mu m$ above the copper layer of the electrode that was first deposited, as described in Figure 5.9a. Some curly regions at the edges of the cantilever can be observed in the right photo, possibly caused by the residual stress of the copper at the time the cantilever was released, according to the possible bending scenarios explained in Chapter 3 (Figure 3.4).

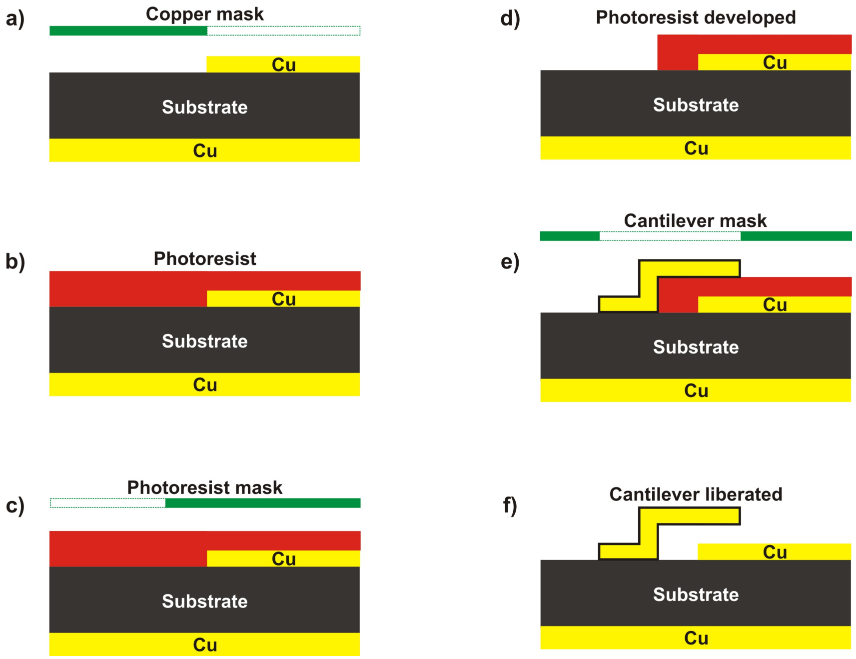

Figure 5.9: Fabrication process flow used for the demonstration of the electrostatic actuation of the switch.

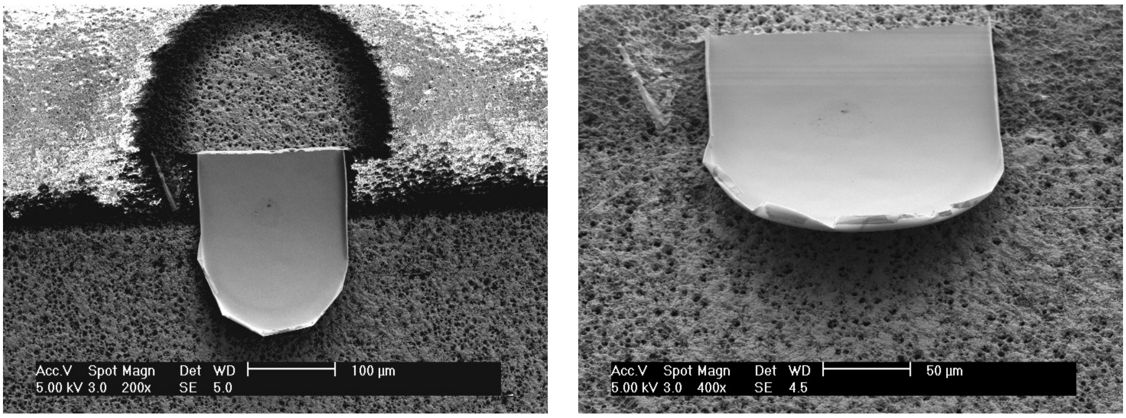

Figure 5.10: SEM images of a RF-MEMS with a Cu electrode beneath the cantilever; top view (left), front view (right).

## 5.4 Electrostatic Actuation

Once the cantilever shown in Figure 5.10 was built, calculations of the *pull down voltage* ($V_p$) were performed using both the CST mechanical simulation and the equations presented in Chapter 3 for the spring constant (k), and for the electrostatic actuation of cantilever beams. The first step was to transfer the exact configuration and dimensions of the physical design shown in Figure 5.10 to CST, in order to calculate the mechanical behaviour of the cantilever. Figure 5.11 shows the 3D design of this switch in the simulator

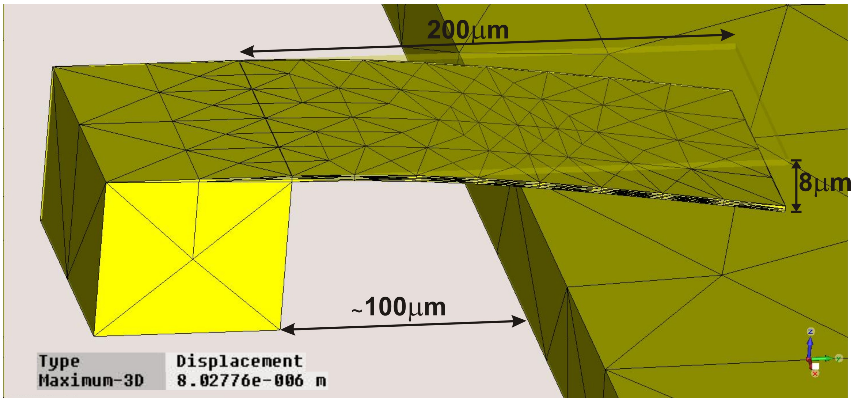

Figure 5.11: Physical cantilever in the simulator with mechanical displacement.

with mechanical displacement of $8\mu m$. The design in Figure 5.11 shows a separation of $100\mu m$ between the anchor and the electrode, similar to the configuration of the physical design. Also, half of the length of the cantilever is considered to be on top of the electrode.

Two main parameters were obtained from this simulation. The stress of the deformed cantilever at the most critical zone of the anchor, which was approximately 36MPa, and the applied force (F) to displace the cantilever $8\mu m$ down at the end of the beam for metal-to-metal contact. The required force, according to the simulation, is $9.6\mu N$. In order to derive the linear spring constant $k$ N/m based on this force, the expression of Eq.(3.1) is used as follows:

$$k = \frac{9.6\mu N}{8\mu m} = 1.2\, N/m \tag{5.4}$$

In order to validate this value, the spring constant is also derived from the expression of Eq.(3.2), taking into account that a uniform force is applied over the entire length of the cantilever. Then the spring constant $k_a$ is given by:

$$k_a = \frac{2(120\, GPa)(100\mu m)}{3} \left(\frac{1\mu m}{200\mu m}\right)^3 = 1\, N/m \tag{5.5}$$

This value is not very far from the one obtained from the mechanical simulation. However, it is possible to see that the electrostatic force caused by the electrode beneath the cantilever does not actuate uniformly along the entire cantilever because of its position. In fact, it actuates over approximately half of the cantilever length. Thus, a better expression for the spring constant is required. The expression of Eq.(3.3) was derived for a non-uniform distribution force, according to Eq.(3.3) the spring constant $k_c$ is given by:

$$k_c = 2(120\, GPa)(100\mu m) \left(\frac{1\mu m}{200\mu m}\right)^3 \frac{1-(100/200)}{3-4(100/200)^3+(100/200)^4} = 0.58\, N/m \tag{5.6}$$

taking into account that $x$ is the $100\mu m$ gap between the anchor and the edge of the electrode, and $l$ is the $200\mu m$ length of the cantilever.

Now, it is possible to derive the required voltage that breaks the mechanical restoring force (F) of the beam. The electrostatic force induced on the cantilever is generated by creating an electric potential difference between the electrode and the cantilever, similar to the one that exists on the plates of a capacitor under an applied voltage as explained in Chapter 3. Therefore, the expression of Eq.(3.7) is used to obtain the voltage (V) as follows:

$$V = \sqrt{\frac{2(0.58\,N/m)}{(8.85\times10^{-12}F/m)(100\mu m)(100\mu m)}(8\mu m)^3} \approx 82\,V \tag{5.7}$$

where $g$ and $\Delta g$ from the expression of Eq.(3.7) are equal in this case, considering that the displacement is the same as the distance between the cantilever and the electrode. If the spring constant $k_a$ is considered instead of $k_c$, the required voltage is approximately 108 V. If the *pull-down voltage* ($V_p$) is calculated from the expression of Eq.(3.8) as follows:

$$V_p = \sqrt{\frac{8(0.58\,N/m)}{27(8.85\times10^{-12}F/m)(100\mu m)(100\mu m)}(8\mu m)^3} \approx 32\,V \tag{5.8}$$

the cantilever should collapse completely by merely applying 32 V, and 42 V if $k_a$ is considered instead.

Experimental results of the required voltage to move down the cantilever in Figure 5.10 show that 70 V is required for a small displacement of around $5\mu m$, and 90 V for a complete displacement of $8\mu m$. Figure 5.12 shows the photos of this experiment, for both the *off-* and *on-state* of the switch. It is not quite easy to see the displacement of the switch when the applied voltage is off and on, in the left and right photo, respectively, to actuate the cantilever. However, if attention is focused on the black regions of the

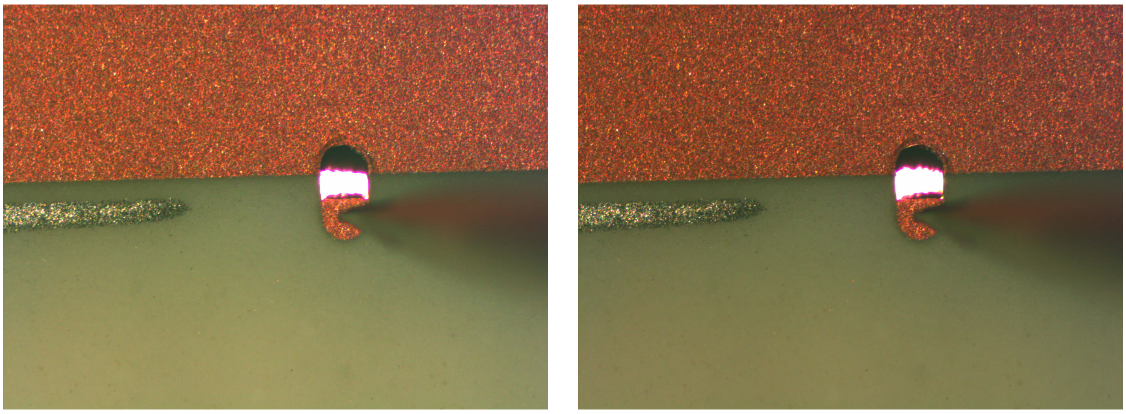

Figure 5.12: Electrostatic actuation of the switch; *off-state* (left) and *on-state* (right).

cantilever, it is possible to see the change of their shapes related with the change of the scattered light seen by the microscope from the structure, due to the movement of the cantilever.

Two probes with different polarization were used for the electrostatic actuation, one connected to the copper layer that forms the electrode, and the other connected to the anchor of the switch, as can be seen in the photos. It is clear that the calculated values of the *pull-down voltage* ($V_p$) differ from the experimental results. However the experimental results are very close to the ones derived from Eq.(5.7). This is probably caused by various factors. First of all, the cantilever in Figure 5.10 is not completely flat and the curly regions at the edges can have a significant impact on the required $V_p$. Second, the cantilever has regions of uneven flatness on the top because of the presence of some residual copper. Third, there is the possibility that a small amount of photoresist remains beneath the cantilever near the anchor, which causes a physical obstacle when the beam is moving down. All these factors might affect the expected collapse of the cantilever when applying the $V_p$. This is why the required voltage to pull down the cantilever was bigger than the expected one.

However, the experimental results show that the required voltage is very close to the voltage calculated to break the mechanical restoring force of the cantilever of around 90 V. In the same manner, other switches were also actuated with a voltage in the range of 70 V to 100 V. This relatively wide range of voltages for the pull down of the cantilevers is attributed to the particular configuration of the switches and factors involved in different experiments developed. For instance, in some experiments the flatness of the switches was better than in others, or their shape or distance to the electrode, or the complete release of the cantilevers. Therefore, the required voltage to pull down the cantilever varied. In spite of this, the experimental results for the switch in Figure 5.10 are sufficiently accurate to validate the approximation of the spring constant ($k$) from the simulated results, and the possibility of electrostatically actuating the switch for a metal contact without breaking it. Also, it demonstrates the mechanical principle of the RF-MEMS to generate an open and short circuit by physically moving a cantilever.

Further analysis to investigate the electromagnetic behaviour is now required to evaluate the effectiveness of the two states for the range of frequencies of interest.

## 5.5 Simulation and Measurement of S-parameters

In order to investigate the RF behaviour of the physical switch from 10 to 14 GHz and particularly at 12.5 GHz, it was necessary to develop an experiment to measure the S-parameters for both the *off-* and *on-state*. Therefore, the next stage of this work was to fabricate a switch on a 50Ω microstrip line with a gap of $200\mu m$, in order to measure the S-parameters when the two sides of the line are connected or disconnected by the switch. The fabrication of the switch on a 50Ω microstrip line was the easiest scenario to measure the S-parameters in terms of fabrication and measurements. This is because the microstrip line was built using a simple mask for the deposition of copper, and because a 50Ω line can be directly matched with 50Ω SMA connectors for measurements using the Network Analyser. Therefore, the initial step of the fabrication process was changed again. Figure 5.13 shows the steps used for the fabrication of cantilevers on a microstrip line. As shown in Figure 5.13a, the initial conditions of the Rogers board changed compared with the two processes used before. For this process, the deposition of a thin copper layer of around $0.5\mu m$, with length of 30 mm and width of 1.62 mm was performed to create the microstrip line on the top of the substrate with the $200\mu m$ gap in the middle. For this step a mask with the overall dimensions, defining the shape of the line, was used for deposition of copper to create the line with a gap. The rest of the process remained identical to the one used before.

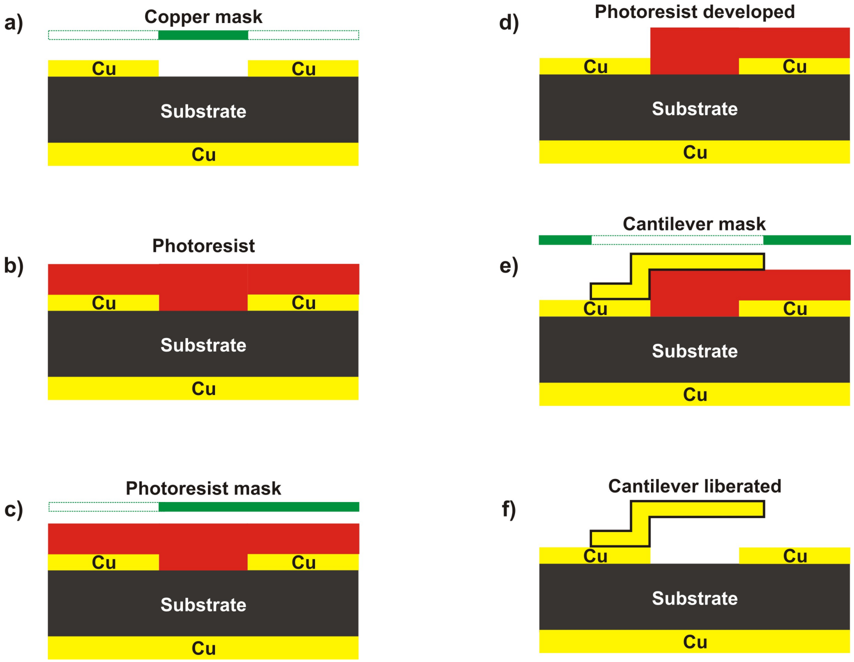

Figure 5.13: Fabrication flow for the measurements of the S-parameters of the switch.

Different switches were built following this process including the one presented in Figure 5.14. As can be seen, it was not possible to align the anchor of the switch exactly with the edge of one of the sides of the transmission line due to alignment difficulties during the manufacturing process. Also, some curly edges, similar to the features observed in previous switches, were obtained. This might suggest the existence of an important residual stress factor during the process of liberation of the cantilevers. However, the fabrication of this and other switches allowed demonstrating of the possibility of fabricating this type of

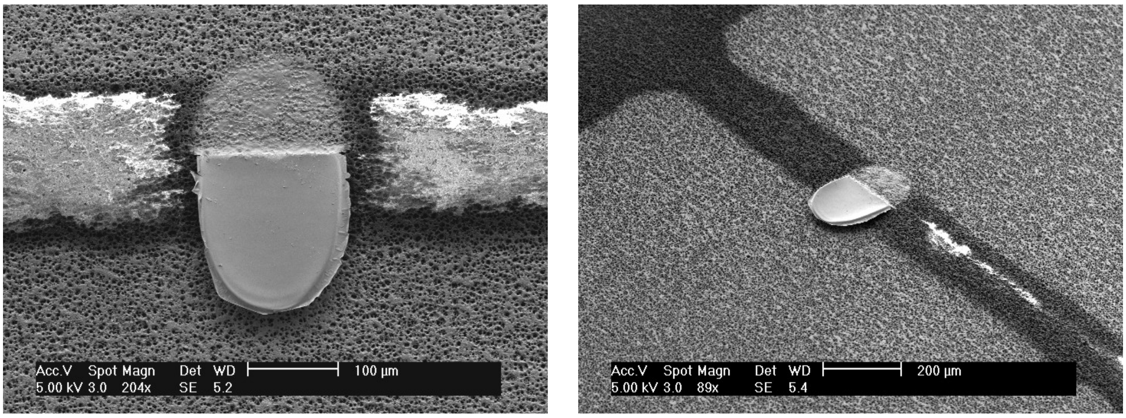

Figure 5.14: SEM images of a RF-MEMS in the *off-state* on a microstrip line; top view (left) and profile view (right).

switch on a microstrip line using the fabrication process suggested. Also, the achievement of the same kind of features on the structure of the cantilever confirms that the process developed for the fabrication of RF-MEMS on PCB works satisfactorily. This finding is significant considering that a main objective of this project is to prove the possibility of monolithically integrating these switches with the reconfigurable phased array antenna on the same PCB. The measurements of the S-parameters were obtained from this and the other two switches shown in Figure 5.15, by soldering 50Ω SMA connectors to the ends of each line. Figure 5.15 shows the switches in the middle of the microstrip lines as tiny bright dots. The S-parameters were measured considering each line with a switch as a two-port network, like the one explained in Figure 5.4, where the device under test is the switch plus the line. Figure 5.16 shows the circuit configuration for these measurements. The network analyser was set in full two-port mode, with one RF cable connected between

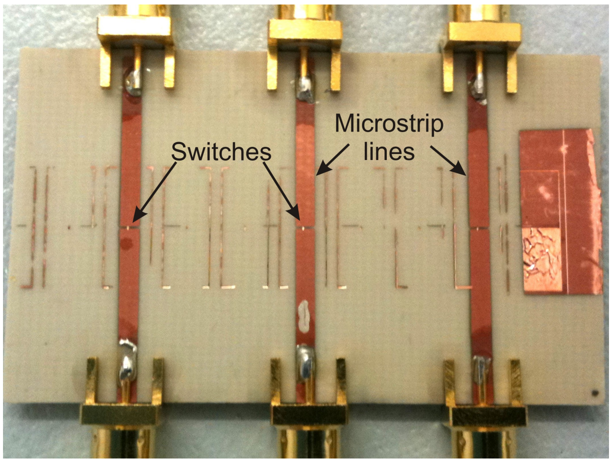

Figure 5.15: Rogers substrate with three RF-MEMS switches on 50Ω microstrip lines.

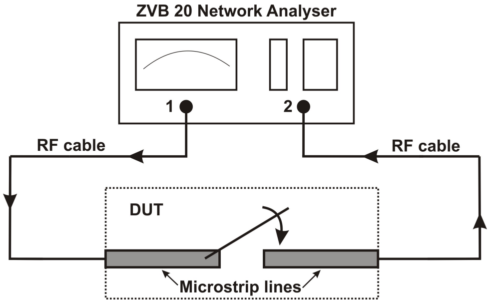

Figure 5.16: Circuit configuration of the measurements of the S-parameters of the switch.

port 1 and one side of the device under test (DUT) by one of the 50Ω SMA connectors. In the same way, another RF cable was used to connect port 2 to the DUT to close the two-port circuit. Therefore, the isolation was obtained from the magnitude of the $S_{21}$ parameter in the *off-state*, whereas the insertion and return loss were obtained from the magnitude of the $S_{21}$ and $S_{11}$ parameters, respectively, in the *on-state*.

The design in Figure 5.15 shows three switches, where the first two are in *off-state*, and the third is in *on-state*. The *on-state* of the third one was not generated with electrostatic force, it was the result of the building process itself. During the liberation of the cantilevers, this switch bent down instead of staying up as the first two. This might be attributed to a failure in the fabrication process that produced either a relative heavy cantilever, enough to approach the maximum force that the anchor can withstand for the up state of the cantilever, or a big residual stress that caused the bending of the beam. However, after evaluating the physical condition of the switch, and the metal-to-metal

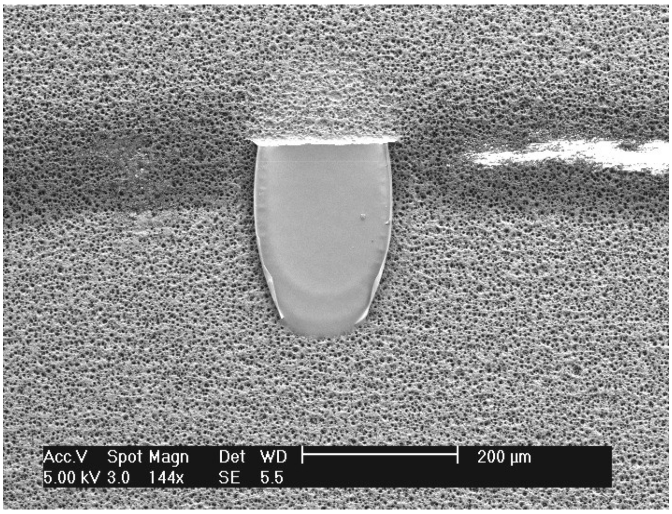

Figure 5.17: SEM image of a RF-MEMS in the *on-state* on a microstrip line.

contact (Figure 5.17), this switch was considered as a good element to perform the initial measurements of the S-parameters for the *on-state* without applying the required DC voltage to actuate the RF-MEMS. Part of this evaluation was a preliminary measurement with the multimeter to verify the DC resistance between the two sides of the microstrip line by the connection of the switch, with a resistance of 4Ω. Taking into account the evident 0Ω obtained for a straight line with the same dimensions, the 4Ω was an initial reference to evaluate the metal-to-metal contact created between the cantilever and the transmission line. Therefore, this and the other two switches allowed measurements of the S-parameters in a "static mode". Thus, measurements were performed using separated switches, i.e. from one permanently in the *on-state* (collapsed one) and from another one fixed in the *off-state*. These measurements were validated with simple simulations by transferring both the dimensions and position of the physical switches on the line to CST, as shown in Figure 5.18. For the *off-state*, the design is simulated without a contact between the cantilever and the transmission line, whereas for the *on-state* it is the opposite situation. Simulated results for the S-parameters were plotted in the same graph with the measured results in order to compare them, as is shown in Figure 5.19 for the *off-state* of the switches.

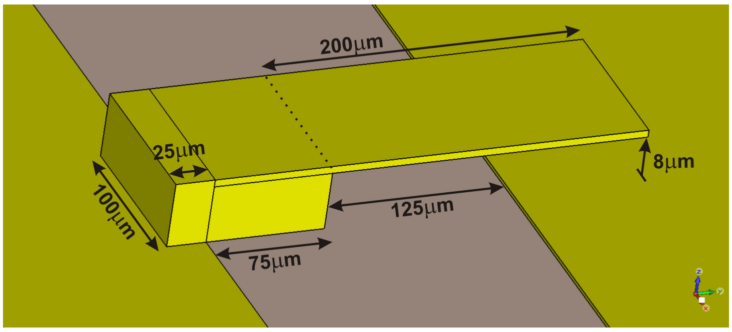

Figure 5.18: RF-MEMS design on the simulator from the physical switches on the microstrip lines.

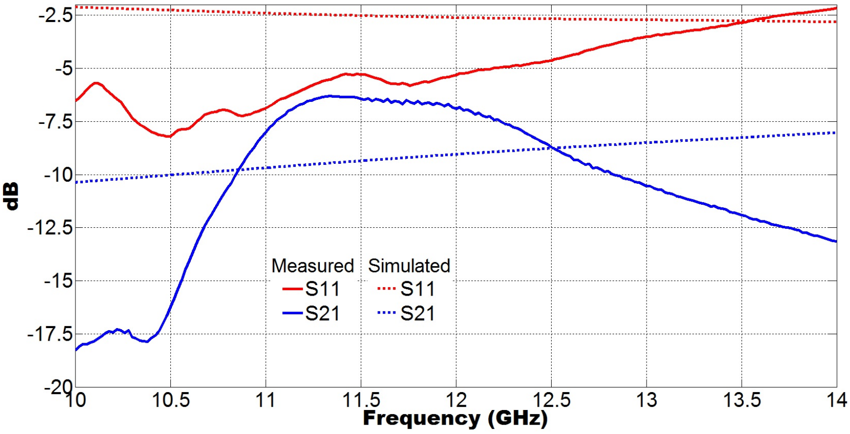

Figure 5.19: S-parameters of the RF-MEMS in the *off-state* on a microstrip line.

The isolation at 12.5 GHz is seen to be around $-8.7\,dB$ for both measured and simulated results. However, measured results below 12.5 GHz show that the isolation is not as good as expected from the simulated results, whereas above 12.5 GHz the result is better. This behaviour is manifested in the $S_{11}$ parameter as well, with lower measured magnitudes below 13.5 GHz. This might be attributed to different aspects. One of them is related to the flatness of the cantilever. Besides the curly edges, it is possible to see in Figure 5.14 that a slight downward curvature is formed in the middle of the cantilever, which can affect the isolation of the switch because the height between the cantilever and transmission line is not as uniform as in the design of the simulator. Another factor is the uncertainty about the complete removal of the sacrificial layer beneath the cantilever, although this may have had a minor effect taking into account that the photoresist is a dielectric. These factors can affect the S-parameters.

In order to evaluate the magnitude of the isolation of these measurements, a comparative value of around $-12\,dB$ at 12.5 GHz was obtained by measuring a microstrip line with a gap of $200\mu m$. This means that the presence of the cantilever on the gap decreased the isolation by a factor of 3.3 dB. Looking at the graph of the measured S-parameters of the line with a gap (Figure 5.20), it is possible to observe a similar behaviour of the graph of the measured $S_{21}$ to the one presented in Figure 5.19, but with a generally lower magnitude for the same frequency range. This is particular observed for frequencies between 11 and 12.5 GHz, with a characteristic increase in the magnitude at these frequencies. Thus, apart from the suggested factors above that caused this particular behaviour in the magnitude of $S_{21}$, it is also possible to say that this is caused by the configuration of the microstrip line. This is the main reason why there is a difference between the simulations and measurements. Despite this difference, the most significant result is the coincidence

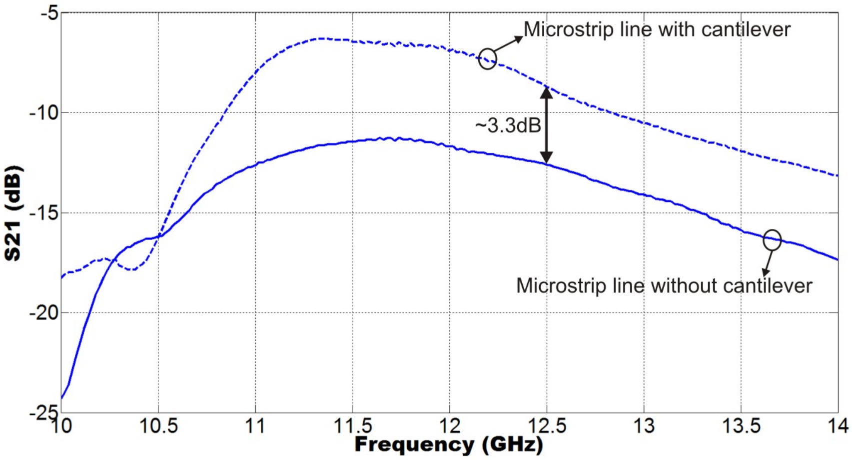

Figure 5.20: Measurements of the isolation of the miscrostrip line with a gap of $200\mu m$, with and without the cantilever

in the magnitude of the isolation at 12.5 GHz for both the measurements and simulations, although an improvement in the simulations should be developed for a better matching of the results for the complete frequency range. It is also significant because it demonstrates the expected effect that the presence of the switch produces on the magnitude of the isolation of the line.

Figure 5.21 shows the simulated and measured results of the S-parameters in the *on-state*. The insertion loss (IL) is $-2.5\,dB$, and return loss (RL) is below $-15\,dB$ at 12.5 GHz for the measured results, whereas the IL is $-1.4\,dB$, and RL is $-17.4\,dB$ for the simulated results. For frequencies below 12.5 GHz, and particularly below 12 GHz, the insertion loss is not as good as expected, whereas at higher frequencies it is more consistent with the simulation. The 1.1 $dB$ of difference in the IL at 12.5 GHz might be attributed to the quality of the metal-to-metal contact, as well as to losses that exist in the physical design and that are not considered in the simulation, related to the fabrication quality. The measured RL shows a good agreement with the simulation at 12.5 GHz, and better behaviour between 10.8 and 12.3 GHz. However higher than 12.5 GHz it starts rising but stays below $-10\,dB$ for most of the frequency range, which for practical purposes, it is possible to say that it presents a good behaviour.

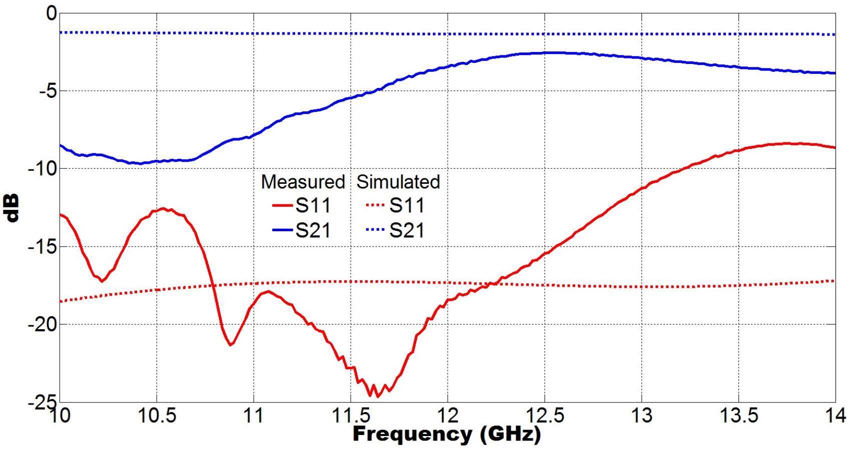

Figure 5.21: S-parameters of the RF-MEMS in the *on-state* on a microstrip line.

In order to evaluate these results, a comparison was done between these and the values obtained by measuring the S-parameters of a simple 50Ω straight line (without gap), with the same dimension as the ones used on the switches for the same frequency range. It was found that the insertion loss of the straight line is a flat graph with a magnitude of $-1\,dB$, and an average of return loss of $-14\,dB$. This indicates that the metal contact of the cantilever on the microstrip line increases the insertion loss by a factor of 1.5 $dB$. This is partially attributed to the quality of the metal-to-metal contact, as explained before. Also, by connecting both sides of a wider line with narrow switches this introduces an important change in the impedance and thus a modification of the insertion loss compared with a straight line, hence, the bigger difference in the magnitude of the insertion loss. The purpose of the measured S-parameters of both the microstrip line with and without a gap is to have a general reference of an ideal real scenario to evaluate the measurements of the switch for both states, along with the results of the simulations. The significance of the measurements of the physical switches is that obeyed the predicted electromagnetic behaviour of the simulated results for both the *off*- and *on-state*. The most successful achievement was the possibility of measuring the S-parameters, and observing a representative change in the magnitude of the $S_{21}$ between the *off*- and *on-state*, to present an open and short circuit, respectively, at 12.5 GHz. The change in the magnitude of the $S_{21}$ was around $6.2\,dB$, which means that approximately 4 times more power was allowed to pass in the *on-state* than in the *off-state*, compared to the expected 5.3 times from the simulations, which represents a small difference. This is significant because it shows that for practical purposes there is a good agreement between simulations and measurements at 12.5 GHz. It is also important because these switches have shown the principle of operation of an RF-MEMS.

Once the measurements of the S-parameters were performed in the "static mode", it was necessary to measure these parameters in a "dynamic mode" with both RF signal and DC voltage for the actuation of the RF-MEMS in the same path, in order to ensure the same electromagnetic behaviour of the switches. Figure 5.22 shows the configuration of the circuit used for the measurements in this particular scenario.

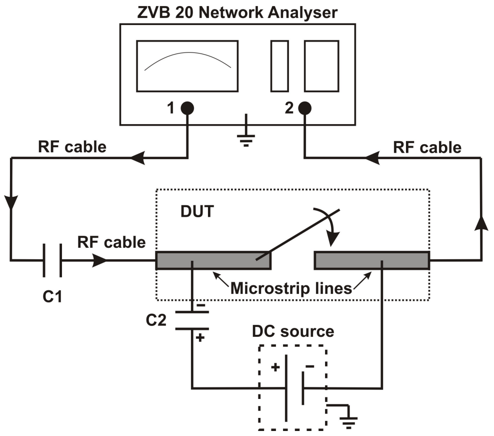

Figure 5.22: Circuit configuration for the measurements of the S-parameters of the switch with both RF signal and DC voltage.

The circuit shows that the network analyser was set in a full two-port mode, with one side of an RF cable connected to port 1, and the other side to a small capacitor of 0.47 pF (C1). Another RF cable was used to connect the other terminal of the capacitor to the device under test (DUT). Port 2 of the network analyser was connected to the other terminal of the DUT to close the two-port network circuit. The calibration of the network analyser was done by considering the RF cables and the capacitor C1. This means that the calibration was done at the input of the DUT in order to try to eliminate the effect of the capacitor on the measurements. For the electrostatic actuation of the switch, a DC voltage source was connected in parallel to the microstrip lines with a capacitor connected in series of $560\mu F$ and up to 200 V (C2). The purpose of the capacitor C1 was to avoid the transmission of DC voltage to the network analyser. The purpose of the capacitor C2 was to prevent the switch from melting when touching the transmission line, by blocking the flow of the current generated when the switch is in short circuit.

Figure 5.23 shows the measured S-parameters. It can be seen that the isolation is

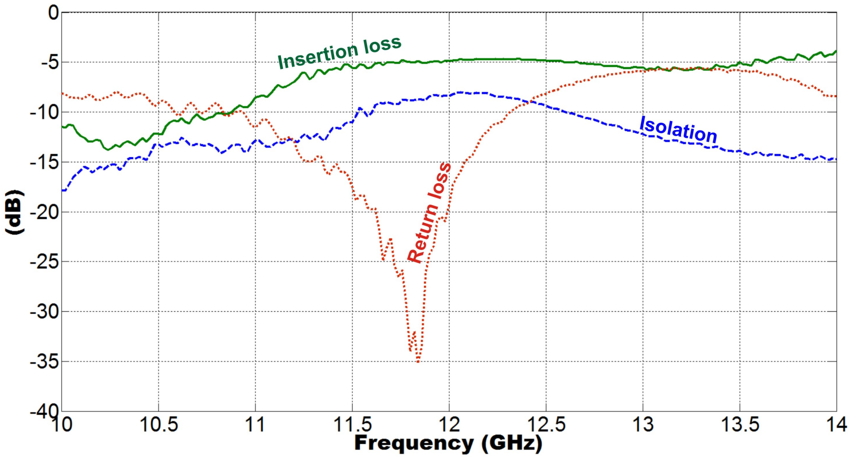

Figure 5.23: S-parameters of the RF-MEMS in the *off*- and *on-state* with both RF signal and DC voltage in the same path.

around $-9.4\,dB$ for the *off-state* and the insertion loss is around $-4.8\,dB$ for the *on-state* at 12.5 GHz. Comparing this isolation with the one obtained in the “static mode”, a slight improvement is observed from $-8.7\,dB$ to the $-9.4\,dB$. Despite this small difference, these results should be essentially the same taking into account that the DC voltage has an effect on the *on-state* only. Hence for practical purposes the isolation can be considered the same. For the insertion loss the situation is different, taking into account that a better magnitude was obtained in the “static mode” of $-2.5\,dB$. This is attributed to the quality of the metal-to-metal contact that is related to different aspects, such as the strength of the electrostatic force applied over the cantilever, the probable oxidation generated on the area of contact, and the flatness of the two structures in contact. These factors might have caused the increase of the insertion loss by around $2.3\,dB$, which reveals the importance of the quality of the metal contact on RF-MEMS for good performance. This is reflected in the magnitude of the return loss as well, with $-8.2\,dB$ instead of the $-15\,dB$ obtained in the “static mode” at 12.5 GHz. This can be explained considering that more power is absorbed and reflected because less power is transmitted to the other side of the transmission line.

The small variations perceptible in the magnitude along the graphs of the S-parameters are attributed to the sensitivity to interference of the capacitor C1, though a previous calibration was developed in order to avoid this effect. Although there is an important minimum at around 11.7 GHz in the RL, all the parameters show similar behaviour to the measurements developed in the “static mode” without DC voltage for the actuation of the switch. The most important finding of these measurements is the change that can be perceived in the magnitude of the $S_{21}$ at 12.5 GHz from the *off-* to the *on-state*, taking into account that this time the RF behaviour of the switch was evaluated with DC voltage in the same path. This change was around 4.5 $dB$, which means that approximately 2.8 times more power was allowed to pass in the *on-state* than in the *off-state* for the measurements in the “dynamic mode”, compared to the 4 times obtained from the “static mode”. This is manly attributed to the quality of the metal contact between the cantilever and the transmission line as explained before. However, it was possible again to show the principle of operation of the RF-MEMS.

Up to this point the measurements of the S-parameters for both states of the RF-MEMS have been carried out, first with RF signal only, and second with both RF and DC voltage for the actuation of the cantilever on the same microstrip line. However, it is also desirable to achieve a better approximation to the design presented in Figure 5.1. For this it is necessary to include an isolated electrode exactly beneath the cantilever to separate the DC voltage from the RF signal.

An experiment was developed for this purpose, which required slight modification of the fabrication process flow shown in Figure 5.13 to include the isolated electrode. In order to add this electrode, an extra step was incorporated, between a) and b), for the deposition of a line of $100\mu m$ of width, and $0.5\mu m$ of thickness that crosses exactly in the middle of the gap of the transmission line. This additional step is shown in Figure 5.24. The rest of the steps of the fabrication process remained identical.

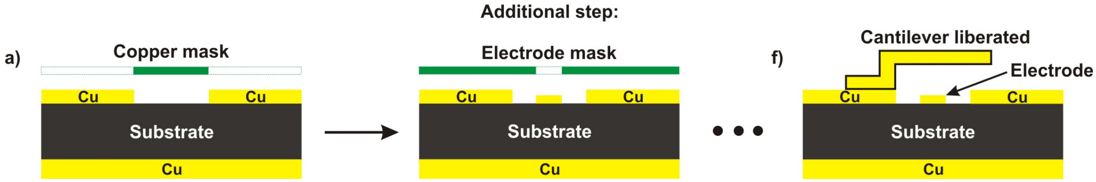

Figure 5.24: Additional step to the fabrication process to create an isolated electrode.

Figure 5.25 shows one of the successful switches built following the modified process on a 50Ω microstrip line with a gap of $200\mu m$, and a line in the middle as the electrode. It is important to mention that the manufacture of these switches with a line as the electrode

Figure 5.25: RF-MEMS switch on a microstrip line with an isolated electrode beneath the cantilever.

is more difficult than the previous ones, considering the required high degree of precision to align the mask involved to create the electrode line of $100\mu m$ width in the middle of a gap of $200\mu m$. Also, it is important to place emphasis on the height difference of $0.5\mu m$ between the electrode and the transmission line. This was done in order to avoid the contact of the cantilever with the electrode when switching down, when connecting the two sides of the transmission line. Then, the thickness of the transmission line was $1\mu m$ instead of the $0.5\mu m$ that was used for the fabrication of the previous switches. It was not possible, however, to measure both states of the switch, as it broke down after performing a few cycles of switching as part of the measurements to obtain the actuation voltage.

The average voltage for the pull-down of the cantilever was 90 V. Only the measurements of the *off-state* of the switch were obtained. These measurements allowed validation of the consistency of the measurements with the simulations. Therefore, the dimensions and configuration of the switch on the line were transferred to a design in CST to validate the results. Figure 5.26 shows the approximate design of the switch used to validate the measurements. From this design, it is possible to observe the isolated electrode be-

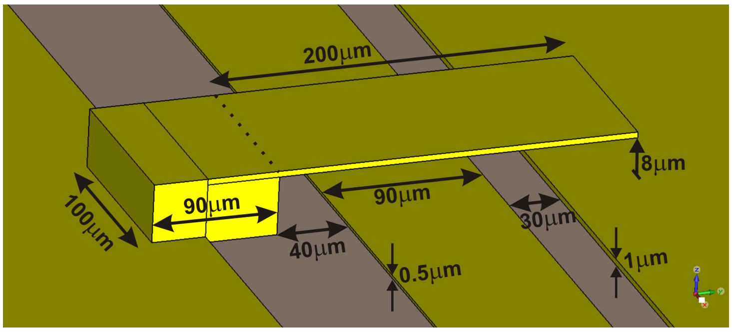

Figure 5.26: RF-MEMS design on the simulator from the physical design on the microstrip lines with an isolated electrode.

neath the cantilever that goes all along the width of the transmission lines, and in the middle of the gap. Based on the simulations of this design and on the measurements, Figure 5.27 presents the S-parameters of the *off-state* of the switch with an isolated electrode. Unexpectedly, the only point where the measurements match the simulations is

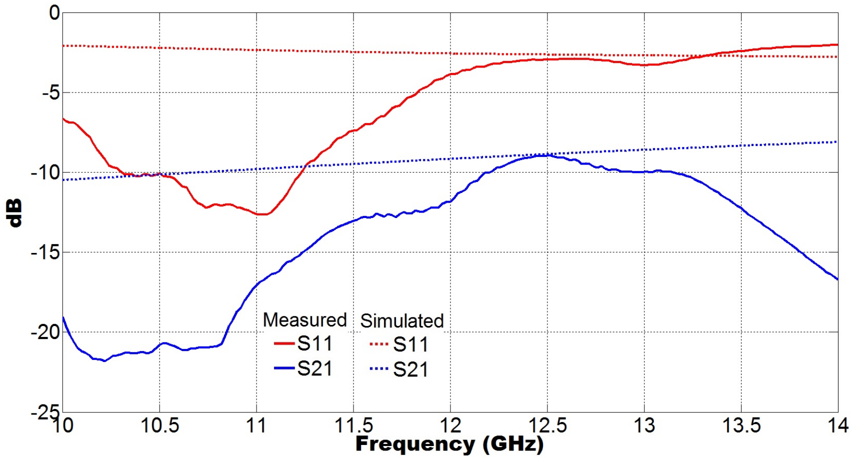

Figure 5.27: S-parameters of the RF-MEMS in the *off-state* on a microstrip line with an isolated electrode.

at 12.5 GHz of around $-8.9\,dB$. The measured isolation is better for the rest of the frequency range. However, looking at the behaviour of the $S_{11}$ parameter below 12 GHz, it seems that the power at these frequencies instead of being reflected, due to the isolation created by the open circuit, is either radiated or consumed due to possible losses of the structure. This might be the effect that the isolated electrode has over the structure. In spite of this, the most important finding is the similar isolation obtained to that of the switches without an isolated electrode. This finding has an important implication considering that this switch was built on a microstrip line with an isolated electrode, as the design of RF-MEMS proposed at the beginning of this chapter. This suggests the potential effectiveness that the fabrication technique has for the manufacturing of switches on PCBs, along with the required good static mechanical and electromagnetic behaviour. It is clear that different aspects in the manufacturing process need to be improved to obtain a reliable RF-MEMS. For instance, by reinforcing the anchor of the switch, and by making the cantilever flatter, it might be possible to obtain better results for both mechanical and electromagnetic behaviour. A last experiment was performed in order to prove this hypothesis. Figure 5.28 shows a thicker cantilever of $2\mu m$ compared with all the previous ones. This switch showed a better stability and flatness on the top of the cantilever than the others. However, due to the contact between the cantilever and the electrode, because of a curvature in the structure at the bottom side of the cantilever, it was not possible to carry out the measurements.

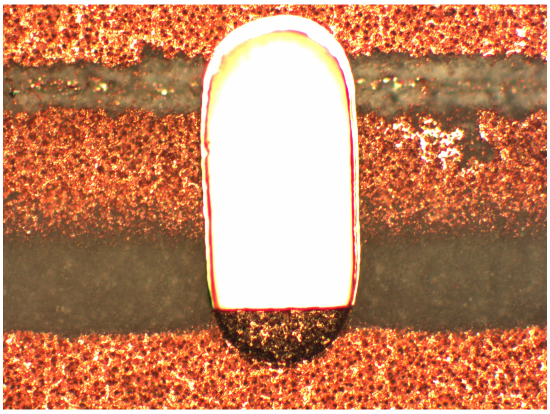

Figure 5.28: A $2\mu m$-thick cantilever on a microstrip line with an isolated electrode.

Nevertheless, the main purpose of the measurements is to verify their electromagnetic consistency with the simulations for the particular frequency of 12.5 GHz, in order to have the elements to validate the novel design of RF-MEMS proposed in Figure 5.1. According to the measurements of the different designs presented so far, the average of the isolation is around $-9\,dB$ in the *off-state*, which implies a good agreement with the simulations. Based on the analysis of the results in the *on-state*, the insertion loss presents a difference of $1.1\,dB$ with the simulations. This difference is likely to be reduced if the quality of the metal contact is improved. The return loss presents a good agreement with the simulations of around $-15\,dB$. Based on the analysis presented and on these findings, it is sufficiently close to validate the results obtained from the simulations of the different designs of RF-MEMS presented so far, particularly at 12.5 GHz. It is also convincing to extrapolate this validation to the results of the S-parameters (Figure 5.5) obtained from the simulations of the novel design of RF-MEMS, considering that the structure of this RF-MEMS is approximately the same as the built ones, along with the settings of the simulations. However, further analysis is presented in the next section based on the equivalent circuit found for the switch, in order to complement this validation. The mechanical simulation allowed the prediction of a very close approximation of the spring constant of the cantilever to calculate the required voltage for actuation.

As part of future work, it would be desirable to build better RF-MEMS to investigate their dynamic mechanical behaviour by performing many cycles of actuation without failure. This would also allow investigation of their electromagnetic performance not only at 12.5 GHz but for all the frequency range of interest. This implies improving the manufacturing technique and developing more experiments.

## 5.6 Equivalent Circuit of the RF-MEMS Switch

Up to this point the electromagnetic analysis of the RF-MEMS has been developed through the electromagnetic simulation of the full design of the switch for each state of actuation. As a supplement to this analysis, in order to simplify calculation and to present clearer electrical characteristics of the switch for each state, the equivalent circuit of the RF-MEMS is presented in this section. The purpose of finding the equivalent circuit for both states of the switch is to verify that it presents a very low capacitance ($C_{\text{off}}$) in the *off-state* for good isolation, and a very low resistance ($R_{on}$ or $R_c$) in the *on-state* to ensure a very low insertion and return loss at the frequency of interest. In order to obtain these parameters, the electromagnetic modelling presented in Chapter 3 gives a general circuit configuration of the switch for both states. This model contemplates the cantilever as a high-impedance transmission line section ($Z_h$), with a series capacitance ($C_s$), or with a contact resistance ($R_c$), for either the *off-* or *on-state*, respectively, with an additional parasitic capacitance ($C_p$) in parallel for both states (see Figure 3.6). This electromagnetic model also estimates a model to obtain the series switch resistance ($R_s$), and the series inductance ($L$) that the switch presents in the *on-state* (see Figure 3.7). Additionally, it allows a good approximation to be obtained for the values of these parameters from either the simulated or measured S-parameters of the switch. Based on this electromagnetic modelling, and on the validation of the simulations of the novel design of the switch (Figure 5.1) in the last section, a first approximation of the general equivalent circuit of the switch is obtained by designing a corresponding circuit to the design presented in Figure 5.29 on the electronic circuit simulator ADS ®.

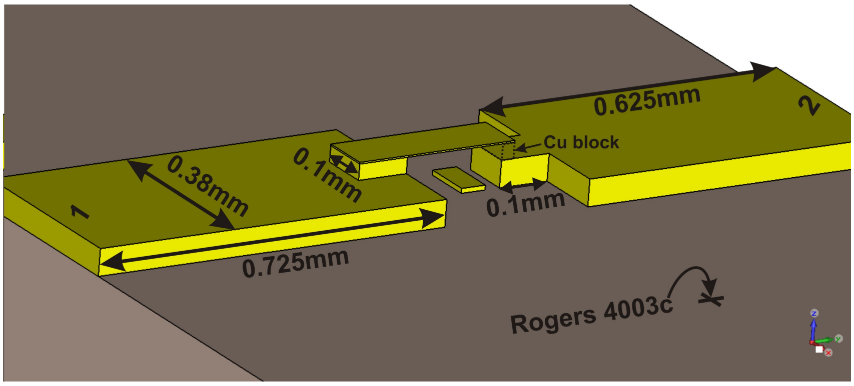

Figure 5.29: 3D design of the RF-MEMS used as a reference for the equivalent circuit.

The design in Figure 5.29 was the one used to obtain the S-parameters in CST (Figure 5.1) for both states of actuation. The only difference is that in this figure the dimensions of the microstrip lines are shown, in order to observe the equivalence of this design with the circuit designed in ADS and presented in Figure 5.30. The position of a Cu block is marked in the design to show the configuration used for the simulation of the switch in the *on-state*. From left to right, the circuit starts with a segment of transmission line

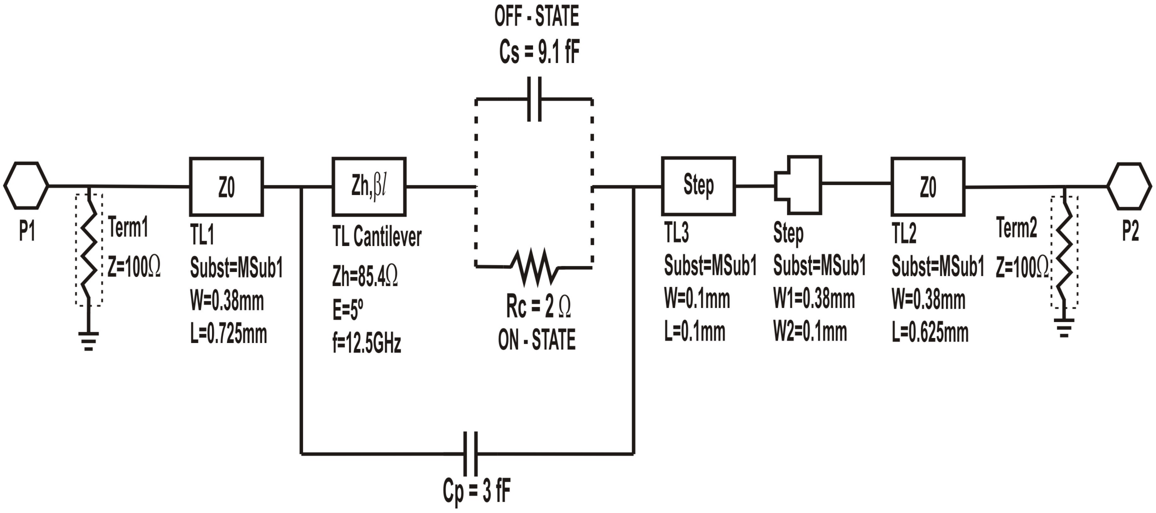

Figure 5.30: Equivalent circuit using a transmission line to represent the cantilever.

(TL1), with length of 0.725 mm, and width of 0.38 mm, on a substrate (MSub1) with equal characteristics to the Rogers 4003c, in order to obtain an equivalent impedance ($Z_0$) to the left transmission line of the design in Figure 5.29 of around 100Ω. Then, the transmission line of high-impedance ($Z_h$) of around 85Ω, and electrical length equivalent to a 5° of phase shift at 12.5 GHz, is connected in series to represent the cantilever in the circuit. Depending on the state of the switch, either the capacitance, $C_s$, or the resistance, $R_c$, are connected in series to represent the effect of the cantilever in the *off-* or *on-state*, respectively, along with a parallel parasitic capacitance $C_p$ of 3 fF. Another small segment of transmission line (TL3), with a length and a width of 0.1 mm, together with a step block on the same MSub1 substrate, are connected in series to represent the transmission line segment for the area of contact of the cantilever. The step block in the circuit is an element required by ADS to join two transmission lines with different dimensions. Thus, another transmission line (TL2), with a length of 0.625 mm and a width of 0.38 mm, for equivalent impedance of 100Ω on the MSub1 substrate is connected in series to represent the right transmission line of the design. Finally, two 100Ω ports (P1&P2) are connected to the end sides of the circuit to perform the simulation and obtain the S-parameters of the two-port network. The elements identified as Term1 and Term2 in the circuit are part of the configuration required in ADS to add the ports, and to simulate the circuit.

The procedure used to ensure that the electromagnetic behaviour of this circuit is equivalent to the design simulated in CST, consisted of optimizing the design to obtain the same input impedance $Z_{in}$ of the switch for each state, in the frequency range of 10 to 14 GHz. Therefore, the results of both simulators (ADS&CST) were compared by contrasting values of input impedance plotted in the Smith Chart, derived from the reflection coefficient at Port 1, or $S_{11}$ parameter, for the frequencies of interest. This is because $Z_{in}$ of a two-port network is obtained from the $S_{11}$ parameter, if Port 2 is terminated in a matched load, by using the following expression:

$$Z_{in} = \frac{Z_0(1 + S_{11})}{(1 - S_{11})} \tag{5.9}$$

where $Z_0$ is the characteristic impedance of the transmission lines of around 100Ω. A manual optimization of the circuit was developed, changing the impedance $Z_h$, and values of the $C_s$ and $R_c$, for the *off-* and *on-state*, respectively, in order to obtain similar values of $Z_{in}$ to the ones obtained from the design simulated in CST. The initial value of $Z_h$ was obtained from the simulation in CST of a segment of transmission line with the same dimensions of the cantilever, and suspended $27\mu m$ from the surface of a Rogers substrate. This impedance was approximately 183Ω. The initial values for $C_s$ and $R_c$ were set based on the background presented in Chapter 3, and on the values expected for these parameters, with a small capacitance in the range of femtofarads, and with a small resistance of no more than 3Ω.

From the optimization process it was found that $Z_h$ is 85.4Ω, the series capacitance $C_s$ is 9.1 fF for the *off-state*, and the contact resistance $R_c$ is 2Ω for the *on-state*. Figure 5.31 shows the input impedance of the design simulated in CST, and the input impedance of the equivalent circuit with the optimized values for the *off-* and *on-state*.

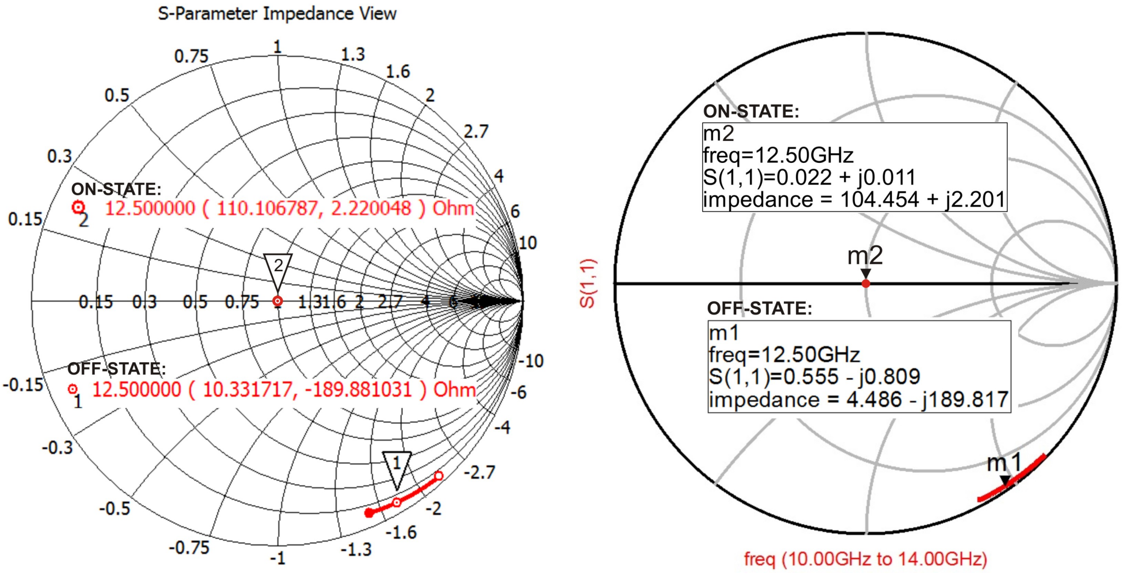

Figure 5.31: Input impedance in the Smith Chart from CST (left), and from ADS (right).

For an expedient comparison of $Z_{in}$ obtained from the two simulators, Table 5.2 compares the input impedances of both scenarios for the frequency range of 10 to 14 GHz. It also shows the magnitude of the transmission coefficient ($S_{21}$) to evaluate the isolation obtained in each simulator. Comparing the imaginary parts of $Z_{in}$ from each simulator, good agreement is seen for all of the frequency range. The negative values of the input impedances demonstrate the capacitive behaviour of the switch at these frequencies. Comparing the real parts of $Z_{in}$, there is a difference of around 5Ω with lower values for the equivalent circuit. This is why the isolation, or magnitude of the $S_{21}$, is better for the equivalent circuit than for the design in CST, due to the losses related to a higher real resistance. Although it was not possible to reduce this difference, these results are important, as they show the similarity of the equivalent circuit for the *off-state* of the switch with the results of the design simulated in CST.

| | **CST** | | **ADS** | |
|---|---|---|---|---|
| **f (GHz)** | **$Z_{in}$ Ω** | **$S_{21}$ dB** | **$Z_{in}$ Ω** | **$S_{21}$ dB** |
| 12.5 | $10.33 - j189.88$ | $-11.60$ | $4.48 - j189.81$ | $-14.47$ |
| 10.0 | $9.90 - j249.15$ | $-13.56$ | $4.42 - j244.90$ | $-16.40$ |
| 11.0 | $10.05 - j222.46$ | $-12.73$ | $4.43 - j220.13$ | $-15.58$ |
| 12.0 | $10.23 - j199.90$ | $-11.96$ | $4.46 - j199.15$ | $-14.86$ |
| 13.0 | $10.43 - j180.55$ | $-11.26$ | $4.50 - j181.20$ | $-14.13$ |
| 14.0 | $10.66 - j163.70$ | $-10.61$ | $4.55 - j165.48$ | $-14.13$ |

Table 5.2: Comparison of the input impedance and transmission coefficient in the *off-state*.

Once a good agreement for the *off-state* of the switch has been shown, it is important to demonstrate that both the value of $Z_h$ and of the parasitic capacitance $C_p$, used for the *off-state*, can also be used for the *on-state*. This means that the electromagnetic behaviour of the switch needs to change from an open to a short circuit, by simply replacing the capacitance $C_s$ for the resistance $R_c$. In order to demonstrate this behaviour, Table 5.3 presents the input impedances obtained from the simulation of the circuit, along with the ones from the simulation of the design in CST for the *on-state* at the frequency range of interest. The magnitudes of the $S_{21}$ are presented as well.

| | **CST** | | **ADS** | |
|---|---|---|---|---|
| **f (GHz)** | **$Z_{in}$ Ω** | **$S_{21}$ dB** | **$Z_{in}$ Ω** | **$S_{21}$ dB** |
| 12.5 | $110.10 + j2.22$ | $-0.10$ | $104.45 + j2.20$ | $-0.09$ |
| 10.0 | $110.44 + j1.83$ | $-0.06$ | $103.49 + j1.80$ | $-0.09$ |
| 11.0 | $110.30 + j1.98$ | $-0.08$ | $103.83 + j1.96$ | $-0.09$ |
| 12.0 | $110.16 + j2.14$ | $-0.09$ | $104.23 + j2.12$ | $-0.09$ |
| 13.0 | $110.04 + j2.29$ | $-0.11$ | $104.69 + j2.27$ | $-0.09$ |
| 14.0 | $109.92 + j2.46$ | $-0.12$ | $105.20 + j2.41$ | $-0.10$ |

Table 5.3: Comparison of the input impedance and transmission coefficient in the *on-state*.

A good agreement is observed between the results of both simulators. A clear change in the input impedances of the circuit is observed with positive imaginary parts suggesting an inductive behaviour. This demonstrates the change of the electromagnetic behaviour of the switch from an open to a short circuit. The low insertion loss, or high value of $S_{21}$, of around $-0.09\,dB$ for practically all the frequencies, demonstrates the transmission of power from port 1 to 2 due to the connection in series of the resistance $R_c$ of $2\Omega$ in the circuit. The difference of $5\Omega$ in the real part between the results of both scenarios is similar to that observed in the *off-state*. In spite of this difference, the similarity of the equivalent circuit to the design simulated in CST for the *on-state* is sufficiently good, taking into account that there is a good equivalence in the imaginary part of the impedances. This similarity is reflected in the magnitudes of the insertion loss with good agreement to the results obtained in CST.

This equivalent circuit allows validation of the electromagnetic behaviour that the switch presents over the contact area of the transmission line for both of its states of actuation. It also grants a first approximation of the possible lumped elements that comprise the switch. For instance, for the *off-state* the series capacitance $C_s$ of 9.1 fF only represents the capacitance that exist between the transmission line and the metal region of the switch exactly above it, and the parallel parasitic capacitance $C_p$ of 3 fF represents the capacitance between the ends of the transmission line and the electrode. Thus, according to Eq.(3.9), the capacitance $C_{\text{off}}$ is:

$$C_{\text{off}} = 9.1\,fF + 3\,fF = 12.1\,fF \tag{5.10}$$

For the *on-state*, the contact resistance $R_c$ of $2\Omega$ represents an approximation to the possible lumped elements that comprise the switch in this state, taking into account that it constitutes the resistance generated in the contact area only. Although the series resistance $R_s$ of the switch is considered to be dominated by $R_c$, it is important to obtain the value of $R_s$.

The electromagnetic modelling presented in Chapter 3 also allows calculation of the $C_{\text{off}}$, $L$, and $R_s$ from the S-parameters of the switch at each state. For instance, $C_{\text{off}}$ can be calculated from the expression in Eq.(3.14). Taking into account that the isolation of the switch (Figure 5.5) is around $-11.6\,dB$ at 12.5 GHz, $C_{\text{off}}$ can be calculated as follows:

$$C_{\text{off}} = \frac{0.26}{(2)(2\pi)(12.5\times 10^{9}\,Hz)(100\Omega)} = 16.7\,fF \tag{5.11}$$

The difference between this value with the 12.1 fF obtained from the equivalent circuit in the *off-state* indicates that the isolation is better in the circuit than in the design of the switch. This was already identified from the results in Table 5.2. However, although the difference between these two values of capacitance suggests an improvement in the accuracy of the equivalent circuit to obtain a lower difference, it was possible to demonstrate the expected behaviour of the switch in the *off-state* with a capacitance in the range of femtofarads.

The value of the inductance of the switch in the *on-state* can be calculated from the return loss of around $-38.4\,dB$, and from the expression in the Eq.(3.17) as follows:

$$L = \frac{(2)(100\Omega)(0.012)}{(2\pi)(12.5 \times 10^{9}\,Hz)} = 30.5\,pH \tag{5.12}$$

The series resistance $R_s$ of the switch in the *on-state* is calculated considering the expression presented in Chapter 3 to obtain the losses of the switch, and from the magnitude of both the return and insertion loss as follows:

$$Power\ loss = 1 - |S_{11}|^2 - |S_{21}|^2 = 1 - (0.00014) - (0.977) \sim 0.023 \tag{5.13}$$

which in decibels is around $-0.1\,dB$, and in nepers around $-0.011\,Np$. Then, from the expression in Eq.(3.10) it is possible to derive the associated resistance to the losses calculated in Eq.(5.13) as follows:

$$R_s \sim (2)(100\Omega)(0.011\,Np) \sim 2.2\Omega \tag{5.14}$$

The value of this resistance is very close to the $2\Omega$ obtained for $R_c$ of the equivalent circuit in the *on-state*, although it is important to mention that the value of $R_c$ is an approximation and any error in calculation can change the value of the insertion loss, and then a bigger difference between these two resistances. The results of these lumped elements ($C_{\text{off}}$, $L$, and $R_s$) confirm the validity of the equivalent circuit with the electromagnetic behaviour of the switch simulated in CST for both states.

However, it is necessary to implement another procedure to ratify these results, taking into account that the equivalent circuit obtained so far considers the cantilever as a segment of transmission line with high-impedance, instead of its equivalent lumped elements for a more accurate representation. It is also necessary because the expressions used to derive the values of the lumped elements from the S-parameters (Eq. 5.11-5.13) are approximations only. Therefore, another different simulation of the design in Figure 5.29 was developed in CST, placing a discrete port of $100\Omega$ exactly in the middle of the gap of the design, connecting both sides of the t-lines. This simulation was performed to obtain the input impedances in the frequency range of 10 to 14 GHz, in order to design an equivalent circuit in ADS able to present the same $Z_{in}$ at each specific frequency, and for each state of the switch, as it was done for the equivalent circuit presented before. This procedure began by simulating first the design comprised only of the transmission lines and the electrode, in order to characterize the electromagnetic behaviour of this structure separately, and to obtain its equivalent lumped elements.

Other simulations were developed next, by adding the cantilever to this structure in order to identify the effect that each state of the switch has over the structure. Therefore, the difference in the input impedance caused by each state was represented by its own equivalent lumped elements. Finally, the lumped elements of each state were connected in parallel to the ones obtained for the structure comprised of the transmission lines and the electrode. Hence, the identification of the equivalent circuit for each state. This sequential procedure is presented next. Figure 5.32 shows both the position of the port on the design used to obtain the input impedances, and the structure comprised of the transmission lines and the electrode only.

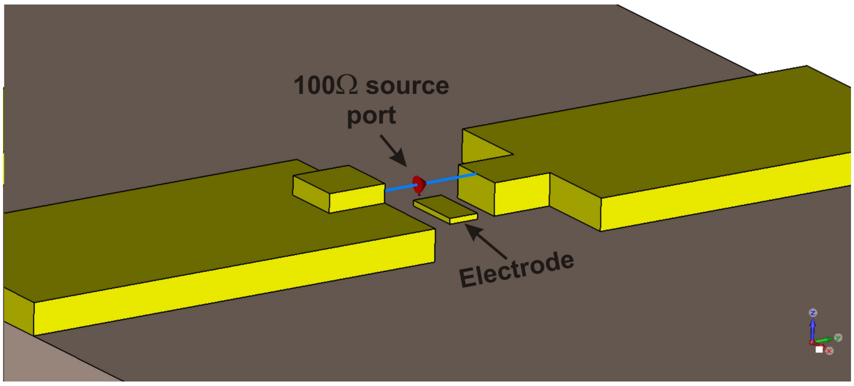

Figure 5.32: Position of the source port to obtain the $Z_{in}$ of the transmission lines with electrode.

Based on the input impedances obtained from this design, Figure 5.33 shows the equivalent circuit that presents the same input impedances for the frequency range of interest. In order to contrast the results from the design simulated in CST with the equivalent circuit, Table 5.4 compares the input impedances for the frequency range of interest. It can be seen that the real and imaginary parts from both simulators show good agreement between them for practically all the frequency range. A slight difference can be observed at some frequencies, but no critical disparity that affects the equivalence

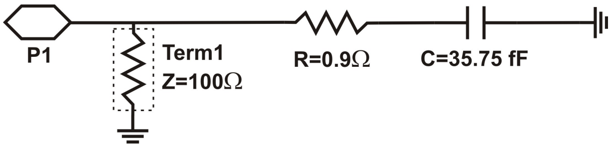

Figure 5.33: Equivalent circuit of the transmission lines with electrode.

| | **CST** | **ADS** |
|---|---|---|
| **f (GHz)** | **$Z_{in}$ Ω** | **$Z_{in}$ Ω** |
| 12.5 | $0.92 - j356.33$ | $0.90 - j356.20$ |
| 10.0 | $1.03 - j456.04$ | $0.90 - j445.18$ |
| 11.0 | $0.98 - j411.00$ | $0.90 - j404.71$ |
| 12.0 | $0.94 - j373.12$ | $0.90 - j370.99$ |
| 13.0 | $0.90 - j340.75$ | $0.90 - j342.47$ |
| 14.0 | $0.88 - j312.70$ | $0.90 - j317.99$ |

Table 5.4: Comparison of the $Z_{in}$ of the design with transmission lines and electrode.

of the circuit with the design. In order to obtain a more accurate equivalent circuit, the effect of the electrode on the design was identified and analysed. Thus, the simulation of the design in Figure 5.32 was performed again, but without the electrode, to identify the difference in the input impedance, and to develop the required change in the circuit of Figure 5.33 to obtain equivalent results. Figure 5.34 shows the modified circuit to get the same input impedances than the design in CST without electrode.

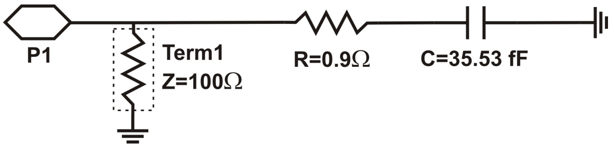

Figure 5.34: Equivalent circuit of the transmission lines without electrode.

As shown in Figure 5.34, only a slight difference in the capacitance from 35.75 fF to 35.53 fF was required to obtain equivalent input impedances. This slight modification arises from the difference in the imaginary part of the impedances presented in Table 5.5, to the ones in Table 5.4. Table 5.5 compares the input impedances of this particular design without electrode. It can be seen that the real and imaginary parts from both simulators

| | **CST** | **ADS** |
|---|---|---|
| **f (GHz)** | **$Z_{in}$ Ω** | **$Z_{in}$ Ω** |
| 12.5 | $0.92 - j358.52$ | $0.90 - j358.41$ |
| 10.0 | $1.04 - j458.99$ | $0.90 - j447.94$ |
| 11.0 | $0.98 - j413.61$ | $0.90 - j407.22$ |
| 12.0 | $0.93 - j375.44$ | $0.90 - j373.28$ |
| 13.0 | $0.90 - j342.82$ | $0.90 - j344.60$ |
| 14.0 | $0.88 - j314.55$ | $0.90 - j319.96$ |

Table 5.5: Comparison of the $Z_{in}$ of the design with transmission lines and without electrode.

show good agreement between them for practically all the frequency range, with only a slight difference at some frequencies. However, the most important point to highlight is the slight difference of around $-j2\Omega$ between the design with and without electrode. This is why only a slight change in the value of the capacitance was required. For practical purposes, this difference is very small and the effect of this particular electrode on the design is neglected. Therefore, the equivalent circuit of Figure 5.33 is used to represent the electromagnetic behaviour of the structure without cantilever, which suggests a capacitive behaviour for the frequency range of interest.

Once the equivalent circuit for this configuration of the design was obtained, another simulation was performed, adding the cantilever to the structure as shown in Figure 5.35.

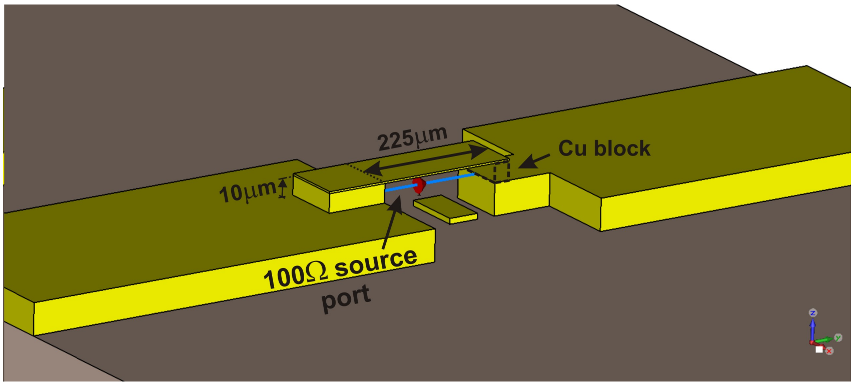

Figure 5.35: Configuration of the design used to obtain the $Z_{in}$ with the effect of the cantilever.

This figure shows the cantilever on the design with the same dimensions and configuration as in the design of Figure 5.1. It also features a Cu block used to simulate the *on-state* of the switch by creating a contact between the cantilever and the transmission line. The design with the switch in the *off-state* was first simulated in order to obtain the input impedances, and the lumped elements that, connected in parallel to the circuit in Figure 5.33, allow calculation of the equivalent impedances for the frequency range of interest. Figure 5.36 shows the equivalent circuit of the design with the switch in the *off-state*. Table 5.6 compares the input impedances of the switch in the *off-state* for the frequency range of interest. It can be seen that the real and imaginary parts from both simulators show good agreement between them for practically all the frequency range. Therefore, it can be said that this equivalent circuit represents a very good approximation to the electromagnetic behaviour of the switch in the *off-state*.

This equivalent circuit suggests that the effect of the cantilever on the design for this state can be represented by a resistance of $0.5\Omega$ in series with a capacitance of 10.75 fF. This finding is significant considering that it provides further support for the value of capacitance $C_{\text{off}}$ of 12.1 fF obtained from the equivalent circuit in Figure 5.30. The slight

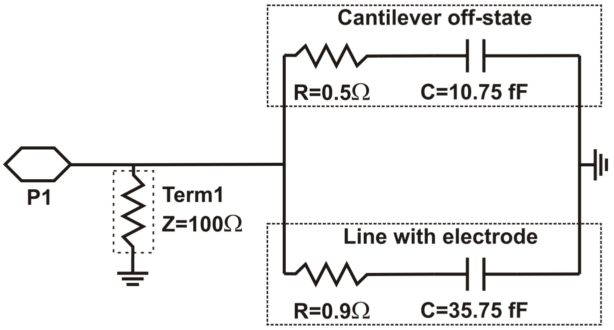

Figure 5.36: Equivalent circuit of the switch in the *off-state*.

| | **CST** | **ADS** |
|---|---|---|
| **f (GHz)** | $Z_{in}\ \Omega$ | $Z_{in}\ \Omega$ |
| 12.5 | $0.60 - j273.83$ | $0.55 - j273.85$ |
| 10.0 | $0.65 - j348.46$ | $0.55 - j342.26$ |
| 11.0 | $0.63 - j314.70$ | $0.55 - j311.15$ |
| 12.0 | $0.60 - j286.37$ | $0.55 - j285.22$ |
| 13.0 | $0.59 - j262.20$ | $0.55 - j263.30$ |
| 14.0 | $0.58 - j241.30$ | $0.55 - j244.47$ |

Table 5.6: Comparison of the $Z_{in}$ of the switch in the *off-state*.

difference between these two capacitances is because the parasitic capacitance $C_p$ of 3 fF, between the open ends of the transmission lines, that has been considered in the circuit of Figure 5.30, has not been taken into account in this circuit within the equivalent lumped elements of the cantilever. This is because $C_p$ is within the equivalent lumped elements of the structure comprised of the transmission lines and electrode only. Hence, it is possible to identify the equivalent lumped elements for the cantilever. However, if this parasitic capacitance is added to the 10.75 fF, it would be possible to say that the $C_{\text{off}}$ of this equivalent circuit is around 13.75 fF.

The same procedure was developed to obtain the equivalent circuit of the design with the switch in the *on-state*. Then, the design in Figure 5.35 was simulated with the Cu block in other to obtain the input impedances for the frequency range of interest. Based on these results, Figure 5.37 shows the equivalent circuit of the design with the switch in the *on-state*. This equivalent circuit shows a resistance of 0.08Ω in series with an inductance of 40.3 pH. This circuit suggests that the electromagnetic behaviour of the switch in the *on-state* is mainly inductive. This is observed in Table 5.7 which compares the input impedances of the switch in the *on-state* for the frequency range of interest. It can be seen that the real and imaginary parts from both simulators show good agreement between them for practically all the frequency range. For this reason, it can be said that this equivalent circuit represents a very good approximation to the electromagnetic

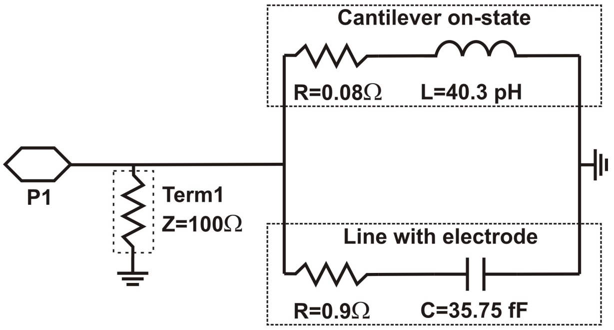

Figure 5.37: Equivalent circuit of the switch in the *on-state*.

| | **CST** | **ADS** |
|---|---|---|
| **f (GHz)** | $Z_{in}\,\Omega$ | $Z_{in}\,\Omega$ |
| 12.5 | $0.08 + j3.19$ | $0.08 + j3.19$ |
| 10.0 | $0.07 + j2.56$ | $0.08 + j2.54$ |
| 11.0 | $0.08 + j2.82$ | $0.08 + j2.80$ |
| 12.0 | $0.08 + j3.07$ | $0.08 + j3.06$ |
| 13.0 | $0.08 + j3.32$ | $0.08 + j3.32$ |
| 14.0 | $0.09 + j3.57$ | $0.08 + j3.58$ |

Table 5.7: Comparison of the $Z_{in}$ of the switch in the *on-state*.

behaviour of the switch in the *on-state*.

The equivalent lumped elements of the cantilever for this state, a resistance in series with an inductance, represent a significant finding considering that it was not possible to obtain before the inductance of 40.3 pH with the equivalent circuit in Figure 5.30. For that circuit, only the contact resistance ($R_c$) of 2Ω was obtained in the *on-state*. Comparing this resistance with the 0.08Ω acquired with this equivalent circuit, it is evident that there is an important difference. Although this is explain in more detail later when presenting the derivation of the S-parameters of the switch for both states, this difference can be reduced by increasing the value of the resistance from 0.08Ω to 1Ω without affecting the electromagnetic behaviour of the circuit in the imaginary part of the input impedances. Only a slight change is observed in the real parts by changing the resistance. This is why this equivalent circuit is considered a very good approach to the electromagnetic behaviour of the switch with the cantilever in the *on-state*. Also the inductance of 40.3 pH can be compared with the one derived in Eq.(5.12) of 30.5 pH, which suggests that the exact value is between these two inductances.

Up to this point the equivalent circuits of the RF-MEMS for its two states of actuation have been obtained from two different procedures. The first one allowed a first approximation to the lumped elements in the area of contact of the switch for each state. The second one allowed the equivalent circuit of the switch with equivalent lumped elements of the cantilever for each state. This second one granted a better characterization of the electromagnetic behaviour of the cantilever for each state by representing these effects with equivalent lumped elements. Therefore, in order to have a conclusive analysis and a better estimation of the lumped elements of the cantilever for each state, the derivation of the S-parameters are presented next, taking into account the lumped elements obtained so far for the cantilever in each state. These derivations are performed considering a two-port network with two segments of transmission lines of impedance $Z_0$ of 100Ω connected in series with the RF-MEMS.

Figure 5.38 shows the configuration of the two-port network. This figure also shows the position of the reference planes, indicated with number 1 and 2, and the incident and reflected wave of voltages, ($V_1^+$, $V_2^+$, and $V_1^-$, $V_2^-$, respectively) to calculate the S-parameters.

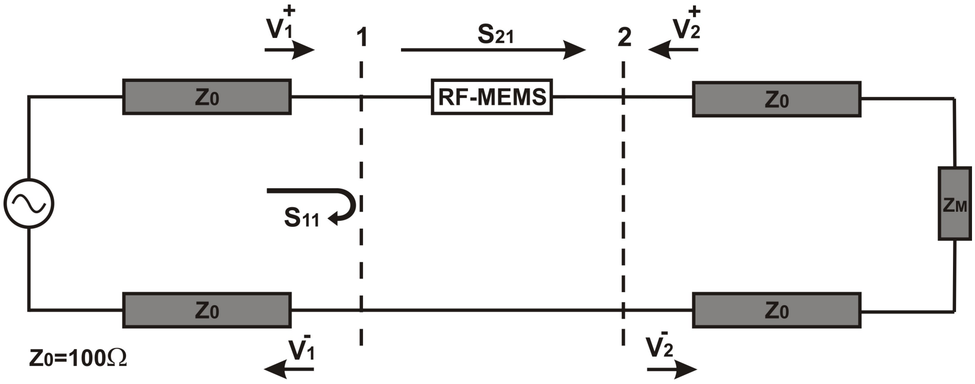

Figure 5.38: Two-port network with the RF-MEMS connected in series.

The derivation of the S-parameters for the *off-state* is obtained first, considering that the lumped elements that comprise the cantilever in this state are, a resistance of 0.5Ω in series with a capacitor $C_{\text{off}}$ of an average value of 13 fF. This capacitance was selected from the average of the $C_{\text{off}}$ obtained from the two equivalent circuits (12.1 fF&13.75 fF), taking into account that all the parasitic capacitances need to be considered in the cantilever.

The first step is to calculate the impedance of the cantilever ($Z_{\text{MEMS}}$) at 12.5 GHz from its equivalent lumped elements as follows:

$$Z_{\text{MEMS}} = 0.5 + \frac{1}{j(2\pi)(12.5 \times 10^9\, Hz)(13 \times 10^{-15}\, F)} = 0.5 - j979.4\Omega$$

The total impedance load, $Z_{TL}$, seen from port 1 is the impedance of the cantilever in series with a 100Ω load ($Z_m$) connected at port 2 to terminate it in a matched load. Therefore, $Z_{TL}$ is:

$$Z_{TL} = 100.5 - j979.4\Omega$$

Considering that the reflection coefficient, $\Gamma$, at port 1 is equal to the $S_{11}$ parameter when all the rest of the ports of the network are terminated in matched loads, this parameter is calculated as follows:

$$S_{11} = \left(\frac{V_1^-}{V_1^+}\right)_{V_2^+=0} = \Gamma = \frac{Z_{TL} - Z_0}{Z_{TL} + Z_0} = \frac{(100.5 - j979.4) - (100)}{(100.5 - j979.4) + (100)} = 0.96 - j0.19\Omega$$

then $|S_{11}| = 0.979$. In order to calculate the $S_{21}$ parameter, which is the transmission of the incident wave of voltage $V_1^+$ from port 1 to port 2, when port 2 is terminated in a matched load, it is necessary to find the relationship between the complete voltages $V_1$ and $V_2$ first. Taking into account that the configuration of the circuit can be seen as a voltage divider, the relationship between $V_1$ and $V_2$ is obtained by finding the voltage ($V_2$) in the matched load ($Z_m$) of 100Ω, when $V_1$ is considered as the source voltage. Then $V_2$ is obtained as follows:

$$V_2 = \frac{Z_m}{Z_{\text{MEMS}} + Z_m} V_1 = \frac{100}{100.5 - j979.4} V_1 = (0.01 + j0.1)V_1$$

Once the relationship between the complete voltages has been found, it is necessary to find the relationship of these with their respective incident and reflected waves of voltage as follows:

$$V_1 = V_1^+ + V_1^- = V_1^+ \left(1 + \frac{V_1^-}{V_1^+}\right) = (1 + S_{11})V_1^+$$

$$V_2 = V_2^+ + V_2^-$$

but considering that $V_2^+ = 0$ due to the termination of port 2 in matched load, then $V_2 = V_2^-$. Thus, the relationship between $V_1$ and $V_2$ is represented as follows:

$$V_2^- = (0.01 + j0.1)(1 + (0.96 - j0.19))V_1^+ = (0.038 + j0.194)V_1^+$$

Then, considering that:

$$S_{21} = \left(\frac{V_2^-}{V_1^+}\right)_{V_2^+=0}$$

it is straightforward to derive the $S_{21}$ as follows:

$$S_{21} = 0.038 + j0.194$$

with $|S_{21}| = 0.197$.

Taking into account that the two-port network with the RF-MEMS in series can be considered as reciprocal and passive, the [S]-matrix is symmetric, which means that

$S_{11}$=$S_{22}$, and $S_{21}$=$S_{12}$. Then, the [S]-matrix for the switch in *off-state* is:

$$\begin{bmatrix} S \end{bmatrix} = \begin{bmatrix} 0.96 - j0.19 & 0.038 + j0.194 \\ 0.038 + j0.194 & 0.96 - j0.19 \end{bmatrix}$$

Once the S-parameters have been calculated, it is possible to obtain the isolation from the $S_{21}$ using the expression of Eq.(5.3) as follows:

$$Iso = 20\log(0.197) = -14.1\,dB \tag{5.15}$$

This isolation is better than the one obtained from the simulation of the design in Figure 5.1 of $-11.6\,dB$. This suggests that the capacitor $C_{\text{off}}$ of 13 fF should be slightly higher. If the derivations of the S-parameters are performed again (using MATLAB) with a higher capacitance, in order to obtain a very similar isolation of around $-11.6\,dB$, then the capacitor is approximately 17 fF. This capacitance is very close to the one calculated from Eq.(5.11), from the expressions presented in Chapter 3 for the calculation of the lumped elements from the S-parameters. These results suggest that the exact value of the capacitance $C_{\text{off}}$ is between 13 fF and 17 fF.

The same procedure is developed for the derivation of the S-parameters in the *on-state* of the switch. For this derivation the lumped elements that comprise the cantilever are a resistance of 0.08Ω in series with an inductance of 40.3 pH. These lumped elements are the ones obtained from the equivalent circuit of Figure 5.37. The first step is to calculate the impedance of the cantilever, $Z_{\text{MEMS}}$, at 12.5 GHz from its equivalent lumped elements as follows:

$$Z_{\text{MEMS}} = 0.08 + j(2\pi)(12.5 \times 10^{9}\,Hz)(40.3 \times 10^{-12}\,H) = 0.08 + j3.16\Omega$$

Next, the total impedance load, $Z_{TL}$, which is the impedance of the cantilever in series with $Z_m$ of 100Ω, as follows:

$$Z_{TL} = 100.08 + j3.16\Omega$$

and the $S_{11}$ parameter:

$$S_{11} = \left(\frac{V_1^-}{V_1^+}\right)_{V_2^+=0} = \Gamma = \frac{Z_{TL} - Z_0}{Z_{TL} + Z_0} = \frac{(100.08 - j3.16) - (100)}{(100.08 - j3.16) + (100)} = 0.0006 + j0.015\Omega$$

then $|S_{11}| = 0.015$. In order to calculate the $S_{21}$ parameter, it is first necessary to find the relationship between the complete voltages $V_1$ and $V_2$, which is the same as the one considered before as a voltage divider. Thus, $V_2$ is obtained as follows:

$$V_2 = \frac{Z_m}{Z_{\text{MEMS}} + Z_m} V_1 = \frac{100}{100.08 + j3.16} V_1 = (0.99 - j0.03) V_1 \tag{5.16}$$

and considering the same relationships of the complete voltages with their incident and reflected waves of voltages:

$$V_1 = V_1^+ + V_1^- = V_1^+ \left(1 + \frac{V_1^-}{V_1^+}\right) = (1 + S_{11}) V_1^+$$

$$V_2 = V_2^+ + V_2^-$$

with $V_2^+ = 0$ due to the termination of port 2 in matched load, then $V_2 = V_2^-$. Thus, the relationship between $V_1$ and $V_2$ is represented as follows:

$$V_2^- = (0.99 - j0.03)(1 + (0.0006 + j0.015))V_1^+ = (0.99 - j0.015)V_1^+$$

and considering that:

$$S_{21} = \left(\frac{V_2^-}{V_1^+}\right)_{V_2^+=0}$$

it is straightforward to derive the $S_{21}$ as follows:

$$S_{21} = 0.99 - j0.015$$

with $|S_{21}| = 0.999$.

Taking into account that the network can be considered reciprocal and passive, the symmetric [S]-matrix for the *on-state* is:

$$\begin{bmatrix} S \end{bmatrix} = \begin{bmatrix} 0.0006 + j0.015 & 0.99 - j0.015 \\ 0.99 - j0.015 & 0.0006 + j0.015 \end{bmatrix}$$

From the derivation of these S-parameters, it is possible to calculate both the insertion and return loss according to the expressions in Eq.(5.1) and Eq.(5.2), respectively, as follows:

$$IL = 20 \log(0.999) = -0.008\, dB \tag{5.17}$$

$$RL = 20 \log(0.015) = -36.4\, dB \tag{5.18}$$

Comparing this IL with the one obtained from the simulation of the design in Figure 5.1 of $-0.1\, dB$, it is clear that the calculated IL is better than $-0.1\, dB$. This finding is significant because it suggests that the value of the resistance of 0.08Ω can be increased in order to obtain a very close value to $-0.1\,dB$, and shows that this resistance can be very similar to the one obtained from the equivalent circuit in Figure 5.30 of 2Ω.

Therefore, if the derivations of the S-parameters are performed again (using MATLAB) with a higher resistance, in order to obtain a very similar IL of around $-0.1\,dB$, the value of the resistance is 2.1Ω for an insertion loss of $-0.092\,dB$. However, with the increase of this resistance, the value of the RL is slightly varied as well, from the original $-36\,dB$ to $-34.5\,dB$. Thus, in order to have a value very near to the one obtained from the simulation in CST of $-38.4\,dB$, the value of the inductance was varied to 30 pH, which is very close to the inductance calculated from Eq.(5.12), in order to get the RL of around $-36.5\,dB$. The optimization of the inductance was performed without affecting the IL. This means that there is a trade-off between the values of the resistance and inductance. Therefore, it is possible to say that the exact inductance is likely to be between 30 pH and 40 pH, whereas the resistance is very close to 2Ω.

Hence, based on the analysis developed in this section, from the results of the equivalent circuits to the ones from the derivation of the S-parameters, it can be concluded that the lumped elements that describe the electromagnetic behaviour of the switch for each state, $C_{\text{off}}$ in the *off-state*, and both the series resistance $R_s$ and inductance $L$ in the *on-state* are:

$$\begin{aligned} 13\,fF \leq C_{\text{off}} &\leq 17\,fF \\ 30\,pH \leq L &\leq 40\,pH \\ 2\,\Omega \leq R_s &\leq 2.2\,\Omega \end{aligned} \tag{5.19}$$

Consequently, the range values for the isolation in the *off-state*, and for the insertion loss and return loss in the *on-state* are:

$$\begin{aligned} -14.1\,dB \leq Iso &\leq -11.7\,dB \\ -0.096\,dB \leq IL &\leq -0.087\,dB \\ -36.3\,dB \leq RL &\leq -34.4\,dB \end{aligned}$$

With these results it is possible to say that the contact resistance $R_c$ or $R_{on}$ is practically the same as $R_s$. This statement is based on the analysis developed in this section, and on the background of Chapter 3 which suggests that $R_s$ is dominated by $R_c$. The values of these equivalent lumped elements are significant because they ratify the good isolation, with a small $C_{\text{off}}$, and the low insertion and return loss, with a small $R_c$, of the switch.

### 5.6.1 Commutation Quality Factor

In order to complement the analysis of the electromagnetic performance of the RF-MEMS, according to [72] there is a figure-of-merit to characterize a two-state switching device called the commutation quality factor (CQF). This CQF is defined as the ratio of the input impedances ($Z_1^{in} = R_1 + jX_1$ and $Z_2^{in} = R_2 + jX_2$) of a reciprocal lossless two-port network, which presents two states characterized by the load impedance pair $Z_1$ and $Z_2$ as shown in Figure 5.39. The general expression to calculate this factor is:

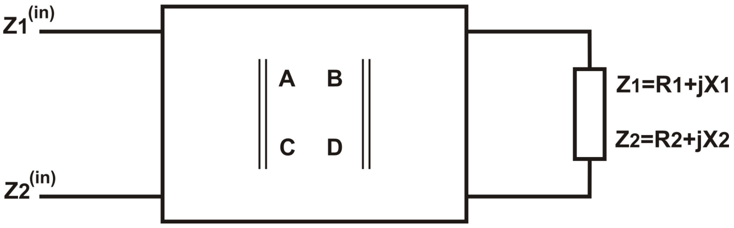

Figure 5.39: Reciprocal lossless two-port network for the derivation of the CQF.

$$K + \frac{1}{K} = \frac{R_1}{R_2} + \frac{R_2}{R_1} + \frac{(X_2 - X_1)^2}{R_1 R_2} \tag{5.20}$$

Where $K$ is the CQF, and $R_1$, $R_2$ and $X_1$, $X_2$ the real and imaginary parts of the input impedances of each state of the switch, respectively. According to [72], any switching component suitable for practical applications requires a rather large CQF, i.e. $K > 1000$. The general expression in Eq.(5.20) can be simplified in two cases:

1. For the case when the real part of the switching device is changed ($R_2 > R_1$, $X_2 = X_1$):
$$K = \frac{R_2}{R_1} \tag{5.21}$$
2. For the case when the imaginary part of the switching device is changed ($R_2 \sim R_1$, and $X_2 > X_1$):
$$K = \frac{(X_2 - X_1)^2}{R_1 R_2} \tag{5.22}$$

where Eq.(5.22) is valid for $K > 200$. Taking into account the simulations in CST of the design in Figure 5.35 for each state of the switch (Tables 5.6 and 5.7), where the imaginary parts of the input impedances are the ones that vary the most between the states, Table 5.8 presents the CQF (K) of the switch derived from Eq.(5.22), for the frequency range of 10 to 14 GHz.

Although the derivation of the CQF is with respect to an ideal lossless reciprocal network, this factor is a good tool to complement the analysis of the electromagnetic

| **f (GHz)** | $\boldsymbol{Z_{in}\,\Omega}$, ***off-state*** $\boldsymbol{Z_1}$ ***on-state*** $\boldsymbol{Z_2}$ | **CQF** (**K**×$10^6$) |
|---|---|---|
| 12.5 | $Z_1 = 0.60 - j273.83$<br>$Z_2 = 0.08 + j3.19$ | 1.59 |
| 10.0 | $Z_1 = 0.65 - j348.46$<br>$Z_2 = 0.07 + j2.56$ | 2.70 |
| 11.0 | $Z_1 = 0.63 - j314.70$<br>$Z_2 = 0.08 + j2.82$ | 2.00 |
| 12.0 | $Z_1 = 0.60 - j286.37$<br>$Z_2 = 0.08 + j3.07$ | 1.74 |
| 13.0 | $Z_1 = 0.59 - j262.20$<br>$Z_2 = 0.08 + j3.32$ | 1.49 |
| 14.0 | $Z_1 = 0.58 - j241.30$<br>$Z_2 = 0.09 + j3.57$ | 1.14 |

Table 5.8: Commutation quality factor of the RF-MEMS.

behaviour of the switch, for each state of actuation, developed so far in this chapter. It is seen from Table 5.8 that the CQF of the switch is much better than the reference value of 1000 suggested by [72] for a component suitable for practical applications.

It is important to mention that the derivations of the CQF were performed using the exact input impedances obtained from the simulations of the design in Figure 5.35 for each state, used as a reference to obtain the equivalent circuits of the switch. Based on the analysis developed for the equivalent circuit in the *on-state* (Figure 5.37), with a resistance of $0.08\Omega$ in series with an inductance of 40.3 pH, it was found that by changing the value of this resistance, up to $2\Omega$, only the real part of the input impedance varies, and the associated insertion loss is near the expected $-0.1\,dB$. Therefore, if the real part of the input impedances ($Z_2$), used to derive the CQF, are varied from 0.08 to $2\Omega$ the values of the CQF are lower than the ones presented in Table 5.8. For instance, the CQF is 63,950 for the frequency of interest at 12.5 GHz. This value is still bigger than the reference value of 1000, which implies the good performance of the switch even though the resistance is increased in order to have a more accurate result. This rather high CQF also means that the switch presents a big impedance difference between the *off-* and *on-state*, which ensures a good open and short circuit, respectively, for the frequency range of interest.

### 5.6.2 Effect of the Electrode

The last analysis of the RF-MEMS studies the effect that the electrode has over the electromagnetic behaviour of the switch. In fact, only the effect that the height of the electrode has over the isolation of the switch is analysed, taking into account that this dimension is the one that has more impact in the design, in case it is appropriate to reduce the magnitude of the *pull-down voltage*. This is because the proposed design of RF-MEMS (Figure 5.1) considers that the thickness of the transmission lines are $17\mu m$, whereas the electrode is $3\mu m$ only. Although this configuration can be changed by reducing the thickness of the transmission lines, like the physical design presented in Figure 5.26 of a switch on a microstrip line with an isolated electrode beneath the cantilever, this analysis is presented to demonstrate that the height of the electrode does not represent an important effect in the isolation.

Figure 5.40 shows the variation in the magnitude of the isolation of the RF-MEMS by increasing the height of the electrode. The effect on the *on-state* is not considered, taking into account that the increased height only represents a potential inclusion of a parasitic capacitance that does not affect the behaviour of the switch when touching down. It is important to mention that the maximum possible height of the electrode is $17\mu m$, due to the physical effect that bigger heights have for the natural operation of the cantilever. The results in Figure 5.40 show that only a slight difference in the isolation is caused from $-11.6\,dB$ to $-11.37\,dB$ with a height from $3\mu m$ to $17\mu m$, respectively. This finding is significant considering that it allows choice of any height of the electrode within this range, without significantly affecting the electromagnetic behaviour of the switch. Therefore, the height can be selected in order to reduce the required *pull-down voltage* to actuate the switch. This depends on the available voltage in the overall design of the system where the RF-MEMS switches are intended to be used. Then, the configuration of the electrode can be adapted accordingly.

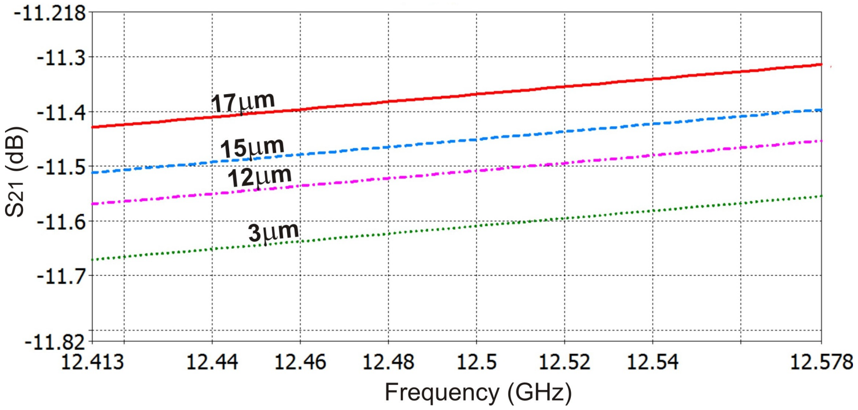

Figure 5.40: Isolation of the RF-MEMS with different heights of the electrode.

Just as an example, a mechanical simulation of the switch with an electrode of $14\mu m$ of height was developed to investigate the required force to bend down the cantilever (Figure 5.41), in order to calculate the *pull-down voltage*.

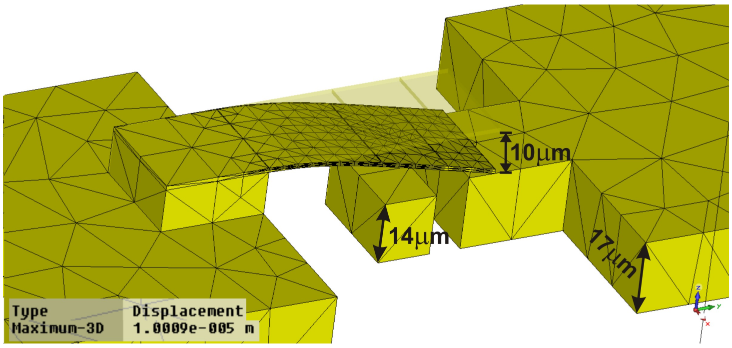

Figure 5.41: Mechanical simulation to bend down $10\mu m$ the cantilever.

This simulation was developed considering the specific zone of the cantilever where the electrostatic force actuates, according to the dimensions of the electrode. It also considers the approximation to the real capacitance that exists between the cantilever and the electrode, if the effect of the fringing fields are taken into account, as explained in Chapter 3. This means that the real capacitance is around 20% to 40 % larger than the parallel-plate capacitor between these structures. Therefore, an approximation to this effect was developed by considering that the width of the cantilever zone, where the electrostatic force actuates, is 30% bigger than the width of the electrode. This means an area of $65\mu m \times 100\mu m$ as shown in Figure 5.42.

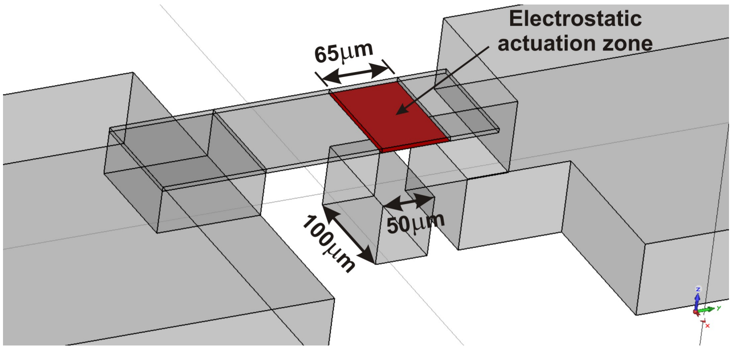

Figure 5.42: Zone of the cantilever where the electrostatic force actuates.

According to this simulation, the required force on the zone to bend down the cantilever is around $5.8\mu N$. The associated spring constant can be derived from Eq.(3.1) as follows:

$$k = \frac{F}{\Delta g} = \frac{5.8\mu N}{10\mu m} = 0.58N/m$$

then, the *pull-down voltage* can be calculated from Eq.(3.8) as follows:

$$V_p = \sqrt{\frac{8k}{27\varepsilon_0 W w}(\Delta g)^3} = \sqrt{\frac{8(0.58\,N/m)}{27(8.85 \times 10^{-12}\,F/m)(50\mu m)(100\mu m)}(10\mu m)^3} \approx 61.2\,V$$

It is important to mention that the voltage calculated here is an example only and it can be changed according to the desired height of the electrode. Nevertheless, this analysis is presented to demonstrate that the required voltage of this design can be within the usual range of 20 V to 100 V, presented in Chapter 3 for an effective switch. An approximation of the real required voltage might not exceed the 100 V for a good fabricated switch, based on the results of the electrostatic actuation of the switches built and measured in this project.

## 5.7 Analysis and Conclusions

**A novel design of DC-contact RF-MEMS cantilever switch** has been proposed, simulated, fabricated, measured, and validated using the analysis of various results. Precise mechanical and electromagnetic performance of the RF-MEMS have been validated and demonstrated. The mechanical stress produced in the anchor of the cantilever when bending down does not approach 260 MPa that the copper can withstand, allowing switching the cantilever without breaking down. The electromagnetic performance of the switch at 12.5 GHz has shown that the isolation in the *off-state* is around $-11.6\,dB$. The insertion loss is around $-0.1\,dB$, and the return loss $-38.4\,dB$ in the *on-state*. These results ensure the good performance of the switch at microwave frequencies, and its potential monolithic integration with the reconfigurable microstrip phased array antenna presented in Chapter 4.

**A cost-effective manufacturing technique** of RF-MEMS cantilever switches on commercial PCBs has been demonstrated using photolithography techniques. The effectiveness of the fabrication process has been demonstrated from the manufacturing of various switches on different configurations, from a flat surface to a microstrip line with an isolated electrode beneath the cantilever. The natural displacement of the cantilevers due to their weight is negligible and their static stability ensures that they will stay fixed while no electrostatic force is applied. A few cycles of actuation have been demonstrated with an external force without breaking down. Different aspects of the fabrication process have been identified as potential factors for the improvement of the technique, such as the material and resolution of the masks. The improvement of the alignment during the fabrication is another factor. Also, the optimization of the technique used for the liberation of the cantilever is another critical aspect in order to obtain successful switches.

**The electrostatic actuation** of various designs of switches has been demonstrated in different experiments, with an average voltage of 90 V. Several cycles of actuation have been performed with electrostatic force to demonstrate the metal-to-metal contact between the cantilever and the transmission line without breaking down.

**Measurement of the S-parameters** have been performed in the *off-* and *on-state* of different RF-MEMS, first with RF signal only, and second with both RF and DC voltage, for the actuation of the cantilever, on the same microstrip line. The analysis and agreement of the measurements with the simulations have allowed validation of the electromagnetic performance of the proposed design of RF-MEMS switch to operate with the reconfigurable phased array antenna. Good agreement between simulations and measurements of different designs of RF-MEMS has been demonstrated with an isolation average of $-9\,dB$ in the *off-state*. A difference of $-1.1\,dB$ has been identified between the simulations and measurements for the insertion loss. It is likely that this difference can be reduced if the quality of the metal-to-metal contact between the cantilever and transmission lines is improved. The measurements of the return loss have also shown good agreement with simulations of around $-15\,dB$.

**Equivalent circuits** of the RF-MEMS have been developed in order to ensure that the switch presents adequate characteristics of an open and short circuit for the frequency range of 10 to 14 GHz, and to allow validation of the design. The electromagnetic behaviour of the switch in the *off-state* for the frequency range of 10 to 14 GHz, is mainly capacitive in the range of the femtofarads to ensure an open circuit, with an approximate capacitance $C_{\text{off}}$ of 15 fF at 12.5 GHz. The electromagnetic behaviour of the switch in the *on-state* for the frequency range of 10 to 14 GHz, is mainly inductive with an approximate inductance $L$ of 35 pH, ensuring a short circuit generated by the metal-to-metal contact between the cantilever and the transmission line with a contact resistance $R_c$, or $R_{on}$, of around 2Ω. The equivalent circuits for both states of the switch have allowed a good approximation of the equivalent lumped elements of the cantilever for the *off-* and *on-state*.

**The commutation quality factor (CQF)** of the switch has been calculated to complement the electromagnetic analysis of each state of the switch. The CQF of around 63,950 at 12.5 GHz is bigger than the reference established at 1000, for a switch suitable for practical applications. This factor suggests the good electromagnetic performance of the switch, ensuring a good open and short circuit for the frequency range of 10 to 14 GHz.

The DC-contact RF-MEMS cantilever switch presented in this chapter is considered to be suitable for the monolithic integration with the reconfigurable microstrip phased array antenna presented in Chapter 4, based on the good electromagnetic performance that the switch presents on the same PCB substrate at 12.5 GHz. In order to demonstrate this, the next chapter presents the performance of the phased array using the RF-MEMS for a dynamic change of the reconfigurability of the system.

# Chapter 6

# Reconfigurable Phased Array Antenna with RF-MEMS Switches

## Contents

## 6.1 Introduction

In Chapter 4 the electronic steering of the main beam of a reconfigurable phased array antenna was demonstrated, by switching the possible connections of two 1-bit digital phase shifters of the design. The most valuable aspect of this demonstration is the possibility to develop this switching by monolithically integrating RF-MEMS switches on the same PCB. For this purpose, in Chapter 5 a novel design of a DC-contact RF-MEMS cantilever switch was developed and tested, in order to establish the precise electromagnetic characteristics of an open and short circuit switch at 12.5 GHz, to operate with the phased array. According to the hypothesis of this project, which states that good performance and low cost of phased array antennas can be achieved by monolithically integrating reliable RF-MEMS on commercial PCBs, the aim of this chapter is to demonstrate that indeed good performance of the phased array is achievable by using the RF-MEMS developed in this work. This is considering that the manufacturing technique for RF-MEMS has demonstrated the aptness of fabricating cantilever switches on commercial PCBs.

In order to demonstrate the good performance of the reconfigurable phased array with the RF-MEMS switches, Section 6.2 presents first the simulation results of the electromagnetic behaviour of the digital phase shifter with the RF-MEMS, in order to demonstrate that adequate phase shifts are obtained by switching the paths of the phase shifter employing the RF-MEMS. The magnitude of the S-parameters are also presented for each state of the phase shifter, to demonstrate its good electromagnetic performance in the frequency range of 10 to 14 GHz. Finally, Section 6.3 presents the simulation results of the reconfigurable phased array antenna with the RF-MEMS phase shifters in order to investigate and evaluate its performance.

## 6.2 Simulation of the RF-MEMS Phase Shifter

It was shown in Chapter 4 that an absolute value of phase shift of 86° is obtained from the phase shifters used on the physical designs of phased array antennas. The progressive feeding of the antennas with this relative phase shift allowed steering of the main beam to $\sim 27°$ in the H-plane. The purpose of this section is to demonstrate that a similar phase shift is obtained by changing the connections of the paths of the phase shifter using the RF-MEMS switches. Figure 6.1 shows a 3D view of the digital phase shifter with four RF-MEMS. According to the labels used in Chapter 4 for the identification of the possible connections of the paths of the phase shifter, first when the reference path is connected (RP-state), and second when the phased path is connected (PP-state), Figure 6.1 also shows the settings for the connection of the phased path, or PP-state, by placing switches 1&2 in the *on-state*, and switches 3&4 in the *off-state*. Simulations of this, and for the particular connections of the reference path as well, with switches 1&2 in the *off-state*, and 3&4 in the *on-state*, were developed in CST Microwave Studio in order to investigate both the phase of the $S_{21}$ parameter, and the magnitude of the S-parameters for each state of the phase shifter. Thus, Figure 6.2 shows both the relative phase of the

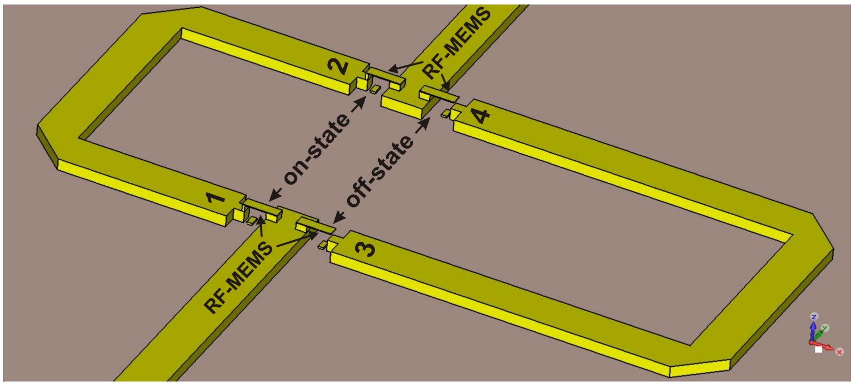

Figure 6.1: RF-MEMS phase shifter with the connection settings for the phased path.

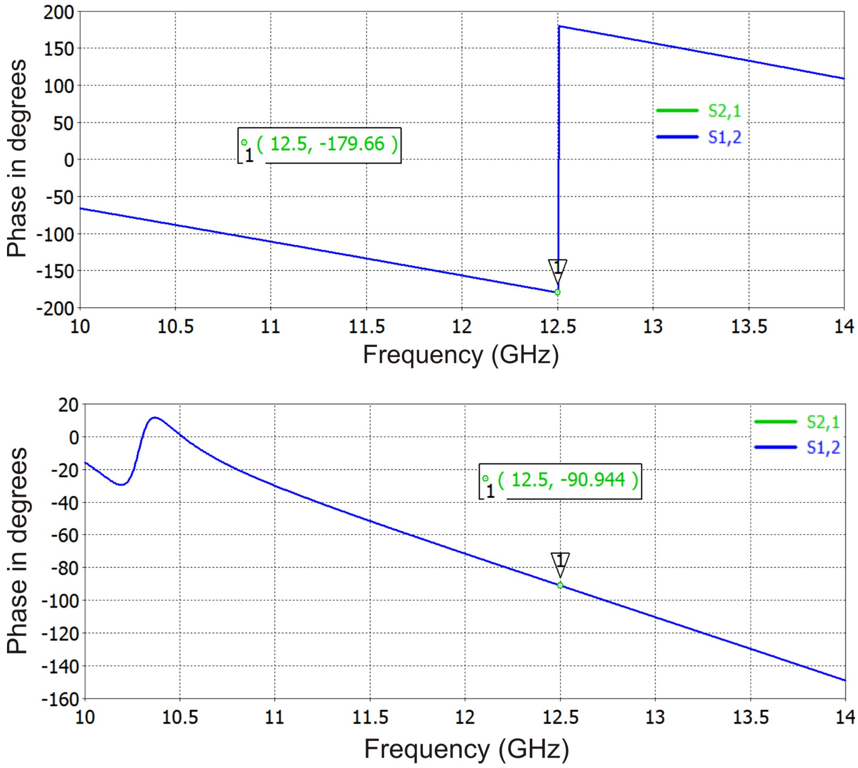

Figure 6.2: Phase shift of the $S_{21}$ for the RP-state (top), and PP-state (bottom) of the RF-MEMS phase shifter.

$S_{21}$ obtained when the reference path is connected (top), and when the phased path is connected as well (bottom). The graphs show that $-179.6°$ is obtained for the reference path and $-90.9°$ for the phased path. These phases generate an absolute phase shift of 88.7°, which is very similar to the 86° obtained without using the RF-MEMS. This slight difference can modify the direction of the steered main beam of the phased array. In order to verify the associated angle with the phase shift of 88.7°, the expression of Eq.(4.8) is solved for $\theta$, with $\phi = 90°$, as follows:

$$\theta = \sin^{-1}\left(\frac{\pm\delta_y}{\beta d_y}\right) = \sin^{-1}\left(\frac{\pm 88.7°}{187.2°}\right) = \pm 28.2° \tag{6.1}$$

The direction of the main beam should steer to $\sim 28°$ in the H-plane of the antenna. This derivation suggests that only a slight difference of $\sim 1°$ should exist with respect to the position of the main beam obtained by using the phase shifters without RF-MEMS.

The magnitude of the S-parameters for each connection of the RF-MEMS phase shifter are presented in Figure 6.3, when the reference path is connected (top), and when the phased path is connected as well (bottom). The magnitude of the S-parameters at 12.5 GHz are $-0.89\,dB$ and $-29.3\,dB$, for the $S_{21}$ and $S_{11}$, respectively, for the con-

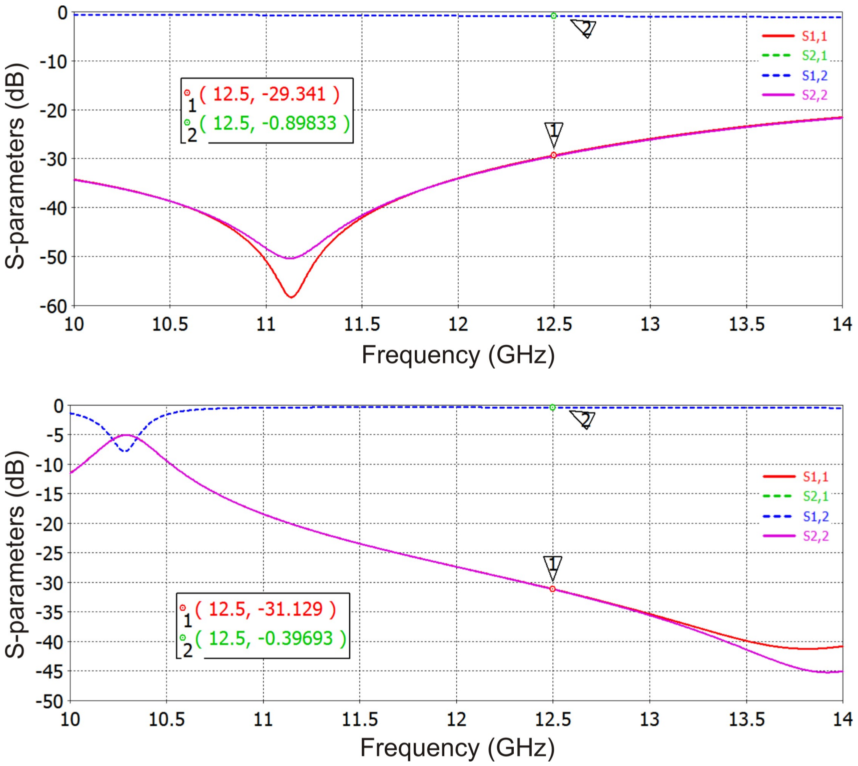

Figure 6.3: S-parameters of the RF-MEMS phase shifter for the RP-state (top), and for the PP-state (bottom).

nection of the reference path. These magnitudes are very similar to the results of the phase shifter without RF-MEMS, of $-0.52\,dB$ and $-31.2\,dB$, for the $S_{21}$ and $S_{11}$, respectively. The results for the phase shifter without RF-MEMS are slightly better, which can be attributed to the different type of configuration used for the connection of the paths. For instance, the RF-MEMS switches in the *on-state* were set by using Cu blocks for the connection between the cantilevers and the transmission lines, whereas segments of transmission lines were used to extend the paths and to close the gaps in the design without RF-MEMS. Then, less reflection and better power transmission is obtained, considering that the segments of transmission lines have the same impedance as the paths, whereas the RF-MEMS cause a change in the impedance of the transmission lines and thus a modification of the S-parameters. This variation, however, is not significant for the operation of the phased array as demonstrated later.

The magnitude of the S-parameters at 12.5 GHz for the connection of the phased path are $-0.39\,dB$ and $-31.1\,dB$, for the $S_{21}$ and $S_{11}$, respectively. Compared to those from the phase shifter without RF-MEMS, of $-0.25\,dB$ and $-32\,dB$, for the $S_{21}$ and $S_{11}$, respectively, there is only a slight difference as well. Despite these minor dissimilarities, the results show good agreement to the ones of the phase shifter without RF-MEMS, which ensures a very similar electromagnetic performance. These findings are significant because they suggest that the RF-MEMS phase shifters will work properly for the reconfigurability of the phased array, taking into account that the phase shifters without RF-MEMS have already been tested. Additionally, the input impedances of the RF-MEMS phase shifter for each connection are $(103.6 + j6.9)\Omega$ and $(97 + j0.65)\Omega$ for the reference and phased path, respectively. These results ensure a good impedance matching with approximately $100\Omega$ in the real part for both connections.

## 6.3 Reconfigurable Phased Array Antenna with RF-MEMS Phase Shifters

Once sufficient electromagnetic performance of the RF-MEMS phase shifters has been demonstrated, the purpose of this section is to demonstrate adequate performance of the reconfigurability of the phased array antenna using the RF-MEMS phase shifters. The evaluation of the performance of this design is based on the analysis of the results of its main parameters. This follows the same procedure explained in Chapter 4, where the performance of the reconfigurable phased array was demonstrated, leaving the design ready with optimum characteristics for the monolithic integration of the RF-MEMS. Therefore, as shown in Figure 6.4, eight RF-MEMS have been integrated into the design of the phased array, with four switches per phase shifter, in order to develop the required connections

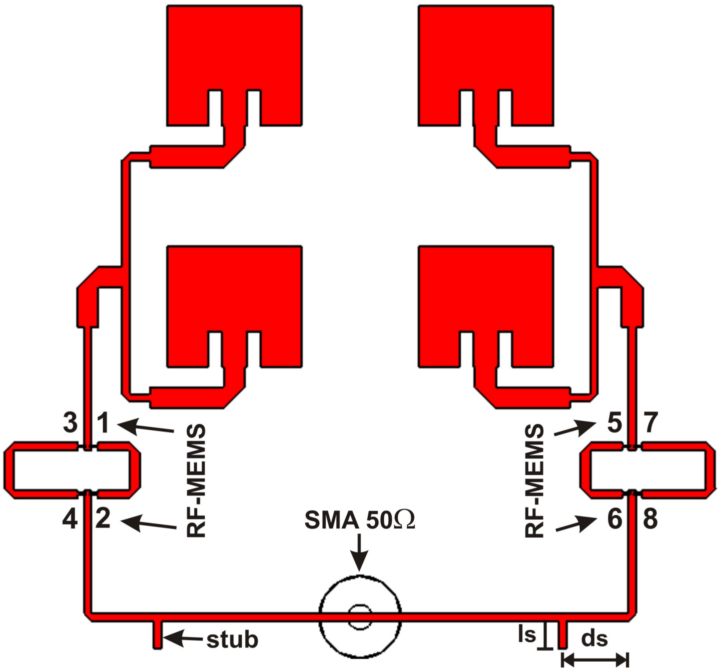

Figure 6.4: Reconfigurable phased array antenna with RF-MEMS phase shifters.

for the reconfigurability of the different states of the phased array. This means that one of the next three states can be performed by switching the RF-MEMS:

1. State 1, which means that only RF-MEMS 3&4, and 7&8 are in the *on-state*
2. State 2, which means that only RF-MEMS 3&4, and 5&6 are in the *on-state*
3. State 3, which means that only RF-MEMS 1&2, and 7&8 are in the *on-state*

The rest of the RF-MEMS that are not considered in each state, are in the *off-state*, which means that the associated paths of the phase shifters to these switches are not connected.

The reconfigurability of the phased array allows the steering of the main beam in the H-plane at −28°, 0°, or 28°, if the phased array is in states 2, 1, or 3, respectively, remembering that 0° corresponds to radiation at broadside.

The phased array with the RF-MEMS phase shifters was simulated for each state in order to investigate and analyse the results of its main electromagnetic parameters. For this purpose, the optimum values found in Chapter 4 for the position and length of the stubs ($ds$ and $ls$) were modified, due to a slight variation in the magnitude of the $S_{11}$, caused by the presence of the RF-MEMS switches on the design. This optimization was developed in order to find common values of the stubs for all the states with the lowest possible magnitude of the $S_{11}$. Then, the common optimum values obtained are: $ds = 3.3\,mm$ and $ls = 1.35\,mm$. These only present a slight difference compared to the ones obtained in Chapter 4, where $ds = 3.5\,mm$ and $ls = 1.1\,mm$. Although there is a small difference, the optimization was developed to improve the impedance matching of the phased array using the RF-MEMS. Figure 6.5 shows the magnitude of the $S_{11}$ parameter obtained for each state, with the optimum values of the stubs for this design.

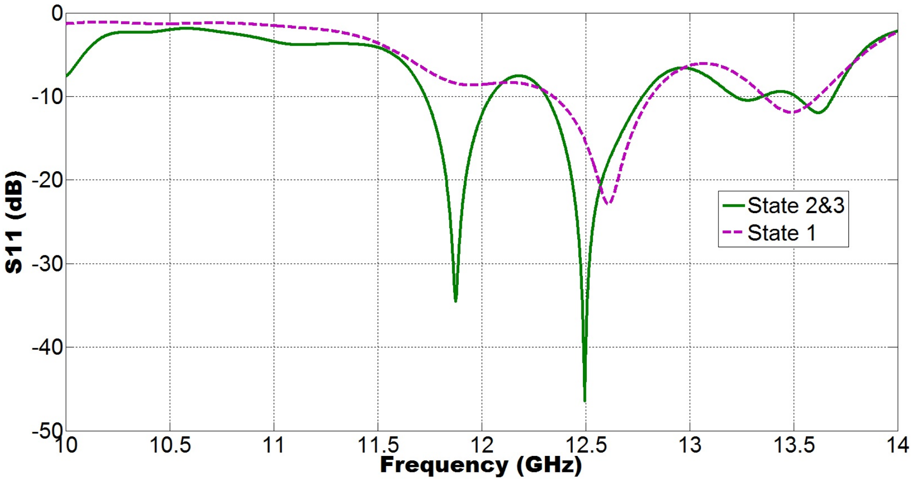

Figure 6.5: Magnitude of the $S_{11}$ for all the states of the reconfigurable phased array antenna with RF-MEMS phase shifters.

The behaviour of the magnitude of the $S_{11}$ for both states, in the frequency range of 10 to 14 GHz, is very similar to the graphs presented in Figure 4.62, where the magnitude of the $S_{11}$ at 12.5 GHz for the state 1 was around $-18.5\,dB$, compared to $-15.4\,dB$ for this design with RF-MEMS switches. Despite this difference, this magnitude still satisfies the standard established before of $\leq -15\,dB$ for finding the main resonant frequency of an antenna in the range of interest. The situation is different for the magnitude of the $S_{11}$ for the states 2&3 at 12.5 GHz, where $-31.3\,dB$ was found for the design without RF-MEMS, and $-46.4\,dB$ for this simulation. In order to compare and analyse the results obtained for the parameters of the phased array related to $S_{11}$, Table 6.1 presents these results for the design with RF-MEMS phase shifters, and Table 6.2 the results obtained from the design without them.

| | **$S_{11}$ dB** | **$Z_{in}\,\Omega$** | **VSWR** | **$BW_{-10dB}$** |
|---|---|---|---|---|
| **State 2&3** | -46.4 | 50.4+0.18j | 1.01 | 460 MHz |
| **State 1** | -15.4 | 69.7+4.65j | 1.40 | 470 MHz |

Table 6.1: Parameters related to the $S_{11}$ of the phased array with RF-MEMS phase shifters.

| | **$S_{11}$ dB** | **$Z_{in}\,\Omega$** | **VSWR** | **$BW_{-10dB}$** |
|---|---|---|---|---|
| **State 2&3** | -31.3 | 51.9-1.96j | 1.05 | 940 MHz |
| **State 1** | -18.5 | 53.0+11.8j | 1.26 | 570 MHz |

Table 6.2: Parameters related to the $S_{11}$ of the phased array without RF-MEMS.

A comparison of the results from Table 6.1 and 6.2 shows that both follow the same behaviour with better results for the states 2&3 than for the state 1. In the case of state 1, better values are found for the design without RF-MEMS than the one with them. For instance, because of the difference in the magnitude of $S_{11}$ of around $3\,dB$, the values of the input impedance, VSWR, and $BW_{-10\,dB}$ are affected and do not present as good results as that of the design without RF-MEMS. These findings suggest the need for a finer tuning for the matching impedance than the one used, either using stubs, or another technique to improve the matching. Nevertheless, the difference between these results is not critical for the radiation performance of the reconfigurable phased array, as will be explained later.

Contrarily, the results of the states 2&3 show better values for the design with RF-MEMS, except for the bandwidth of the $S_{11}$ ($BW_{-10dB}$). This narrow bandwidth is the result of the high value that $|S_{11}|$ presents within the frequency range from 12 to 12.5 GHz. If this part had been lower than $-10\,dB$, the $BW_{-10dB}$ would have been around 1 GHz, which is very similar to the value obtained from the design without the RF-MEMS. Despite these disparities, the radiation characteristics of the reconfigurable phase array with RF-MEMS phase shifters is not critically affected, as it can be seen comparing the results of the parameters related to the radiation pattern in Table 6.3 and 6.4.

| | $\boldsymbol{G}$ **dBi** | $\boldsymbol{BW^{\circ}_{-3dB}}$ | **BW** | **SLL dB** | $\boldsymbol{\theta^{\circ}}$ |
|---|---|---|---|---|---|
| **State 2&3** | 9.4 | 47.8 | 11.90-13.23 GHz=1.35 GHz | -6.2 | 28 |
| **State 1** | 8.13 | 64.9 | 12.35-13.60 GHz=1.25 GHz | -24.8 | 0 |

Table 6.3: Parameters related to the radiation pattern of the phased array with RF-MEMS phase shifters.

| | $\boldsymbol{G}$ **dBi** | $\boldsymbol{BW^{\circ}_{-3dB}}$ | **BW** | **SLL dB** | $\boldsymbol{\theta^{\circ}}$ |
|---|---|---|---|---|---|
| **State 2&3** | 9.7 | 47.6 | 11.42-13.17 GHz=1.75 GHz | -6.7 | 27 |
| **State 1** | 8.6 | 62.9 | 11.80-13.15 GHz=1.35 GHz | -25.3 | 0 |

Table 6.4: Parameters related to the radiation pattern of the phased array without RF-MEMS switches.

It can be seen from the tables that the parameters follow the same behaviour, with bigger gain for the states 2&3 than for the state 1. Only a slight difference is found between almost all of the values. For instance, contrasting the results of the states 2&3, a bigger gain is found from the design without RF-MEMS than the one with them. This can be attributed to the scan loss that exists in any phased array, considering that the steered beam is at 27° for the design without RF-MEMS, whereas the beam is at 28° for the one with them. This is manifested as well in the magnitude of the side lobe levels, where the biggest is for the design with RF-MEMS, considering that the magnitude of the main side lobe increases as the main beam is steered more. The results of the beamwidth ($BW_{-3dB}$) show good agreement between them. Comparing the bandwidth (BW), a narrow one is found for the design with RF-MEMS. This can be attributed to the fact that the design becomes more selective in frequency due to the presence of the RF-MEMS, which are designed to mainly work at 12.5 GHz.

Almost the same relation exists comparing the results of state 1, with a slightly bigger difference in the gain between the designs. These results are significant because they indicate that the radiation performance of the reconfigurable phased array with RF-MEMS phase shifters is the same as the one investigated and evaluated without them. This means that the switches work properly for the electromagnetic performance of the phased array. This finding help prove the hypothesis of this work, because with this evidence it indicates that the use of these RF-MEMS can dynamically change the reconfigurability of the phased array, and the direction of the main beam with acceptable radiation characteristics. In order to appreciate the radiation pattern of the phased array, Figure 6.6 presents its 3D view and Figure 6.7 the polar plots, for the state 2 (top), state 1 (middle), and state 3 (bottom) in each figure.

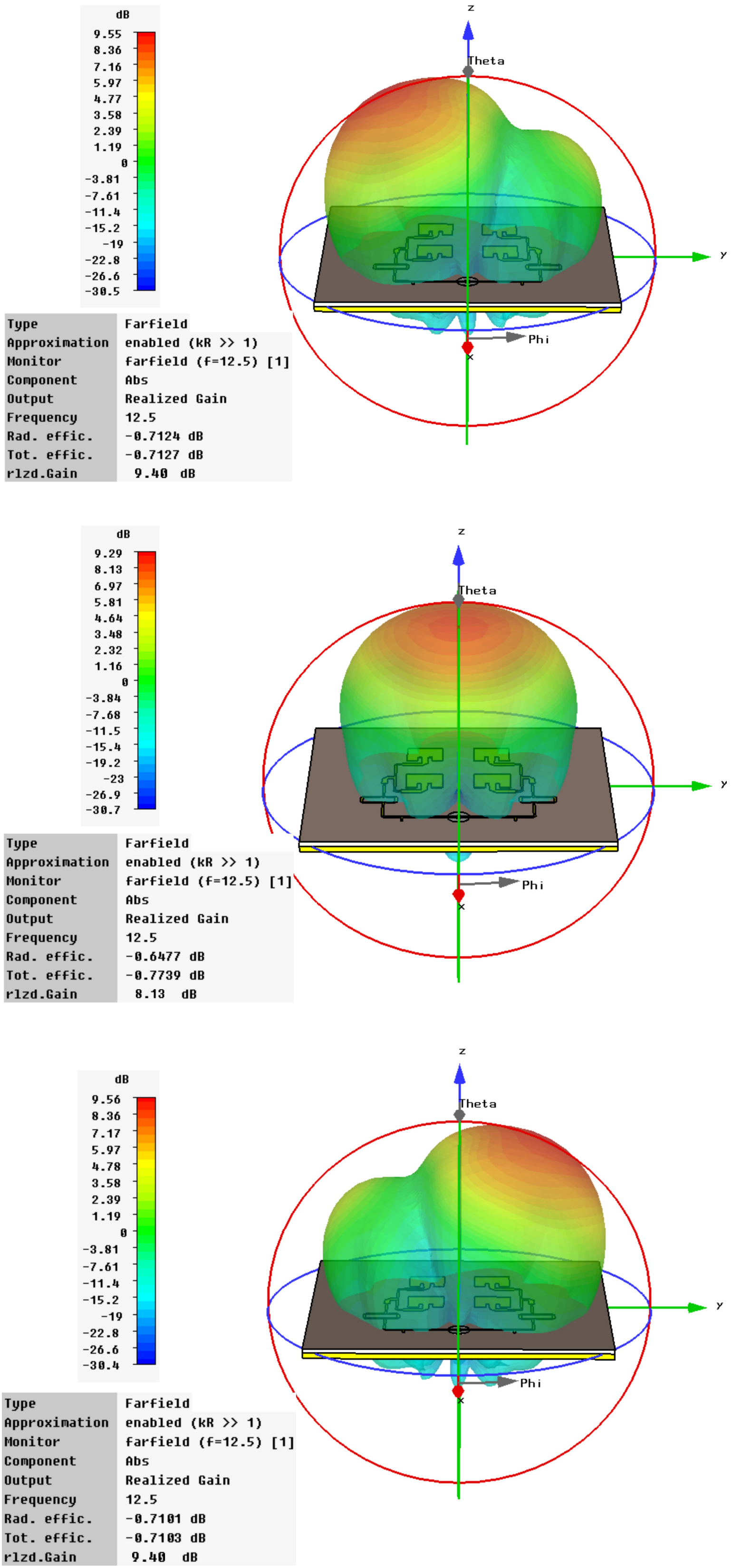

| Type | Farfield |
|---|---|
| Approximation | enabled (kR >> 1) |
| Monitor | farfield (f=12.5) [1] |
| Component | Abs |
| Output | Realized Gain |
| Frequency | 12.5 |
| Rad. effic. | -0.7124 dB |
| Tot. effic. | -0.7127 dB |
| rlzd.Gain | 9.40 dB |

| Type | Farfield |
|---|---|
| Approximation | enabled (kR >> 1) |
| Monitor | farfield (f=12.5) [1] |
| Component | Abs |
| Output | Realized Gain |
| Frequency | 12.5 |
| Rad. effic. | -0.6477 dB |
| Tot. effic. | -0.7739 dB |
| rlzd.Gain | 8.13 dB |

| Type | Farfield |
|---|---|
| Approximation | enabled (kR >> 1) |
| Monitor | farfield (f=12.5) [1] |
| Component | Abs |
| Output | Realized Gain |
| Frequency | 12.5 |
| Rad. effic. | -0.7101 dB |
| Tot. effic. | -0.7103 dB |
| rlzd.Gain | 9.40 dB |

Figure 6.6: 3D radiation pattern of the reconfigurable phased array with RF-MEMS phase shifters; state 2 (top), state 1 (middle), and state 3 (bottom).

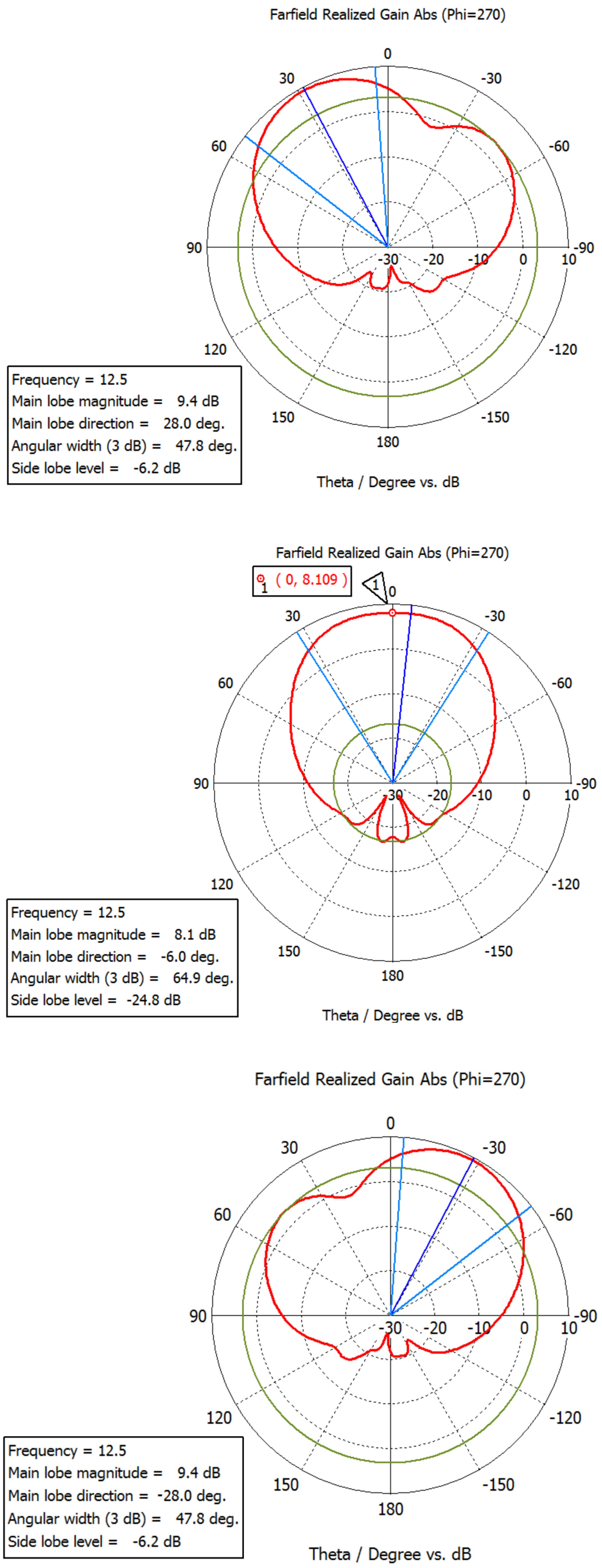

Figure 6.7: Polar plot of the radiation pattern of the reconfigurable phased array with RF-MEMS phase shifters; state 2 (top), state 1 (middle), and state 3 (bottom).

It is possible, then, to conclude that this design of reconfigurable phase array antenna with RF-MEMS phase shifters, is able to electronically steer the main beam to three different positions, as it is shown in Figure 6.8, by only manipulating the switching of the RF-MEMS for the desired direction of the beam. It is important to mention that Figure 6.8 presents the radiation patterns in linear scale.

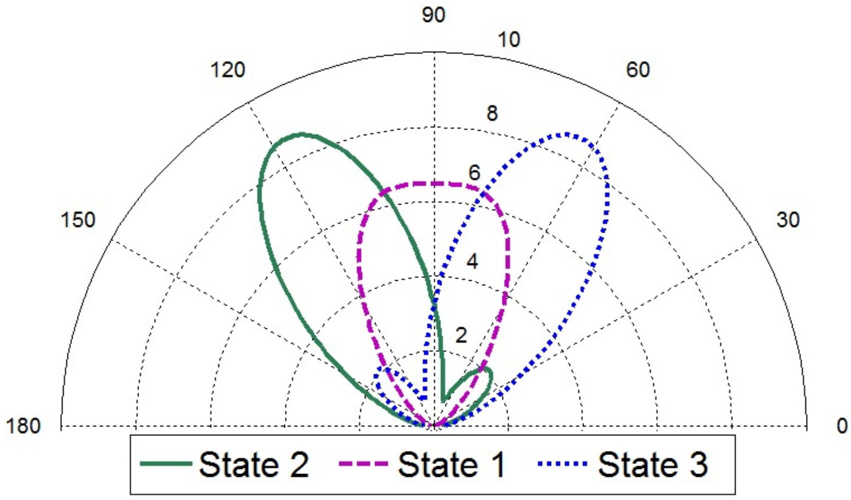

Figure 6.8: Electronically steering of the main beam of the reconfigurable phased array antenna with RF-MEMS phase shifters.

## 6.4 Conclusions

In this chapter the demonstration of the reconfigurability of an all-monolithically integrated architecture of phased array antenna with RF-MEMS phase shifters has been presented. This demonstration has been developed based on the validation of the simulations of the reconfigurable phased array antennas and RF-MEMS presented in Chapters 4 and 5, respectively. It has been proved that the electronic steering of the main beam, with acceptable radiation characteristics, can be dynamically controlled using the novel design of DC-contact RF-MEMS cantilever switch proposed in this work.

The dynamic reposition of the main beam at $\sim -28°$, $0°$, and $\sim 28°$ in the H-plane has been demonstrated by changing the connections of eight RF-MEMS placed on the two digital phase shifters. This architecture has shown a gain of around $8.1\,dBi$ and $9.4\,dBi$ for radiation at broadside and 28°, respectively, bandwidth of around 1.3 GHz, and side lobe level of around $-24\,dB$ and $-6.2\,dB$ for radiation at broadside and main beam at $\pm 28°$, respectively. It has shown also that a limited bandwidth is obtained by using the RF-MEMS in the phased array.

This finding has important implications. First, it demonstrates that the RF-MEMS is able to operate with the phased array, with precise electromagnetic characteristics to perform an open or short circuit at 12.5 GHz. Second, that various switches can be placed in the digital phase shifters without affecting the performance of the phased array. Third, it suggests that RF-MEMS switches can be fabricated on the phased array using the process developed in this work. This will allow the monolithic integration of the switches with the phase shifters. Finally, these results support the hypothesis of this work, because good performance of the phased array antenna has been demonstrated using RF-MEMS switches, whilst monolithically integrating using a cost-effective manufacturing process on a commercial PCB.

# Chapter 7

# Conclusions

## Contents

## 7.1 Summary

There has been growing research interest in developing reliable RF-MEMS switches, as such devices demonstrate distinct advantages over p-i-n diodes and GaAs FETs. Current advances in semiconductor technologies, such as SiGe, CMOS, and silicon on insulator (SOI) transistors switches have allowed production of low cost and high-performance switches for different applications, where current RF-MEMS technology cannot compete. Recent analyses, referenced at the outset of this project, however, have pointed out a wide range of applications ideally suited for RF-MEMS, where neither silicon nor GaAs technologies can meet their requirements. This is because some crucial characteristics of RF-MEMS such as high isolation, low insertion loss, and low power consumption are better than those of their counterparts at high frequencies up to 50 GHz.

One of the potential areas of application that would directly benefit from reliable RF-MEMS switches is a system of intelligent base-station antennas with scanning capabilities, particularly on the receive and low power circuit portions, such as satellite communications in the Ku-band (10.9 - 12.75 GHz) for land mobile terminals.

There are various requirements that phased array antennas and RF-MEMS technologies should meet to make an impact on the market. Phased array antennas should be of adequate performance, relative low cost, and small size, which could be provided by reliable RF-MEMS if these are fully integrated on the same board using a cost-effective technology.

Therefore, this work has addressed this problem by proposing a solution for the main requirements of phased array antennas and RF-MEMS technologies. In this project, a novel DC-contact RF-MEMS cantilever switch on a commercial PCB has been designed, fabricated, and measured at the frequency of operation of 12.5 GHz. Also, microstrip phased array antennas suitable for the monolithic integration of various RF-MEMS have been designed and measured, in order to obtain a representative architecture with acceptable radiation characteristics to demonstrate that the novel RF-MEMS is able to operate with the phased array at 12.5 GHz.

This research has been developed in sequential stages to demonstrate that good performance of an all-monolithic architecture should be obtained by integrating the novel RF-MEMS with the phased array antenna on the same PCB.

First, reconfigurable microstrip phased array antennas were designed for the frequency of operation of 12.5 GHz. Simulations and optimization of the phased arrays were developed in order to obtain acceptable performance. Next, measurements of the physical designs were performed. Finally, the suitable performance of a reconfigurable phased array antenna was demonstrated through the validation of simulations with measurements.

Second, a novel DC-contact RF-MEMS cantilever switch was designed and simulated to operate with the phased array. Then, optimization of the dimensions of the switch was carried out in order to obtain precise mechanical and electromagnetic performance at 12.5 GHz. In order to approach a solution for low cost and fully integration of RF-MEMS on the same PCB as that of the phased array, several experiments were performed until an effective manufacturing technique of switches was obtained. Then, the effectiveness of the technique was demonstrated through the fabrication and evaluation of various RF-MEMS cantilever switches. Therefore, measurements of various fabricated switches were performed to confirm their mechanical stability and electrostatic actuation for several cycles of operation. Measurements of the S-parameters of these switches were also carried out. Then, the precise mechanical and electromagnetic performance of the novel switch was demonstrated through the validation of the simulations with measurements of all the fabricated switches. Finally, the equivalent circuits and commutation quality factor of the novel switch were obtained to complement the analysis of the correct electromagnetic performance of the switch at high frequencies.

Third, once the suitable performance of both the reconfigurable microstrip phased array antenna and RF-MEMS cantilever switch were demonstrated, the integration of both was performed in a simulation, resulting in an all-monolithic architecture. Finally, the demonstration of the good performance of the phased array with RF-MEMS has been provided.

## 7.2 Achievements and Discussion

In this work, it has been demonstrated that good performance and cost-effective phased array antennas, with RF-MEMS monolithically integrated on the same PCB, are potentially viable, specifically:

1. Reconfigurable $2 \times 2$ microstrip phased array antennas have been developed and fabricated on Rogers 4003c substrate. The designs are based on two digital phase shifters implemented using the switched delay-line technique, suitable for monolithic integration of eight copper DC-contact RF-MEMS cantilever switches operating at 12.5 GHz.

   The reconfigurability of these phased arrays has been demonstrated at 12.5 GHz, measuring their radiation characteristics with the main beam steered 0° towards ±29° in the H-plane. The measurements have shown that the phased arrays provide an average gain of $8.2\,dBi$, bandwidth of 1 GHz, and side lobe level of $-26\,dB$ for radiation at broadside and $-8.2\,dB$ for radiation at ±29°. The most valuable aspect of these results is the potential of developing the dynamic reposition of the main beam by monolithically integrating RF-MEMS with the antenna elements on the same PCB.

   These phased array antennas have been designed based on a main goal of obtaining a representative architecture for the monolithic integration of the RF-MEMS for operation at 12.5 GHz. Therefore, the evaluation of the performance of these arrays has been mainly focused to show the operability of the RF-MEMS on this type of reconfigurable antennas.

2. A new manufacturing technique using photolithography processes has been developed for RF-MEMS cantilever switches based on thin copper films ($1\mu m - 2\mu m$) on Rogers 4003c substrate.

   Although this manufacturing technique is based on well-known photolitography and deposition processes, the optimization of every single step of the fabrication flow amounts for developing a new technique for this particular type of RF-MEMS, considering that the effectiveness of this technique has been demonstrated through the fabrication of various cantilever switches. The most outstanding aspect is the simplicity and the cost-effectiveness of this process. Although this manufacturing technique might only represent the demonstration of an effective fabrication process for reliable RF-MEMS on PCBs, it has been the most important stage developed in this work, because it has allowed fabrication of various switches for different measurements to validate the designs.

3. A novel DC-contact RF-MEMS cantilever switch has been developed on Rogers 4003c for operation at the frequency of 12.5 GHz.

   Precise mechanical and electromagnetic performance of the RF-MEMS have been demonstrated by comparing simulations with measurements of various fabricated switches. Several cycles of operation of the switch have been demonstrated using electrostatic force, with a pull down average voltage of 90 V. The electromagnetic performance of the RF-MEMS at 12.5 GHz has been validated, showing that the isolation in the *off-state* is $-11.6\,dB$, insertion loss is $-0.1\,dB$ and the return loss is $-38.4\,dB$ in the *on-state*. Equivalent lumped elements of the cantilever have also shown that the RF-MEMS possess a very low capacitance $C_{\mathrm{off}}$ of around 15 fF in the *off-state*, a very low resistance $R_{on}$ of around $2\Omega$ and an inductance $L$ of around 35 pH, both in the *on-state*. These lumped elements confirm the effective isolation and low insertion loss of the switch at 12.5 GHz. The most valuable aspect from the investigation of the electromagnetic performance of the switch has been its suitable behaviour to operate with phased array antennas on the same PCB.

4. An all-monolithically integrated architecture of microstrip phased array antenna with RF-MEMS has been simulated.

   The acceptable performance of this phased array has been demonstrated by electronically steering the main beam towards $-28°$, $0°$, and $28°$ in the H-plane at 12.5 GHz. This has been done by changing the connections of eight RF-MEMS implemented into the two digital phased shifters. Simulations of the architecture have shown that it provides a gain of $8.1\,dBi$ for radiation at broadside, and $9.4\,dBi$ for main beam steered towards $28°$ in the H-plane, a bandwidth of around 1.3 GHz, and side lobe level of around $-24\,dB$ for radiation at broadside and $-6.2\,dB$ for radiation towards $28°$ in the H-plane. The simulation results have also shown that the RF-MEMS are able to operate with the phased array when integrated on the same PCB, without affecting the radiation characteristics of the antennas.

The most outstanding fact is that these results strongly support the hypothesis of this work,"good performance and low cost phased array antennas can be achieved by monolithically integrating reliable RF-MEMS on commercial PCBs".

## 7.3 Analysis of the Hypothesis

Following the results presented above, it is potentially viable to fabricate an all - monolithically integrated architecture of microstrip phased array antenna with RF-MEMS on the same PCB, to dynamically change the position in space of the main beam with acceptable radiation characteristics. This approach helps to prove part of the hypothesis of this work about the good performance of an all-monolithic architecture of phased array with RF-MEMS.

The low-cost of an entire design has been partially demonstrated based on the designs, results, and analysis developed in this project. For instance, a microstrip phased array antenna built on Rogers 4003c board implies a low production cost of around £1, taking into account the low price of both the board and the fabrication of the antenna based on printing circuit processing techniques. An estimation of the fabrication cost of the RF-MEMS on the same PCB can be obtained based on the price of the photoresist and copper, which are the main two materials for the production of the switches, and on the several experimentations developed in this project for the manufacturing of the cantilevers. According to this, the production of nine switches costs around £2. This means that the cost of each switch is approximately £0.2. However, these figures are initial estimations considering that in this project it has been demonstrated only the precise electromagnetic performance of the switches to operate with the phased array at 12.5 GHz for several cycles, which means that the demonstration of the dynamic mechanical performance is missing for a reliable design of RF-MEMS able to perform billions of cycles. This can potentially increase the production cost of the RF-MEMS in the way of finding a reliable switch, taking into account that the effectiveness of the reconfigurable system will mainly depend on this feature. The production cost could also increase when building the RF-MEMS within the phased array, taking into account that this stage has not been developed in this work. For these reasons, it is possible to say that only part of the hypothesis about the low cost of an all-monolithic architecture has been proven.

Although the most important achievement in this work has been the fabrication and measurement of different copper RF-MEMS cantilever switches, for precise electromagnetic performance to operate with phased array antennas at high frequencies, this project also represents a starting point for further work to obtain a reliable RF-MEMS switch. The performance of the fabricated switches is not exactly ideal, particularly regarding their mechanical behaviour. However, this work has allowed demonstration of the principle of operation of RF-MEMS, fully accomplishing the challenge and aim of this project. Furthermore, this work has opened an attractive opportunity to continue working on this particular type of RF-MEMS, taking into account that they represent a potential solution for low cost and fully integration of RF-MEMS in different RF systems.

## 7.4 Future Work

The first task to perform is the building and characterization of the all-monolithic architecture of reconfigurable phased array antenna with RF-MEMS developed in this work. This implies designing the DC biasing network for the electrostatic actuation of the eight switches integrated on the architecture in order to perform the measurements. Once this has been done, there are a number of improvements, as well as future research to be carried out, based on the achievements of this work.

For instance, although the design of the phased array antenna presented in this project has demonstrated acceptable performance at 12.5 GHz, it is only a representative architecture that shows the operability of RF-MEMS on this type of reconfigurable systems, particularly for an attractive commercial application at this frequency, such as land mobile terminals for satellite communications in the Ku-band. Therefore, a better design in terms of gain, directivity, bandwidth, side lobe level, and polarization should be developed in order to satisfy all the specific requirements for this or other attractive applications. Another improvement would be to use other feeding techniques in order to place the feeding network out of the main plane of the antennas, to avoid radiation interference [73]. For instance, the aperture coupled feeding technique can be used to place the feeding network in the back of the structure of the architecture, leaving the antennas in the front to obtain the radiation pattern generated from these elements only. The development of this technique requires a multilayer design of at least two substrates, which could increase the complexity and production cost of the architecture. Therefore, a trade-off between cost and efficiency should be assessed if this technique is chosen. The size and shape of the digital phase shifters can be improved as well, in order to reduce the power loss related to the length of the microstrip lines used for the design [74]. For instance, if instead of using straight microstrip lines, curve lines are used to compress the overall size of each bit of the digital phase shifters, this can result in a compact layout and the overall length of the lines can be reduced. However, an effective design has to be developed in terms of impedance matching, considering that for this case the microstrip lines would be closer than the original design, generating more important interferences and mutual impedances.

Regarding RF-MEMS, it is desirable to improve the manufacturing technique in order to achieve one able to develop millions of cycles of operation. For instance, if the anchor of the switch was reinforced and the cantilever flattened, it might be possible to ensure better stability and metal-to-metal contact when switching down. This way it would be possible to perform more measurements to investigate both the mechanical and electromagnetic performance. Thus, the analysis and demonstration of the dynamic mechanical performance of the switch could be developed.

Once a precise RF-MEMS is built, further tests are required, such as switching speed, metal-to-metal contact quality, power handling, stress-stabilization, and creeping of the cantilever, in order to ensure that a reliable RF-MEMS has been obtained. As explained at the outset of this thesis, the design of a faithful RF-MEMS requires expertise in different specialized areas. Therefore, further research on these aspects is required, taking into account that there is no standard method for developing this type of switch. For instance, it might be possible to improve the metal-to-metal contact by gold plating the cantilever in this zone in order to avoid oxidation. However, the addition of the deposition of another metal for the creation of the cantilever might cause the bending of the beam and the degradation of the performance of the switch. This could also increase the production cost, considering that gold is more expensive than copper. Future research can also be carried out for an effective fabrication of an entire system comprised of phased array antenna, RF-MEMS, and DC biasing network. This means finding the best option for the all-inclusive fabrication.

Having reliable RF-MEMS built on PCB, there is interesting potential to extend these types of MEMS not only for passive phased array antennas, but also for other attractive commercial applications. This is because it has been demonstrated that the electromagnetic performance of the switch can be improved if the thickness of the PCB is reduced, then the operability of the switch can be extended to other frequency bands.

Because of all these potentials, the research carried out in this thesis represents an important contribution for further development of reliable RF-MEMS at very low cost for high frequencies, like the one presented here.

# Symbols and Abbreviations

| **Symbol** | **Unit** | **Parameter** |
|---|---|---|
| $\vec{E}$ | $V/m$ | electric field vector |
| $\vec{H}$ | $H/m$ | magnetic field vector |
| $\beta$ | $m^{-1}$ | phase constant or wave number in a medium |
| $\lambda$ | $m$ | wavelength in a medium |
| $\lambda_0$ | $m$ | wavelength in free space |
| $\lambda_g$ | $m$ | wavelength in a substrate |
| $\sigma$ | $S/m$ | electrical conductivity |
| $\rho$ | $C/m^3$ | electric charge density |
| $E$ | $V/m$ | electric field |
| $H$ | $A/m$ | magnetic field |
| $\gamma$ | $m^{-1}$ | complex propagation constant; or angle in space |
| $\omega$ | $rad/s$ | angular frequency |
| $\mu$ | $H/m$ | permeability |
| $\varepsilon$ | $F/m$ | permittivity |
| $\varepsilon_r$ | | relative dielectric constant of a medium |
| $\varepsilon_e$ | | effective dielectric constant in a microstrip line |
| $\nu_p$ | $m/s$ | phase velocity |
| $\Psi$ | $rad$ | progressive phase |
| $\delta$ | $rad$ | phase excitation |
| $d_x$ | $m$ | distance in x-axis direction |
| $d_y$ | $m$ | distance in y-axis direction |
| $\Gamma$ | | reflection coefficient |
| $T$ | | transmission coefficient |
| $v_p$ | $m/s$ | phase velocity in a microstrip line |
| $c$ | $m/s$ | speed of light |

| **Symbol** | **Unit** | **Parameter** |
|---|---|---|
| $k_0$ | $m^{-1}$ | propagation constant in free space |
| $k$ | $m^{-1}$ | propagation constant or wave number in a medium |
| $k_c$ | $m^{-1}$ | cutoff propagation constant in a medium |
| $\mu_0$ | $H/m$ | permeability in free space |
| $\varepsilon_0$ | $F/m$ | permittivity in free space |
| $Z_0$ | $\Omega$ | characteristic impedance |
| $f_r$ | Hz | resonant frequency |
| $Z_{in}$ | $\Omega$ | input impedance |
| $Y_{in}$ | $S$ | input admittance |
| $Z$ | $\Omega$ | impedance |
| $Y$ | $S$ | admittance |
| $G_{1,2}$ | $S$ | conductance |
| $B$ | $S$ | susceptance |
| $X$ | $\Omega$ | reactance |
| $Z_T$ | $\Omega$ | quarter wave transformer impedance |
| $C_{\text{off}}$ | $F$ | capacitance in the *off-state* of an RF-MEMS |
| $R_{on}$ | $\Omega$ | resistance in the *on-state* of an RF-MEMS |
| $F$ | $N$ | mechanical force |
| $F_e$ | $N$ | electric force |
| $k$ | $N/m$ | spring constant |
| $\Delta g$ | $m$ | linear deflection of a beam |
| $V_p$ | $V$ | *pull-down voltage* of an RF-MEMS |
| $Z_h$ | $\Omega$ | high impedance transmission line of a cantilever |
| $\tan\delta$ | | loss tangent |

| **Abbreviation** | **Meaning** |
|---|---|
| RF | Radio Frequency |
| RF-MEMS | Radio Frequency-MicroElectroMechanicalSystems |
| GaAs FET | Gallium Arsenide Field-Effect Transistor |
| SOI | Silicon on Insulator |
| SOS | Silicon on Sapphire |
| SiGe | Silicon-Germanium |
| CMOS | Complementary Metal-Oxide-Semiconductor |
| PCB | Printed Circuit Board |
| CPW | Coplanar Waveguide Transmission Line |
| DC | Direct Current |
| T/R | Transmitter-Receiver |
| AF | Array Factor |
| $BW_{-3\,dB}$ | Half-Power Beamwidth |
| $BW_{-10\,dB}$ | Bandwidth of the reflection coefficient below -10 dB |
| $G/T_s$ | Antenna-gain-to-noise-figure |
| $BW$ | Bandwidth of an antenna |
| $SLL$ | Side Lobe Level of an antenna |
| $SWR$ | Standing Wave Ratio |
| MMIC | Monolithic Microwave Integrated Circuits |
| WLAN | Wireless Local Area Network |
| WiMAX | Worldwide Interoperability for Microwave Access |
| SATCOM | Satellite Communications |
| TEM | Transverse Electromagnetic |
| TM | Transverse Magnetic |
| GPS | General Position System |
| GEO | Geostationary Satellite |
| LEO | Low Earth Orbit |
| DBS | Digital Broadcast Satellite |
| DVB-S | Digital Video Broadcast over Satellite |
| HEMT | High Electron Mobility Transistor |
| S-parameters | Scattering parameters |
| SPNT | Single Pole N-Throw |
| DUT | Device Under Test |
| CQF | Commutation Quality Factor |

# Bibliography

[1] C. A. Balanis, *Antenna Theory*, 2nd ed. New York, USA: John Wiley & Sons, Inc., 1997.

[2] D. Pearce, *Radio Propagation Notes and Examples.* York, UK: The University of York, 2011.

[3] R. J. Mailloux, *Phased Array Antenna Handbook*, 1st ed. Boston, MA., USA: Artech House, Inc., 2005.

[4] E. Brookner, "Phased arrays around the world - progress and future trends," in *Proc. IEEE Int Phased Array Systems and Technology Symp*, 2003, pp. 1–8.

[5] S. Stapleton and G. S. Quon, "A cellular base station phased array antenna system," in *Vehicular Technology Conference, 1993., 43rd IEEE*, 1993, pp. 93–96.

[6] J. Schoebel, T. Buck, M. Reimann, M. Ulm, M. Schneider, A. Jourdain, G. Carchon, and H. A. C. Tilmans, "Design considerations and technology assessment of phased-array antenna systems with rf mems for automotive radar applications," *Microwave Theory and Techniques, IEEE Transactions on*, vol. 53, no. 6, pp. 1968–1975, 2005.

[7] M. Geissler, F. Woetzel, M. Bottcher, S. Korthoff, A. Lauer, M. Eube, and R. Gieron, "Innovative phased array antenna for maritime satellite communications," in *Antennas and Propagation, 2009. EuCAP 2009. 3rd European Conference on*, 2009, pp. 735–739.

[8] M. Tripodi, F. DiMarca, T. Cadili, C. Mollura, F. DiMaggio, and M. Russo, "Ka band active phased array antenna system for satellite communication on the move terminal," in *Satellite Telecommunications (ESTEL), 2012 IEEE First AESS European Conference on*, 2012, pp. 1–4.

[9] R. Wallis, J. Bruzzi, and P. Malouf, "Testing of the messenger spacecraft phased-array antenna," *Antennas and Propagation Magazine, IEEE*, vol. 47, no. 1, pp. 204–209, 2005.

[10] B. Cetiner, H. Jafarkhani, J.-Y. Qian, H. J. Yoo, A. Grau, and F. De Flaviis, "Multifunctional reconfigurable mems integrated antennas for adaptive mimo systems," *Communications Magazine, IEEE*, vol. 42, no. 12, pp. 62–70, 2004.

[11] S. Vaccaro, D. L. del Rio, R. T. Sanchez, and R. Baggen, "Low cost phased array for mobile ku-band satellite terminal," in *Proc. Fourth European Conf. Antennas and Propagation (EuCAP)*, 2010, pp. 1–5.

[12] S. Vaccaro, D. Llorens del Rio, J. Padilla, and R. Baggen, "Low cost ku-band electronic steerable array antenna for mobile satellite communications," in *Antennas and Propagation (EUCAP), Proceedings of the 5th European Conference on*, 2011, pp. 2362–2366.

[13] R. Baggen, S. Holzwarth, M. Bottcher, and B. Sanadgol, "Phased array technology for mobile user terminals," in *Proc. 5th European Conf. Antennas and Propagation (EUCAP)*, 2011, pp. 2631–2635.

[14] G. M. Rebeiz, *RF MEMS: Theory, Design, and Technology*, 1st ed. New Jersey, USA: John Wiley & Sons, Inc., 2003.

[15] G. M. Rebeiz and J. B. Muldavin, "RF MEMS switches and switch circuits," vol. 2, no. 4, pp. 59–71, 2001.

[16] G. Rebeiz, C. Patel, S. Han, C.-H. Ko, and K. Ho, "The search for a reliable mems switch?: Metal-contact switches," *Microwave Magazine, IEEE*, vol. 14, no. 1, pp. 57–67, 2013.

[17] Y. Uno, K. Narise, T. Masuda, K. Inoue, Y. Adachi, K. Hosoya, T. Seki, and F. Sato, "Development of spdt-structured rf mems switch," in *Solid-State Sensors, Actuators and Microsystems Conference, 2009. TRANSDUCERS 2009. International*, 2009, pp. 541–544.

[18] J. Maciel, S. Majumder, J. Lampen, and C. Guthy, "Rugged and reliable ohmic mems switches," in *Microwave Symposium Digest (MTT), 2012 IEEE MTT-S International*, 2012, pp. 1–3.

[19] C. Patel and G. Rebeiz, "A high power temperature stable rf mems metal-contact switch with orthogonal anchors and force-enhancing stoppers," in *Microwave Symposium Digest (MTT), 2011 IEEE MTT-S International*, 2011, pp. 1–4.

[20] K.-L. Wong, *Compact and Broadband Microstrip Antennas*, 1st ed. New York, USA: John Wiley & Sons, Inc., 2002.

[21] B. Ghodsian, C. Jung, B. A. Cetiner, and F. De Flaviis, "Development of RF-MEMS switch on PCB substrates with polyimide planarization," vol. 5, no. 5, pp. 950–955, 2005.

[22] M. W. B. Silva, S. E. Barbin, and L. C. Kretly, "Fabrication and testing of RF-MEMS switches using PCB techniques," in *Proc. SBMO/IEEE MTT-S Int. Microwave and Optoelectronics Conf. (IMOC)*, 2009, pp. 96–100.

[23] R. Ramadoss, S. Lee, Y. C. Lee, V. Bright, and K. Gupta, "Fabrication, assembly, and testing of rf mems capacitive switches using flexible printed circuit technology," *Advanced Packaging, IEEE Transactions on*, vol. 26, no. 3, pp. 248–254, 2003.

[24] R. Ramadoss, S. Lee, Y. Lee, V. Bright, and K. Gupta, "Rf-mems capacitive switches fabricated using printed circuit processing techniques," *Microelectromechanical Systems, Journal of*, vol. 15, no. 6, pp. 1595–1604, 2006.

[25] H.-P. Chang, J. Qian, B. Cetiner, F. De Flaviis, M. Bachman, and G. P. Li, "Rf mems switches fabricated on microwave-laminate printed circuit boards," *Electron Device Letters, IEEE*, vol. 24, no. 4, pp. 227–229, 2003.

[26] G. Wang, D. Thompson, E. M. Tentzeris, and J. Papapolymerou, "Low cost rf mems switches using lcp substrate," in *Microwave Conference, 2004. 34th European*, vol. 3, 2004, pp. 1441–1444.

[27] A. Sundaram and R. Ramadoss, "X-band rf mems phase shifters suitable for printed phased array antennas," in *Antennas and Propagation Society International Symposium, 2004. IEEE*, vol. 4, 2004, pp. 3972–3975 Vol.4.

[28] R. Ramadoss, A. Sundaram, and L. Feldner, "Rf mems phase shifters based on pcb mems technology," *Electronics Letters*, vol. 41, no. 11, pp. 654–656, 2005.

[29] A. Sundaram, M. Maddela, R. Ramadoss, and L. M. Feldner, "MEMS-based electronically steerable antenna array fabricated using PCB technology," vol. 17, no. 2, pp. 356–362, 2008.

[30] R. J. Jr and R. Ramadoss, "A mems-based electrostatically tunable circular microstrip patch antenna," *Journal of Micromechanics and Microengineering*, vol. 17, no. 1, p. 812, 2006.

[31] B. Cetiner, J. Qian, H. Chang, M. Bachman, G. P. Li, and F. De Flaviis, "Monolithic integration of rf mems switches with a diversity antenna on pcb substrate," *Microwave Theory and Techniques, IEEE Transactions on*, vol. 51, no. 1, pp. 332–335, 2003.

[32] W. Gautier, A. Stehle, C. Siegel, B. Schoenlinner, V. Ziegler, U. Prechtel, and W. Menzel, “Hybrid integrated RF-MEMS phased array antenna at 10ghz,” in *Proc. 38th European Microwave Conf. EuMC 2008*, 2008, pp. 139–142.

[33] W. Gautier, V. Ziegler, A. Stehle, B. Schoenlinner, U. Prechtel, and W. Menzel, “RF-MEMS phased array antenna on low-loss LTCC substrate for ka-band data link,” in *Proc. European Microwave Conf. EuMC 2009*, 2009, pp. 914–917.

[34] N. Kingsley and J. Papapolymerou, “Organic “wafer-scale” packaged miniature 4-bit RF MEMS phase shifter,” vol. 54, no. 3, pp. 1229–1236, 2006.

[35] N. Kingsley, G. E. Ponchak, and J. Papapolymerou, “Reconfigurable RF MEMS phased array antenna integrated within a liquid crystal polymer (LCp) system-on-package,” vol. 56, no. 1, pp. 108–118, 2008.

[36] J. D. Kraus, *Antennas*, 2nd ed. New York, USA: McGraw-Hill, 1988.

[37] D. M. Pozar, *Microwave Engineering*, 2nd ed. New York, USA: John Wiley & Sons, Inc., 1998.

[38] C. T. P. Song, A. Mak, B. Wong, D. George, and R. D. Murch, “Compact low cost dual polarized adaptive planar phased array for WLAN,” vol. 53, no. 8, pp. 2406–2416, 2005.

[39] C.-H. Weng, H.-W. Liu, C.-H. Ku, and C.-F. Yang, “Dual circular polarisation microstrip array antenna for WLAN/WiMAX applications,” *Electronics Letters*, vol. 46, no. 9, pp. 609–611, 2010.

[40] N. Ab Wahab, Z. Bin Maslan, W. N. W. Muhamad, and N. Hamzah, “Microstrip rectangular 4x1 patch array antenna at 2.5ghz for wimax application,” in *Proc. Second Int Computational Intelligence, Communication Systems and Networks (CICSyN) Conf*, 2010, pp. 164–168.

[41] M. K. A. Rahim, A. Asrokin, M. H. Jamaluddin, M. R. Ahmad, T. Masri, and M. Z. A. A. Aziz, “Microstrip patch antenna array at 5.8 GHz for point to point communication,” in *Proc. Int. RF and Microwave Conf. RFM 2006*, 2006, pp. 216–219.

[42] R. Erickson, R. Gunnarsson, T. Martin, L.-G. Huss, L. Pettersson, P. Andersson, and A. Ouacha, “Wideband and wide scan phased array microstrip patch antennas for small platforms,” in *Proc. Second European Conf. Antennas and Propagation EuCAP 2007*, 2007, pp. 1–6.

[43] O. M. Khan, Z. Ahmad, and D. Q. Islam, “Ku band microstrip patch antenna array,” in *Proc. Int. Conf. Emerging Technologies ICET 2007*, 2007, pp. 35–40.

[44] T. F. Lai, W. Nor, L. Mahadi, and N. Soin, “Circular patch microstrip array antenna for ku-band,” 2008.

[45] P. Soontornpipit, C. Furse, and Y. C. Chung, “Design of implantable microstrip antenna for communication with medical implants,” *Microwave Theory and Techniques, IEEE Transactions on*, vol. 52, no. 8, pp. 1944–1951, 2004.

[46] P. Hooijmans, “Rf front end application and technology trends,” in *Design Automation Conference, 2003. Proceedings*, 2003, pp. 73–78.

[47] E. Lutz, H. Bischl, H. Ernst, D. Giggenbach, M. Holzbock, A. Jahn, and M. Werner, “Development and future applications of satellite communications,” in *Personal, Indoor and Mobile Radio Communications, 2004. PIMRC 2004. 15th IEEE International Symposium on*, vol. 4, 2004, pp. 2342–2346 Vol.4.

[48] E. Del Re, L. Ronga, and L. Piercucci, “Trends in satellite communications,” in *Communications, 2002. ICC 2002. IEEE International Conference on*, vol. 5, 2002, pp. 2983–2988 vol.5.

[49] R. A. Pearson, J. Vazquez, M. W. Shelley, A. Payne, V. Stoiljkovic, and M. Steel, “Next generation mobile SATcom terminal antennas for a transformed world,” in *Proc. 5th European Conf. Antennas and Propagation (EUCAP)*, 2011, pp. 2341–2345.

[50] L. Baggen, S. Vaccaro, D. Llorens del Rio, and G. Langgartner, “Compact phased arrays for mobile terminals,” in *Proc. Int. Semiconductor Conf. (CAS)*, vol. 01, 2010, pp. 3–9.

[51] R. Azadegan, “A ku-band planar antenna array for mobile satellite tv reception with linear polarization,” *Antennas and Propagation, IEEE Transactions on*, vol. 58, no. 6, pp. 2097–2101, 2010.

[52] Y. Ito and S. Yamazaki, “A mobile 12 ghz dbs television receiving system,” *Broadcasting, IEEE Transactions on*, vol. 35, no. 1, pp. 56–62, 1989.

[53] J. Guo, Z. Xu, C. Qian, and W. Dou, “An active array antenna system for satellite communication on-the-move,” in *Signals Systems and Electronics (ISSSE), 2010 International Symposium on*, vol. 2, 2010, pp. 1–4.

[54] D.-W. Kang, K.-J. Koh, and G. M. Rebeiz, "A *ku*-band two-antenna four-simultaneous beams SiGe BiCMOS phased array receiver," vol. 58, no. 4, pp. 771–780, 2010.

[55] C. Patel and G. Rebeiz, "Rf mems metal-contact switches with mn-contact and restoring forces and low process sensitivity," *Microwave Theory and Techniques, IEEE Transactions on*, vol. 59, no. 5, pp. 1230–1237, 2011.

[56] S. Gong, H. Shen, and N. S. Barker, "A 60-GHz 2-bit switched-line phase shifter using sp4t RF-MEMS switches," vol. 59, no. 4, pp. 894–900, 2011.

[57] H. Shen, S. Gong, and N. S. Barker, "DC-contact RF MEMS switches using thin-film cantilevers," in *Proc. European Microwave Integrated Circuit Conf. EuMIC 2008*, 2008, pp. 382–385.

[58] S. Gong, H. Shen, and N. S. Barker, "Study of broadband cryogenic DC-contact RF MEMS switches," vol. 57, no. 12, pp. 3442–3449, 2009.

[59] R. Stefanini, M. Chatras, P. Blondy, and G. Rebeiz, "Miniature mems switches for rf applications," *Microelectromechanical Systems, Journal of*, vol. 20, no. 6, pp. 1324–1335, 2011.

[60] I. C. Reines, C. L. Goldsmith, C. D. Nordquist, C. W. Dyck, G. M. Kraus, T. A. Plut, P. S. Finnegan, F. Austin, IV, and C. T. Sullivan, "A low loss RF MEMS ku-band integrated switched filter bank," vol. 15, no. 2, pp. 74–76, 2005.

[61] K. Y. C. H U Rahman and R. Ramer, "Cantilever beam designs for rf mems switches," *Journal of Micromechanics and Microengineering, IOP Science*, vol. 20, no. 7, 2010.

[62] "Rogers corporation," http://www.rogerscorp.com/acm/producttypes/9/RO4000-Laminates.aspx, accessed: 26-09-2013.

[63] T. Weiland, "Rf microwave simulators - from component to system design," in *Microwave Conference, 2003. 33rd European*, vol. 2, 2003, pp. 591–596 vol.2.

[64] C. A. Balanis, *Advanced Engineering Electromagnetics*, 1st ed. New York, USA: John Wiley & Sons, Inc., 1989.

[65] "Computer simulation technology," http://www.cst.com, accessed: 01-10-2013.

[66] M. Page-Jones and M. Capstick, "Single layer patch arrays exploiting a quasibalanced feeder to improve the radiation pattern," *Microwaves, Antennas and Propagation, IEE Proceedings*, vol. 146, no. 6, pp. 434–438, 1999.

[67] D. Degryse, B. Vandevelde, and E. Beyne, “Fem study of deformation and stresses in copper wire bonds on cu lowk structures during processing,” in *Electronic Components and Technology Conference, 2004. Proceedings. 54th*, vol. 1, 2004, pp. 906–912 Vol.1.

[68] S. L. Y. B. V. Ramadoss, R. Lee and K. Gupta, “Mems capacitive series switch fabricated using pcb technology,” *InterScience, Wiley Periodicals, Inc.*, vol. 17, no. 4, pp. 387–397, 2006.

[69] K. Walsh, J. Norville, and Y. chong Tai, “Photoresist as a sacrificial layer by dissolution in acetone,” in *Proc. 14th IEEE Int. Conf. Micro Electro Mechanical Systems MEMS 2001*, 2001, pp. 114–117.

[70] D. T. Mendoza-Rosales, A. E. Martynyuk, J. I. Martinez-Lopez, and J. Rodriguez-Cuevas, “Frequency selective surfaces based on ring slots loaded with monolithically integrated capacitors,” *IET Microwaves, Antennas & Propagation*, vol. 6, no. 3, pp. 245–250, 2012.

[71] G.-L. Tan and G. M. Rebeiz, “A DC-contact MEMS shunt switch,” vol. 12, no. 6, pp. 212–214, 2002.

[72] I. B. Vendik, O. G. Vendik, and E. L. Kollberg, “Commutation quality factor of two-state switchable devices,” vol. 48, no. 5, pp. 802–808, 2000.

[73] W. Yun and Y.-J. Yoon, “A wide-band aperture coupled microstrip array antenna using inverted feeding structures,” *Antennas and Propagation, IEEE Transactions on*, vol. 53, no. 2, pp. 861–862, 2005.

[74] G.-L. Tan, R. Mihailovich, J. Hacker, J. DeNatale, and G. Rebeiz, “Low-loss 2- and 4-bit ttd mems phase shifters based on sp4t switches,” *Microwave Theory and Techniques, IEEE Transactions on*, vol. 51, no. 1, pp. 297–304, 2003.